

Fully coupled Maxwell-Kohn-Sham systems:

Electromagnetic field propagation in Schrödinger-like form
and
ab initio self-consistent light-matter simulations

vorgelegt von
Diplom-Physiker

René Jestädt

ORCID: 0000-0003-4815-401X

von der Fakultät II - Mathematik und Naturwissenschaften
der Technischen Universität Berlin
zur Erlangung des akademischen Grades
Doktor der Naturwissenschaften
Dr. rer. nat.

genehmigte Dissertation

Promotionsausschuss:

Vorsitzende:	Prof. Dr. Ulrike Woggon
Gutachter:	Prof. Dr. Angel Rubio
Gutachter:	Prof. Dr. Andreas Knorr
Gutachter:	Prof. Dr. Walter Pfeiffer

Tag der wissenschaftlichen Aussprache: 10.04.2019

Berlin 2020

Abstract

Light-matter interactions have always been an essential aspect of research. They cover the main properties of light and matter in atomic and molecular systems, in condensed phase, in chemical reactions, and in optics. This thesis presents a feasible implementation to simulate three-dimensional, real-time, real-space, self-consistently coupled light-matter systems based on the theoretical background of a generalized Pauli-Fierz field theory. Due to the one-to-one correspondence between external fields and internal variables, we use a Kohn-Sham construction to approach the many-body problem in a non-relativistic low energy regime. The formalism leads in mean-field and effective nuclei approximation to coupled Ehrenfest-Maxwell-Pauli-Kohn-Sham equations.

In the first part of the thesis, we use a complex bilinear representation of the classical microscopic and macroscopic Maxwell's equations based on the Riemann-Silberstein vector. Maxwell's equations in Riemann-Silberstein representation have the form of an inhomogeneous Schrödinger equation, which allows to introduce time-evolution operators similar to quantum mechanics and to use existing time-evolution algorithms. In this manner, the Riemann-Silberstein propagation scheme can solve the microscopic Maxwell's equation in vacuum and the macroscopic ones in linear media.

Such a Riemann-Silberstein implementation for propagating electromagnetic fields requires proper boundary conditions. Therefore, we introduce incident plane wave boundaries to simulate incoming plane waves, as well as perfectly matched layer boundaries for efficient absorption.

We demonstrate our novel Riemann-Silberstein Maxwell propagation implementation for different typical electromagnetic applications, for instance, external current densities, plane wave propagation and field scattering in a linear medium. Our approach provides an alternative method of simulating electromagnetic fields compared to the standard finite-difference time-domain approach.

In the second part of the thesis, we couple the Kohn-Sham current density from our generalized Pauli-Fierz Hamiltonian self-consistently to the Riemann-Silberstein propagator, and in turn the electromagnetic field to the Kohn-Sham Hamiltonian. Including the back-reaction of the matter on the electromagnetic field goes beyond what is typically considered in literature. Starting with full minimal coupling, we derive for the Kohn-Sham Hamiltonian a multipole expansion based on the Power-Zienau-Woolley transformation.

We introduce a predictor-corrector scheme that provides a practical method to simulate self-consistent light-matter systems. Propagating both, the matter wave functions as well as the electromagnetic fields alongside, allows to improve the efficiency by exploiting the different length- and time-scales of light and matter. As a consequence of taking the back-reaction of the electromagnetic field into account,

we are able to define electromagnetic detectors next to the absorbing boundaries, which allows to analyze directly spectroscopic signals in the outgoing radiation in the far-field of the simulation box.

We present a first application of our novel approach by inducing plasmons in a nanoplasmonic system by an external laser and investigate the corresponding nano-optical effects, in particular the electromagnetic field enhancements in the vicinity of the nanoparticles. It reveals that the self-consistent fully coupled forward-backward simulations lead to significant changes in observables compared to a conventional forward-only coupling. The differences are larger than the ones found between using local density and gradient corrected approximations for the exchange-correlation functionals. Additionally, the directly measured outgoing electromagnetic fields show also harmonic generation only beyond dipole approximation.

Overall, the presented implementation is a comprehensive tool to handle fully coupled light-matter systems, especially for nano-optics, nano-plasmonics, (photo) electro-catalysis, light propagation with orbital angular momentum or light-tailored chemical reactions in optical cavities.

Deutsche Zusammenfassung

Die Wechselwirkung zwischen elektromagnetischen Feldern und Materie bildet die Basis für den Zusammenhalt von Atomen, Molekülen und Festkörpern. Während eine fundamentale Theorie der Wechselwirkung geladener Teilchen und Photonen durch die Mitte des 20. Jahrhunderts entwickelte Quantenelektrodynamik sehr exakt beschrieben wird, wird der Einfluss und die Berechnung mit steigender Teilchenzahl immer schwieriger. Aus diesem Grund werden oft vereinfachte Modelle oder Näherungen angewandt, bei denen nicht die volle Wechselwirkung berücksichtigt wird. So wird meist die Rückkopplung der Materie auf das elektromagnetische Feld vernachlässigt oder vereinfacht.

In dieser Arbeit wird auf Basis eines generalisierten Pauli-Fierz Hamiltonians die vollständige Licht-Materie Kopplung betrachtet und mithilfe der quantenelektrodynamischen Dichtefunktionaltheorie eine Methode und Implementierung vorgestellt, die realistische, dreidimensionale Licht-Materie Vielteilchensysteme simulieren kann.

Zu Beginn der Arbeit wird eine alternative Beschreibung der inhomogenen Maxwell'schen Gleichungen mit Hilfe des komplexen, bilinearen Riemann-Silberstein Vektors präsentiert. In dieser Darstellung wird das mikroskopische elektromagnetische Feld durch zwei linear unabhängige Riemann-Silberstein Vektoren beschrieben, die einmal selbst und deren Riemann-Silberstein Maxwell Gleichungen durch komplexe Konjugation ineinander übergehen.

Es kann gezeigt werden, dass mit den zwei verschiedenen Vektordarstellungen die Spin-Natur, hier in Form der Helizität, des Photonfeldes dargestellt wird. In der Riemann-Silberstein Darstellung haben die kombinierten Ampère'schen und Faraday'schen Gleichungen eine zur Schrödinger Gleichung äquivalente Form.

Damit lässt sich die zeitliche Entwicklung des elektromagnetischen Feldes durch eine quantenmechanische Propagation darstellen. Basierend auf dieser Riemann-Silberstein Formulierung wird eine Implementierung beschrieben, die die Zeitentwicklung elektromagnetischer Felder berechnet. Dazu gehören verschiedene Randbedingungen, wie einfallende ebene Wellen und absorbierende Box-Ränder, die ausgehende Signale möglichst ohne Reflexionen simuliert. Anhand mehrerer typischer Beispielanwendungen wird demonstriert, dass die Implementierung eine Alternative zur gängigen Finite-Differenzen-Methode oder Finite-Elemente-Methode für elektromagnetische Felder bietet.

Im weiteren Verlauf der Arbeit wird die klassische Stromdichte der Maxwell Gleichungen durch die quantenmechanische Betrachtung der Materie bestimmt. Dazu wird ausgehend von einem verallgemeinerten Pauli-Fierz Hamiltonian ein Kohn-Sham Hamiltonian verwendet, dessen Stromdichte direkt an das elektromagnetische Feld gekoppelt ist. In umgekehrter Richtung beeinflusst das elektromagnetische Feld die Materie durch minimale Kopplung. Ausgehend vom Prinzip der minimalen

Kopplung geht der Hamiltonian mithilfe der Power-Zienau-Woolley Transformation in einen Hamiltonian über, dessen Wechselwirkung zwischen elektromagnetischem Feld und Materie durch Multipolterme des elektromagnetischen Feldes dargestellt wird.

Damit die beiden Systeme, Materie und elektromagnetisches Feld, selbstkonsistent propagieren, wird ein Prädiktor-Korrektor-Verfahren eingeführt. Zusätzlich werden die unterschiedlichen Längen- und Zeitskalen der Systeme ausgenutzt, um eine bessere Effizienz der Implementierung vor allem bei großen Systemen zu erhalten.

Der letzte Teil der Arbeit zeigt den Einfluss der vollständigen Vorwärts-Rückwärts-Kopplung am Beispiel eines nanoplasmonischen Dimers. Es wird verglichen zwischen konventioneller, rein vorwärts gekoppelter Licht-Materie Simulation mit der hier neu entwickelten, vollständigen, selbstkonsistenten Licht-Materie Kopplung.

Die zum Teil stark abweichenden Ergebnisse werden anschaulich dargestellt und verdeutlichen die Notwendigkeit der Betrachtung einer vollständigen Licht-Materie Kopplung. Diese Einschätzung wird auch durch Berechnungen mit unterschiedlichen Dichtefunktionalen verdeutlicht, bei der die Unterschiede der Ergebnisse zwischen den Funktionalen der lokalen und gradientkorrigierten Dichtenäherung kleiner sind als die Unterschiede zwischen vorwärts und vollständiger Kopplung.

Insgesamt bietet die Implementierung damit eine praktikable Möglichkeit vollständig gekoppelte Systeme zu simulieren, z.B. für die Nanooptik, Nanoplasmonik oder Elektrokatalyse, um nur einige zu nennen.

Contents

Abstract	I
Deutsche Zusammenfassung	III
Contents	V
Introduction	1
Notation	7
1 Maxwell's equations in Riemann-Silberstein formalism	9
1.1 Riemann-Silberstein microscopic Maxwell's equations	10
1.1.1 Definition of the microscopic Riemann-Silberstein vectors . . .	10
1.1.2 Microscopic Maxwell's equations	12
1.1.3 Curl operation in representation of spin-1 matrices	13
1.1.4 Riemann-Silberstein Maxwell Hamiltonian and eigensystem . .	15
1.1.5 Combined six-component helicity Riemann-Silberstein vector .	17
1.1.6 Photon - anti-photon relation of the six-component Riemann-Silberstein vector	20
1.1.7 Scalar product of the six-component Riemann-Silberstein vector	23
1.1.8 Eigenstate expansion of the Riemann-Silberstein six-vector . .	25
1.2 Riemann-Silberstein approach for macroscopic Maxwell's equations . .	25
1.2.1 Riemann-Silberstein Maxwell's equations for a linear medium .	26
1.2.2 Definition of the macroscopic Riemann-Silberstein vectors . . .	27
1.2.3 Macroscopic Maxwell's equations	28
1.2.4 Combined helicity Riemann-Silberstein six-vector in a linear medium	31
2 Riemann-Silberstein time-evolution of Maxwell fields in Schrödinger-like form	35
2.1 Time-evolution of homogeneous microscopic Maxwell's equations . . .	35
2.2 Time-evolution of inhomogeneous microscopic Riemann-Silberstein six- vector	38
2.3 Time-evolution of macroscopic Maxwell's equations in a linear medium	41

2.4	Conservation of electric and magnetic Gauß laws in time	43
3	Implementation of the Riemann-Silberstein Maxwell propagation in the real-time real-space code Octopus	47
3.1	Discretized three-dimensional grid for the Maxwell field	48
3.1.1	Riemann-Silberstein Maxwell grid	48
3.1.2	Finite difference stencil	50
3.1.3	Parallelization strategy in the first principles code octopus . . .	55
3.2	Discretized Riemann-Silberstein time-evolution operators	55
3.3	Maxwell-propagation with Octopus	58
3.3.1	Comparison of the Octopus Maxwell-propagation with the electromagnetic propagation program MEEP	58
3.3.2	Longitudinal and transverse electromagnetic fields and currents	62
3.4	Maxwell boundaries	69
3.4.1	Absorbing boundaries by mask function	71
3.4.2	Absorbing boundaries by perfectly matched layer	73
3.4.3	Comparison of absorbing mask and perfectly matched layer boundaries	84
3.4.4	Incident plane waves boundaries	85
3.4.5	Numerical dispersion for plane waves propagation	91
3.4.6	Incident waves boundaries plus absorbing boundaries	94
3.5	Riemann-Silberstein Maxwell propagation for linear media	96
4	Theoretical fundamentals of light-matter coupling	103
4.1	Relativistic covariant notation	103
4.2	Relativistic decomposition of spin particles and derivation of Maxwell's equations	105
4.3	Multi-species Hamiltonian	110
4.4	Quantum-electrodynamical density-functional theory for multi species	116
4.5	Coupled Maxwell-Pauli-Kohn-Sham equations	118
4.6	Classical limit for Nuclei	123
5	Maxwell-Pauli-Kohn-Sham propagation on a three-dimensional grid	127
5.1	Riemann-Silberstein Maxwell's equations with Kohn-Sham current density	128
5.2	Riemann-Silberstein Maxwell propagation coupled to the Kohn-Sham current density	135
5.3	Discretized time-evolution and Time-reversal symmetry of the Maxwell system	138
5.4	Discretized time-evolution and Time-reversal symmetry of the matter system	140
5.5	Kohn-Sham interaction Hamiltonian	142
5.5.1	Full minimal coupling	142

5.5.2	Multipole expansion	143
5.5.3	Transverse Riemann-Silberstein vector calculation	145
5.6	Maxwell-Kohn-Sham multi-scale implementation	146
5.6.1	Multi-grid types	146
5.6.2	Multi-scales in time	148
5.6.3	Finite difference operators and parallelization strategy	149
5.6.4	Predictor-corrector method	151
5.6.5	Forward coupling	151
5.6.6	Forward and backward coupling	152
5.7	Ehrenfest-Maxwell-Pauli-Kohn-Sham approach	153
5.8	Simulation of open quantum systems with the Maxwell-Kohn-Sham propagation	154
5.9	Electromagnetic detectors	154
5.10	Broken time reversal symmetry	156
6	Applications	157
6.1	Laser pulse simulation scheme for a plasmonic nanoparticle system and simulation parameters	158
6.1.1	Na ₂₉₇ -dimer geometry and optical spectra	159
6.1.2	Simulation boxes and grid alignment	161
6.1.3	Measurement and detector regions	163
6.1.4	Laser pulse shape	163
6.1.5	Propagators	165
6.2	Results from Ehrenfest-Maxwell-Pauli-Kohn-Sham simulations	166
6.2.1	Electric field enhancement	169
6.2.2	Next order in multipole coupling and energies	176
6.2.3	Electromagnetic detectors and harmonic generation	179
6.2.4	Ion motion	182
6.2.5	Comparison of different density functionals	183
	Summary, conclusion and outlook	185
	Appendices	189
A	Non-relativistic Pauli Hamiltonian in Coulomb gauge	191
A.1	Vector potential and Coulomb gauge	191
A.2	Pauli-equation as non-relativistic limit of coupled light-matter systems	194
A.3	Free matter Hamiltonians	195
A.4	Photon Hamiltonian	197
A.5	Interaction Hamiltonians	203
A.5.1	Longitudinal (Coulomb) interactions	203
A.5.2	Transverse interactions	206
	List of Figures	211

Contents

List of Tables	213
Bibliography	215
Publication	226
Acronyms	228
Acknowledgements	229
Colophon	230

Introduction

The complexity of light-matter interactions for realistic systems is very challenging for a full ab initio theoretical description. In this work, we present a first feasible methodology to simulate fully coupled systems. First, we summarize in the following the state of the art how complex light-matter systems are usually considered.

One common way to describe the interaction of electromagnetic fields with matter relies on the reduction of the considered degrees of freedom. The choices for what is considered relevant depends on the aspects of interest. Historically as a consequence of this, the description of light-matter interactions has developed into different sub-fields. In case of quantum physics, one large area of research considers low-energy quantum physics which is again divided into different topics, i.e., quantum chemistry, quantum optics and solid-state physics.

Each of these research areas is focussing on different aspects of low-energy physics and is based on the assumption that the effects that are in the focus of the respective other fields are rather small. The two main different aspects in this case can be summarized as follows. In quantum chemistry and solid state physics, the electromagnetic field is typically treated as a given environment that determines material science and a focus is on a detailed description of matter. On the other hand in quantum optics, certain matter properties are prescribed and a focus is placed on the electromagnetic fields.

In this context, it becomes clear, that the theoretical methodology of considering the two topics depends on the corresponding subfield. Hence, some literature describes the matter degrees of freedom more detailed [1, 2, 3, 4], or in turn the electromagnetic fields [5, 6, 7].

While both research directions have reached significant progress in the past decades, mostly relying on the assumption of neglecting one main part, recent experiments go beyond this conventional picture into the regime, where both, light and matter, reveal a strong mutual correlation. Such strongly coupled systems, e.g., polaritons as light-matter hybrid states, can be observed when molecules are placed into nanocavities [8], microcavities [9] or other large nanostructures [10]. The large number of atoms inside nanostructures or molecules causes in most cases strong coupling effects [11], which has also an effect on a larger scale for chemical properties. As a consequence, strong electromagnetic fields can modify chemical reactions [12], changes in commonly used selection rules can be observed [13], or energy transfer can be altered [14]. Similar

to chemical reactions, the optical behavior changes significantly in strongly coupled systems.

New features in spectroscopy have been found, e.g., the enhancement of Raman processes [15], creation of polariton condensates [16] or retardation effects like energy transfer induced by attosecond laser pulses [17]. Indeed, research in strongly coupled systems has revealed neglected properties and new materials. We emphasize along these lines, e.g., detailed optical responses [18, 19], or a new color (Vantablack) arising for long nanotubes, which absorb almost any visual light [18].

Additionally, photons carrying angular momentum [20, 21, 22] have been proposed for large volume and long distance information transport [23], and even some processes in living bacteria show strong coupling effects [24].

The common underlying basis of all previously listed examples is the triad of particle species of electrons, nuclei, and photons. The ab initio description of all three kinds of particle species together in one picture is in most cases considered in a reduced form to consider only the important ones [25], since all their corresponding degrees of freedom lead to a non-feasible problem.

One way to reduce the degrees of freedom is based on the limit of a one- or two-dimensional spatial description, while keeping the full particle interactions. Here, the full rotational symmetry is missing, and all its corresponding effects.

Model systems are another option to simplify the considered degrees of freedom, which still try to catch most relevant features of the real system, but they neglect also per construction some effects. Consequently, the choice of a model system is a pre-decision which effects can be observed.

In a third way, one particle species and the corresponding degrees of freedom are only considered as an external perturbation of the system. Hence, the back-reaction on this external particle species is neglected, which always breaks the conservation of energy. The driven matter system gains too much energy when the particles get excited since they cannot screen the external electromagnetic field due to their induced current. However, in electronic structure theory, for example, photons and nuclei are typically only external variables, which leads to solvable systems [1] with different kinds of methods [26, 27, 28, 29, 30, 31, 32]. Due to the simplification of the full problem, many effects cannot be observed, which are caused by the neglected back-reaction. As a consequence, some techniques add more degrees of freedom, e.g., the electron-nucleus interaction via exact-factorization [33, 34] or trajectory-based solutions [35, 36, 37].

But taking all three interactions into account including the photon field, is up to now only considered in a very limited set of approaches. Only very recently some theoretical developments have emerged that attempt to treat matter and electromagnetic radiation on an equal ab initio footing. Examples include cases where light-matter coupling is treated classically [38, 39, 40, 41, 42, 43, 44, 45, 46] or as a quantized field [47, 48, 49, 50, 51, 52, 53, 54]. Up to now only a few works describe all three particle types on the same level of description [55, 56, 57, 58]. This leads to interesting light-matter behavior, e.g. due to modified Maxwell's equations in

vacuum [59], as well as polariton states with new potential-energy surfaces [60] or detailed chemical structures [61]. These researches followed the bottom-up direction to describe the fully coupled picture in terms of quantum electrodynamics. They provide applications to investigate the full particle interactions, but their applications are limited to few particle systems.

This is where the present work is framed and follow the opposite top-down direction of handling with a large number of particles with mass. Since it is not possible to consider the full quantum nature of such large systems especially the degrees of freedom of the photons, we introduce a semi-classical method of coupled electromagnetic mean-field and quantum-mechanical matter. This first approximation should give us an impression how strong the electromagnetic back-reaction change the results compared to conventional simulations. Additionally such a mean-field simulation provides a basis which can be expand and modified by new developed QED approaches to catch more quantum effects.

The previously discussed methods to simplify the complete problem, like neglecting nuclear motion or using the dipole approximation of the Maxwell-matter coupling are not applicable to larger realistic (three-dimensional, non-model) systems. The present work aims at describing electrons, nuclei and photons on an equal *ab initio* level. The starting point for our approach is a generalized Pauli-Fierz Hamiltonian for non-relativistic quantum electrodynamics (QED) [62, 25]. Using density functional theory, this formulation in a multi-species and multi-scale ansatz leads to coupled Maxwell-Pauli-Kohn-Sham equations (MPKS) [63].

In a first numerical application for a nanoplasmonic dimer, we demonstrate the difference of considering only the forward coupling of electromagnetic fields to matter and compare to self-consistent forward and backward coupling between light and matter. Taking this feature and varying different options, e.g., the degrees of freedom of ion motion or the multipole expansion terms for Maxwell to matter coupling, and different density functionals, gives a first overview of new effects and perspectives for self-consistent light-matter coupling. We show that common stating that missing correlations among one type of particles (e.g. electrons) is the cause for a disagreement between theory and experiment can be misleading. Instead, the cause for a discrepancy might also be the conventionally omitted self-consistent light-matter coupling.

Our first implementation based on the newly introduced theoretical technique is a comprehensive tool to investigate experimental results, or design and control novel materials. Additionally we emphasize here, that simulating the physically electromagnetic field including the back-reaction of the matter superposed with the external field has the advance to be directly detected. For instance, we can analyze the outgoing electromagnetic field at the simulation box boundaries. In contrast, conventional simulations obtain the corresponding spectroscopy indirectly by investigating only the matter reaction. Therefore, our implementation can measure the error between such usual "indirect" spectroscopy and the "real" emitted electromagnetic field.

The present PhD focuses on the combination of propagating the quantum mechanical matter, the corresponding internal and external electromagnetic fields, and their mutual coupling. Hence, we provide a mathematical and physically consistent framework to deal with in interactions of classical light with matter at arbitrary strength, length and time scales. We have organized the thesis as follows.

Using the Riemann-Silberstein vector of classical electrodynamics, we show in chapter 1 how to rewrite the microscopic Maxwell's equations in Schrödinger like form. Additionally in a similar manner, we obtain the macroscopic Maxwell's equations in linear media which requires a linear combination of the two electromagnetic helicity states of the electromagnetic field, i.e., Riemann-Silberstein vectors, which refer to different spin states.

Following the usual construction of quantum-mechanical time-evolution operators, we show in chapter 2 how to construct the Riemann-Silberstein time-evolution operators for homogeneous and inhomogeneous propagations in vacuum or linear media. In this representation, the implemented code provides a method for simulating the propagation of electromagnetic fields which is an alternative to the commonly used finite difference time domain method (FDTD) [64, 65].

Consequently, in chapter 3 we describe the practical details of the Maxwell implementation on a three-dimensional grid including useful boundary conditions as absorbing boundaries, a perfectly matched layer formulation for the Riemann-Silberstein case, incident plane waves and a combination of both. For each of these features, we demonstrate some applications to demonstrate the stand-alone electromagnetic field propagation simulation.

After introducing the novel Riemann-Silberstein electromagnetic field simulation, we summarize and introduce in chapter 4 the fundamentals of quantum electrodynamics to obtain the generalized many-body Pauli-Fierz Hamiltonian, which forms the basis to couple quantized matter variables like current and charge densities to the classical electromagnetic fields. Furthermore, we employ this Pauli-Fierz Hamiltonian to develop a density-functional theory (DFT) [66, 67] for non-relativistic QED for photons, electrons and effective nuclei on the level of a generalized quantum-electrodynamical density-functional theory (QEDFT) [62, 49, 25].

Taking the mean-field approximation of the electromagnetic field and nuclei, we arrive at coupled Ehrenfest-Maxwell-Pauli-Kohn-Sham (EMPKS) equations that build the basis for our coupled light-matter implementation, which is introduced in detail in chapter 5. This chapter also includes a discussion for using multi-scale grids and time steps to properly handle the different features of the systems, as well as full minimal-coupling and the multipole expansion, and a predictor-corrector scheme for self-consistent forward-backward coupling of light and matter.

In chapter 6, the significance of the entire forward-backward coupling is taken into account and compared to the commonly used forward-coupling in a first Maxwell-Kohn-Sham application for a nanoplasmonic system excited by a laser. Applying different simulation options, we investigate the near-field effects of the electromagnetic fields, especially their field enhancements. Furthermore, we decompose the total field into a longitudinal and transverse fields, and investigate the interference

of both transverse internal and external fields with corresponding frequency shift. The advantage of propagating the total electromagnetic fields on a numerical grid allows us to define corresponding electromagnetic detectors to analyze the outgoing electromagnetic radiation in the far-field. This provides a novel simulation tool to record commonly employed spectroscopies that are used in experiments.

In the [summary, conclusion and outlook](#), we recapitulate the complex work that was required to achieve our novel introduced methodology of considering electromagnetic field and matter fully coupled. Further, we emphasize the main aspects and results of our first applications which demonstrate that we provide a proper ab initio implementation which opens a new research area in material science and optics. Stepping forward in a field that was thought of being non-reachable means that a lot of new arising problems can be tackled in the near future. Hence, the insights of this thesis can be seen as a basic ingredient for future theoretical developments, for instance, finding methods to include QEDFT effects [52, 54, 57, 58, 25, 48].

Notation

In this thesis, we use from chapter 4 on relativistic notation, which we introduce in more detail in Sec. 4.1.

The two main aspects of the relativistic notation are the indices positions, i.e., lower or upper index, and two types of index letters, i.e., Greek or Latin letters. In both cases, the letter index represents a set of vector components or, if there are two different indices, a set of matrix elements. A pair of an identical letter with opposite positions (one upper and one lower index) in a formula represents a sum over all considered components (Einstein summation).

To sum up shortly, we have the following index notation for vector components and matrix elements with $k = \{1, 2, 3\}$, $l = \{1, 2, 3\}$, $\mu = \{0, 1, 2, 3\}$, $\nu = \{0, 1, 2, 3\}$

lower index a_k , upper index a^k for a vector \vec{a} ,
 lower indices m_{kl} , upper indices m^{kl} for a matrix m ,
 Greek index a_μ , Latin index a_k for a vector \vec{a} ,
 Greek indices $m_{\mu\nu}$, Latin indices m^{kl} for a matrix m ,
 and the Einstein summation $a_k a^k \equiv \sum_k a_k a^k$.

Besides the vector or matrix component labels as indices, we have a number of different arbitrary running indices and also symbols and names to label the considered variable. Therefore, we use in the present thesis a general label notation for variables, where italic letters indices denote a vector component or matrix element indices.

If the italic letter represents a general running index instead of an explicit vector component or matrix element, we put the running index inside parentheses. For example, The result Y gives the sum of N pairwise different variables $X_{(n)}$ and $X_{\text{lab},(n)}$ with running index n in italic letter

$$Y = \sum_{(n)}^N (X_{(n)} + X_{\text{lab},(n)}) .$$

Here, "lab" denotes an additional label with non-italic letters for the second variable X_{lab} , whereas the first one X has no extra variable label. In the same manner, we

Notation

denote an initial time as $t_{(0)}$ or concrete position vectors as $\vec{r}_{(1)}, \vec{r}_{(2)}$. In contrast, we keep for standard physical constants the usual notations, e.g.,

speed of light in vacuum c_0 ,

electric permittivity ϵ_0 ,

magnetic permeability μ_0 .

Chapter 1

Maxwell's equations in Riemann-Silberstein formalism

Classical electrodynamics describes the evolution of electric and magnetic fields, determined by the four Maxwell's equations, separately known as Ampère's law, Faraday's law, electric and magnetic Gauss law. All equations are first order differential equations. They can be classified into two groups.

The two Gauß laws, which belong to the first group, contain only first order spatial derivatives (second order if working with the scalar and vector potentials, as in standard text books).

On the other hand, Ampère's law and Faraday's law, which belong to the second group, include a first order time derivative and determine the time evolution as the underlying equations of motion for Maxwell fields (also second order in space and time in vector and scalar potential representation).

In non-relativistic quantum mechanics, the determining time-evolution equation is the Schrödinger equation which has also a first order time derivative but second order spatial derivatives. Historically it was noticed very early that Ampère's law and Faraday's law can be cast in an equivalent Schrödinger-like form [68, 69, 70, 71]. Since electromagnetic fields are given in terms of three-component vectors, the Schrödinger-form of Maxwell's equations contains a matrix-valued Hamiltonian. Taking this into account and the fact that the Maxwell's equations are Lorentz-invariant, the corresponding Maxwell Hamiltonian matrix has similarities to the four-dimensional Dirac Hamiltonian.

Indeed, we illustrate in the following that the basic form of the Maxwell-Schrödinger Hamiltonian is based on spin-1 matrices that are analogous to the Dirac gamma matrices. Based on these features, we highlight mathematical similarities of a classical Maxwell field description and quantum mechanics to emphasize the utility of this alternative representation of electrodynamics. The mathematical similarity of both physical systems become increasingly important when we consider quantum electrodynamics (QED) in chapter 4.

1.1 Riemann-Silberstein microscopic Maxwell's equations

The microscopic Maxwell's equations describe both electromagnetic fields and the matter variables i.e, charge and current density in vacuum. In 1907, Ludwik Silberstein defined a six-dimensional bilinear complex vector for the two real three-dimensional electric and magnetic fields [68]. To set up a whole basis set for arbitrary electromagnetic field superpositions, it is necessary to define two different kinds of such complex vectors, which differ only in the sign of the imaginary part. We discuss later, that both vectors can be referred to positive respectively negative helicity of light [72].

Based on the Riemann-Silberstein vector, we transform the Maxwell's equations into two complex equations by combining Faraday's law and Ampère's law and equally the two Gauß laws into one [73]. We combine the positive and negative helicity Riemann-Silberstein vectors in a six-dimensional vector and describe a formalism similar to quantum mechanics. Therefore, we introduce a curl operation identity using quantum mechanical spin-1 matrices to replace the curl operations in Faraday's and Ampère's law as well as in the Riemann-Silberstein combination. The spin-1 matrix operation is not the only similarity to equations in quantum mechanics.

We deduce, that the Riemann-Silberstein combination of Faraday's and Ampère's law is equivalent to a homogeneous time-dependent Schrödinger equation, that becomes inhomogeneous in the presence of current densities. Our formalism is based on the considerations in Ref. [72, 73]. In case of Maxwell's equations in vacuum, it is sufficient to use either the positive helicity Riemann-Silberstein vector and its Maxwell Riemann-Silberstein equations or vice versa the negative version to determine the electromagnetic fields and their propagation in time.

1.1.1 Definition of the microscopic Riemann-Silberstein vectors

The Riemann-Silberstein approach of classical electrodynamics maps both three-dimensional electromagnetic fields into one bilinear complex vector, called Riemann-Silberstein vector and generally expressed by $\vec{F}(\vec{r}, t)$ [68, 73, 74]. Due to unit considerations it is useful to multiply real part and imaginary part of \vec{F} by different factors depending on the permittivity ϵ in the real part and permeability μ in the imaginary part. In general, two complex vectors $\vec{a} + i\vec{b}$ and $\vec{a} - i\vec{b}$ with real \vec{a} , and \vec{b} are linearly independent. Hence, the Riemann-Silberstein vector can be written in two linearly independent versions, where the plus respectively minus sign between real and imaginary part is shown by a superscript sign index.

We start with the two variants of Riemann-Silberstein vectors in vacuum, denoted as $\vec{F}_+(\vec{r}, t)$ and $\vec{F}_-(\vec{r}, t)$. In the vacuum case, the electric permittivity and magnetic permeability are equal to the natural constants ϵ_0 , μ_0 , hence the two Riemann-

Silberstein vectors in vacuum are defined by [73]

$$\vec{F}_+(\vec{r}, t) = \sqrt{\frac{\epsilon_0}{2}} \vec{E}(\vec{r}, t) + i\sqrt{\frac{1}{2\mu_0}} \vec{B}(\vec{r}, t), \quad (1.1.1)$$

$$\vec{F}_-(\vec{r}, t) = \sqrt{\frac{\epsilon_0}{2}} \vec{E}(\vec{r}, t) - i\sqrt{\frac{1}{2\mu_0}} \vec{B}(\vec{r}, t), \quad (1.1.2)$$

in terms of the electric field $\vec{E}(\vec{r}, t)$ and magnetic field $\vec{B}(\vec{r}, t)$ at position \vec{r} at time t . We note here a general form for the indices notation in this thesis. Italic letters indices denote a component or running index, whereas non-italic letters and symbols names the considered variable. Additionally, italic letters and integers inside parentheses label a running index. In the following, we denote often \pm , which means $+$ or $-$ and \mp vice versa as two possible options for the sign. The upper sign option is linked to formulas for the positive defined $\vec{F}_+(\vec{r}, t)$, and consequently the lower sign option represents the ones for the negative defined $\vec{F}_-(\vec{r}, t)$.

The two vectors $\vec{F}_\pm(\vec{r}, t)$ are directly linked since they are always the complex conjugate $\vec{F}_\pm^*(\vec{r}, t)$ of each other

$$\vec{F}_-(\vec{r}, t) = \vec{F}_+^*(\vec{r}, t), \quad \vec{F}_+(\vec{r}, t) = \vec{F}_-^*(\vec{r}, t). \quad (1.1.3)$$

The two prefactors $\sqrt{\epsilon_0/2}$ and $\sqrt{1/2\mu_0}$ are selected such that the square of the absolute value of $\vec{F}_+(\vec{r}, t)$ or $\vec{F}_-(\vec{r}, t)$ results in the classical energy density $u(\vec{r}, t)$ of the Maxwell fields [73]

$$u(\vec{r}, t) = \frac{1}{2} \left(\epsilon_0 \vec{E}^2(\vec{r}, t) + \frac{1}{\mu_0} \vec{B}^2(\vec{r}, t) \right). \quad (1.1.4)$$

Therefore, the energy density $u(\vec{r}, t)$ in Eq. (1.1.4) is equal to the scalar product of two complex Riemann-Silberstein vectors with

$$u(\vec{r}, t) = \vec{F}_+^*(\vec{r}, t) \cdot \vec{F}_+(\vec{r}, t) = \vec{F}_-^*(\vec{r}, t) \cdot \vec{F}_-(\vec{r}, t). \quad (1.1.5)$$

The back transformation to obtain the electromagnetic fields $\vec{E}(\vec{r}, t)$ and $\vec{B}(\vec{r}, t)$ from the Riemann-Silberstein vectors $\vec{F}_\pm(\vec{r}, t)$ can be written as

$$\vec{E}(\vec{r}, t) = \sqrt{\frac{1}{2\epsilon_0}} \left(\vec{F}_+(\vec{r}, t) + \vec{F}_+^*(\vec{r}, t) \right) = \sqrt{\frac{1}{2\epsilon_0}} \left(\vec{F}_+(\vec{r}, t) + \vec{F}_-(\vec{r}, t) \right), \quad (1.1.6)$$

$$\vec{B}(\vec{r}, t) = -i\sqrt{\frac{\mu_0}{2}} \left(\vec{F}_+(\vec{r}, t) - \vec{F}_+^*(\vec{r}, t) \right) = -i\sqrt{\frac{\mu_0}{2}} \left(\vec{F}_+(\vec{r}, t) - \vec{F}_-(\vec{r}, t) \right). \quad (1.1.7)$$

1.1.2 Microscopic Maxwell's equations

Based on the previously defined vectors $\vec{F}_{\pm}(\vec{r}, t)$, it is possible to describe two equations which are equivalent to the microscopic Maxwell's equations with electric field $\vec{E}(\vec{r}, t)$, magnetic field $\vec{B}(\vec{r}, t)$, charge density $\rho(\vec{r}, t)$ and current density $\vec{j}(\vec{r}, t)$ in vacuum. The well known microscopic Maxwell's equations in SI units are given by [75]

$$\nabla \cdot \vec{E}(\vec{r}, t) = \epsilon_0^{-1} \rho(\vec{r}, t) , \quad (1.1.8)$$

$$\nabla \cdot \vec{B}(\vec{r}, t) = 0 , \quad (1.1.9)$$

$$\nabla \times \vec{E}(\vec{r}, t) = -\frac{\partial}{\partial t} \vec{B}(\vec{r}, t) , \quad (1.1.10)$$

$$\nabla \times \vec{B}(\vec{r}, t) = \mu_0 \left(\vec{j}(\vec{r}, t) + \epsilon_0 \frac{\partial}{\partial t} \vec{E}(\vec{r}, t) \right) . \quad (1.1.11)$$

The electric charge density contribution $\rho(\vec{r}, t)$ on the right-hand side of the electric Gauß law in Eq. (1.1.8) causes a longitudinal field component. Conversely, the contribution of the charge density can be obtained by the longitudinal field component of the electric field. In contrast, the magnetic field Gauß law in Eq. (1.1.9) shows that the magnetic field is always solenoidal at all times.

Taking these Gauß law conditions into account, the two remaining Eq. (1.1.10) and Eq. (1.1.11) determine the time-evolution of the Maxwell field. In Eq. (1.1.10) the curl of the electric field describes the time variation of the magnetic field. In contrast to Faraday's law, the time variation of the electric Field in Ampère's law depends in general on the curl of the magnetic field but also on the displacement current density $\vec{j}(\vec{r}, t)$.

In case of mapping the two relevant electromagnetic field vectors into a complex Riemann-Silberstein vector $\vec{F}_{\pm}(\vec{r}, t)$, it is possible to combine the electric and magnetic Gauß laws as well as the remaining Faraday's and Ampère's law into one equation.

The two divergence conditions in Eq. (1.1.8) and Eq. (1.1.9) represented by the two Riemann-Silberstein vectors $\vec{F}_{\pm}(\vec{r}, t)$ are given by [73]

$$\nabla \cdot \vec{F}_{\pm}(\vec{r}, t) = \sqrt{\frac{1}{2\epsilon_0}} \rho(\vec{r}, t) . \quad (1.1.12)$$

Although we obtained two equations here, one for $\vec{F}_+(\vec{r}, t)$ and one for $\vec{F}_-(\vec{r}, t)$, both Gauß laws hold in both equations simultaneously. Furthermore, the right-hand side is equal irrespectively of applying the divergence operation to positive $\vec{F}_+(\vec{r}, t)$ or negative $\vec{F}_-(\vec{r}, t)$, and emphasizes the solenoidal magnetic vector field in the imaginary part. The difference between the positive or negative version of Eq. (1.1.12) consists of the intrinsic positive helicity described by the $\vec{F}_+(\vec{r}, t)$ version or negative

helicity for the $\vec{F}_-(\vec{r}, t)$ version which we consider later in this section.

In a similar way, the two time-derivative Maxwell's equations, Faraday's law in Eq. (1.1.10) and Ampère's law in Eq. (1.1.11), can be written in terms of the Riemann-Silberstein vectors defined in Eq. (1.1.1) and Eq. (1.1.2) and the speed of light in vacuum $c_0 = \frac{1}{\sqrt{\epsilon_0 \mu_0}}$. We arrive at the form [73]

$$i \frac{\partial}{\partial t} \vec{F}_\pm(\vec{r}, t) = \pm c_0 \vec{\nabla} \times \vec{F}_\pm(\vec{r}, t) - i \frac{1}{\sqrt{2\epsilon_0}} \vec{j}(\vec{r}, t). \quad (1.1.13)$$

The comparison of the plus and minus version of the combined Faraday's and Ampère's laws in Eq. (1.1.13) shows that the signs of the terms on the right-hand side are not equal for both cases. The $\vec{F}_-(\vec{r}, t)$ version of Eq. (1.1.13) requires a change of sign for the curl operation term on the right-hand side compared to the $\vec{F}_+(\vec{r}, t)$ equation. This change in sign is contrary to the previously discussed Gauß laws in Riemann-Silberstein representation in Eq. (1.1.12). However, this becomes more clear later in this section, when we consider the corresponding helicity of $\vec{F}_\pm(\vec{r}, t)$.

1.1.3 Curl operation in representation of spin-1 matrices

Now, after combining Maxwell's equations with a bilinear vector, we search for a relation of these Riemann-Silberstein equations with the well known ones in quantum mechanics, especially the time-dependent Schrödinger form. The curl operation in Eq. (1.1.13) is equivalent to a spin-1 matrix-vector operation. This operation obeys the following cross product for general vectors \vec{a} and \vec{b} [73]

$$\vec{a} \times \vec{b} = -i(\vec{S} \cdot \vec{a})\vec{b}, \quad (1.1.14)$$

where the vector \vec{S} of spin-1 matrices is defined in Cartesian representation by

$$\vec{S} = \begin{pmatrix} \mathbf{S}^1 \\ \mathbf{S}^2 \\ \mathbf{S}^3 \end{pmatrix}, \quad (1.1.15)$$

with

$$\mathbf{S}^1 = \begin{pmatrix} 0 & 0 & 0 \\ 0 & 0 & -i \\ 0 & i & 0 \end{pmatrix}, \quad \mathbf{S}^2 = \begin{pmatrix} 0 & 0 & i \\ 0 & 0 & 0 \\ -i & 0 & 0 \end{pmatrix}, \quad \mathbf{S}^3 = \begin{pmatrix} 0 & -i & 0 \\ i & 0 & 0 \\ 0 & 0 & 0 \end{pmatrix}. \quad (1.1.16)$$

The corresponding Cartesian basis vectors are denoted as

$$\vec{e}_{(1)} = \begin{pmatrix} 1 \\ 0 \\ 0 \end{pmatrix}, \quad \vec{e}_{(2)} = \begin{pmatrix} 0 \\ 1 \\ 0 \end{pmatrix}, \quad \vec{e}_{(3)} = \begin{pmatrix} 0 \\ 0 \\ 1 \end{pmatrix}, \quad (1.1.17)$$

so that the identity of the cross product in Eq. (1.1.14) can readily be seen, and an arbitrary \vec{a} with its components

$$\vec{a} = \begin{pmatrix} a_x \\ a_y \\ a_z \end{pmatrix} \quad (1.1.18)$$

is expressed with Cartesian basis set by

$$\vec{a} = a_x \vec{e}_{(1)} + a_y \vec{e}_{(2)} + a_z \vec{e}_{(3)}. \quad (1.1.19)$$

However, there is a second representation, the spherical representation, which is discussed in greater detail in Ref. [71] and which we briefly introduce here. In quantum mechanics, the spherical representation is the common spin representation, where one coordinate axis is distinguished. One spin-matrix is chosen such that its eigenvalues are on the diagonal and that the corresponding eigenvector is parallel to this distinguished axis.

We denote the spherical representation

$$\vec{\tilde{S}} = \begin{pmatrix} \tilde{S}^1 \\ \tilde{S}^2 \\ \tilde{S}^3 \end{pmatrix}, \quad (1.1.20)$$

with a tilde above the letters. It is common to chose the eigenvector axis along the z-axis and therefore $\vec{\tilde{e}}_{(3)} = \vec{e}_{(3)}$. Furthermore, the eigenvalues of the spin-1 matrix are 1, 0, -1, so that the \tilde{S}_3 matrix is

$$\tilde{S}^3 = \begin{pmatrix} 1 & 0 & 0 \\ 0 & 0 & 0 \\ 0 & 0 & -1 \end{pmatrix}. \quad (1.1.21)$$

The two other matrices \tilde{S}_1 , and \tilde{S}_2 are obtained by a proper rotation using the Wigner-D rotation matrices $\mathcal{D}^{(j)}(\alpha, \beta, \beta)$ in Ref. [76] with rotation angles α, β, β and $j = 1$ which corresponds to spin 1. The proper rotations for \tilde{S}_1 and \tilde{S}_2 are in accord with [71] given by

$$\tilde{S}^1 = \mathcal{D}^{(1)}(0, \pi/2, 0) \tilde{S}_3 \mathcal{D}^{(1)}(0, -\pi/2, 0) = \frac{1}{\sqrt{2}} \begin{pmatrix} 0 & 1 & 0 \\ 1 & 0 & 1 \\ 0 & 1 & 0 \end{pmatrix}, \quad (1.1.22)$$

$$\tilde{S}^2 = \mathcal{D}^{(1)}(0, 0, \pi/2) \tilde{S}_1 \mathcal{D}^{(1)}(0, 0, -\pi/2) = \frac{i}{\sqrt{2}} \begin{pmatrix} 0 & -1 & 0 \\ 1 & 0 & -1 \\ 0 & 1 & 0 \end{pmatrix}. \quad (1.1.23)$$

Consequently, we have to transform the basis vectors in Eqs. (1.1.17) to the corresponding spherical basis vectors $\vec{e}_{(1)}$, $\vec{e}_{(2)}$, $\vec{e}_{(3)}$

$$\vec{e}_{(1)} = \begin{pmatrix} -\frac{1}{\sqrt{2}} \\ -i\frac{1}{\sqrt{2}} \\ 0 \end{pmatrix}, \quad \vec{e}_{(2)} = \begin{pmatrix} \frac{1}{\sqrt{2}} \\ -i\frac{1}{\sqrt{2}} \\ 0 \end{pmatrix}, \quad \vec{e}_{(3)} = \begin{pmatrix} 0 \\ 0 \\ 1 \end{pmatrix}. \quad (1.1.24)$$

Hence, the arbitrary vector \vec{a} in Eq. (1.1.18) can be transformed into spherical representation \vec{a} using the spherical basis set in Eqs. (1.1.24) with

$$\vec{a} = \tilde{a}_x \vec{e}_{(1)} + \tilde{a}_y \vec{e}_{(2)} + \tilde{a}_z \vec{e}_{(3)}. \quad (1.1.25)$$

Finally, the Riemann-Silberstein vectors $\vec{F}_{\pm}(\vec{r}, t)$ and their underlying operations can be expressed in both representations, the Cartesian or the spherical.

However, it is more convenient to use the Cartesian representation of the cross product with three equivalent coordinates. If we substitute the vector \vec{a} in Eq. (1.1.14) by a nabla vector $\vec{\nabla}$ and \vec{b} by the Riemann-Silberstein vectors $\vec{F}_{\pm}(\vec{r}, t)$, we get a curl operation described by spin-1 matrices

$$\vec{\nabla} \times \vec{F}_{\pm}(\vec{r}, t) = -i \left(\vec{\mathbf{S}} \cdot \vec{\nabla} \right) \vec{F}_{\pm}(\vec{r}, t). \quad (1.1.26)$$

Hence, the combined Ampère's and Faraday's law in Eq. (1.1.13) results in

$$i \frac{\partial}{\partial t} \vec{F}_{\pm}(\vec{r}, t) = \mp i c_0 \left(\vec{\mathbf{S}} \cdot \vec{\nabla} \right) \vec{F}_{\pm}(\vec{r}, t) - i \frac{1}{\sqrt{2\epsilon_0}} \vec{j}(\vec{r}, t), \quad (1.1.27)$$

with the upper sign for positive helicity and lower sign for negative helicity. Without any loss of generality, we can multiply the whole equation in Eq. (1.1.27) by Planck's constant \hbar to get an inhomogeneous Schrödinger like Maxwell equation

$$i\hbar \frac{\partial}{\partial t} \vec{F}_{\pm}(\vec{r}, t) = \mp i\hbar c_0 \left(\vec{\mathbf{S}} \cdot \vec{\nabla} \right) \vec{F}_{\pm}(\vec{r}, t) - i \frac{\hbar}{\sqrt{2\epsilon_0}} \vec{j}(\vec{r}, t), \quad (1.1.28)$$

one for $\vec{F}_{+}(\vec{r}, t)$ and another one for $\vec{F}_{-}(\vec{r}, t)$.

1.1.4 Riemann-Silberstein Maxwell Hamiltonian and eigensystem

Owing to the replacement of the curl operation by spin-1 matrix representation, the quantum mechanical momentum operator \vec{p}

$$\vec{p} = -i\hbar \vec{\nabla} \quad (1.1.29)$$

appears in Eq. (1.1.28). It is also well known that the energy-momentum relation of a photon is

$$E = c_0 \vec{p}. \quad (1.1.30)$$

Thus, with all these similarities, we can define a Hamiltonian-like operator H_{Mx} in position space [73]

$$H_{\text{Mx}} = -i\hbar c_0 \left[\vec{\nabla} \cdot \vec{\mathcal{S}} \right], \quad (1.1.31)$$

which has the explicit form

$$H_{\text{Mx}} = \hbar c_0 \begin{bmatrix} 0 & -\frac{\partial}{\partial z} & \frac{\partial}{\partial y} \\ \frac{\partial}{\partial z} & 0 & -\frac{\partial}{\partial x} \\ -\frac{\partial}{\partial y} & \frac{\partial}{\partial x} & 0 \end{bmatrix}. \quad (1.1.32)$$

The momentum operator Eq. (1.1.29) transforms directly the Hamiltonian-like operator H_{Mx} in Eq. (1.1.31) into momentum space and H_{Mx} in momentum space takes the form

$$H_{\text{Mx}} = c_0 \vec{\mathcal{S}} \cdot \vec{p}. \quad (1.1.33)$$

Expressed in the Riemann-Silberstein formalism, Faraday's and Ampère's law can be written as an inhomogeneous Schrödinger equation [73]

$$i\hbar \frac{\partial}{\partial t} \vec{F}_{\pm}(\vec{r}, t) = \pm H_{\text{Mx}} \vec{F}_{\pm}(\vec{r}, t) \mp i \frac{\hbar}{\sqrt{2\epsilon_0}} \vec{j}(\vec{r}, t). \quad (1.1.34)$$

The bilinear Riemann-Silberstein complex vectors $\vec{F}_{\pm}(\vec{r}, t)$ describe the Maxwell's field vectors, i.e the electric and magnetic field, analogously to wave functions in quantum mechanics. It combines all Maxwell's equations that contain temporal derivatives into only one equation and reveals another important feature of quantum mechanical equations for the Maxwell's equations. In such a spin-1 matrices representation with first order time derivative multiplied by imaginary unit and Planck constant \hbar acting on the Riemann-Silberstein vector on the left-hand side as well as a Hamiltonian-like operator acting on the same Riemann-Silberstein vector on the right-hand side, it is possible to construct a time-evolution operator for Maxwell's fields.

In case of homogeneous Maxwell's equations without any current or charge densities in space, the combined Faraday's and Ampère's equation takes directly the form of a time dependent Schrödinger equation

$$i\hbar \frac{\partial}{\partial t} \vec{F}_{\pm}(\vec{r}, t) = \pm H_{\text{Mx}} \vec{F}_{\pm}(\vec{r}, t). \quad (1.1.35)$$

In addition, analogous to the stationary solution of the Schrödinger equation in quantum mechanics, the stationary solution of the Maxwell's wave equation in Eq. (1.1.35)

can be considered as a factor of spatial dependent function and a time-dependent phase factor

$$\vec{F}_{\pm}(\vec{r}, t) = e^{-i\omega t} \vec{F}_{\pm}(\vec{r}, t_{(0)}) , \quad (1.1.36)$$

with constant eigenmode frequency ω . This separation of $\vec{F}_{\pm}(\vec{r}, t)$ leads to the eigenvalue problem for the Riemann-Silberstein Maxwell's wave equation

$$\begin{aligned} i\hbar \frac{\partial}{\partial t} \vec{F}_{\pm}(\vec{r}, t) &= \pm H_{\text{Mx}} \vec{F}_{\pm}(\vec{r}, t) \\ \Rightarrow \quad \omega \hbar \vec{F}_{\pm}(\vec{r}, t) &= c_0 (\pm \vec{S} \cdot \vec{p}) \vec{F}_{\pm}(\vec{r}, t) , \end{aligned} \quad (1.1.37)$$

which is the stationary Riemann-Silberstein wave equation similar to the one in quantum mechanics.

Thus, it is equally possible to expand the Riemann-Silberstein fields by a superposition in terms of their eigenfunctions with eigenmodes ω . In case of positive ω in Eq. (1.1.37), the helicity, defined as the projection of the momentum \vec{p} on the spin vector \vec{S} , is positive for $\vec{F}_{+}(\vec{r}, t)$ and negative for $\vec{F}_{-}(\vec{r}, t)$. Consequently $\vec{F}_{+}(\vec{r}, t)$ and its corresponding equation is referred to positive helicity and $\vec{F}_{-}(\vec{r}, t)$ and its corresponding equation to negative helicity.

1.1.5 Combined six-component helicity Riemann-Silberstein vector

For all previously considered Riemann-Silberstein Maxwell's equations, we always found two equivalent expressions, one equation for $\vec{F}_{+}(\vec{r}, t)$ and one for $\vec{F}_{-}(\vec{r}, t)$. Similar to the works of Ref. [73, 77], we introduce a formalism which combines both vectors. Instead of writing two equations, both variants can be expressed combined into one by building a six-dimensional vector $\mathcal{F}(\vec{r}, t)$ and its complex conjugate one $\mathcal{F}^{\dagger}(\vec{r}, t)$ which contains both $\vec{F}_{+}(\vec{r}, t)$ and $\vec{F}_{-}(\vec{r}, t)$ and are given by [73]

$$\mathcal{F}(\vec{r}, t) = \begin{pmatrix} \vec{F}_{+}(\vec{r}, t) \\ \vec{F}_{-}(\vec{r}, t) \end{pmatrix} , \quad (1.1.38)$$

$$\mathcal{F}^{\dagger}(\vec{r}, t) = \begin{pmatrix} \vec{F}_{-}^{\dagger}(\vec{r}, t) \\ \vec{F}_{+}^{\dagger}(\vec{r}, t) \end{pmatrix} . \quad (1.1.39)$$

We call $\mathcal{F}(\vec{r}, t)$ the six-component Riemann-Silberstein vector of a system and all Maxwell's equations can be written in terms of $\mathcal{F}(\vec{r}, t)$, which always contain the positive and negative helicity equations. The first three components of $\mathcal{F}(\vec{r}, t)$ correspond to the positive helicity equations of $\vec{F}_{+}(\vec{r}, t)$, whereas the last three components represent the negative helicity equations of $\vec{F}_{-}(\vec{r}, t)$.

Next, we want to express the microscopic Maxwell's equations in terms of the newly introduced six-dimensional vector $\mathcal{F}(\vec{r}, t)$ in Eq. (1.1.38). In addition to the introduced $\mathcal{F}(\vec{r}, t)$, other variables have to be adapted in a similar way. Hence, the

two-dimensional Riemann-Silberstein charge density $\mathcal{Q}(\vec{r}, t)$ can be written as

$$\mathcal{Q}(\vec{r}, t) = \begin{pmatrix} 1 \\ 1 \end{pmatrix}_{2 \times 1} \otimes \left(\frac{1}{\sqrt{2\epsilon_0}} \rho(\vec{r}, t) \right)_{1 \times 1}. \quad (1.1.40)$$

Furthermore, the 2x6 dimensional Riemann-Silberstein divergence operator, built by a Kronecker product of a 2x2 matrix and the 1x3 transposed nabla operator vector, is

$$\mathcal{D} = \begin{pmatrix} 1 & 0 \\ 0 & 1 \end{pmatrix}_{2 \times 2} \otimes \left(\vec{\nabla} \right)_{1 \times 3}^\top = \begin{pmatrix} \frac{\partial}{\partial x} & \frac{\partial}{\partial y} & \frac{\partial}{\partial z} & 0 & 0 & 0 \\ 0 & 0 & 0 & \frac{\partial}{\partial x} & \frac{\partial}{\partial y} & \frac{\partial}{\partial z} \end{pmatrix}. \quad (1.1.41)$$

The two equations in Eq. (1.1.12) which represent the Gauß laws condition are equivalent to

$$\mathcal{D} \cdot \mathcal{F}(\vec{r}, t) = \mathcal{Q}(\vec{r}, t), \quad (1.1.42)$$

where we use a dot product formalism denoted by a bold dot product symbol \cdot .

The introduced Riemann-Silberstein dot product acts as a 6x2 matrix \mathcal{V} on the six-dimensional $\mathcal{F}(\vec{r}, t)$ with its two three-dimensional vectors $\vec{F}_\pm(\vec{r}, t)$. The 6x2 \mathcal{V} contains four arbitrary three-dimensional vectors $\vec{V}_{(1)}$, $\vec{V}_{(2)}$, $\vec{V}_{(3)}$, and $\vec{V}_{(4)}$. We define the dot product with

$$\begin{aligned} \mathcal{V} \cdot \mathcal{F}(\vec{r}, t) &= \begin{pmatrix} \vec{V}_{(1)}^\top & \vec{V}_{(2)}^\top \\ \vec{V}_{(3)}^\top & \vec{V}_{(4)}^\top \end{pmatrix}_{2 \times 6} \cdot \begin{pmatrix} \vec{F}_+(\vec{r}, t) \\ \vec{F}_-(\vec{r}, t) \end{pmatrix}_{6 \times 1} \\ &= \begin{pmatrix} \vec{V}_{(1)} \cdot \vec{F}_+(\vec{r}, t) + \vec{V}_{(2)} \cdot \vec{F}_-(\vec{r}, t) \\ \vec{V}_{(3)} \cdot \vec{F}_+(\vec{r}, t) + \vec{V}_{(4)} \cdot \vec{F}_-(\vec{r}, t) \end{pmatrix}_{2 \times 1}. \end{aligned} \quad (1.1.43)$$

The small dot product symbols on the very right-hand side of Eq. (1.1.43) represent common three-dimensional scalar products. Hence, this dot product maps a 6x2 matrix and a six-dimensional vector into a two-dimensional vector. where the upper component again represents the positive helicity, and the lower component the negative one.

Furthermore, the two Riemann-Silberstein combined Ampère's and Faraday's laws given in Eq. (1.1.34) take the form

$$i\hbar \frac{\partial}{\partial t} \mathcal{F}(\vec{r}, t) = \mathcal{H} \mathcal{F}(\vec{r}, t) - i\hbar \mathcal{J}(\vec{r}, t). \quad (1.1.44)$$

Here, the Hamiltonian-like 6x6 matrix \mathcal{H} is a Kronecker product of a diagonal 2x2 matrix and the 3x3 H_{Mx} matrix of Eq. (1.1.31). It is given by

$$\begin{aligned} \mathcal{H} &= \begin{pmatrix} 1 & 0 \\ 0 & -1 \end{pmatrix}_{2 \times 2} \otimes \left(-i\hbar c_0 \left[\vec{\nabla} \cdot \vec{\mathcal{S}} \right] \right)_{3 \times 3} \\ &= \begin{pmatrix} 1 & 0 \\ 0 & -1 \end{pmatrix}_{2 \times 2} \otimes \left(H_{\text{Mx}} \right)_{3 \times 3}, \end{aligned} \quad (1.1.45)$$

which yields a six-dimensional vector after acting on $\mathcal{F}(\vec{r}, t)$. The remaining current density inhomogeneity in Eq. (1.1.34) is substituted by $\mathcal{J}(\vec{r}, t)$

$$\mathcal{J}(\vec{r}, t) = \begin{pmatrix} 1 \\ 1 \end{pmatrix}_{2 \times 1} \otimes \left(\frac{1}{\sqrt{2\epsilon_0}} \vec{j} \right)_{3 \times 1} \quad (1.1.46)$$

in Eq. (1.1.44). In case of $\mathcal{J}(\vec{r}, t)$ equal zero, Eq. (1.1.44) becomes a homogeneous Schrödinger-like form with

$$i\hbar \frac{\partial}{\partial t} \mathcal{F}(\vec{r}, t) = \mathcal{H} \mathcal{F}(\vec{r}, t). \quad (1.1.47)$$

Following the $\mathcal{H} \mathcal{F}(\vec{r}, t)$ operation, we emphasize some properties of general $\mathcal{O}(\vec{r}, t) \mathcal{F}(\vec{r}, t)$ operations defined by a general operator $\mathcal{O}(\vec{r}, t)$, which contains four 3x3 matrices

$$\mathcal{O}(\vec{r}, t) = \begin{pmatrix} O_{11}(\vec{r}, t) & O_{12}(\vec{r}, t) \\ O_{21}(\vec{r}, t) & O_{22}(\vec{r}, t) \end{pmatrix}. \quad (1.1.48)$$

Therefore, $\mathcal{F}'(\vec{r}, t) = \mathcal{O}(\vec{r}, t) \mathcal{F}(\vec{r}, t)$ yields

$$\begin{pmatrix} F'_+(\vec{r}, t) \\ F'_-(\vec{r}, t) \end{pmatrix} = \begin{pmatrix} O_{11}(\vec{r}, t) \vec{F}_+(\vec{r}, t) + O_{12}(\vec{r}, t) \vec{F}_-(\vec{r}, t) \\ O_{21}(\vec{r}, t) \vec{F}_-(\vec{r}, t) + O_{22}(\vec{r}, t) \vec{F}_+(\vec{r}, t) \end{pmatrix}. \quad (1.1.49)$$

Obviously the different helicity vectors $\vec{F}_+(\vec{r}, t)$ and $\vec{F}_-(\vec{r}, t)$ couple to each other, if the terms $O_{12}(\vec{r}, t)$ and $O_{21}(\vec{r}, t)$ are non-zero. Without loss of generality we can express the general operator $\mathcal{O}(\vec{r}, t)$ by a Kronecker product of the two matrices $m_{(i)}$ and $o_{(i)}(\vec{r}, t)$

$$\mathcal{O}(\vec{r}, t) = \sum_i \left(m_{(i)} \right)_{2 \times 2} \otimes \left(o_{(i)}(\vec{r}, t) \right)_{3 \times 3}. \quad (1.1.50)$$

The prefix 2x2 matrix $m_{(i)}$ only consists of elements 1 or -1 , the second $o_{(i)}(\vec{r}, t)$ contains all other necessary operations so that Eq. (1.1.50) is satisfied. We already used this formalism in Eq. (1.1.45) to define the Hamiltonian-like \mathcal{H} . Consequently, since the off-diagonal entries of $m_{(i)}$ are zero and only the diagonal entries are 1 or -1 , it can readily be seen that $o_{(i)}(\vec{r}, t)$ do not couple the two helicity vectors. In the following, we therefore call the first 2x2 matrix in Eq. (1.1.50) "coupling" matrix, as it shows if the two Riemann-Silberstein vectors $\vec{F}_\pm(\vec{r}, t)$ couple to each other. The second 3x3 "operation" matrix contains all necessary physical variables and operations to satisfy the underlying Maxwell's equations.

With respect of Eq. (1.1.34), we have in principle two independent equations combined into one in Eq. (1.1.44). Hence, there is per construction no coupling between the two linear independent Riemann-Silberstein vectors $\vec{F}_+(\vec{r}, t)$ and $\vec{F}_-(\vec{r}, t)$. Note, this is only valid for the common classical microscopic Maxwell's equations shown

in Eqs. (1.1.8) - (1.1.11). We show in the next section, that a correct description of Maxwell's equation in a linear medium requires a coupling between the positive and negative Riemann-Silberstein vectors. In summary, Eq. (1.1.44) gives us a general and clear form to describe the Maxwell's equations in vacuum as a Schrödinger-like equation well known for describing quantum mechanical wave functions.

However, there is one difference to quantum mechanical systems. The Maxwell fields have to satisfy the two Gauß laws as secondary condition. We focus on this condition and how it is conserved during time propagation in chapter 2.

1.1.6 Photon - anti-photon relation of the six-component Riemann-Silberstein vector

We now have a general form with both helicity Riemann-Silberstein vectors in one equation. However, this expression of Maxwell vectors in form of a six-dimensional Riemann-Silberstein vector requires some considerations, which are extensively elaborated in Ref. [73, 72].

The six-component vector $\mathcal{F}(\vec{r}, t)$ without any relation between the upper and the lower three-vector doubles the degrees of freedom. This extra freedom has to be constrained to satisfy the photon particle antiparticle relation. Solutions of relativistic quantum mechanics, especially plane wave solutions can have in general positive frequencies that correspond to particles with positive energies or negative frequencies that correspond to antiparticles with negative energies. In contrast to the different particle antiparticle pairs for matter wave functions, the anti-photons are identical with photons. Hence, this condition reduces the degrees of freedom.

First, we take the electric field $\vec{E}_{\text{pw}}^{(+)}(\vec{r}, t)$ and magnetic field $\vec{B}_{\text{pw}}^{(+)}(\vec{r}, t)$ for positive frequencies and $\vec{E}_{\text{pw}}^{(-)}(\vec{r}, t)$, $\vec{B}_{\text{pw}}^{(-)}(\vec{r}, t)$ for negative frequencies of an electromagnetic plane wave with initial electric field $\vec{E}_0(\vec{k})$, initial magnetic field $\vec{B}_0(\vec{k})$, wave vector \vec{k} and ω as the absolute value of the frequency. Hence, the plane waves with positive frequencies take the form [75]

$$\vec{E}_{\text{pw}}^{(+)}(\vec{r}, t) = \vec{E}_{(0)}(\vec{k}) \exp \left[i \left(\vec{k} \cdot \vec{r} - \omega t \right) \right], \quad (1.1.51)$$

$$\vec{B}_{\text{pw}}^{(+)}(\vec{r}, t) = \vec{B}_{(0)}(\vec{k}) \exp \left[i \left(\vec{k} \cdot \vec{r} - \omega t \right) \right], \quad (1.1.52)$$

whereas the ones with negative frequencies are given by [75]

$$\vec{E}_{\text{pw}}^{(-)}(\vec{r}, t) = \vec{E}_{(0)}(\vec{k}) \exp \left[i \left(\vec{k} \cdot \vec{r} + \omega t \right) \right], \quad (1.1.53)$$

$$\vec{B}_{\text{pw}}^{(-)}(\vec{r}, t) = \vec{B}_{(0)}(\vec{k}) \exp \left[i \left(\vec{k} \cdot \vec{r} + \omega t \right) \right]. \quad (1.1.54)$$

The electromagnetic plane waves additionally obey the relations [75]

$$\vec{k} \cdot \vec{E}_{\text{pw}}^{(\pm)}(\vec{r}, t) = \vec{k} \cdot \vec{B}_{\text{pw}}^{(\pm)}(\vec{r}, t) = 0, \quad (1.1.55)$$

$$\vec{B}_{\text{pw}}^{(\pm)}(\vec{r}, t) = \frac{1}{c_0} \frac{\vec{k}}{|\vec{k}|} \times \vec{E}_{\text{pw}}^{(\pm)}(\vec{r}, t). \quad (1.1.56)$$

Using the definitions of the Riemann-Silberstein vectors in Eq. (1.1.1) and Eq. (1.1.2) for building the corresponding initial vectors $\vec{F}_+(\vec{k})$ and $\vec{F}_-(\vec{k})$ for a given wavevector \vec{k} with $\vec{F}_\pm^*(\vec{k}) = \vec{F}_\mp(\vec{k})$ leads to the Riemann-Silberstein plane wave expressions $\vec{F}_{\text{pw}}^{(+)}(\vec{r}, t)$ for positive frequencies

$$\vec{F}_{\text{pw},+}^{(+)}(\vec{r}, t) = \vec{F}_+(\vec{k}) \exp \left[i \left(\vec{k} \cdot \vec{r} - \omega t \right) \right] = \vec{F}_+^*(\vec{k}) \exp \left[i \left(\vec{k} \cdot \vec{r} + \omega t \right) \right], \quad (1.1.57)$$

$$\vec{F}_{\text{pw},-}^{(+)}(\vec{r}, t) = \vec{F}_-(\vec{k}) \exp \left[i \left(\vec{k} \cdot \vec{r} - \omega t \right) \right] = \vec{F}_-^*(\vec{k}) \exp \left[i \left(\vec{k} \cdot \vec{r} + \omega t \right) \right], \quad (1.1.58)$$

and $\vec{F}_{\text{pw}}^{(-)}(\vec{r}, t)$ for negative frequencies

$$\vec{F}_{\text{pw},+}^{(-)}(\vec{r}, t) = \vec{F}_+(\vec{k}) \exp \left[i \left(\vec{k} \cdot \vec{r} + \omega t \right) \right] = \vec{F}_+^*(\vec{k}) \exp \left[i \left(\vec{k} \cdot \vec{r} - \omega t \right) \right], \quad (1.1.59)$$

$$\vec{F}_{\text{pw},-}^{(-)}(\vec{r}, t) = \vec{F}_-(\vec{k}) \exp \left[i \left(\vec{k} \cdot \vec{r} + \omega t \right) \right] = \vec{F}_-^*(\vec{k}) \exp \left[i \left(\vec{k} \cdot \vec{r} - \omega t \right) \right]. \quad (1.1.60)$$

The last equivalence Eqs. (1.1.57) - (1.1.60) follows from the plane wave conditions in Eq. (1.1.55) and Eq. (1.1.56) for the wave vector \vec{k} and magnetic field $\vec{B}_{\text{pw}}(\vec{r}, t)$. It means that every Riemann-Silberstein plane wave with positive energy respectively positive frequency and vice versa negative energy respectively negative frequency can be expressed by the complex conjugate Riemann-Silberstein vector plane wave amplitude $\vec{F}_\pm^*(\vec{k})$ multiplied by the plane wave exponential function but with opposite frequency. Hence taking Eqs. (1.1.57) - (1.1.60) into account leads to the complex conjugates

$$\vec{F}_{\text{pw},\pm}^{(+)*}(\vec{r}, t) = \vec{F}_{\text{pw},+}^{(-)}(\vec{r}, t), \quad (1.1.61)$$

$$\vec{F}_{\text{pw},\pm}^{(-)*}(\vec{r}, t) = \vec{F}_{\text{pw},+}^{(+)}(\vec{r}, t). \quad (1.1.62)$$

Since every electromagnetic field and therefore every Riemann-Silberstein vector can be expressed by an infinite sum of plane waves, we can find a Riemann-Silberstein vector $\vec{F}_\pm^{(+)}(\vec{r}, t)$ which only contains positive frequencies by

$$\vec{F}_\pm^{(+)}(\vec{r}, t) = \int_0^\infty d^3k \vec{F}_\pm(\vec{k}) \exp \left[i \left(-\vec{k} \cdot \vec{r} - \omega_{\vec{k}} t \right) \right], \quad (1.1.63)$$

and a negative counterpart $\vec{F}_\pm^{(-)}(\vec{r}, t)$ by

$$\vec{F}_\pm^{(-)}(\vec{r}, t) = \int_0^\infty d^3k \vec{F}_\pm(\vec{k}) \exp \left[i \left(-\vec{k} \cdot \vec{r} + \omega_{\vec{k}} t \right) \right], \quad (1.1.64)$$

where $\omega_{\vec{k}}$ depends implicitly on the wave vector \vec{k} with $\omega_{\vec{k}} = c|\vec{k}|$. Taking Eq. (1.1.61) and Eq. (1.1.62) gives also the correspond complex conjugates for Eq. (1.1.63) and

Eq. (1.1.64)

$$\vec{F}_{\pm}^{(+)*}(\vec{r}, t) = \int_0^{\infty} d^3k \vec{F}_{\pm}^*(\vec{k}) \exp \left[-i \left(-\vec{k} \cdot \vec{r} - \omega_{\vec{k}} t \right) \right], \quad (1.1.65)$$

$$\vec{F}_{\pm}^{(-)*}(\vec{r}, t) = \int_0^{\infty} d^3k \vec{F}_{\pm}^*(\vec{k}) \exp \left[-i \left(-\vec{k} \cdot \vec{r} + \omega_{\vec{k}} t \right) \right]. \quad (1.1.66)$$

In the following we deduce that the complex conjugate relation in Eq. (1.1.61) and Eq. (1.1.62) for general electromagnetic fields using the particle-antiparticle relation of photons.

In principle, we can build two separate Riemann-Silberstein six-vectors, one for positive frequencies $\mathcal{F}^{(+)}(\vec{r}, t)$

$$\mathcal{F}^{(+)}(\vec{r}, t) = \begin{pmatrix} \vec{F}_{+}^{(+)}(\vec{r}, t) \\ \vec{F}_{-}^{(+)}(\vec{r}, t) \end{pmatrix}, \quad (1.1.67)$$

and another $\mathcal{F}^{(-)}(\vec{r}, t)$ for negative frequencies

$$\mathcal{F}^{(-)}(\vec{r}, t) = \begin{pmatrix} \vec{F}_{+}^{(-)}(\vec{r}, t) \\ \vec{F}_{-}^{(-)}(\vec{r}, t) \end{pmatrix}. \quad (1.1.68)$$

However, as mentioned before, this degree of freedom is reduced due to the fact that photon and anti-photon are described by the same $\mathcal{F}(\vec{r}, t)$. According to quantum mechanical particle-antiparticle conjugation [78, 77] the anti-photon vector $\mathcal{F}^a(\vec{r}, t)$ of a photon vector $\mathcal{F}(\vec{r}, t)$ has to obey

$$\mathcal{F}^a(\vec{r}, t) = \begin{pmatrix} 0 & 1 \\ 1 & 0 \end{pmatrix} \mathcal{F}^*(\vec{r}, t), \quad (1.1.69)$$

and the antiparticles are defined as the particles corresponding to negative energy. In terms of electromagnetic fields, this corresponds to photons with negative frequencies. Since the photon and anti-photon Therefore, if we substitute $\mathcal{F}(\vec{r}, t)$ on the right-hand side of Eq. (1.1.69) by positive energy referred $\mathcal{F}^{(+)}(\vec{r}, t)$, we obtain the constraint condition for the anti-photon Riemann-Silberstein vector $\mathcal{F}^{(-)}(\vec{r}, t)$

$$\mathcal{F}^{(-)}(\vec{r}, t) = \begin{pmatrix} 0 & 1 \\ 1 & 0 \end{pmatrix} \mathcal{F}^{(+)*}(\vec{r}, t), \quad (1.1.70)$$

or vice versa the anti-photon vector $\mathcal{F}^{(+)}(\vec{r}, t)$ for $\mathcal{F}^{(-)}(\vec{r}, t)$ leads to the condition

$$\mathcal{F}^{(+)}(\vec{r}, t) = \begin{pmatrix} 0 & 1 \\ 1 & 0 \end{pmatrix} \mathcal{F}^{(-)*}(\vec{r}, t). \quad (1.1.71)$$

Taking Eqs. (1.1.67) - (1.1.68) and Eqs. (1.1.70) - (1.1.71) leads with Eq. (1.1.3) to the final condition for $\vec{F}_{\pm}^{(+)}(\vec{r}, t)$ and $\vec{F}_{\pm}^{(-)}(\vec{r}, t)$

$$\vec{F}_{+}^{(+)}(\vec{r}, t) = \vec{F}_{+}^{(-)*}(\vec{r}, t), \quad (1.1.72)$$

$$\vec{F}_{-}^{(+)}(\vec{r}, t) = \vec{F}_{-}^{(-)*}(\vec{r}, t) \quad (1.1.73)$$

to hold the correct particle-antiparticle relation for photons and reduce the previously discussed doubled degrees of freedom. As a consequence, $\mathcal{F}^{(+)}(\vec{r}, t)$ can always be constructed from an arbitrary Riemann-Silberstein vector $\vec{F}_{\pm}(\vec{r}, t)$ by splitting $\vec{F}_{\pm}(\vec{r}, t)$ into positive and negative frequency parts and inserting the positive frequency and helicity part $\vec{F}_{+}^{(+)}(\vec{r}, t)$ and the complex conjugate part $\vec{F}_{+}^{(-)*}(\vec{r}, t)$ into $\mathcal{F}(\vec{r}, t)$ [73]

$$\mathcal{F}^{(+)}(\vec{r}, t) = \begin{pmatrix} \vec{F}_{+}^{(+)}(\vec{r}, t) \\ \vec{F}_{-}^{(+)}(\vec{r}, t) \end{pmatrix} = \begin{pmatrix} F_{+}^{(+)}(\vec{r}, t) \\ F_{+}^{(-)*}(\vec{r}, t) \end{pmatrix}, \quad (1.1.74)$$

and similar the construction for $\mathcal{F}^{(-)}(\vec{r}, t)$ takes the form

$$\mathcal{F}^{(-)}(\vec{r}, t) = \begin{pmatrix} \vec{F}_{+}^{(-)}(\vec{r}, t) \\ \vec{F}_{-}^{(-)}(\vec{r}, t) \end{pmatrix} = \begin{pmatrix} F_{+}^{(-)}(\vec{r}, t) \\ F_{+}^{(+)*}(\vec{r}, t) \end{pmatrix}. \quad (1.1.75)$$

Since $\mathcal{F}^{(-)}(\vec{r}, t)$ can be directly obtained from $\mathcal{F}^{(+)}(\vec{r}, t)$, we consider in the following only $\mathcal{F}^{(+)}(\vec{r}, t)$, drop the index (+), and write only $\mathcal{F}(\vec{r}, t)$.

1.1.7 Scalar product of the six-component Riemann-Silberstein vector

In analogy to quantum mechanics, we introduce a scalar product formalism for the six-component Riemann-Silberstein vector $\mathcal{F}(\vec{r}, t)$ similar to Ref. [77]. With the previous considerations, we can define the scalar product for an arbitrary 6x6 dimensional operator $\mathcal{O}(\vec{r}, t)$ which contains four 3x3 matrices

$$\mathcal{O}(\vec{r}, t) = \begin{pmatrix} O_{11}(\vec{r}, t) & O_{12}(\vec{r}, t) \\ O_{21}(\vec{r}, t) & O_{22}(\vec{r}, t) \end{pmatrix}. \quad (1.1.76)$$

Hence, the scalar product for $\mathcal{F}(\vec{r}, t)$ based on Eq. (1.1.38) is defined as

$$\begin{aligned} \langle \mathcal{F}(t) | \mathcal{O} | \mathcal{F}(t) \rangle &= \int_{-\infty}^{\infty} d^3r \mathcal{F}^{\dagger}(\vec{r}, t) \mathcal{H}^{-1} \mathcal{O}(\vec{r}, t) \mathcal{F}(\vec{r}, t) \\ &= \begin{pmatrix} \int_{-\infty}^{\infty} d^3r \vec{F}_{-}(\vec{r}, t) [\mathcal{H}^{-1}]_{11} O_{11}(\vec{r}, t) \vec{F}_{+}(\vec{r}, t) + \vec{F}_{-}(\vec{r}, t) [\mathcal{H}^{-1}]_{21} O_{12}(\vec{r}, t) \vec{F}_{-}(\vec{r}, t) \\ \int_{-\infty}^{\infty} d^3r \vec{F}_{+}(\vec{r}, t) [\mathcal{H}^{-1}]_{12} O_{21}(\vec{r}, t) \vec{F}_{+}(\vec{r}, t) + \vec{F}_{+}(\vec{r}, t) [\mathcal{H}^{-1}]_{22} O_{22}(\vec{r}, t) \vec{F}_{-}(\vec{r}, t) \end{pmatrix}. \end{aligned} \quad (1.1.77)$$

The right-hand side of Eq. (1.1.77) uses the inverse of \mathcal{H} given in Eq. (1.1.45) and in principle can be expressed in terms of four submatrices by

$$\mathcal{H}^{-1} = \begin{pmatrix} [\mathcal{H}^{-1}]_{11} & [\mathcal{H}^{-1}]_{12} \\ [\mathcal{H}^{-1}]_{21} & [\mathcal{H}^{-1}]_{22} \end{pmatrix}, \quad (1.1.78)$$

which is also used on the right-hand side in Eq. (1.1.77). Unfortunately, \mathcal{H} is a non-invertible singular matrix. However, we keep the expressions in Eq. (1.1.77) and Eq. (1.1.78) since relevant physical operators for $\mathcal{O}(\vec{r}, t)$ can be expressed or factorized by \mathcal{H} , which means, that it cancels the corresponding inverse \mathcal{H} expression in Eq. (1.1.77) [73].

In contrast to the usual scalar product with only one scalar number as result, our defined scalar product consists of two scalar numbers representing the upper and lower helicity vectors $\vec{F}_+(\vec{r}, t)$ and $\vec{F}_-(\vec{r}, t)$ of $\mathcal{F}(\vec{r}, t)$. Since $\vec{F}_+^*(\vec{r}, t) = \vec{F}_-(\vec{r}, t)$ and $\vec{F}_-^*(\vec{r}, t) = \vec{F}_+(\vec{r}, t)$, the first integral of the upper component on the right-hand side and the second integral of the lower component on the right-hand side represent the usual integrals to obtain the physical scalar products. However, in our definition, if $O_{12}(\vec{r}, t)$ and $O_{21}(\vec{r}, t)$ are non-zero, we obtain additional scalars for each component that concerns coupling between the helicity vectors.

Another difference to usual scalar products in quantum mechanics is the inverse \mathcal{H} operator in Eq. (1.1.77). The reason for this modification is based on the energy density $u(\vec{r}, t)$ formula in the Riemann-Silberstein formalism. From Eq. (1.1.79) we already explained the prefactors for the real and imaginary part of the Riemann-Silberstein vector and it is equivalent to

$$\begin{pmatrix} u(\vec{r}, t) \\ u(\vec{r}, t) \end{pmatrix} = \begin{pmatrix} \vec{F}_-(\vec{r}, t) \cdot \vec{F}_+(\vec{r}, t) \\ \vec{F}_+(\vec{r}, t) \cdot \vec{F}_-(\vec{r}, t) \end{pmatrix}. \quad (1.1.79)$$

Hence, the electric energy of a system is given by

$$\begin{pmatrix} E(t) \\ E(t) \end{pmatrix} = \begin{pmatrix} \int d^3r \vec{F}_-(\vec{r}, t) \cdot \vec{F}_+(\vec{r}, t) \\ \int d^3r \vec{F}_+(\vec{r}, t) \cdot \vec{F}_-(\vec{r}, t) \end{pmatrix}, \quad (1.1.80)$$

which could equivalently be expressed similar to a quantum mechanical expectation value with

$$\langle E(t) \rangle = \langle \mathcal{F}(t) | \mathcal{H} | \mathcal{F}(t) \rangle, \quad (1.1.81)$$

if the scalar product of the six-dimensional Riemann-Silberstein formalism is defined like in
Eq. (1.1.77). Therefore, the introduced Riemann-Silberstein scalar product can be used for other operators similar to the one in quantum mechanics.

Most physical operators can be expressed in terms of \mathcal{H} with additional operators, so that it eliminates the inverse of \mathcal{H} in Eq. (1.1.77). If $\mathcal{O}(\vec{r}, t)$ in Eq. (1.1.76) is

a physical operator, the upper and lower value on the left-hand side of Eq. (1.1.77) are always equal since the photon-anti-photon relation in Eq. (1.1.74) holds. An overview of some physical operators for the photon field, which has similarities to the corresponding quantum operators is given in [73].

In quantum mechanics, the expectation value describes the mean expectation value for a large number of measurements, whereas the Riemann-Silberstein scalar product calculates the integrated mean field value. We note here, that the mean field value of the Maxwell fields at a certain point in space can be seen as the quantum mechanical expectation value of the field, which is obtained by a very large photon number. In this picture, it is sufficient to approximate the Maxwell field by a mean field vector and neglect photon fluctuations [79].

1.1.8 Eigenstate expansion of the Riemann-Silberstein six-vector

We already considered stationary solutions for the Riemann-Silberstein vectors $\vec{F}_{\pm}(\vec{r}, t)$, which are given in Eq. (1.1.36) and satisfy the corresponding eigenvalue problem in Eq. (1.1.37). Consequently, the corresponding stationary solution ansatz of the six-component Riemann-Silberstein vector takes the form

$$\mathcal{F}(\vec{r}, t) = e^{-i\omega t} \mathcal{F}(\vec{r}, t_{(0)}) . \quad (1.1.82)$$

This solves the updated eigenvalue problem Eq. (1.1.37) for six-component Riemann-Silberstein vectors with operator \mathcal{H} in Eq. (1.1.45)

$$\mathcal{H}\mathcal{F}(\vec{r}, t) = \hbar\omega\mathcal{F}(\vec{r}, t) . \quad (1.1.83)$$

Following the usual quantum mechanical wave function expansion, we can use an eigenvalue and eigenstate expansion of the Riemann-Silberstein six-vector by

$$\mathcal{F}(\vec{r}, t) = \sum_{(j)} e^{-i\omega_{(j)}t} \mathcal{F}_{(j)}(\vec{r}) \quad (1.1.84)$$

to expand the six-component Riemann-Silberstein vector in terms of its eigenvalues $\omega_{(j)}$ and eigenstates $\mathcal{F}_{(j)}(\vec{r})$. The corresponding eigensystem can be numerically calculated using an adequate basis set and the scalar product in Eq. (1.1.77) with $\mathcal{O}(\vec{r}, t) = \mathcal{H}$ to get a Hamiltonian matrix, which can be diagonalized to obtain the requested eigenvalues ω_j and eigenstates $\mathcal{F}_{(j)}(\vec{r})$.

1.2 Riemann-Silberstein approach for macroscopic Maxwell's equations

The previously considered microscopic Maxwell's equations describe the Maxwell fields, charge, and current density in vacuum. In large matter systems with a huge amount of atoms, the correct Maxwell fields can be obtained in principle by solving

Maxwell's equations in vacuum. Finding a solution or a proper approximation is barely reachable due to the large particle number with corresponding charge densities and current densities that have to be taken into account.

However, quite a lot of atoms are bound by cores and additionally the atomic cores are often bound in a structure, whereas some electrons are able to move freely inside the matter. Thus, the current density inside the matter can be split into two parts. One part describes the bound charge density $\rho_{\text{bound}}(\vec{r}, t)$, whose distribution and motion in terms of a bound current density $\vec{j}_{\text{bound}}(\vec{r}, t)$ is only visible on atomic scale and ensures the stability of the bound system. The remaining free charge density $\rho_{\text{free}}(\vec{r}, t)$ can move through the whole matter and causes a free current density $\vec{j}_{\text{free}}(\vec{r}, t)$, which both are macroscopically measurable in contrast to the bound variables. The effects of the bound charges and currents are summarized in additional vector fields, the electric displacement field $\vec{D}(\vec{r}, t)$ and the H-field $\vec{H}(\vec{r}, t)$. Both fields and the electromagnetic fields, $\vec{E}(\vec{r}, t)$, $\vec{B}(\vec{r}, t)$, determine the macroscopic Maxwell's equations.

In contrast to the microscopic Maxwell's equations, we show that the macroscopic description in a linear medium in terms of Riemann-Silberstein vectors requires a linear combination of both helicity vectors $\vec{F}_{\pm}(\vec{r}, t)$ [73, 74]. Now, the macroscopic Riemann-Silberstein six-vector $\mathcal{F}_{\text{lm}}(\vec{r}, t)$ becomes more important since the corresponding 6x6 matrices couple the upper $\vec{F}_{\text{lm},+}(\vec{r}, t)$ and the lower $\vec{F}_{\text{lm},-}(\vec{r}, t)$ vectors of $\mathcal{F}_{\text{lm}}(\vec{r}, t)$. In this section we follow the previously considered steps of the microscopic Riemann-Silberstein Maxwell's equations in Sec. 1.1 to find the correspond macroscopic ones. To get a more general form, we add electric and magnetic loss.

1.2.1 Riemann-Silberstein Maxwell's equations for a linear medium

In a linear medium, the total charge density $\rho(\vec{r}, t)$ and current density $\vec{j}(\vec{r}, t)$ are split into two components, one microscopically bound and one free component. The sum of both components corresponds of course still to the total values of the system, so that the total $\rho(\vec{r}, t)$ and $\vec{j}(\vec{r}, t)$ of the system are given by

$$\rho(\vec{r}, t) = \rho_{\text{bound}}(\vec{r}, t) + \rho_{\text{free}}(\vec{r}, t), \quad (1.2.1)$$

$$\vec{j}(\vec{r}, t) = \vec{j}_{\text{bound}}(\vec{r}, t) + \vec{j}_{\text{free}}(\vec{r}, t). \quad (1.2.2)$$

If the requested Maxwell fields are more of interest on a macroscopic scale, where the detailed behavior of the Maxwell fields inside the matter system is negligible, it is sufficient not to take into account all bound charges and currents and to use a macroscopic mean value for the fields instead. It is shown in common textbooks like Ref. [75, 80], that the influence of the bound charge density $\rho_{\text{bound}}(\vec{r}, t)$ and current density $\vec{j}_{\text{bound}}(\vec{r}, t)$ on the total electric and magnetic field can be expressed by two additional vector fields, the polarisation $\vec{P}(\vec{r}, t)$ and the magnetization $\vec{M}(\vec{r}, t)$. Hence, the relevant mean fields, the displacement field $\vec{D}(\vec{r}, t)$ and magnetic $\vec{H}(\vec{r}, t)$ field, are a superposition of the electric and magnetic field $\vec{E}(\vec{r}, t)$, $\vec{B}(\vec{r}, t)$ in vacuum

with $\vec{P}(\vec{r}, t)$ or $\vec{M}(\vec{r}, t)$, and take the form [80]

$$\vec{D}(\vec{r}, t) = \epsilon_0 \vec{E}(\vec{r}, t) + \vec{P}(\vec{r}, t), \quad (1.2.3)$$

$$\vec{H}(\vec{r}, t) = \frac{1}{\mu_0} \vec{B}(\vec{r}, t) - \vec{M}(\vec{r}, t). \quad (1.2.4)$$

In general, the briefly introduced vectors $\vec{P}(\vec{r}, t)$, and $\vec{M}(\vec{r}, t)$ are given by a series expansion with matter specific tensors [75]. In the following, we consider only linear isotropic media, where $\vec{P}(\vec{r}, t)$ and $\vec{M}(\vec{r}, t)$ are always parallel to $\vec{E}(\vec{r}, t)$ and $\vec{B}(\vec{r}, t)$. Hence, $\vec{D}(\vec{r}, t)$ and $\vec{B}(\vec{r}, t)$ depend linearly on $\vec{E}(\vec{r}, t)$ and $\vec{B}(\vec{r}, t)$, which turns Eq. (1.2.3) and Eq. (1.2.4) into

$$\vec{D}(\vec{r}, t) = \epsilon_0 (1 + \chi_{\text{el}}(\vec{r})) \vec{E}(\vec{r}, t), \quad (1.2.5)$$

$$\vec{B}(\vec{r}, t) = \mu_0 (1 + \chi_{\text{mag}}(\vec{r})) \vec{H}(\vec{r}, t), \quad (1.2.6)$$

with the electric susceptibility $\chi_{\text{el}}(\vec{r})$ and magnetic susceptibility $\chi_{\text{mag}}(\vec{r})$ which are matter specific and in general depend on space [80].

All scalar prefactors in front of $\vec{E}(\vec{r}, t)$ and $\vec{H}(\vec{r}, t)$ can be summarized in a corresponding linear coefficient, namely the electric permittivity $\epsilon(\vec{r})$ and magnetic permeability $\mu(\vec{r})$. Using the equations Eqs. (1.2.3) - (1.2.6), the variables $\epsilon(\vec{r})$, $\mu(\vec{r})$, $\vec{P}(\vec{r}, t)$, and $\vec{M}(\vec{r}, t)$ for a linear medium are given by

$$\epsilon(\vec{r}, t) = \epsilon_0 (1 + \chi_{\text{el}}(\vec{r})) , \quad (1.2.7)$$

$$\mu(\vec{r}, t) = \mu_0 (1 + \chi_{\text{mag}}(\vec{r})) , \quad (1.2.8)$$

$$\vec{P}(\vec{r}, t) = \epsilon_0 \chi_{\text{el}}(\vec{r}) \vec{E}(\vec{r}, t), \quad (1.2.9)$$

$$\vec{M}(\vec{r}, t) = \mu_0 \chi_{\text{mag}}(\vec{r}) \vec{H}(\vec{r}, t). \quad (1.2.10)$$

1.2.2 Definition of the macroscopic Riemann-Silberstein vectors

The macroscopic Riemann-Silberstein vectors in a linear isotropic medium have a similar form like the previously introduced microscopic ones in Eqs. (1.1.1) - (1.1.2). Since the electric permittivity $\epsilon(\vec{r})$ and the magnetic permeability $\mu(\vec{r})$ now depend on space, the electric constant ϵ_0 as well as the magnetic constant μ_0 in the definitions are replaced by their space dependent corresponding variables from Eqs. (1.2.7) - (1.2.8). Therefore, the Riemann-Silberstein vectors $\vec{F}_{\text{lm},\pm}(\vec{r}, t)$ in a linear medium are defined as [73]

$$\vec{F}_{\text{lm},+}(\vec{r}, t) = \sqrt{\frac{\epsilon(\vec{r})}{2}} \vec{E}(\vec{r}, t) + i \sqrt{\frac{1}{2\mu(\vec{r})}} \vec{B}(\vec{r}, t) \quad (1.2.11)$$

for the positive helicity vector $\vec{F}_{\text{lm},+}(\vec{r}, t)$, and

$$\vec{F}_{\text{lm},-}(\vec{r}, t) = \sqrt{\frac{\epsilon(\vec{r})}{2}} \vec{E}(\vec{r}, t) - i \sqrt{\frac{1}{2\mu(\vec{r})}} \vec{B}(\vec{r}, t) \quad (1.2.12)$$

for the negative helicity vector $\vec{F}_{\text{lm},-}(\vec{r}, t)$ where the subindex "lm" stands for "linear medium".

Similar to the microscopic electromagnetic energy density $u(\vec{r}, t)$ in Eq. (1.1.79) in terms of the microscopic Riemann-Silberstein vector, the macroscopic electromagnetic energy density $u_{\text{lm}}(\vec{r}, t)$ in a linear medium is given by [75]

$$u_{\text{lm}}(\vec{r}, t) = \frac{1}{2} \left(\vec{E}(\vec{r}, t) \cdot \vec{D}(\vec{r}, t) + \vec{B}(\vec{r}, t) \cdot \vec{H}(\vec{r}, t) \right). \quad (1.2.13)$$

Using Eqs. (1.2.5) - (1.2.8) and Eqs. (1.2.11) - (1.2.12) lead directly to the equivalent form of the electromagnetic energy density $u_{\text{lm}}(\vec{r}, t)$ in terms of the macroscopic Riemann-Silberstein vectors

$$\begin{aligned} u_{\text{lm}}(\vec{r}, t) &= \vec{F}_{\text{lm},\pm}^*(\vec{r}, t) \cdot \vec{F}_{\text{lm},\pm}(\vec{r}, t) \\ &= \vec{F}_{\text{lm},\mp}(\vec{r}, t) \cdot \vec{F}_{\text{lm},\pm}(\vec{r}, t). \end{aligned} \quad (1.2.14)$$

Again, with Eqs. (1.2.5) - (1.2.8) we obtain the four underlying macroscopic Maxwell fields $\vec{E}(\vec{r}, t)$, $\vec{D}(\vec{r}, t)$, $\vec{B}(\vec{r}, t)$, and $\vec{H}(\vec{r}, t)$

$$\vec{E}(\vec{r}, t) = \sqrt{\frac{1}{2\epsilon(\vec{r})}} \left(\vec{F}_{\text{lm},+}^*(\vec{r}, t) + \vec{F}_{\text{lm},+}(\vec{r}, t) \right) = \sqrt{\frac{1}{2\epsilon(\vec{r})}} \left(\vec{F}_{\text{lm},-}(\vec{r}, t) + \vec{F}_{\text{lm},+}(\vec{r}, t) \right), \quad (1.2.15)$$

$$\vec{D}(\vec{r}, t) = \sqrt{\frac{\epsilon(\vec{r})}{2}} \left(\vec{F}_{\text{lm},+}^*(\vec{r}, t) + \vec{F}_{\text{lm},+}(\vec{r}, t) \right) = \sqrt{\frac{\epsilon(\vec{r})}{2}} \left(\vec{F}_{\text{lm},-}(\vec{r}, t) + \vec{F}_{\text{lm},+}(\vec{r}, t) \right), \quad (1.2.16)$$

$$\vec{B}(\vec{r}, t) = i\sqrt{\frac{\mu(\vec{r})}{2}} \left(\vec{F}_{\text{lm},+}^*(\vec{r}, t) - \vec{F}_{\text{lm},+}(\vec{r}, t) \right) = i\sqrt{\frac{\mu(\vec{r})}{2}} \left(\vec{F}_{\text{lm},-}(\vec{r}, t) - \vec{F}_{\text{lm},+}(\vec{r}, t) \right), \quad (1.2.17)$$

$$\vec{H}(\vec{r}, t) = i\sqrt{\frac{1}{2\mu(\vec{r})}} \left(\vec{F}_{\text{lm},+}^*(\vec{r}, t) - \vec{F}_{\text{lm},+}(\vec{r}, t) \right) = i\sqrt{\frac{1}{2\mu(\vec{r})}} \left(\vec{F}_{\text{lm},-}(\vec{r}, t) - \vec{F}_{\text{lm},+}(\vec{r}, t) \right). \quad (1.2.18)$$

1.2.3 Macroscopic Maxwell's equations

Based on the microscopic Maxwell's equations in Eqs. (1.1.8) - (1.1.11), and by applying a macroscopic field averaging for the Maxwell fields inside a medium, we arrive at the macroscopic Maxwell's equations [75, 80]

$$\vec{\nabla} \cdot \vec{D}(\vec{r}, t) = \rho_{\text{free}}(\vec{r}, t), \quad (1.2.19)$$

$$\vec{\nabla} \cdot \vec{B}(\vec{r}, t) = 0, \quad (1.2.20)$$

$$\vec{\nabla} \times \vec{E}(\vec{r}, t) = -\frac{\partial}{\partial t} \vec{B}(\vec{r}, t), \quad (1.2.21)$$

$$\vec{\nabla} \times \vec{H}(\vec{r}, t) = \frac{\partial}{\partial t} \vec{D}(\vec{r}, t) + \vec{j}_{\text{free}}(\vec{r}, t). \quad (1.2.22)$$

Similar to the Riemann-Silberstein Maxwell's equation in Sec. 1.1.2, we want now to combine the four Maxwell's Eqs. (1.2.19) - (1.2.22) in a linear medium to arrive at Riemann-Silberstein equations. Only the unbounded free part of the charge density and current density determine the electromagnetic field on a macroscopic scale. Based on those four Maxwell's equations in a medium there is an equivalent description in terms of bilinear Riemann-Silberstein vectors and spin-1 matrices, which can be obtained similar to the vacuum considerations.

We start with a complex addition of the two Gauß laws in Eqs. (1.2.19) - (1.2.20)

$$\vec{\nabla} \cdot \vec{D}(\vec{r}, t) \pm i\vec{\nabla} \cdot \vec{B}(\vec{r}, t) = \rho_{\text{free}}(\vec{r}, t). \quad (1.2.23)$$

This equation can be expressed in terms of the Riemann-Silberstein vectors $\vec{F}_{\text{lm},\pm}(\vec{r}, t)$ and is equivalent to

$$\vec{\nabla} \cdot \vec{F}_{\text{lm},\pm}(\vec{r}, t) + \vec{K}_{\mp}(\vec{r}) \cdot \vec{F}_{\text{lm},+}(\vec{r}, t) + \vec{K}_{\pm}(\vec{r}) \cdot \vec{F}_{\text{lm},-}(\vec{r}, t) = \frac{1}{\sqrt{2\epsilon(\vec{r})}} \rho_{\text{free}}(\vec{r}, t), \quad (1.2.24)$$

with

$$\vec{K}_{\pm}(\vec{r}) = \frac{(\vec{\nabla}\epsilon(\vec{r}))}{4\epsilon(\vec{r})} \pm \frac{(\vec{\nabla}\mu(\vec{r}))}{4\mu(\vec{r})}, \quad \vec{K}_{\mp}(\vec{r}) = \frac{(\vec{\nabla}\epsilon(\vec{r}))}{4\epsilon(\vec{r})} \mp \frac{(\vec{\nabla}\mu(\vec{r}))}{4\mu(\vec{r})}. \quad (1.2.25)$$

Note, that the macroscopic Gauß laws conditions in Eq. (1.2.24) can only be obeyed by a linear combination of both, $\vec{F}_{\text{lm},+}(\vec{r}, t)$ and $\vec{F}_{\text{lm},-}(\vec{r}, t)$, which is in contrast to the microscopic equation Eq. (1.2.24), where already only one of the different helicity vectors $\vec{F}_{\text{lm},\pm}(\vec{r}, t)$ satisfies the Gauß conditions. Hence, the correct macroscopic Maxwell's equations require a coupling of the two helicity Riemann-Silberstein vectors.

The same situation arises, when we consider the transformation of the macroscopic Faraday's and Ampère's laws in Eqs. (1.2.21) - (1.2.22) for the corresponding Riemann-Silberstein equation. Later in chapter 3, we need a more general form of Faraday's and Ampère's law. Therefore, we expand both equations in Eqs. (1.2.21) - (1.2.22) by an additional term to describe a damping of the electromagnetic field, e.g., in a lossy medium region. The damping terms are assumed to be proportional to the electromagnetic field. The underlying constants of proportionality are the electric conductivity $\sigma_{\text{el}}(\vec{r})$ and the magnetic conductivity $\sigma_{\text{mag}}(\vec{r})$.

Therefore, Faraday's law and Ampère's law in Eqs. (1.2.21) - (1.2.22) with lossy electric and magnetic layer are given by

$$\vec{\nabla} \times \vec{E}(\vec{r}, t) = -\left(\frac{\partial}{\partial t} + \sigma_{\text{mag}}(\vec{r})\right)\vec{B}(\vec{r}, t), \quad (1.2.26)$$

$$\vec{\nabla} \times \vec{H}(\vec{r}, t) = \left(\frac{\partial}{\partial t} + \sigma_{\text{el}}(\vec{r})\right)\vec{D}(\vec{r}, t) + \vec{j}_{\text{free}}(\vec{r}, t). \quad (1.2.27)$$

By separating the temporal derivative terms on the right-hand side and adding Eq. (1.2.26) as imaginary part to Eq. (1.2.27) and multiplying the whole equation by the imaginary unit leads to

$$\begin{aligned}
 i\frac{\partial}{\partial t}\left(\epsilon(\vec{r})\vec{E}(\vec{r},t) \pm i\vec{B}(\vec{r},t)\right) &= \pm\vec{\nabla} \times \vec{E}(\vec{r},t) + i\vec{\nabla} \times \frac{1}{\mu(\vec{r})}\vec{B}(\vec{r},t) \\
 &\quad \pm \sigma_{\text{mag}}(\vec{r},)\vec{B}(\vec{r},t) - i\sigma_{\text{el}}(\vec{r})\vec{D}(\vec{r},t) \\
 &\quad - i\vec{j}_{\text{free}}(\vec{r},t) .
 \end{aligned} \tag{1.2.28}$$

As before in the Gauß Riemann-Silberstein equation in a medium, it is not possible to describe the Faraday's and Ampère's law only with one of the Riemann-Silberstein vectors, either $\vec{F}_{\text{lm},+}(\vec{r},t)$ or $\vec{F}_{\text{lm},-}(\vec{r},t)$. Therefore, after substituting the Maxwell fields with the corresponding Riemann-Silberstein vector expressions in Eq. (1.2.28), using the curl operator in spin-1 matrix representation from Eq. (1.1.26), and multiplying with the Planck constant \hbar , the final form of Faraday's and Ampère's law as Riemann-Silberstein equation is

$$\begin{aligned}
 i\hbar\frac{\partial}{\partial t}\vec{F}_{\text{lm},\pm}(\vec{r},t) &= \pm\hbar c(\vec{r})\vec{\nabla} \times \vec{F}_{\text{lm},\pm}(\vec{r},t) - i\hbar\frac{1}{\sqrt{2\epsilon(\vec{r})}}\vec{j}_{\text{free}}(\vec{r},t) \\
 &\quad \mp \hbar c(\vec{r})\vec{K}_{\pm}(\vec{r}) \times \vec{F}_{\text{lm},+}(\vec{r},t) \\
 &\quad \mp \hbar c(\vec{r})\vec{K}_{\mp}(\vec{r}) \times \vec{F}_{\text{lm},-}(\vec{r},t) \\
 &\quad - i\hbar\sigma_{\text{el,mag},\pm}(\vec{r})\vec{F}_{\text{lm},+}(\vec{r},t) \\
 &\quad - i\hbar\sigma_{\text{el,mag},\mp}(\vec{r})\vec{F}_{\text{lm},-}(\vec{r},t) .
 \end{aligned} \tag{1.2.29}$$

Here $\vec{K}_{\pm}(\vec{r})$, $\vec{K}_{\mp}(\vec{r})$ are defined by Eq. (1.2.25) and $\sigma_{\text{el,mag},\pm}(\vec{r},t)$, $\sigma_{\text{el,mag},\mp}(\vec{r},t)$ are defined by

$$\sigma_{\text{el,mag},\pm}(\vec{r}) = \frac{1}{2} [\sigma_{\text{el}}(\vec{r}) \pm \sigma_{\text{mag}}(\vec{r})] , \quad \sigma_{\text{el,mag},\mp}(\vec{r}) = \frac{1}{2} [\sigma_{\text{el}}(\vec{r}) \mp \sigma_{\text{mag}}(\vec{r})] . \tag{1.2.30}$$

All terms in Eq. (1.2.29) agree with the result of Ref. [74] for the macroscopic Riemann-Silberstein equations in a linear medium, except the lossy layer terms in the third line of this equation, which contain the layer property functions $\sigma_{\text{el,mag},\pm}(\vec{r})$ and $\sigma_{\text{el,mag},\mp}(\vec{r})$. These terms will become relevant later when we introduce a perfectly matched layer to absorb outgoing electromagnetic radiation.

To summarize, in contrast to the previous microscopic considerations, the additional spatial dependency due to the media properties requires an important modification in both Riemann-Silberstein Maxwell's equations, in the combined two Gauß laws as well as in the combined Faraday's and Ampère's laws. In both cases, it is not possible anymore to find a form obeying Maxwell's equations depending on only one of the

$\vec{F}_{\text{lm},+}(\vec{r}, t)$ or $\vec{F}_{\text{lm},-}(\vec{r}, t)$ terms. As a consequence, Riemann-Silberstein Maxwell's equations in a medium have to be formulated as a six-dimensional problem which we consider in the next section.

1.2.4 Combined helicity Riemann-Silberstein six-vector in a linear medium

The fact that macroscopic Riemann-Silberstein vectors $\vec{F}_{\text{lm},\pm}(\vec{r}, t)$ couple to each other in the macroscopic Riemann-Silberstein equations in Eq. (1.2.24) and Eq. (1.2.29) demonstrates clearly the necessity of the six-dimensional representation of the Riemann-Silberstein Maxwell's vector, like previously considered in Sec. 1.1.5. Referring to the microscopic definition of $\mathcal{F}(\vec{r}, t)$ in Eq. (1.1.38), the corresponding macroscopic six-component Riemann-Silberstein vector $\mathcal{F}_{\text{lm}}(\vec{r}, t)$ is defined as

$$\mathcal{F}_{\text{lm}}(\vec{r}, t) = \begin{pmatrix} \vec{F}_{\text{lm},+}(\vec{r}, t) \\ \vec{F}_{\text{lm},-}(\vec{r}, t) \end{pmatrix}. \quad (1.2.31)$$

Therefore, the corresponding total combined Maxwell Riemann-Silberstein Gauß law takes with the scalar product definition of Eq. (1.1.43) the form [73]

$$\mathcal{D}_{\text{lm}}(\vec{r}, t) \cdot \mathcal{F}(\vec{r}, t) = \mathcal{Q}_{\text{lm}}(\vec{r}, t) \quad (1.2.32)$$

with the six-dimensional Riemann-Silberstein free charge density $\mathcal{Q}_{\text{lm}}(\vec{r}, t)$

$$\mathcal{Q}_{\text{lm}}(\vec{r}, t) = \begin{pmatrix} 1 \\ 1 \end{pmatrix}_{2 \times 1} \otimes \left(\frac{1}{\sqrt{2\epsilon(\vec{r})}} \rho_{\text{free}}(\vec{r}, t) \right)_{1 \times 1} \quad (1.2.33)$$

and a six-dimensional operator $\mathcal{D}_{\text{lm}}(\vec{r}, t)$

$$\begin{aligned} \mathcal{D}_{\text{lm}}(\vec{r}, t) = & \begin{pmatrix} 1 & 0 \\ 0 & 1 \end{pmatrix}_{2 \times 2} \otimes \left(\vec{\nabla} \right)_{1 \times 3}^{\top} \\ & + \begin{pmatrix} 1 & 1 \\ 1 & 1 \end{pmatrix}_{2 \times 2} \otimes \left(\frac{(\vec{\nabla} \epsilon(\vec{r}))}{4\epsilon(\vec{r})} \right)_{1 \times 3}^{\top} \\ & + \begin{pmatrix} -1 & 1 \\ 1 & -1 \end{pmatrix}_{2 \times 2} \otimes \left(\frac{(\vec{\nabla} \mu(\vec{r}))}{4\mu(\vec{r})} \right)_{1 \times 3}^{\top} \end{aligned} \quad (1.2.34)$$

that corresponds to the divergence operator in the common Gauß laws. The Gauß law in the Riemann-Silberstein representation does not only depend on the electric permittivity $\epsilon(\vec{r})$ and magnetic permeability $\mu(\vec{r})$, but also on their spatial derivatives $\vec{\nabla} \epsilon(\vec{r})$ and $\vec{\nabla} \mu(\vec{r})$.

Next, we convert the remaining Riemann-Silberstein equation in Eq. (1.2.29) into a six-dimensional representation. First, we define similar to the six-dimensional

Riemann-Silberstein charge density $\mathcal{Q}(\vec{r}, t)$ in Eq. (1.2.33) an adequate six-dimensional Riemann-Silberstein current density $\mathcal{J}(\vec{r}, t)$ with

$$\mathcal{J}_{\text{lm}}(\vec{r}, t) = \begin{pmatrix} 1 \\ 1 \end{pmatrix}_{2 \times 1} \otimes \left(\frac{1}{\sqrt{2\epsilon(\vec{r}, t)}} \vec{J}_{\text{free}}(\vec{r}, t) \right)_{3 \times 1}. \quad (1.2.35)$$

Let us define $H_{\text{Mx,lm}}(\vec{r})$

$$H_{\text{Mx,lm}}(\vec{r}) = -i\hbar c(\vec{r}) \vec{\nabla} \cdot \vec{\mathbf{S}}, \quad (1.2.36)$$

which depends explicitly on spatial coordinates due to the speed of light $c(\vec{r})$ inside a linear medium. The combined coupled equations in Eq. (1.2.29) can be expressed in a similar inhomogeneous Schrödinger like form as in Eq. (1.1.44) with

$$i\hbar \frac{\partial}{\partial t} \mathcal{F}(\vec{r}, t) = \mathcal{H}_{\text{lm}}(\vec{r}) \mathcal{F}(\vec{r}, t) - i\hbar \mathcal{J}_{\text{free}}(\vec{r}, t), \quad (1.2.37)$$

where $\mathcal{H}_{\text{lm}}(\vec{r})$ consists of

$$\mathcal{H}_{\text{lm}}(\vec{r}) = \mathcal{H}_{\text{lm,(0)}}(\vec{r}) + \mathcal{K}_{\text{lm}}(\vec{r}). \quad (1.2.38)$$

The operator $\mathcal{H}_{\text{lm,(0)}}(\vec{r})$ only contains the uncoupled part with the spin-curl operation representing the first term on the right-hand side of Eq. (1.2.29), and could also be expressed as a Kronecker product of $H_{\text{Mx,lm}}(\vec{r})$

$$\mathcal{H}_{\text{lm,(0)}}(\vec{r}) = \begin{pmatrix} 1 & 0 \\ 0 & -1 \end{pmatrix}_{2 \times 2} \otimes \left(H_{\text{Mx,lm}}(\vec{r}) \right)_{3 \times 3}. \quad (1.2.39)$$

Note, that the macroscopic $\mathcal{H}_{\text{lm}}(\vec{r})$ only locally depends on space. We see in chapter 5, that this fact changes if we consider the Maxwell-matter coupling in the fundamental microscopic regime and some non-localized terms arise.

Finally, all remaining terms except the first one on the right-hand side of Eq. (1.2.29) are represented by $\mathcal{K}_{\text{lm}}(\vec{r})$ and it includes all coupling terms which determine mainly the properties of a linear medium and is explicitly given by

$$\begin{aligned} \mathcal{K}_{\text{lm}}(\vec{r}) = & \begin{pmatrix} -1 & -1 \\ 1 & 1 \end{pmatrix}_{2 \times 2} \otimes \left(-i\hbar \frac{c(\vec{r})}{4\epsilon(\vec{r})} \left[\vec{\mathbf{S}} \cdot \left(\vec{\nabla} \epsilon(\vec{r}) \right) \right] \right)_{3 \times 3} \\ & + \begin{pmatrix} -1 & 1 \\ -1 & 1 \end{pmatrix}_{2 \times 2} \otimes \left(-i\hbar \frac{c(\vec{r})}{4\mu(\vec{r})} \left[\vec{\mathbf{S}} \cdot \left(\vec{\nabla} \mu(\vec{r}) \right) \right] \right)_{3 \times 3} \\ & + \begin{pmatrix} -1 & -1 \\ -1 & -1 \end{pmatrix}_{2 \times 2} \otimes \left(i\hbar \frac{\sigma_{\text{el}}(\vec{r})}{2} \mathbb{1}_{(3)} \right)_{3 \times 3} \\ & + \begin{pmatrix} -1 & 1 \\ 1 & -1 \end{pmatrix}_{2 \times 2} \otimes \left(i\hbar \frac{\sigma_{\text{mag}}(\vec{r})}{2} \mathbb{1}_{(3)} \right)_{3 \times 3}, \end{aligned} \quad (1.2.40)$$

where $\mathbb{1}_{(3)}$ gives the three-dimensional identity matrix. We replaced again all occurring cross products and curl operations by the corresponding spin-1 representation from Eq. (1.1.14) and Eq. (1.1.26). In a medium without any electromagnetic loss, both conductivities $\sigma_{\text{el}}(\vec{r})$ and $\sigma_{\text{mag}}(\vec{r})$ are equal to zero and the remaining equation is equal to the common Maxwell Faraday's and Ampère's laws shown in Eq. (1.2.21) and Eq. (1.2.22) which agrees with the corresponding equations in Ref. [73].

In principle, the common expression of the macroscopic Maxwell's equations in Eqs. (1.2.19) - (1.2.22) and the Riemann-Silberstein correspondence representation in Eq. (1.2.32) and Eq. (1.2.37) are exactly equal for an isotropic linear medium, but in case of border surfaces with sharp edges, e.g., between two different homogeneous media, the spatial derivatives of $\vec{\nabla}\epsilon(\vec{r})$ and $\vec{\nabla}\mu(\vec{r})$ are not continuous. Hence, the spatial derivatives at the border surface are not defined. This fact has to be taken into account in case of numerical calculations of the spatial derivatives. However, in a homogeneous medium with constant $\epsilon(\vec{r})$ and $\mu(\vec{r})$, the extra terms are equal to zero due to the fact that $\vec{\nabla}\epsilon(\vec{r}, t) = 0$ and $\vec{\nabla}\mu(\vec{r}) = 0$.

In Sec. 1.1.7 and Sec. 1.1.8, we introduced the Riemann-Silberstein scalar product and the eigenstate expansion of the Riemann-Silberstein six-vectors. Note, that both can also be applied for the macroscopic Riemann-Silberstein six-vector $\mathcal{F}_{\text{lm}}(\vec{r}, t)$ in an isotropic linear medium, if $\mathcal{F}(\vec{r}, t)$ is replaced by $\mathcal{F}_{\text{lm}}(\vec{r}, t)$ and the operator \mathcal{H} from Sec. 1.1.7 and Sec. 1.1.8 by $\mathcal{H}_{\text{lm}}(\vec{r})$.

So far, our considerations have shown that if the Maxwell fields are defined as a complex bilinear Riemann-Silberstein vector, the microscopic and macroscopic Maxwell's equations can be expressed in Schrödinger form. The main difference to matter wave functions is the additional constraint that the Riemann-Silberstein vector has to obey the Gauß law. We show in chapter 4 that this constraint automatically arises for the homogeneous Maxwell's equations, if we consider the Maxwell fields as quantum mechanical relativistic spin-1 fields. In this picture, the Riemann-Silberstein vector fulfills the relativistic energy-momentum relation only if the Gauß law holds.

Chapter 2

Riemann-Silberstein time-evolution of Maxwell fields in Schrödinger-like form

The underlying fundamental equations, which determine the electromagnetic field in time are Faraday's and Ampère's law, since they describe the temporal changes of the corresponding field. Both equations are directly coupled to each other so that both equations have to be consistent. This circumstance makes it difficult to find an analytic solution for the time-evolution of the electromagnetic field. We introduce in this chapter a consistent and efficient propagation scheme to solve these coupled equations numerically.

Based on the transformed Maxwell's equations in Schrödinger-like form that we introduced in the previous chapter, we develop here a Schrödinger-like time-evolution of the electromagnetic fields for three different cases. The first one describes simple homogeneous microscopic Maxwell's equations without any charge or current densities, the second one adds microscopic charge and current densities to an inhomogeneous Schrödinger-like time evolution operator. Finally, both of these two derivations for a Maxwell time-evolution operator can be combined to find the corresponding one for Maxwell's equations in a linear medium including lossy layers.

2.1 Time-evolution of homogeneous microscopic Maxwell's equations

In chapter 1, we have used the Riemann-Silberstein vector to transform the common microscopic Maxwell's equations into two combined equations, one for the Gauß laws and one for Ampère's and Faraday's laws. Whereas the Gauß laws constitute a side condition which has to be valid for all times, the combined Ampère's and Faraday's laws which contains first order time derivative determine the propagation of the field.

First, we use the six-dimensional microscopic Riemann-Silberstein six-vector $\mathcal{F}(\vec{r}, t)$ defined in Eq. (1.1.38) and start with the simplest case without charge and current densities. Hence, all Eqs. (1.1.8) - (1.1.11) reduce to homogeneous differential equations.

The microscopic Riemann-Silberstein Gauß law in Eq. (1.1.42) with $\mathcal{Q}(\vec{r}, t)$ equal to zero becomes

$$\mathcal{D} \cdot \mathcal{F}(\vec{r}, t) = 0 . \quad (2.1.1)$$

We request this condition for an initial Riemann-Silberstein six-vector $\mathcal{F}(\vec{r}, t_{(0)})$ with initial time $t_{(0)}$ and show in Sec. 2.4 that the time-evolution in Eq. (1.1.44) preserves this constraint, if it is given for an initial time.

For the homogeneous case without any current density $\mathcal{J}(\vec{r}, t)$ as inhomogeneity, Eq. (1.1.44) can be rewritten as

$$\frac{\partial}{\partial t} \mathcal{F}(\vec{r}, t) = -\frac{i}{\hbar} \mathcal{H} \mathcal{F}(\vec{r}, t) . \quad (2.1.2)$$

Obviously, this equation is formally equivalent to the general quantum mechanical time-dependent Schrödinger equation [81, 82]

$$i\hbar \frac{\partial}{\partial t} \psi(\vec{r}, t) = \hat{H}_{\text{qm}} \psi(\vec{r}, t) \quad (2.1.3)$$

with a scalar quantum mechanical wave function $\psi(\vec{r}, t)$ and a quantum mechanical Hamiltonian \hat{H}_{qm} . For a given wave function $\psi(\vec{r}, t_{(0)})$ at time $t_{(0)}$ and a general given time-independent Hamiltonian \hat{H}_{qm} , that describes the system, the future wave function for $t > t_{(0)}$ is determined by the well known time-evolution operator $\hat{U}_{\text{qm}}(t, t_{(0)})$ [82]

$$\hat{U}_{\text{qm}}(t, t_{(0)}) = \exp \left[\frac{-i(t - t_{(0)}) \hat{H}_{\text{qm}}}{\hbar} \right] , \quad (2.1.4)$$

such that the wave function at time t can be obtained by

$$\psi(\vec{r}, t) = \hat{U}_{\text{qm}}(t, t_{(0)}) \psi(\vec{r}, t_{(0)}) . \quad (2.1.5)$$

Our purpose here is to derive the corresponding time evolution operator $\mathcal{U}(t, t_{(0)})$ for the Riemann-Silberstein six-vector $\mathcal{F}(\vec{r}, t_{(0)})$ to get the time evolved $\mathcal{F}(\vec{r}, t)$ from starting time $t_{(0)}$ to time t with

$$\mathcal{F}(\vec{r}, t) = \mathcal{U}(t, t_{(0)}) \mathcal{F}(\vec{r}, t_{(0)}) . \quad (2.1.6)$$

Similar to the derivation of the quantum mechanical time-evolution operator $\hat{U}_{\text{qm}}(t, t_{(0)})$, we start with the properties of the evolution operator to ensure the correct form of $\mathcal{U}(t, t_{(0)})$.

All following requested time-evolution properties are equivalent to those in quantum mechanics, which are listed in Ref. [83].

First, for time t equal to $t_{(0)}$ the operator $\mathcal{U}(t_{(0)}, t_{(0)})$ has to obey

$$\mathcal{U}(t_{(0)}, t_{(0)}) = \mathbb{1}_{(6)} , \quad (2.1.7)$$

with $\mathbb{1}_{(6)}$ being the six-dimensional unity matrix so that the initial $\mathcal{F}(\vec{r}, t_{(0)})$ remains identical. In quantum mechanics, all wave functions have to be normalized at all times. Consequently the quantum mechanical time-evolution operator is unitary. In case of Maxwell fields, we do not have exactly the normalization condition, but the total field energy $E = \langle \mathcal{F} | \mathcal{F} \rangle$ has to be constant in time if there is no coupling to matter or any loss. Using Eq. (1.1.81) and Eq. (2.1.6) to get the energy of the field yields the condition

$$\langle \mathcal{F}(t_{(0)}) | E | \mathcal{F}(t_{(0)}) \rangle \equiv \langle \mathcal{F}(t) | \mathcal{H} | \mathcal{F}(t) \rangle \quad (2.1.8)$$

$$\langle \mathcal{F}(t_{(0)}) | E | \mathcal{F}(t_{(0)}) \rangle \equiv \langle \mathcal{U}(t, t_{(0)}) \mathcal{F}(t_{(0)}) | \mathcal{H} | \mathcal{U}(t, t_{(0)}) \mathcal{F}(t_{(0)}) \rangle .$$

According to the definition of the Riemann-Silberstein scalar product in Eq. (1.1.77), we obtain the explicit integral form

$$\begin{aligned} \int_{-\infty}^{\infty} d^3r \mathcal{F}^\dagger(\vec{r}, t_{(0)}) \mathcal{F}(\vec{r}, t_{(0)}) &\equiv \int_{-\infty}^{\infty} d^3r (\mathcal{U}(t, t_{(0)}) \mathcal{F}(\vec{r}, t_{(0)}))^\dagger \mathcal{U}(t, t_{(0)}) \mathcal{F}(\vec{r}, t_{(0)}) \\ \int_{-\infty}^{\infty} d^3r \mathcal{F}^\dagger(\vec{r}, t_{(0)}) \mathcal{F}(\vec{r}, t_{(0)}) &\equiv \int_{-\infty}^{\infty} d^3r \mathcal{F}^\dagger(\vec{r}, t_{(0)}) \mathcal{U}^\dagger(t, t_{(0)}) \mathcal{U}(t, t_{(0)}) \mathcal{F}(\vec{r}, t_{(0)}) . \end{aligned} \quad (2.1.9)$$

Therefore, to satisfy the equation in Eq. (2.1.9) the time-evolution operator has to obey the unitary condition

$$\mathcal{U}^\dagger(t, t_{(0)}) \mathcal{U}(t, t_{(0)}) = \mathbb{1}_{(6)} . \quad (2.1.10)$$

Furthermore, the time evolution operator has the composition property. Two intermediate operators propagating a vector first from time $t_{(0)}$ to t' and afterwards from t' to the final time t , are equal to

$$\mathcal{U}(t, t_{(0)}) = \mathcal{U}(t, t') \mathcal{U}(t', t_{(0)}) . \quad (2.1.11)$$

We request the same properties for the time-evolution operator like in quantum mechanics, and chose the same infinitesimal ansatz for the Riemann-Silberstein vector $\mathcal{F}(\vec{r}, t)$. Consequently, the Maxwell time-evolution operator $\mathcal{U}(t, t_{(0)})$ is a operator-valued 6x6 matrix. Starting with an infinitesimal small time propagation $t + dt$, we assume that the difference between the identity matrix $\mathbb{1}_6$ and $\mathcal{U}(t_{(0)} + dt, t_{(0)})$

is linear and first order of dt . Similar as in quantum mechanics, we chose the first order of an exponential series with the exponent $-\frac{i}{\hbar}$ and get the infinitesimal form

$$\mathcal{U}(t_{(0)} + dt, t_{(0)}) = \mathbb{1}_{(6)} - \frac{i}{\hbar} \mathcal{H} dt \quad (2.1.12)$$

with the Maxwell Hamiltonian operator \mathcal{H} in Eq. (1.1.45) as an linear approximated ansatz. Eq. (2.1.12) is clearly the unity operator for $dt \rightarrow 0$. Due to the Hermitian operator \mathcal{H} the unitary condition yields

$$\mathcal{U}^\dagger \mathcal{U} = \left(\mathbb{1}_{(6)} + \frac{i}{\hbar} \mathcal{H} dt \right) \left(\mathbb{1}_{(6)} - \frac{i}{\hbar} \mathcal{H} dt \right) = \mathbb{1}_{(6)} + \frac{1}{\hbar^2} \mathcal{H}^2 (dt)^2, \quad (2.1.13)$$

which is equal to $\mathbb{1}_{(6)}$ after truncating all non-linear higher order terms in dt for infinitesimal considerations. The composition $\mathcal{U}(t_{(0)} + dt + dt, t_{(0)})$ applied to the ansatz in Eq. (2.1.12) gives

$$\begin{aligned} \mathcal{U}(t_{(0)} + dt + dt, t_{(0)}) &= \mathcal{U}(t_{(0)} + dt + dt, t_{(0)} + dt) \mathcal{U}(t_{(0)} + dt, t_{(0)}) \\ &= \left(\mathbb{1}_{(6)} - \frac{i}{\hbar} \mathcal{H} dt \right) \left(\mathbb{1}_{(6)} - \frac{i}{\hbar} \mathcal{H} dt \right) \\ &= \mathbb{1}_{(6)} - 2 \frac{i}{\hbar} \mathcal{H} dt - \frac{1}{\hbar^2} \mathcal{H} (dt)^2. \end{aligned} \quad (2.1.14)$$

The required composition condition holds if we take only first order terms in dt into account. Hence, $\mathcal{U}(t_{(0)} + dt + dt, t_{(0)})$ differs only by a linear term in dt from the identity operator.

Next, each time interval $t_{(0)}$ to t can be separated in N time steps with $\Delta t_N = (t - t_{(0)})/N$. In the limit $N \rightarrow \infty$, Δt reaches the infinitesimal time step dt . Obviously, if we apply Eq. (2.1.12) N times to the latest updated Riemann-Silberstein six-vector, the total time-evolution operator from $t_{(0)}$ to t in one operation is obtained by

$$\lim_{N \rightarrow \infty} \left(\mathbb{1}_{(6)} - \frac{i}{\hbar} \mathcal{H} \left(\frac{t - t_{(0)}}{N} \right) \right)^N = \exp \left[-\frac{i}{\hbar} (t - t_{(0)}) \mathcal{H} \right]. \quad (2.1.15)$$

This provides us with the Riemann-Silberstein time-evolution operator \mathcal{U}

$$\mathcal{U}(t, t_{(0)}) = \exp \left[-\frac{i}{\hbar} (t - t_{(0)}) \mathcal{H} \right]. \quad (2.1.16)$$

2.2 Time-evolution of inhomogeneous microscopic Riemann-Silberstein six-vector

Any charge or current density in vacuum makes Maxwell's equations inhomogeneous and the inhomogeneous contributions have a main influence on the Maxwell field propagation. In the presence of charge and current densities, the underlying

Riemann-Silberstein equations in the six-dimensional representation in Eq. (1.1.42) and Eq. (1.1.44) have also charge and current density terms, which make them inhomogeneous as well. The Riemann-Silberstein divergence condition is now equal to Eq. (1.1.42), given by

$$\mathcal{D} \cdot \mathcal{F}(\vec{r}, t) = \mathcal{Q}(\vec{r}, t) \quad (2.2.1)$$

with operator \mathcal{D} from Eq. (1.1.41) and the two-component Riemann-Silberstein charge density $\mathcal{Q}(\vec{r}, t)$ in Eq. (1.1.40). According to the previous Sec. 2.1, we consider Eq. (2.2.1) is given for the initial $\mathcal{F}(\vec{r}, t_{(0)})$ at the initial time $t_{(0)}$ and this constraint is conserved after applying the time-evolution operator and obtaining $\mathcal{F}(\vec{r}, t)$. We show the proof for this assumption later in Sec. 2.4.

As before in Sec. 2.1, the main time-evolution equations are Faraday's and Ampère's equations in Eq. (1.1.44). Including the inhomogeneous contributions, the equation of motion then reads

$$\frac{\partial}{\partial t} \mathcal{F}(\vec{r}, t) = -\frac{i}{\hbar} \mathcal{H} \mathcal{F}(\vec{r}, t) - \mathcal{J}(\vec{r}, t). \quad (2.2.2)$$

Again, also here a mathematical analogy to quantum mechanics can be drawn. As shown in Ref. [84, 85], one can construct time-evolution schemes for inhomogeneous Schrödinger equations. In the following, we apply these considerations for our propagation of Maxwell's fields in the Riemann-Silberstein form. Let us start with the substitution of the inhomogeneity term $\mathcal{J}(\vec{r}, t)$ in Eq. (2.2.2) with

$$\mathcal{J}(\vec{r}, t) = \mathcal{A}(\vec{r}, t) \mathcal{F}(\vec{r}, t_{(0)}), \quad (2.2.3)$$

using the initial $\mathcal{F}(\vec{r}, t_{(0)})$ and a 6x6-dimensional matrix $\mathcal{A}(\vec{r}, t)$ given by

$$\begin{aligned} \mathcal{A}(\vec{r}, t) = & \begin{pmatrix} 1 & 0 \\ 0 & 0 \end{pmatrix}_{2 \times 2} \otimes \frac{1}{\sqrt{2\epsilon_0}} \begin{pmatrix} \frac{j_x(\vec{r}, t) F_{+,x}^*(\vec{r}, t_{(0)})}{|F_{+,x}|} & 0 & 0 \\ 0 & \frac{j_y(\vec{r}, t) F_{+,y}^*(\vec{r}, t_{(0)})}{|F_{+,y}|} & 0 \\ 0 & 0 & \frac{j_z(\vec{r}, t) F_{+,z}^*(\vec{r}, t_{(0)})}{|F_{+,z}|} \end{pmatrix}_{3 \times 3} \\ & + \begin{pmatrix} 0 & 0 \\ 0 & 1 \end{pmatrix}_{2 \times 2} \otimes \frac{1}{\sqrt{2\epsilon_0}} \begin{pmatrix} \frac{j_x(\vec{r}, t) F_{-,x}^*(\vec{r}, t_{(0)})}{|F_{-,x}|} & 0 & 0 \\ 0 & \frac{j_y(\vec{r}, t) F_{-,y}^*(\vec{r}, t_{(0)})}{|F_{-,y}|} & 0 \\ 0 & 0 & \frac{j_z(\vec{r}, t) F_{-,z}^*(\vec{r}, t_{(0)})}{|F_{-,z}|} \end{pmatrix}_{3 \times 3}. \end{aligned} \quad (2.2.4)$$

Here we assume that the initial Riemann-Silberstein vector $\mathcal{F}(\vec{r}, t_{(0)})$ is non-zero for all \vec{r} . In analogy to the homogeneous time evolution ansatz in Eq. (2.1.6), we assume that $\mathcal{F}(\vec{r}, t)$ can be obtained by the inhomogeneous time-evolution operator $\mathcal{W}(t, t_{(0)})$ and the initial $\mathcal{F}(\vec{r}, t_{(0)})$ by

$$\mathcal{F}(\vec{r}, t) = \mathcal{W}(t, t_{(0)}) \mathcal{F}(\vec{r}, t_{(0)}). \quad (2.2.5)$$

Using Eq. (2.2.5) and Eq. (2.2.3) in Eq. (2.2.2) leads to

$$\frac{\partial}{\partial t} \mathcal{W}(t, t_{(0)}) \mathcal{F}(\vec{r}, t_{(0)}) = -\frac{i}{\hbar} \mathcal{H} \mathcal{W}(t, t_{(0)}) \mathcal{F}(\vec{r}, t_{(0)}) - \mathcal{A}(\vec{r}, t) \mathcal{F}(\vec{r}, t_{(0)}) . \quad (2.2.6)$$

Hence, the corresponding equation for the inhomogeneous time-evolution operator without the initial Riemann-Silberstein six-vector $\mathcal{F}(\vec{r}, t_{(0)})$ is

$$\frac{\partial}{\partial t} \mathcal{W}(t, t_{(0)}) = -\frac{i}{\hbar} \mathcal{H} \mathcal{W}(t, t_{(0)}) - \mathcal{A}(\vec{r}, t) . \quad (2.2.7)$$

The ansatz for the inhomogeneous time-evolution operator is to factorize $\mathcal{W}(t, t_{(0)})$ into the homogeneous time-evolution operator $\mathcal{U}(t, t_{(0)})$ from Eq. (2.1.16) and a second operator $\mathcal{Z}(t)$ so that

$$\mathcal{W}(t, t_{(0)}) = \mathcal{U}(t, t_{(0)}) \mathcal{Z}(t) . \quad (2.2.8)$$

The time evolution operator depends on times t and $t_{(0)}$, whereas the additional factor $\mathcal{Z}(t)$ depends only on time t . If we directly take the time derivative of $\mathcal{W}(t, t_{(0)})$ and compare the result with Eq. (2.2.7), we arrive at the differential equation

$$\mathcal{A}(\vec{r}, t) = \mathcal{U}(t, t_{(0)}) \frac{\partial}{\partial t} \mathcal{Z}(t) , \quad (2.2.9)$$

which leads us, after integrating, to the solution for $\mathcal{Z}(t)$

$$\mathcal{Z}(t) = \mathcal{Z}(t_{(0)}) + \int_{t_{(0)}}^t d\tau \mathcal{U}^{-1}(\tau, t_{(0)}) \mathcal{A}(\tau) = \mathbb{1}_{(6)} + \int_{t_{(0)}}^t d\tau \mathcal{U}(t_{(0)}, \tau) \mathcal{A}(\tau) . \quad (2.2.10)$$

The initial value $\mathcal{Z}(t_{(0)})$ is equal to the identity operator $\mathbb{1}_{(6)}$ if we take into account, that $\mathcal{W}(t_{(0)}, t_{(0)})$ also has to be the identity operator $\mathbb{1}_{(6)}$ in this case since \mathcal{W} has to hold the time-evolution property in Eq. (2.1.7). Finally, the appropriate solution for the inhomogeneous time-evolution operator $\mathcal{W}(t, t_{(0)})$ is given by [84, 85]

$$\mathcal{W}(t, t_{(0)}) = \mathcal{U}(t, t_{(0)}) - \int_{t_{(0)}}^t d\tau \mathcal{U}(t, \tau) \mathcal{A}(\vec{r}, \tau) \quad (2.2.11)$$

including the homogeneous Riemann-Silberstein time-evolution operator $\mathcal{U}(t, \tau)$ of Eq. (2.1.16). Note, although the solution in Eq. (2.2.11) of the inhomogeneous time-propagation in Eq. (2.2.2) obeys the initial condition $\mathcal{W}(t_{(0)}, t_{(0)}) = \mathbb{1}_{(6)}$, $\mathcal{W}(t, t_{(0)})$ breaks in general the composition criterion in Eq. (2.1.11) of a valid time-evolution operator which means that

$$\mathcal{W}(t, t_{(0)}) \neq \mathcal{W}(t, t') \mathcal{W}(t', t_{(0)}) . \quad (2.2.12)$$

Nevertheless, we can use Eq. (2.2.5) and Eq. (2.2.11) to obtain a formal solution of the Riemann-Silberstein six-vector \mathcal{F} with

$$\mathcal{F}(\vec{r}, t) = \mathcal{U}(t, t_{(0)})\mathcal{F}(\vec{r}, t_{(0)}) - \int_{t_{(0)}}^t \mathcal{U}(t, \tau)\mathcal{A}(\tau)\mathcal{F}(\vec{r}, t_{(0)}) . \quad (2.2.13)$$

Using again the auxiliary term for expressing the current density in Eq. (2.2.3) and reverting the substitution means that the condition in Eq. (2.2.4) which implies that $\mathcal{F}(\vec{r}, t_{(0)})$ has to be non-zero for all \vec{r} is no restriction any more. The following final explicit expression

$$\mathcal{F}(\vec{r}, t) = \mathcal{U}(t, t_{(0)})\mathcal{F}(\vec{r}, t_{(0)}) - \int_{t_{(0)}}^t d\tau \mathcal{U}(t, \tau)\mathcal{J}(\vec{r}, \tau) \quad (2.2.14)$$

describes the time propagation of $\mathcal{F}(\vec{r}, t)$ in vacuum with a current density contribution. It can be seen that for a vanishing current density with \mathcal{J} equal to zero, the remaining part in Eq. (2.2.14) is consistent with the homogeneous time evolution described by Eq. (2.1.6).

If we analyze the structure of $\mathcal{U}(t, t_{(0)})$ in Eq. (2.1.16) in more detail, we find that the time evolution operator $\mathcal{U}(t, t_{(0)})$ does not couple the different Riemann-Silberstein vectors $\vec{F}_+(\vec{r}, t)$ and $\vec{F}_-(\vec{r}, t)$. The reason for this is based on the structure of \mathcal{H} in Eq. (1.1.45). Its off-diagonal blocks are zero. This block structure with zero off diagonal blocks holds for the exponential series expansion in Eq. (2.1.16). This means, in case of the microscopic Maxwell propagation it is sufficient to consider only one Riemann-Silberstein vector and its corresponding diagonal block of $\mathcal{U}(t, t_{(0)})$ for the full propagation. This reduction is very useful to reduce significantly computational cost in an actual implementation of the approach.

2.3 Time-evolution of macroscopic Maxwell's equations in a linear medium

The time-evolution equations derived previously in Sec. 2.1 and Sec. 2.2 can also be used for the macroscopic time evolution of the Riemann-Silberstein six-vector $\mathcal{F}_{\text{lm}}(\vec{r}, t)$ in isotropic linear media. The homogeneous Schrödinger-like time-evolution equation for the macroscopic $\mathcal{F}_{\text{lm}}(\vec{r}, t)$ is with Eq. (1.2.37) given by

$$\frac{\partial}{\partial t}\mathcal{F}_{\text{lm}}(\vec{r}, t) = -\frac{i}{\hbar}\mathcal{H}_{\text{lm}}(\vec{r}, t)\mathcal{F}_{\text{lm}}(\vec{r}, t) . \quad (2.3.1)$$

In contrast to the previously considered microscopic equation in Eq. (2.1.2), the present Eq. (2.3.1) includes the time-dependent operator $\mathcal{H}_{\text{lm}}(\vec{r}, t)$ given in Eq. (1.2.38), which leads in general to a modified time-evolution operator compared

to Eq. (2.1.16). Using the same steps and properties as in Sec. 2.1 result in the homogeneous macroscopic time evolution operator ansatz $\mathcal{U}_{\text{lm}}(t_{(0)} + dt, t_{(0)})$

$$\mathcal{U}_{\text{lm}}(t_{(0)} + dt, t_{(0)}) = \mathbb{1}_{(6)} - \frac{i}{\hbar} \mathcal{H}_{\text{lm}}(\vec{r}, t_{(0)}) dt \quad (2.3.2)$$

for an infinitesimal time step. The first order linear approximation for the time evolution operator $\mathcal{U}_{\text{lm}}(t_{(0)} + \Delta t, t_{(0)})$ with a time step $\Delta t = t - t_{(0)}$ is

$$\mathcal{U}_{\text{lm}}(t_{(0)} + \Delta t, t_{(0)}) \approx -\frac{i}{\hbar} \int_{t_{(0)}}^{t_{(0)} + \Delta t} \mathcal{H}_{\text{lm}}(\vec{r}, \tau) d\tau. \quad (2.3.3)$$

Again, we split a time interval $t_{(0)}$ to t in N small intervals with $\Delta t_N = (t - t_{(0)})/N$, which gives us for the limit $N \rightarrow \infty$ for $\mathcal{U}_{\text{lm}}(t, t_{(0)})$ the following Dyson series

$$\mathcal{U}_{\text{lm}}(t, t_{(0)}) = N \rightarrow \infty \left[\mathbb{1}_{(6)} + \sum_{k=1}^N \left(-\frac{i}{\hbar} \right)^k \prod_{m=1}^k \int_{t_{(0)}}^{m\Delta t_N} d\tau_m \mathcal{H}_{\text{lm}}(\vec{r}, \tau_m) \right]. \quad (2.3.4)$$

The Dyson series in Eq. (2.3.4) can be simplified by symmetric considerations of the integrals and their limits so that we can use for each time integral the lower limit with $t_{(0)}$ and the upper one with t . However, we have to add a factor to correct double counting. This rearrangement of the Dyson series is derived in Ref. [83]. In general, the medium Hamiltonian $\mathcal{H}_{\text{lm}}(\vec{r}, t)$ has the property of $[\mathcal{H}_{\text{lm}}(\vec{r}, t_1), \mathcal{H}_{\text{lm}}(\vec{r}, t_1)] \neq 0$, which means that the ordering of $\mathcal{H}_{\text{lm}}(\vec{r}, \tau_m)$ is relevant and the times have to be time ordered. Therefore, we use in the final expression for $\mathcal{U}_{\text{lm}}(t, t_{(0)})$ the time ordering operator \mathcal{T} which is defined also in Ref. [83]

$$\begin{aligned} \mathcal{U}_{\text{lm}}(t, t_{(0)}) &= N \rightarrow \infty \left[\mathbb{1}_{(6)} + \sum_{k=1}^N \frac{1}{k!} \left(-\frac{i}{\hbar} \right)^k \mathcal{T} \prod_{m=1}^k \int_{t_{(0)}}^t d\tau_m \mathcal{H}_{\text{lm}}(\vec{r}, \tau_m) \right] \\ &= \mathcal{T} \exp \left[- \int_{t_{(0)}}^t d\tau \frac{i}{\hbar} \mathcal{H}_{\text{lm}}(\vec{r}, \tau) \right]. \end{aligned} \quad (2.3.5)$$

In case of a time independent static isotropic linear medium, the Hamiltonian operator in Eq. (1.2.38) is constant in time and therefore the integral in Eq. (2.3.5) can be directly calculated and the time-evolution operator results in the same simple form as in the microscopic case in Eq.(2.1.16)

$$\mathcal{U}_{\text{lm}}(t, t_{(0)}) = \exp \left[-\frac{i}{\hbar} (t - t_{(0)}) \mathcal{H}_{\text{lm}}(\vec{r}) \right]. \quad (2.3.6)$$

Until now, we have only considered the time-evolution of the homogeneous Maxwell's equations in linear media, which is a very restricted assumption since free charges

and free current densities are not allowed in this case. In general, the free charge density in Eq. (1.2.33) and free current density in Eq. (1.2.35) lead to the underlying divergence condition in Eq. (1.2.32) and the inhomogeneous Schrödinger-like equation of Eq. (1.2.37), which is equal to

$$\frac{\partial}{\partial t} \mathcal{F}_{\text{lm}}(\vec{r}, t) = -\frac{i}{\hbar} \mathcal{H}_{\text{lm}} \mathcal{F}_{\text{lm}}(\vec{r}, t) - \mathcal{J}_{\text{free}}(\vec{r}, t). \quad (2.3.7)$$

All steps for the derivation in Sec. 2.2 are also valid here. Hence, replacing the microscopic Hamiltonian \mathcal{H} and current density term $\mathcal{J}(\vec{r}, t)$ in the general microscopic time evolution equation in Eq. (2.2.14) by the macroscopic Hamiltonian $\mathcal{H}_{\text{lm}}(\vec{r})$ from Eq. (1.2.38) and current density $\mathcal{J}_{\text{lm}}(\vec{r}, t)$ from Eq. (1.1.46) leads directly to the time-evolution equation in isotropic linear media

$$\mathcal{F}_{\text{lm}}(\vec{r}, t) = \mathcal{U}_{\text{lm}}(t, t_{(0)}) \mathcal{F}_{\text{lm}}(\vec{r}, t_{(0)}) - \int_{t_{(0)}}^t d\tau \mathcal{U}_{\text{lm}}(t, \tau) \mathcal{J}_{\text{lm}}(\vec{r}, \tau). \quad (2.3.8)$$

The included homogeneous time evolution operator $\mathcal{U}_{\text{lm}}(t, t_{(0)})$ is given by Eq. (2.3.5), depending on the time-dependent properties of the medium. Due to the space dependent Hamiltonian $\mathcal{H}_{\text{lm}}(\vec{r})$ inside the time-evolution operator $\mathcal{U}_{\text{lm}}(t, t_{(0)})$, that couples each other the $\vec{F}_{\text{lm},+}(\vec{r}, t)$ and $\vec{F}_{\text{lm},-}(\vec{r}, t)$ components of $\mathcal{F}_{\text{lm}}(\vec{r}, t)$ it is not possible to consider only the upper three or lower three components in Eq. (2.3.8) as we can do in the microscopic case. Here in a linear medium, it is always necessary to evolve the full six-component vector $\mathcal{F}_{\text{lm}}(\vec{r}, t)$ in time.

Note, in this section we do not consider the Maxwell Gauß laws side conditions, As before in the previous considered cases, if the condition Eq. (1.2.32) holds for $\mathcal{F}(\vec{r}, t_{(0)})$, the divergence side condition is satisfied during the time propagation. We prove this important property for the Maxwell time propagation in the following section.

2.4 Conservation of electric and magnetic Gauß laws in time

In the previous three Sec. 2.1 - 2.3, we have always assumed that the corresponding divergence constraints hold if they are given for an initial Maxwell Riemann-Silberstein six-vector $\mathcal{F}(\vec{r}, t_{(0)})$. Finally, in this section we prove our assumption for all previously considered cases.

Since the homogeneous divergence condition in Eq. (2.1.1) is a special case of the inhomogeneous divergence condition, we start with the more general microscopic inhomogeneous divergence condition in Eq. (2.2.1)

$$\mathcal{D} \cdot \mathcal{F}(\vec{r}, t_{(0)}) = \mathcal{Q}(\vec{r}, t_{(0)}), \quad (2.4.1)$$

which we request to hold for a given Maxwell Riemann-Silberstein vector $\mathcal{F}(\vec{r}, t_{(0)})$ at $t_{(0)}$. Now, we have to show that the same condition holds at later times t with

$$\mathcal{D} \cdot \mathcal{F}(\vec{r}, t) = \mathcal{Q}(\vec{r}, t), \quad (2.4.2)$$

if we use the inhomogeneous Maxwell time-evolution operator in Eq. (2.2.14) to reach $\mathcal{F}(\vec{r}, t)$ from the starting vector $\mathcal{F}(\vec{r}, t_{(0)})$. Therefore, inserting Eq. (2.2.14) into Eq. (2.4.2) yields

$$\mathcal{D} \cdot \mathcal{F}(\vec{r}, t) = \mathcal{D} \cdot \left[\mathcal{U}(t, t_{(0)}) \mathcal{F}(\vec{r}, t_{(0)}) \right] - \mathcal{D} \cdot \left[\int_{t_{(0)}}^t d\tau \mathcal{U}(t, \tau) \mathcal{J}(\vec{r}, \tau) \right]. \quad (2.4.3)$$

In the following, we use that the Riemann-Silberstein dot product in Eq. 1.1.43 with the divergence operator \mathcal{D} acting on $\mathcal{H}\mathcal{F}(\vec{r}, t)$ is equal to zero

$$\mathcal{D} \cdot (\mathcal{H}\mathcal{F}(\vec{r}, t)) = \begin{pmatrix} 0 \\ 0 \end{pmatrix} \quad (2.4.4)$$

for all times and for all $\mathcal{F}(\vec{r}, t)$. Using this property and expanding $\mathcal{U}(t, \tau)$ in Eq. (2.1.16) in terms of the defining exponential series, we see that only the first term of the series, the identity operator returns a non-zero value. All other terms are obtained by a Riemann-Silberstein dot product after the Hamiltonian \mathcal{H} was applied on a certain updated $\mathcal{F}(\vec{r}, t)$ vector. Thus, the first term in Eq. (2.4.3) results exactly in the initial condition

$$\mathcal{D} \cdot [\mathcal{U}(t, t_{(0)}) \mathcal{F}(\vec{r}, t_{(0)})] = \mathcal{D} \cdot \mathcal{F}(\vec{r}, t_{(0)}) = \mathcal{Q}(\vec{r}, t_{(0)}). \quad (2.4.5)$$

Here, we can already see that the special case of homogeneous divergence conditions in Eq. (2.1.1) holds with Eq. (2.4.5). For the general inhomogeneous divergence condition, we have to consider the inhomogeneity term in Eq. (2.4.3). This term has to contribute to the charge density and to $\mathcal{Q}(\vec{r}, t_{(0)})$ in such way, that it updates the charge density in time, considering always the divergence constraint Eq. (2.4.2). The inhomogeneity term includes the current density which is directly connected to the charge density by the continuity equation [75]

$$\frac{\partial}{\partial t} \rho(\vec{r}, t) + \vec{\nabla} \cdot \vec{j}(\vec{r}, t) = 0. \quad (2.4.6)$$

In terms of the Riemann-Silberstein charge and current density $\mathcal{J}(\vec{r}, t)$ and $\mathcal{Q}(\vec{r}, t)$ in Eq. (1.1.40) and Eq. (1.1.46), it takes the form

$$\frac{\partial}{\partial t} \mathcal{Q}(\vec{r}, t) + \mathcal{D} \cdot \mathcal{J}(\vec{r}, t) = 0. \quad (2.4.7)$$

Finally, we move the divergence operator inside the integral in Eq. (2.4.3) and use the series expression of $\mathcal{U}(t, \tau)$ to conclude, that only the identity operator term of the series leads to a contribution. Hence, Eq. (2.4.3) takes the form

$$\mathcal{D} \cdot \mathcal{F}(\vec{r}, t) = \mathcal{Q}(\vec{r}, t_{(0)}) - \int_{t_{(0)}}^t d\tau \mathcal{D} \cdot \mathcal{J}(\vec{r}, \tau) . \quad (2.4.8)$$

In a last step, using the continuity Eq. (2.4.7), we substitute $\mathcal{D} \cdot \mathcal{J}(\vec{r}, \tau)$ by the time derivative of the Riemann-Silberstein charge density $\mathcal{Q}(\vec{r}, t)$ and obtain

$$\mathcal{D} \cdot \mathcal{F}(\vec{r}, t) = \mathcal{Q}(\vec{r}, t_{(0)}) + \int_{t_{(0)}}^t \frac{\partial}{\partial \tau} \mathcal{Q}(\vec{r}, \tau) d\tau = \mathcal{Q}(\vec{r}, t) . \quad (2.4.9)$$

This result is directly the equation in Eq. (2.4.2) and proves our assumption, that the divergence side conditions in Eq. (2.1.1) and Eq. (2.2.1) hold during evolution of time, if the initial vector obeys this condition.

All previous steps can be repeated by using the corresponding macroscopic variables $\mathcal{F}_{\text{lm}}(\vec{r}, t)$, $\mathcal{D}_{\text{lm}}(\vec{r}, t)$, $\mathcal{H}_{\text{lm}}(\vec{r}, t)$, $\mathcal{J}_{\text{lm}}(\vec{r}, t)$, and $\mathcal{U}_{\text{lm}}(\vec{r}, t)$ from Sec. 1.2.4 and Sec. 2.3 to prove that also the divergence condition for a linear medium in Eq. (1.2.32) holds for a time propagation with Eq. (2.3.8).

Chapter 3

Implementation of the Riemann-Silberstein Maxwell propagation in the real-time real-space code Octopus

The time-evolution of classical electromagnetic fields has been discussed extensively in literature during the last decades. In general, solving the Maxwell's equations in three-dimensional space takes some effort. In only very few special cases, e.g., electromagnetic plane waves, or Gaussian beams in the paraxial limit, it is possible to find a closed-form analytical expression that describes exactly the electromagnetic fields in time. But there are several techniques to evolve the fields in time approximately.

A commonly used method in classical electrodynamics is the so called Yee-algorithm [64] or finite-difference-time-domain (FDTD) method. This method splits the electric field and magnetic field into two separated grids. Both grids have the same spacing but they are shifted by half of the spacing in each direction so that no point of the two different grids lies on the top of each other. In a similar way, one full propagation step in time is split in two steps, each propagates half of the time interval. For each half time step, the Yee-algorithm provides an update of either Faraday's or Ampère's law.

In contrast, our considered Riemann-Silberstein propagation scheme is based on only one grid for the complex Riemann-Silberstein six-vector and both, Faraday's and Ampère's law, are evolved simultaneously in one step. In case of considering only the electromagnetic fields, the Yee algorithm is one of the most popular and efficient Maxwell-propagation methods. On the other hand, time evolution in quantum mechanics is very well described and implemented in quantum mechanical simulations in terms of time-evolution operators.

In chapters 1 and 2, we have shown how to transform the Maxwell's equation into a

Schrödinger-like form and how to evolve them with time-evolution schemes similar to quantum mechanics. We exploit here this mathematical similarity to implement the electromagnetic field propagation in Octopus, an open-source code that simulates quantum mechanical many-body problems using time-dependent density functional theory (DFT) [66]. Since Octopus provides efficient algorithms to evolve quantum mechanical wave functions, i.e., Kohn-Sham (KS) orbitals [86], in time, we treat each dimension of the six-component Riemann-Silberstein vector as one KS orbital. Additionally, we adapt and expand the quantum mechanical time-evolution algorithms in Octopus to solve Maxwell’s equations in Riemann-Silberstein form.

In this chapter, we introduce our implementation of a Maxwell propagation scheme in Octopus. Furthermore, we show two different methods for absorbing boundaries. The first one is equivalent to mask absorption in quantum mechanics and easier to implement than the second one, the perfectly matched layer absorption. Based on the Bérenger method in Ref. [87] for a perfectly matched layer in FDTD, we adapt this scheme for the Riemann-Silberstein time evolution.

After introducing these features, we compare our implementation with the MIT¹ Electromagnetic Equation Propagation (MEEP) [88], a program to simulate classical electromagnetic problems.

3.1 Discretized three-dimensional grid for the Maxwell field

In this section, we discuss the three-dimensional grid and spatial derivative operations for the six-component Riemann-Silberstein vector $\mathcal{F}(\vec{r}, t)$. After introducing the basic setup of the grid and operations, we describe the parallelization strategy to divide the computational tasks into separate partitions to speed up the calculation.

3.1.1 Riemann-Silberstein Maxwell grid

We describe the electromagnetic field as complex Riemann-Silberstein vector field, discretized on a three-dimensional Cartesian grid. Hence, in contrast to FDTD, the grid points of both fields are not shifted and lie on top of each other. The whole simulation box is divided into inner and boundary regions. In the inner box region, the real physical equations are applied to simulate ”free” Riemann-Silberstein propagation. The boundary region is adjusted to fulfill the corresponding simulation condition, for example absorbing boundaries or incident plane waves.

A two-dimensional slice of the simulation box and the boundary region is shown in Figure 3.1, where the grid points with light-grey background illustrate the inner region of the simulation box. The outer grid points are marked by the dark-grey background. The outer box limits are determined by L_u for direction $u \in \{x', y', z'\}$

¹Massachusetts Institute of Technology

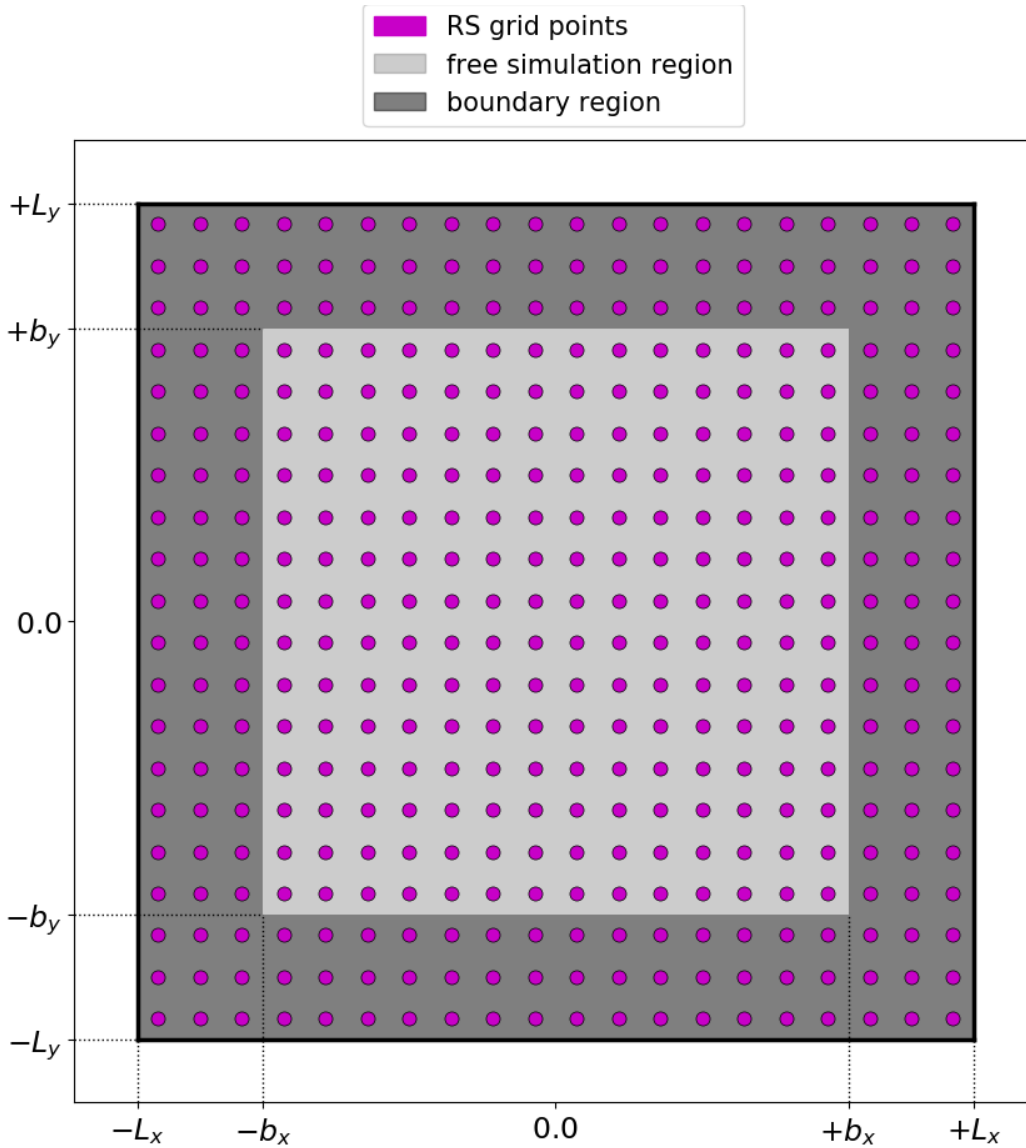


Figure 3.1: The figure shows a two-dimensional slice of the three-dimensional simulation box with different simulation regions. The inner light-grey region shows all grid points where Maxwell's equations are propagated. The dark-grey region contains the grid points to simulate the correct boundary conditions. The underlying equations in this case are artificial modified Maxwell's equations to satisfy the boundary conditions. The inner free Maxwell propagation area is limited by the boundary box limits b_x and b_y of the boundary region and the whole box is limited by the outer limits L_x and L_y .

and the boundary region is limited by b_u . We note, that L_u and b_u are always positive and the box center is always located at the Cartesian origin. The total box dimension in each direction is $-L_u$ to $+L_u$, and the inner borders of the free propagation region are $-b_u$ and $+b_u$, whereas the area between $b_u < |u| < L_u$ describes the boundary regions. In general, the points are always equidistant in the same dimension but the spacing in each direction can be chosen independently. All mathematical spatial operators, for example spatial derivatives are determined by the grid points.

3.1.2 Finite difference stencil

As shown in chapter 2, the Riemann-Silberstein time-evolution depends on first order spatial derivatives. Such derivatives for each grid point can be obtained by the finite-difference method which is explained in detail in Ref. [89, 90, 91] and briefly summarized in the next steps. For a given function $f(x)$, it is assumed that the function value $f(x_{(0)} + \Delta x)$ at point $x_{(0)} + \Delta x$ with small Δx and the known function value $f(x_{(0)})$ at $x_{(0)}$ correspond to a Taylor expansion of n^{th} order

$$f(x_{(0)} + \Delta x) = f(x_{(0)}) + \sum_{n=1}^{\infty} \frac{1}{n!} \frac{d^n f(x)}{dx^n} (\Delta x)^n . \quad (3.1.1)$$

The $n!$ factor denotes the factorial of n . Without loss of generality the function $f(x)$ can also be expanded at point $x_{(0)} - \Delta x$, which modifies Eq. (3.1.1) to

$$f(x_{(0)} - \Delta x) = f(x_{(0)}) + \sum_{n=1}^{\infty} (-1)^n \frac{1}{n!} \frac{d^n f(x)}{dx^n} (\Delta x)^n . \quad (3.1.2)$$

In both cases, solving for the first derivative $f'(x)$ leads to

$$\begin{aligned} f'(x) &= \frac{f(x + \Delta x) - f(x)}{\Delta x} - \sum_{n=2}^{\infty} \frac{1}{n!} \frac{d^n f(x)}{dx^n} (\Delta x)^{n-1} \\ &= \frac{f(x + \Delta x) - f(x)}{\Delta x} + \mathcal{O}(\Delta x) , \end{aligned} \quad (3.1.3)$$

and

$$\begin{aligned} f'(x) &= \frac{f(x) - f(x - \Delta x)}{\Delta x} - \sum_{n=2}^{\infty} (-1)^n \frac{1}{n!} \frac{d^n f(x)}{dx^n} (\Delta x)^{n-1} \\ &= \frac{f(x) - f(x - \Delta x)}{\Delta x} + \mathcal{O}(\Delta x) , \end{aligned} \quad (3.1.4)$$

where the remaining term $\mathcal{O}(\Delta x)$ represents the difference between the exact value $f'(x)$ and the finite difference term in Eq. (3.1.4). For an equidistant regular grid, the small Δx is equal to the spacing between two grid points, i.g. $x_{(i)}$ and $x_{(i+1)}$ or $x_{(i)}$ and $x_{(i-1)}$

$$\Delta x = x_{(i+1)} - x_{(i)} = x_{(i)} - x_{(i-1)} . \quad (3.1.5)$$

Therefore, by using the function values $f(x_i)$ at the grid points $x_{(i-1)}, x_{(i)}, x_{(i+1)}$, the Taylor series in Eq. (3.1.3) can be expressed as

$$f'(x_{(i)}) = \frac{f(x_{(i+1)}) - f(x_{(i)})}{\Delta x} + \mathcal{O}(\Delta x), \quad (3.1.6)$$

which is called forward expansion. Consequently the backward expansion of Eq. (3.1.4) takes the form

$$f'(x_{(i)}) = \frac{f(x_{(i)}) - f(x_{(i-1)})}{\Delta x} + \mathcal{O}(\Delta x). \quad (3.1.7)$$

A third formula, called center difference formula, is given by adding Eq. (3.1.6) from Eq. (3.1.7) and solving for $f'(x_i)$

$$f'(x_{(i)}) = \frac{f(x_{(i+i)}) - f(x_{(i-1)})}{2\Delta x} + \mathcal{O}(\Delta x^3). \quad (3.1.8)$$

In contrast to the forward and backward difference formula, the even terms of $\Delta x^2, \Delta x^4 \dots$ in the center difference formula vanish. Therefore, the remaining term in Eq. (3.1.8) has the order of Δx^3 , which means that the center difference formula is more accurate. The accuracy can also be increased by using additional grid points.

Assuming the spatial derivative $f'(x_{(i)})$ at point $x_{(i)}$ can be expressed as a linear combination of the grid point function values of $f(x_{(i)})$ and the next nearest ones, the ansatz for the formula in center difference calculation with accuracy of order n is given by

$$\begin{aligned} f'(x_{(i)}) = & a_{(i-n)}f(x_{(i-n)}) + \dots + a_{(i-1)}f(x_{(i-1)}) + a_i f(x_{(i)}) \\ & + a_{(i+1)}f(x_{(i+1)}) + \dots + a_{(i+n)}f(x_{(i+n)}). \end{aligned} \quad (3.1.9)$$

Therefore the required number of grid points is $2n+1$. The coefficients $a_{(i-n)} \dots a_{(i+n)}$ have to be determined by $2n$ equations, n forward and n backward Taylor series of order n of the functions $f(x_{(i-n)}), \dots, f(x_{(i-1)}), f(x_{(i)}), f(x_{(i+1)}), \dots, f(x_{(i+n)})$. For a given order n the Taylor series takes the form

$$\begin{aligned} f(x_{(i+n)}) &= f(x_{(i)} + n\Delta x) = f(x_{(i)}) + \frac{n}{1!}f'(x_{(i)})\Delta x + \dots + \frac{n^n}{n!}f^{(n)}(x_{(i)})\Delta x^n + \mathcal{O}(\Delta x^{n+1}) \\ &\vdots \\ f(x_{(i+1)}) &= f(x_{(i)} + \Delta x) = f(x_{(i)}) + f'(x_{(i)})\Delta x + \dots + n f^{(n)}(x_{(i)})\Delta x^n + \mathcal{O}(\Delta x^{n+1}) \\ f(x_{(i)}) &= f(x_{(i)}) \\ f(x_{(i-1)}) &= f(x_{(i)} - \Delta x) = f(x_{(i)}) - f'(x_{(i)})\Delta x + \dots - \frac{n^n}{n!}f^{(n)}(x_{(i)})\Delta x^n + \mathcal{O}(\Delta x^{n+1}) \\ &\vdots \\ f(x_{(i-n)}) &= f(x_{(i)} - n\Delta x) = f(x_{(i)}) - n f'(x_{(i)})\Delta x + \dots + \frac{(-n)^n}{n!}f^{(n)}(x_{(i)})\Delta x^n + \mathcal{O}(\Delta x^{n+1}). \end{aligned} \quad (3.1.10)$$

Here, $f^{(n)}(x)$ denotes the n -th derivative of $f(x)$. The functions $f(x_{(i-n)}), \dots, f(x_{(i-1)}), f(x_{(i+1)}), \dots, f(x_{(i+n)})$ on the right-hand side of Eq. (3.1.9) can be substituted by the Eqs. (3.1.10). Hence, the first derivative $f'(x_{(i)})$ is given by

$$f'(x_{(i)}) = b_0 f(x_{(i)}) + b_1 f'(x_{(i)}) + b_2 f''(x_{(i)}) + \dots + f^{(n)}(x_{(i)}) \quad (3.1.11)$$

with

$$\begin{aligned} b_{(0)} &= a_{(i-n)} + \dots + a_{(i-1)} + a_{(i)} + a_{(i+1)} + \dots + a_{(i+n)} \\ b_{(1)} &= (na_{(i-n)} + \dots + 2a_{(i-2)} + a_{(i-1)} + a_{(i+1)} + 2a_{(i+2)} + \dots + na_{(i+n)}) \Delta x \\ b_{(2)} &= \frac{1}{2}(n^2 a_{(i-n)} + \dots + 4a_{(i-2)} + a_{(i-1)} + a_{(i+1)} + 4a_{(i+2)} + \dots + n^2 a_{(i+n)}) \Delta x^2 \\ &\quad \vdots \\ b_{(n)} &= \frac{1}{n!}(n^n a_{(i-n)} + \dots + 2^n a_{(i-2)} + a_{(i-1)} + a_{(i+1)} + 2^n a_{(i+2)} + \dots + n^n a_{(i+n)}) \Delta x^n. \end{aligned} \quad (3.1.12)$$

Equating left-hand and right-hand side in Eq. (3.1.11) leads to the condition, that only b_1 in Eq. (3.1.13) is equal to one. Whereas all other remaining coefficients b_i are equal to zero. Consequently, the coefficients a_i in Eq. (3.1.9) can be obtained by a system of linear equations

$$\begin{aligned} 0 &= a_{(i-n)} + \dots + a_{(i-1)} + a_{(i)} + a_{(i+1)} + \dots + a_{(i+n)}, \\ 1 &= (na_{(i-n)} + \dots + 2a_{(i-2)} + a_{(i-1)} + a_{(i+1)} + 2a_{(i+2)} + \dots + na_{(i+n)}) \Delta x, \\ 0 &= \frac{1}{2}(n^2 a_{(i-n)} + \dots + 4a_{(i-2)} + a_{(i-1)} + a_{(i+1)} + 4a_{(i+2)} + \dots + n^2 a_{(i+n)}) \Delta x^2, \\ &\quad \vdots \\ 0 &= \frac{1}{n!}(n^n a_{(i-n)} + \dots + 2^n a_{(i-2)} + a_{(i-1)} + a_{(i+1)} + 2^n a_{(i+2)} + \dots + n^n a_{(i+n)}) \Delta x^n. \end{aligned} \quad (3.1.13)$$

Of course, the whole system of linear equations can be expressed equivalently as a matrix vector product

$$\begin{pmatrix} 1 & \dots & 1 & 1 & 1 & \dots & 1 \\ -n\Delta x & \dots & -2\Delta x & 0 & 2\Delta x & \dots & n\Delta x \\ -\frac{1}{2}n^2\Delta x^2 & \dots & -4\Delta x^2 & 0 & 4\Delta x^2 & \dots & \frac{1}{2}n^2\Delta x^2 \\ \vdots & & \vdots & \vdots & \vdots & & \vdots \\ -\frac{1}{n!}n^n\Delta x^n & \dots & 2^n\Delta x^n & 0 & 2^n\Delta x^n & \dots & \frac{1}{n!}n^n\Delta x^n \end{pmatrix} \begin{pmatrix} a_{(i-n)} \\ \vdots \\ a_{(i-1)} \\ a_{(i)} \\ a_{(i+1)} \\ \vdots \\ a_{(i+n)} \end{pmatrix} = \begin{pmatrix} 0 \\ 1 \\ 0 \\ \vdots \\ 0 \end{pmatrix}. \quad (3.1.14)$$

There are several techniques shown in Ref. [92] to solve Eq. (3.1.14). The resulting coefficients $a_{(i-n)}, \dots, a_{(i+n)}$ define a one-dimensional stencil which is here a $(2n+1)$ -dimensional vector. Multiplying this vector with the function values that correspond

to the stencil coefficient yields with Eq. (3.1.9)

$$f'(x_{(i)}) \approx \begin{pmatrix} a_{(i-n)} & \cdots & a_{(i)} & \cdots & a_{(i+n)} \end{pmatrix} \cdot \begin{pmatrix} f(x_{(i-n)}) \\ \vdots \\ f(x_{(i)}) \\ \vdots \\ f(x_{(i+n)}) \end{pmatrix}. \quad (3.1.15)$$

In the previous steps, we briefly introduced the finite difference method to derive the approximated first derivative of a function on a discrete grid in one dimension.

Since we consider the Maxwell field propagation in three dimensions, we have to extend the one-dimensional stencil to a three-dimensional one. While the one-dimensional stencil is a chain, the two- and three-dimensional stencils form a two-dimensional respectively three-dimensional cross stencils. Figure 3.2 illustrates such a cross stencil in the xy-plane. For a given three-dimensional function $f(x_{(i)}, y_{(j)}, z_{(k)})$ at the grid points $x_{(i)}, y_{(j)}, z_{(k)}$, the corresponding finite difference coefficients are $a_{x,(i-n)} \dots a_{x,(i+n)}$ for the partial derivative in x, and $a_{y,(j-n)} \dots a_{y,(j+n)}$, respectively $a_{z,(k-n)} \dots a_{z,(k+n)}$ for the remaining two partial derivatives. Similar to Eq. (3.1.15), the approximation for the spatial partial derivatives take the form

$$\frac{\partial}{\partial x} f(x, y, z) \approx \begin{pmatrix} a_{x,(i-n)} & \cdots & a_{x,(i+n)} & 0 & \cdots & 0 & 0 & \cdots & 0 \end{pmatrix} \cdot \begin{pmatrix} f(x_{(i-n)}) \\ \vdots \\ f(x_{(i+n)}) \\ f(y_{(j-n)}) \\ \vdots \\ f(y_{(j+n)}) \\ f(z_{(k-n)}) \\ \vdots \\ f(z_{(k+n)}) \end{pmatrix}, \quad (3.1.16)$$

$$\frac{\partial}{\partial y} f(x, y, z) \approx \begin{pmatrix} 0 & \cdots & 0 & a_{y,(j-n)} & \cdots & a_{y,(j+n)} & 0 & \cdots & 0 \end{pmatrix} \cdot \begin{pmatrix} f(x_{(i-n)}) \\ \vdots \\ f(x_{(i+n)}) \\ f(y_{(j-n)}) \\ \vdots \\ f(y_{(j+n)}) \\ f(z_{(k-n)}) \\ \vdots \\ f(z_{(k+n)}) \end{pmatrix}, \quad (3.1.17)$$

$$\frac{\partial}{\partial z} f(x, y, z) \approx \begin{pmatrix} 0 & \cdots & 0 & 0 & \cdots & 0 & a_{z,k-n} & \cdots & a_{z,k+n} \end{pmatrix} \cdot \begin{pmatrix} f(x_{(i-n)}) \\ \vdots \\ f(x_{(i+n)}) \\ f(y_{(j-n)}) \\ \vdots \\ f(y_{(j+n)}) \\ f(z_{(k-n)}) \\ \vdots \\ f(z_{(k+n)}) \end{pmatrix}. \quad (3.1.18)$$

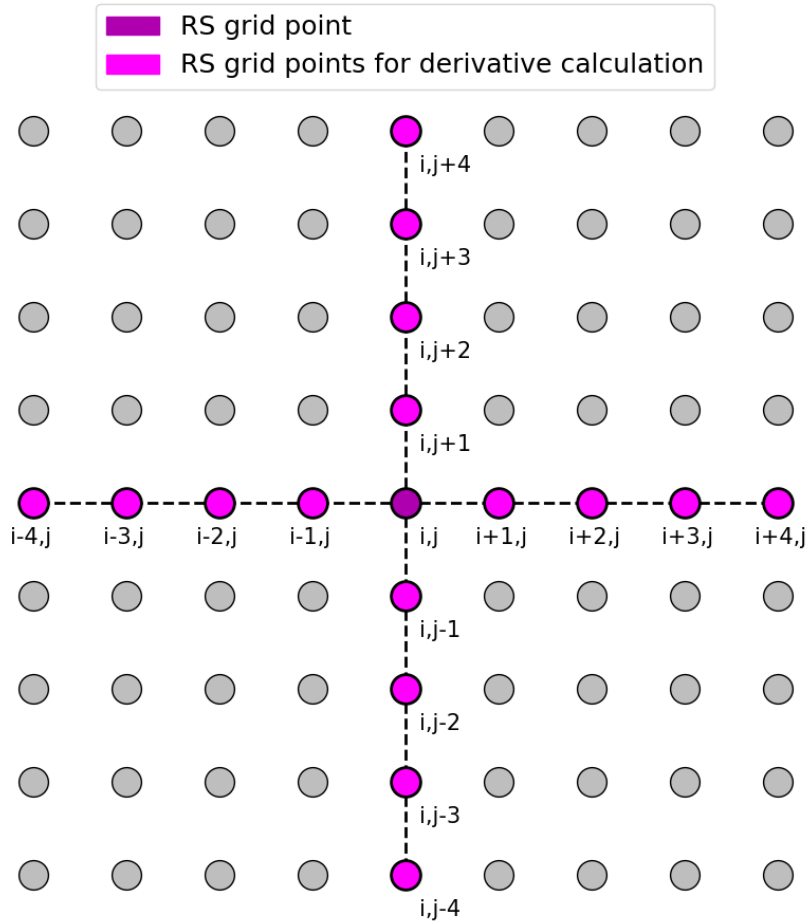


Figure 3.2: Two-dimensional stencil. All grid points which determine the first derivative of $f_{(i),(j)}$ at point $x_{(i),(j)}$ build a cross of $2n + 1$ grid points in each dimension, where n denotes the accuracy order of the derivative. The figure shows an example for such a two-dimensional stencil for $n = 4$.

The stencil and grid point vectors in Eqs. (3.1.16) - (3.1.18) have the size $6n + 1$. All operations are independent in each dimension, since we do not consider mixed derivatives for the Maxwell time propagation.

3.1.3 Parallelization strategy in the first principles code octopus

Large grids increase the computational cost. To speed up the calculations, it is useful to divide the computational task into several partitions and use parallel processors. Taking the grid setup from Sec. 3.1.1, we employ a domain parallelization. A schematic plot of a divided grid into four domains is shown in Figure 3.3.

Each of the four partitions covers only a part of the whole grid. The partial grids have to take the boundary region of the total grid into account. Furthermore, to achieve a correct calculation which is equivalent to the serial case, the derivative operation has to be equivalent. In the boundary region, the operation stencils contain several stencil points which are located on another domain. The cross stencil shown in Figure 3.3 for a grid point in partition 3 illustrates this case, where two stencil points lie in partition 1 and one point in partition 2.

To obtain a correct parallelization, the processors send and receive the necessary data for each time step. Octopus uses domain parallelization [93] for the Kohn-Sham orbitals. Therefore, we adapt this scheme for the six-component Riemann-Silberstein vector and treat each vector component as a Kohn-Sham orbital.

3.2 Discretized Riemann-Silberstein time-evolution operators

In Sec. 2.2, we derived the time-evolution Eq. (2.2.14) to evolve the six-component Riemann-Silberstein vector $\mathcal{F}(\vec{r}, t)$, which has the explicit form

$$\mathcal{F}(\vec{r}, t) = \mathcal{U}(t, t_{(0)})\mathcal{F}(\vec{r}, t_{(0)}) - \int_{t_{(0)}}^t d\tau \mathcal{U}(t, \tau) \mathcal{J}(\vec{r}, \tau). \quad (3.2.1)$$

In general, the solution of the Riemann-Silberstein time-evolution is not analytical. However, a recursive time-evolution of the Riemann-Silberstein vector with a rather small time step Δt yields a numerical solution. The size of Δt is chosen such that the propagation stays stable. Therefore, the recursive form to obtain the next Riemann-Silberstein vector $\mathcal{F}(\vec{r}, (m+1)\Delta t)$ from a given $\mathcal{F}(\vec{r}, m\Delta t)$ at the discrete time $m\Delta t$ leads from Eq. (3.2.1) to

$$\mathcal{F}(\vec{r}, (m+1)\Delta t) = \mathcal{U}((m+1)\Delta t, m\Delta t)\mathcal{F}(\vec{r}, m\Delta t) - \int_{m\Delta t}^{(m+1)\Delta t} d\tau \mathcal{U}(\tau, m\Delta t) \mathcal{J}(\vec{r}, \tau). \quad (3.2.2)$$

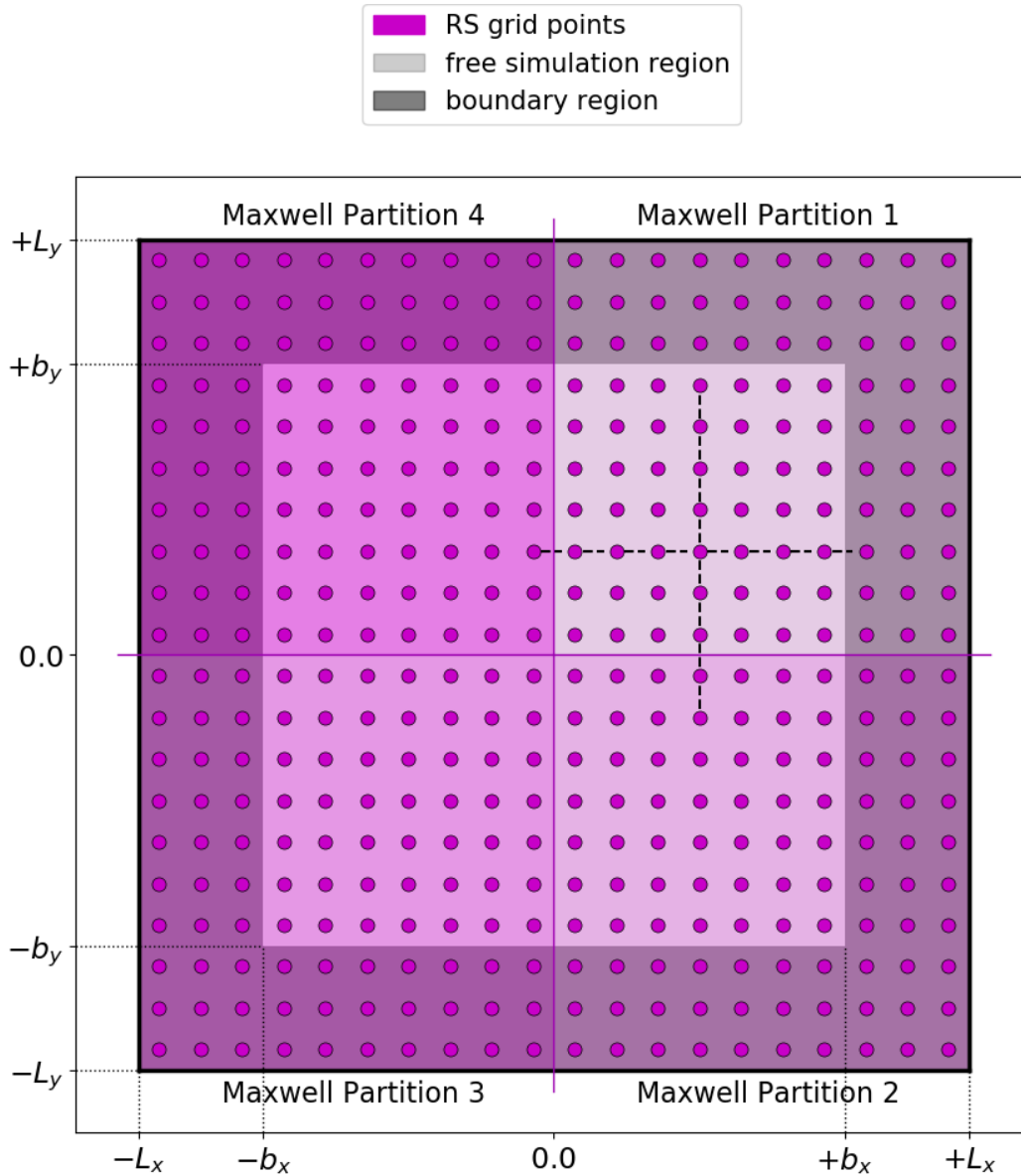


Figure 3.3: Parallelization scheme for dividing the Maxwell grid into four partitions. The cross in partition 1 illustrates a two-dimensional stencil of order $n = 4$. Some stencil points are located in different partitions, which has to be taken into account. For each propagation step, the necessary variables at the grid boundaries are sent and received by the neighbouring partitions.

The integral on the right-hand side is approximated by the trapezoidal rule. This leads to the discrete time evolution equation

$$\begin{aligned} \mathcal{F}(\vec{r}, (m+1)\Delta t) \approx & \mathcal{U}((m+1)\Delta t, m\Delta t)\mathcal{F}(\vec{r}, m\Delta t) - \frac{\Delta t}{2}\mathcal{U}((m+1)\Delta t, m\Delta t)\mathcal{J}(\vec{r}, m\Delta t) \\ & - \frac{\Delta t}{2}\mathcal{J}(\vec{r}, (m+1)\Delta t). \end{aligned} \quad (3.2.3)$$

We put the Riemann-Silberstein vector $\mathcal{F}(\vec{r}, t)$ and the Riemann-Silberstein current density $\mathcal{J}(\vec{r}, t)$ on a three-dimensional Cartesian grid as it is introduced in Sec. 3.1.1. Hence, both variables at the grid position $\vec{r}_{(i),(j),(k)}$ are denoted by

$$\mathcal{F}(\vec{r}_{(i),(j),(k)}) = \mathcal{F}(x_{(i)}, y_{(j)}, z_{(k)}) \quad (3.2.4)$$

and

$$\mathcal{J}(\vec{r}_{(i),(j),(k)}) = \mathcal{J}(x_{(i)}, y_{(j)}, z_{(k)}). \quad (3.2.5)$$

The time-evolution operator $\mathcal{U}(t, t_{(0)})$ that is required in Eq. (3.2.1), has been introduced in Eq. (2.1.16). This operator is a matrix exponential that acts on the Riemann-Silberstein vector. For our electromagnetic time-evolution simulation, we truncate the series expansion. Some stability tests versus efficiency have shown, that the fourth order of the exponential series leads in most cases to stable and efficient runs. Furthermore, the spatial partial derivative is calculated with the three-dimensional derivative stencil, which we discussed in Sec. 3.1.2. To speed up large system calculations, we use the parallelization in domain strategy from Sec. 3.1.3. The location of the grid points is determined by the dimensions of the simulation box and by the grid spacing $\Delta x, \Delta y, \Delta z$, which can be selected independently.

On the other hand, the time step parameter Δt has to be chosen such that the propagation remains stable and accurate. A very well-known criterion for Δt that always leads to stable runs is described by the Courant-Friedrichs-Lewy (CFL) condition [94, 95]

$$\Delta t_{\text{Mx,CFL}} \leq \frac{S_{\text{CFL,max}}}{c_0 \sqrt{\frac{1}{\Delta x^2} + \frac{1}{\Delta y^2} + \frac{1}{\Delta z^2}}}, \quad (3.2.6)$$

and depends basically on the grid point spacing $\Delta x, \Delta y, \Delta z$, and the Courant number $S_{\text{CFL,max}}$. The $S_{\text{CFL,max}}$ number changes for different propagation methods. In case of FDTD in three dimensions, $S_{\text{CFL,max}}$ is equal to one [94, 95] which we used for all of our simulations. We have performed convergence tests for our implemented Riemann-Silberstein Maxwell time-evolution and have found that also Courant numbers a little larger than one leads to stable and accurate simulations. However, we could not find a fixed value for $S_{\text{CFL}} > S_{\text{CFL,max}}$ which is valid universally. The actual maximal value varies and depends on the grid spacing.

3.3 Maxwell-propagation with Octopus

After introducing the Maxwell-Riemann-Silberstein propagation scheme on a three-dimensional grid, we show in this section the first electromagnetic field simulations performed with our new implementation. We consider as example a case where a given external current density is prescribed for the solution of Maxwell's equations. The current density has a Gaussian shape in space and time and is located in the center of the simulation box. The box size is chosen large enough such that the electromagnetic fields do not reach the box boundaries within the simulation time. For a validation of our implementation, we compare our results with the electromagnetic evolution program MEEP. We also show for this example that the Gauß laws are obeyed in time.

3.3.1 Comparison of the Octopus Maxwell-propagation with the electromagnetic propagation program MEEP

The program MIT² Electromagnetic Equation Propagation (MEEP) [88] is a common simulation package for electromagnetic field propagations. The implemented Maxwell field propagation in MEEP is based on the Finite Difference Time Domain method (FDTD) and the Yee-algorithm [64]. The underlying electromagnetic simulation grid is split into two grids shifted by half of the grid spacing of the corresponding direction. As a consequence, the required spatial and time derivative points for the propagation equation are in the middle of two sample grid points. Therefore, the center finite difference method leads to the first derivative equation, here for simplicity discussed in one dimension

$$f'(x_{(0)}) = \frac{f(x_{(0)} + \frac{\Delta x}{2}) - f(x_{(0)} - \frac{\Delta x}{2})}{\Delta x} - \frac{1}{3!} f'''(x_{(0)}) \left(\frac{\Delta x}{2}\right)^2 + \dots \quad (3.3.1)$$

In case of the Yee grid, there are no grid points at the derivative point $x_{(0)}$ but next to it at $x_{(0)} - \Delta x/2$ and $x_{(0)} + \Delta x/2$. We also use the center finite difference discretization in Octopus, but the derivative points lie always on top of a sample grid point. Thus, the derivative equation takes the form

$$f'(x_{(0)}) = \frac{f(x_{(0)} + \Delta x) - f(x_{(0)} - \Delta x)}{2\Delta x} - \frac{1}{3!} f'''(x_{(0)}) (\Delta x)^2 + \dots, \quad (3.3.2)$$

which means that the error of $f'(x_{(0)})$ is smaller for the Yee-algorithm if we consider the same order terms of the finite difference method. However, the MEEP finite difference stencil operation is always of order two whereas the Octopus stencil order can be set to higher orders to obtain better accuracy for the derivative operators. The MEEP internal unit for the speed of light is equal one. Consequently, the electric permittivity in vacuum ϵ_0 and the magnetic permeability in vacuum μ_0 are also equal to one. To compare our electromagnetic field propagation with MEEP, we set

²Massachusetts Institute of Technology

our internal constants in Octopus equal to the MEEP internal units, which means that $\epsilon_0 = \mu_0 = c_0 = 1$ with finite difference order of two for the runs in this section. Additionally, the exponential series expansion order for our introduced Riemann-Silberstein time-evolution operator $\mathcal{U}(t, t_{(0)})$ in Eq. (2.1.16) is four.

As test scenarios, we simulate four different spatial and temporal shaped external current densities inside a box and plot several relevant physical variables. For all runs, we use the same spatial current density distribution $\vec{j}_{(0)}(\vec{r})$ with unit vector in z-direction \vec{e}_z

$$\vec{j}_{(0)}(\vec{r}) = \vec{e}_z \exp\left(\frac{-x^2 - y^2 - z^2}{2}\right). \quad (3.3.3)$$

The external current flows along the z-axis and has a three-dimensional Gaussian shape. Figure 3.4 visualizes the spatial current amplitude in the xy-plane. We chose the following four spatial and time dependent current densities $\vec{j}_{(i)}(\vec{r}, t)$ with $i = \{1, 2, 3, 4\}$

$$\vec{j}_{(1)}(\vec{r}, t) = \vec{j}_{(0)}(\vec{r}) \exp\left(-\frac{(t-10.0)^2}{8}\right), \quad (3.3.4)$$

$$\vec{j}_{(2)}(\vec{r}, t) = \vec{j}_{(0)}(\vec{r}) \left[\exp\left(-\frac{(t-10.0)^2}{8}\right) - \exp\left(-\frac{(t-12.0)^2}{8}\right) \right], \quad (3.3.5)$$

$$\vec{j}_{(3)}(\vec{r}, t) = \vec{j}_{(0)}(\vec{r}) \exp\left(-\frac{(t-10.0)^2}{8}\right) \sin\left(2.0(t - 10.0)\right), \quad (3.3.6)$$

$$\vec{j}_{(4)}(\vec{r}, t) = \vec{j}_{(0)}(\vec{r}) \exp\left(-\frac{(t-10.0)^2}{8}\right) \cos\left(2.0(t - 10.0)\right). \quad (3.3.7)$$

We select a cubic simulation box of length 80.0, i.e., the box length parameter referring to the simulation box scheme in Figure 3.1 are given by $L_x = L_y = L_z = 40.0$. We use a zero boundary condition, which means that the field variables are set to zero at the simulation box limits. We select a sufficiently large box that the boundary effects cannot influence the simulation during the simulation time. For all four test currents in Eqs. (3.3.4) - (3.3.7), we evaluate the electric field, the magnetic field, the electromagnetic energy density at the box point (5, 0, 0) as well as the integrated electromagnetic energy inside the simulation box. The grid spacing in each dimension is $\Delta x = \Delta y = \Delta z = 0.2$, which leads to a mutual time step in MEEP and Octopus of $\Delta t = 0.1$. An overview of all relevant parameters for both simulations is shown in Table 3.1.

Figure 3.5 shows the comparison of our Maxwell propagation implementation in Octopus and MEEP for the different current densities in Eqs. (3.3.4) - (3.3.7). All results are evaluated at point (5, 0, 0). In the first panels 1 - a) to 4 - a), we plot the initial current density $\vec{j}(\vec{r}, t)$ in z-direction. Due to the spatial shape of the current density, the maximum value of $\vec{j}(\vec{r}, t)$ is damped by the factor $e^{-5^2/2}$. The next

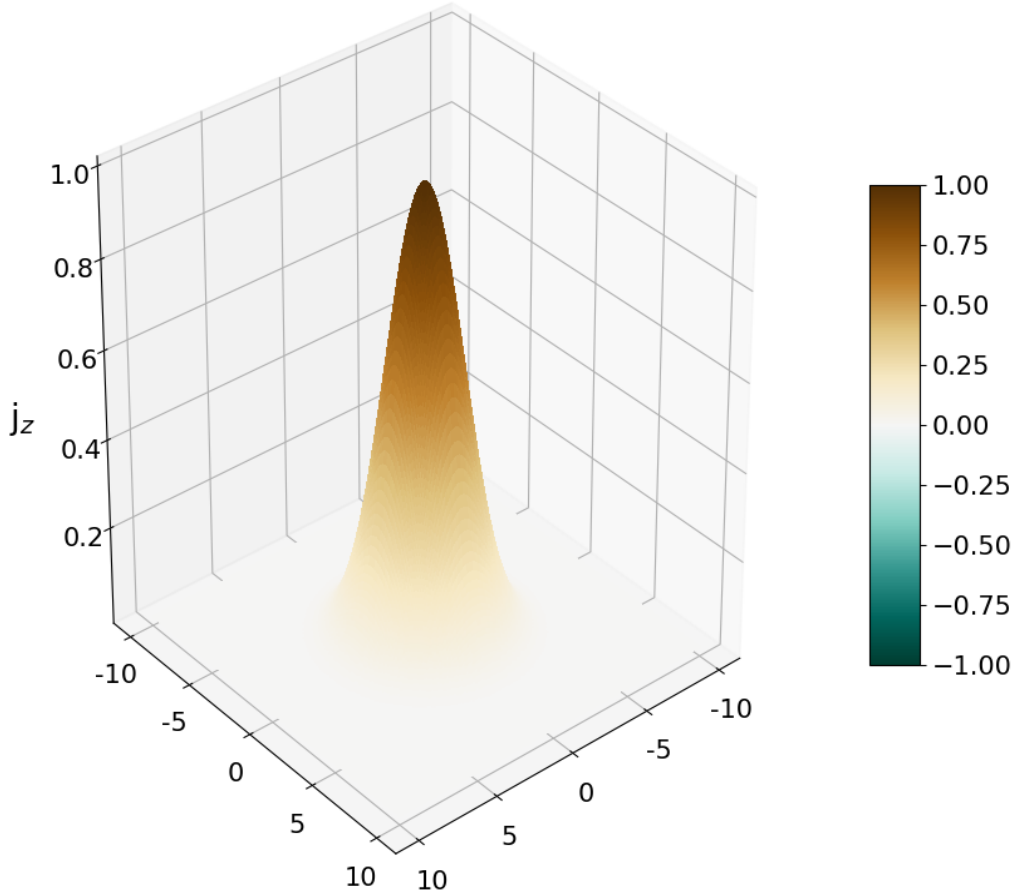


Figure 3.4: The spatial external current density distribution for the comparison calculation with MEEP is a three-dimensional Gaussian function represented in Eq. (3.3.3). The only contribution is along the z -axis. The figure shows a two-dimensional cut through the xy -plane.

panels 1 - b) to 4 - b) and 1 - c) to 4 - c) show the electric field in z -direction and the magnetic field in y -direction also both at coordinate $(5, 0, 0)$. The Maxwell energy densities at this point calculated by Octopus and MEEP are plotted in the panels 1 - c) to 4 - c). The last panels 1 - d) to 4 - d) illustrate the total Maxwell energy inside the box of size $-40.0 \leq x \leq 40.0$, $-40.0 \leq y \leq 40.0$, and $-40.0 \leq z \leq 40.0$.

As a first summary, we can confirm that our implementation of a Maxwell propagation yields the same results as MEEP. Each curve of the electric and magnetic fields in Figure 3.5 in panels b) respectively c) and the Maxwell energy density in d), calculated by Octopus, is covered by the corresponding MEEP curve. Additionally, all four total energies inside the two simulation boxes match and confirm that our implementation leads to similar results like MEEP.

variable	MEEP units
L_x	40.0
L_y	40.0
L_z	40.0
$\Delta x, \Delta y, \Delta z$	0.2
finite difference order	2
exponential order	4
Δt	0.1
ϵ_0	1
μ_0	1
c_0	1

Table 3.1: Simulation parameters for the Octopus and MEEP comparison run.

Next, we consider some field reactions in more detail. According to Eqs. (3.3.4) - (3.3.7), the spatial center is at the origin of the box and the temporal center of the current densities is at time $t = 10.0$. Therefore, the electromagnetic field reaction is shifted by $\Delta t = 5.0$ time in MEEP units to reach the evaluation point at $(5, 0, 0)$.

In contrast to all other electric fields, which return to zero later in time, the electric field in Figure 3.5 1 - b) takes a constant value around $t = 25.0$. At this point, we refer to Sec. 2.4, where we show that the Maxwell side condition, the electric and magnetic Gauß laws, hold during our Maxwell propagation. The reason for this feature is based on the continuity equation which we discuss in the next section.

Looking at the Gaussian pulse with sine carrier wave in 3 - a), we notice that it is very similar shaped to the electric field reaction of the Gaussian pulse with cosine carrier wave in 4 - b). In the same way, the magnetic field reaction in 3 - c) is similar to the current density in 4 - a). This similarity can be explained by taking Faraday's and Ampère's laws with Eq. (2.2.2), rearranged to

$$i\hbar \frac{\partial}{\partial t} \mathcal{F}(\vec{r}, t) + i\hbar \mathcal{J}(\vec{r}, t) = \mathcal{H} \mathcal{F}(\vec{r}, t) . \quad (3.3.8)$$

In principle, the current density term can be expressed by

$$\begin{aligned} \mathcal{J}(\vec{r}, t) &= \frac{\partial}{\partial t} \mathcal{F}_{\mathcal{J}}(\vec{r}, t) , \\ \Rightarrow \mathcal{F}_{\mathcal{J}}(\vec{r}, t) &= \int_{t(0)}^t d\tau \mathcal{J}(\vec{r}, \tau) , \end{aligned} \quad (3.3.9)$$

where $\mathcal{F}_{\mathcal{J}}(\vec{r}, t)$ denotes the integral of $\mathcal{J}(\vec{r}, \tau)$. Consequently, Eq. (3.3.8) becomes

$$i\hbar \frac{\partial}{\partial t} (\mathcal{F}(\vec{r}, t) + \mathcal{F}_{\mathcal{J}}(\vec{r}, t)) = \mathcal{H}\mathcal{F}(\vec{r}, t). \quad (3.3.10)$$

Since the integral of the Gaussian shaped pulse with sine carrier wave is given by a Gaussian shaped pulse with cosine carrier wave and vice versa, the previously described similarity of the corresponding signals become clear. The fact, that both shapes are only similar and not equal can be understood with the first Riemann-Silberstein field variable $\mathcal{F}(\vec{r}, t)$ in Eq. (3.3.10) which influences slightly the resulting field.

3.3.2 Longitudinal and transverse electromagnetic fields and currents

To demonstrate the properties of longitudinal and transverse current densities, we take a further look at the four calculations in Sec. 3.3.1. Using Eq. (3.3.23) for the current densities $\vec{j}_{(1)}(\vec{r}, t) - \vec{j}_{(2)}(\vec{r}, t)$ from Eqs. (3.3.4) - (3.3.7) gives the corresponding motion of charge densities $\rho_{(1)}(\vec{r}, t) - \rho_{(2)}(\vec{r}, t)$, which we express approximately since they contain more error functions with constant arguments, i.e.,

$$\rho_{(1)}(\vec{r}, t) \approx \sqrt{2\pi} z \left| \vec{j}_{(0)}(\vec{r}) \right| \left[\text{Erf}\left(\frac{t-10.0}{2\sqrt{2}}\right) + 1 \right], \quad (3.3.11)$$

$$\rho_{(2)}(\vec{r}, t) \approx \sqrt{2\pi} z \left| \vec{j}_{(0)}(\vec{r}) \right| \left[\text{Erf}\left(\frac{t-10.0}{2\sqrt{2}}\right) - \text{Erf}\left(\frac{t-12.0}{2\sqrt{2}}\right) \right], \quad (3.3.12)$$

$$\rho_{(3)}(\vec{r}, t) \approx \sqrt{\frac{\pi}{2}} z \left| \vec{j}_{(0)}(\vec{r}) \right| e^{-8} \left[\text{Erf}\left(\frac{t-(10.0+8.0i)}{2\sqrt{2}}\right) - \text{Erf}\left(\frac{t-(10.0-8.0i)}{2\sqrt{2}}\right) + 2.677e^{-3} \right], \quad (3.3.13)$$

$$\rho_{(4)}(\vec{r}, t) \approx \sqrt{\frac{\pi}{2}} z \left| \vec{j}_{(0)}(\vec{r}) \right| e^{-8} \left[\text{Erf}\left(\frac{t-(10.0+8.0i)}{2\sqrt{2}}\right) - \text{Erf}\left(\frac{t-(10.0-8.0i)}{2\sqrt{2}}\right) + 2.0 \right]. \quad (3.3.14)$$

with the error function $\text{Erf}(t)$. For large time $t \rightarrow \infty$, Eqs. (3.3.11) - (3.3.14) yield approximately

$$\rho_{(1)}(\vec{r}, t \rightarrow \infty) \approx 2\sqrt{2\pi} z \left| \vec{j}_{(0)}(\vec{r}) \right|, \quad (3.3.15)$$

$$\rho_{(2)}(\vec{r}, t \rightarrow \infty) \approx 0, \quad (3.3.16)$$

$$\rho_{(3)}(\vec{r}, t \rightarrow \infty) \approx 0, \quad (3.3.17)$$

$$\rho_{(4)}(\vec{r}, t \rightarrow \infty) \approx 0. \quad (3.3.18)$$

Consequently, the current density $\vec{j}_{(1)}(\vec{r}, t)$ moves charges just along one direction, which leads to a permanent positive charge density distribution $\rho_{(1)}(\vec{r}, t \rightarrow \infty)$ inside

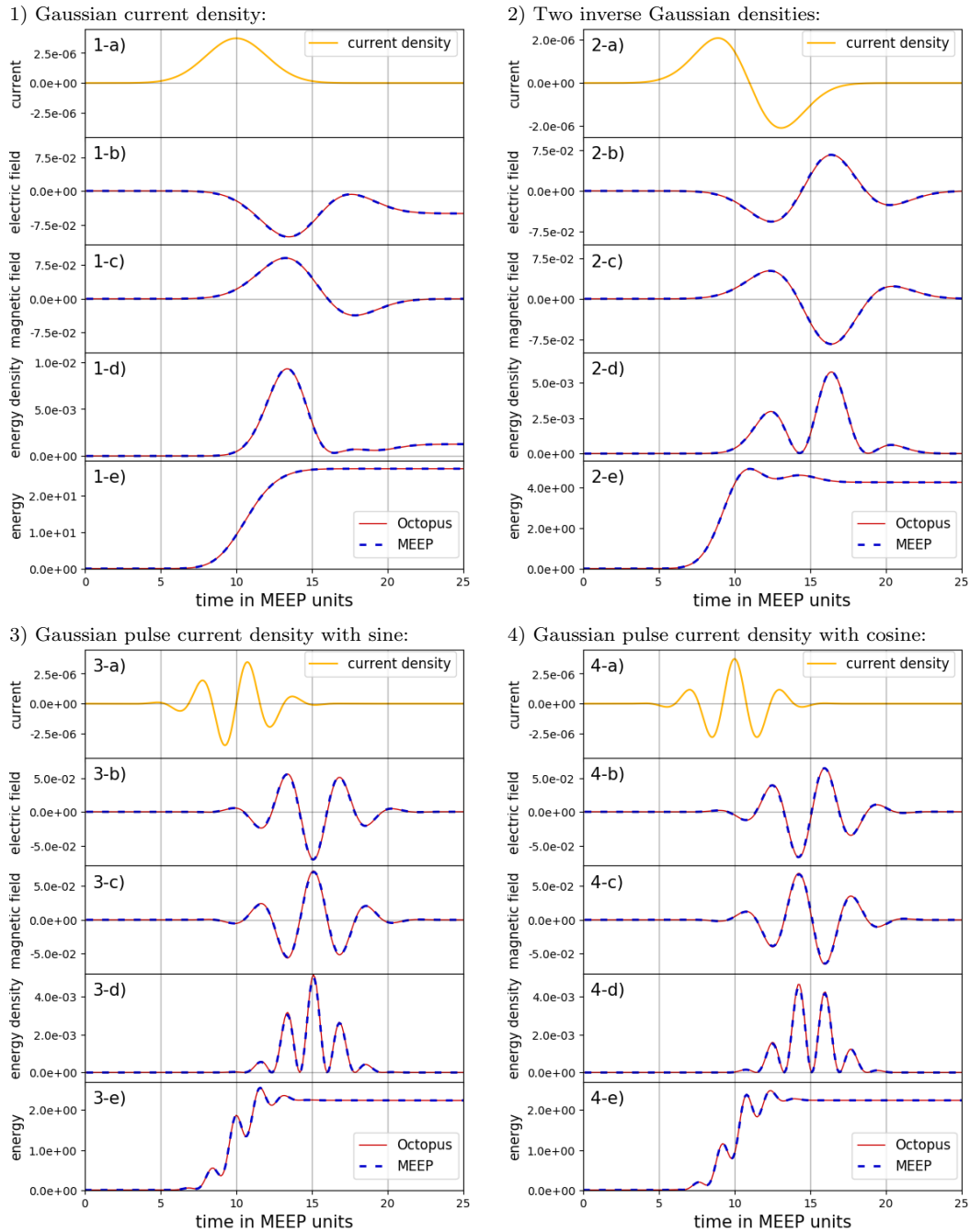


Figure 3.5: Electromagnetic variables at grid point $(5, 0, 0)$ for a Gaussian external current signal, calculated by the Octopus and MEEP simulations. The external current density, shown in a), causes an electromagnetic field reaction, which is plotted as electric field in b), magnetic field in c) and energy density in d). The last curves in e) show the total electromagnetic energy inside the simulation box. Both simulation results, Octopus and MEEP, agree and differences are of negligible magnitude.

the simulation box, whereas the remaining current densities $\vec{j}_{(2)}(\vec{r}, t)$, $\vec{j}_{(3)}(\vec{r}, t)$, and $\vec{j}_{(4)}(\vec{r}, t)$ also move charges, but in both directions so that they in total approximately cancel out and leave an almost zero charge density. The charge density $\rho_{(1)}(\vec{r}, t)$ causes a static electric field for $t \rightarrow \infty$, whereas the remaining three charge densities are very close to zero.

Therefore, the electric field in Figure 3.5 1 - b) reaches approximately a constant electric field at time $t = 25.0$, and the three other electric fields in Figures 3.5 2 - b) to 4 - b) decrease to zero. Figure 3.6 illustrates some snapshots of the electric field propagation polarized in z-direction for selected time steps.

All four snapshots of the panels a) are taken at time $t = 16.0$. They all show a spherical outgoing waves of different shapes. The number of oscillations depend on the corresponding number of temporal oscillations of the current pulses given in Eqs. (3.3.4) - (3.3.7). The spherical waves propagate to the outside, which can be seen in the four panels 1 - 4 a), until they left the box in panels 1 - 4 b) at time $t = 25.0$ and 1 - 4 c) at time $t = 30.0$. Again, according to Eq. (3.3.15) the current density $\vec{j}_{(1)}(\vec{r}, t)$ causes a permanent charge density. Consequently, besides the outgoing wave in Figure 3.6 1 - a) to 1 - c), a permanent electric field with Gaussian shape arises which is centered at the origin.

In the above examples the question arises, what kind of field, i.e., longitudinal or transverse, leads to the outgoing waves or localized field inside the simulation box. Therefore in the following, we decompose the Maxwell's equations in Riemann-Silberstein representation into a longitudinal and transverse set of equations.

Due to the continuity equation, a given external current density leads to an implicit motion of charge, which also ensures that the Maxwell constraint, i.e., the two Gauß laws hold. The continuity equation relates the current density and charge density by [75]

$$\vec{\nabla} \cdot \vec{j}(\vec{r}, t) = -\frac{\partial}{\partial t} \rho(\vec{r}, t). \quad (3.3.19)$$

Without loss of generality, the current density can be split via the Helmholtz decomposition into a longitudinal component $\vec{j}_{\parallel}(\vec{r}, t)$ and a transverse one $\vec{j}_{\perp}(\vec{r}, t)$ [75]

$$\vec{j}(\vec{r}, t) = \vec{j}_{\parallel}(\vec{r}, t) + \vec{j}_{\perp}(\vec{r}, t). \quad (3.3.20)$$

Using the Helmholtz decomposition leads to

$$\vec{\nabla} \cdot \vec{j}_{\perp}(\vec{r}, t) = 0, \quad \vec{\nabla} \cdot \vec{j}_{\parallel}(\vec{r}, t) = -\frac{\partial}{\partial t} \rho(\vec{r}, t). \quad (3.3.21)$$

As a consequence, we split the Riemann-Silberstein current density $\mathcal{J}(\vec{r}, t)$ into the longitudinal Riemann-Silberstein part $\mathcal{J}_{\parallel}(\vec{r}, t)$, build by $\vec{j}_{\parallel}(\vec{r}, t)$, and the transverse one $\mathcal{J}_{\perp}(\vec{r}, t)$ using $\vec{j}_{\perp}(\vec{r}, t)$. Taking the Riemann-Silberstein current density $\mathcal{Q}(\vec{r}, t)$, Eq. (3.3.19) is equivalent to the six-dimensional Riemann-Silberstein representation

$$\mathcal{D} \cdot \mathcal{J}(\vec{r}, t) = \mathcal{D} \cdot \mathcal{J}_{\parallel}(\vec{r}, t) = -\frac{\partial}{\partial t} \mathcal{Q}(\vec{r}, t). \quad (3.3.22)$$

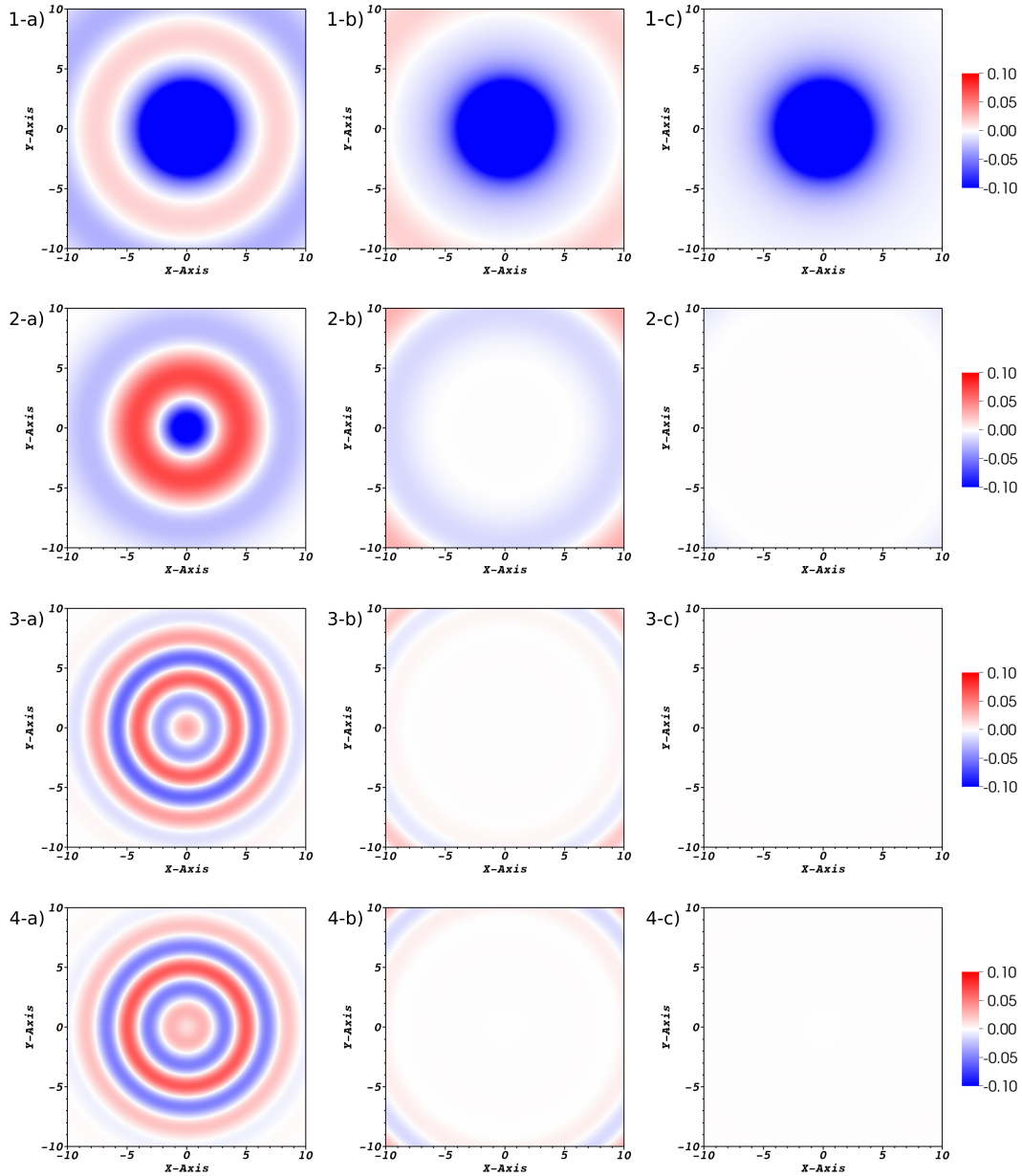


Figure 3.6: Contour snapshots along the xy -plane of the electric field in z -direction for the electromagnetic field propagation using the four external currents of Eqs. (3.3.4) - (3.3.7). The first panels 1 - 4 a) show the electric field at time $t = 16.0$. The arising spherical waves move radially to the outside, which is illustrated in panels 1 - 4 b) at $t = 25.0$. The last snapshots in panels 1 - 4 c) taken at $t = 30.0$ visualize that the electric fields return to zero after the current pulse. An exception is the first one, where the permanent charge density causes a corresponding static electric field.

Using Eq. (2.4.9) leads to

$$\mathcal{Q}(\vec{r}, t) = \mathcal{Q}(\vec{r}, t_{(0)}) - \int_{t_{(0)}}^t d\tau \mathcal{D} \cdot \mathcal{J}_{\parallel}(\vec{r}, \tau) = \mathcal{Q}(\vec{r}, t_{(0)}) + \int_{t_{(0)}}^t d\tau \frac{\partial}{\partial t} \mathcal{Q}(\vec{r}, t). \quad (3.3.23)$$

Since the Riemann-Silberstein Maxwell's Eqs. (1.1.42) and (1.1.44) are linear and the continuity equation has to hold, we can separate the field equations into longitudinal and transverse equations with $\mathcal{F} = \mathcal{F}_{\parallel} + \mathcal{F}_{\perp}$, $\mathcal{D} \cdot \mathcal{F}_{\parallel} = \mathcal{Q}$, and $\mathcal{D} \cdot \mathcal{F}_{\perp} = 0$

$$\mathcal{D} \cdot \mathcal{F}_{\parallel}(\vec{r}, t) = \mathcal{Q}(\vec{r}, t) = \mathcal{Q}(\vec{r}, t_{(0)}) - \int_{t_{(0)}}^t d\tau \mathcal{D} \cdot \mathcal{J}_{\parallel}(\vec{r}, \tau), \quad (3.3.24)$$

$$i\hbar \frac{\partial}{\partial t} \mathcal{F}_{\parallel}(\vec{r}, t) = \mathcal{H} \mathcal{F}_{\parallel}(\vec{r}, t) - i\hbar \mathcal{J}_{\parallel}(\vec{r}, t), \quad (3.3.25)$$

$$\mathcal{D} \cdot \mathcal{F}_{\perp}(\vec{r}, t) = 0, \quad (3.3.26)$$

$$i\hbar \frac{\partial}{\partial t} \mathcal{F}_{\perp}(\vec{r}, t) = \mathcal{H} \mathcal{F}_{\perp}(\vec{r}, t) - i\hbar \mathcal{J}_{\perp}(\vec{r}, t). \quad (3.3.27)$$

According to Eq. (3.3.9) we introduce the two auxiliary six-component Riemann-Silberstein vectors $\mathcal{F}_{\mathcal{J}_{\parallel}}(\vec{r}, t)$ and $\mathcal{F}_{\mathcal{J}_{\perp}}(\vec{r}, t)$

$$\mathcal{F}_{\mathcal{J}_{\parallel}}(\vec{r}, t) = \int_{t_{(0)}}^t d\tau \mathcal{J}_{\parallel}(\vec{r}, \tau), \quad (3.3.28)$$

$$\mathcal{F}_{\mathcal{J}_{\perp}}(\vec{r}, t) = \int_{t_{(0)}}^t d\tau \mathcal{J}_{\perp}(\vec{r}, \tau), \quad (3.3.29)$$

which are longitudinal respectively transverse. In terms of these Riemann-Silberstein vectors, Eqs. (3.3.25) and (3.3.27) become

$$i\hbar \frac{\partial}{\partial t} \left(\mathcal{F}_{\parallel}(\vec{r}, t) + \mathcal{F}_{\mathcal{J}_{\parallel}}(\vec{r}, t) \right) = \mathcal{H} \mathcal{F}_{\parallel}(\vec{r}, t), \quad (3.3.30)$$

$$i\hbar \frac{\partial}{\partial t} \left(\mathcal{F}_{\perp}(\vec{r}, t) + \mathcal{F}_{\mathcal{J}_{\perp}}(\vec{r}, t) \right) = \mathcal{H} \mathcal{F}_{\perp}(\vec{r}, t). \quad (3.3.31)$$

As a consequence, the charge density and the longitudinal part of the current density contribute to the longitudinal Riemann-Silberstein vector, whereas only the transverse current density causes a transverse electromagnetic field. Additionally, due to the continuity equation, a longitudinal current implies always a motion of charge, which can be obtained only by inspecting the underlying electromagnetic field. In turn, a transverse current density means that although the current density can change in time, there is no motion of charge and the charge density stays always constant.

Using our previous considerations for Figure 3.6 means that only the transverse part of the total current leads to the observed outgoing waves in all four cases. In contrast, the longitudinal part of the current density causes the localized electromagnetic field. This can only be seen in Figure 3.6 1 - a) to 1 - c) since the corresponding current density flows only into the positive z-direction. The remaining three current densities in 2 - 4) have a reverse current that moves the charge density almost back into its initial state at the end of the current pulse.

To investigate the relation of transverse and longitudinal contributions further, we show in the following two simulations with one longitudinal and one transverse current density. As longitudinal $\vec{j}_{\text{long}}(\vec{r}, t)$ and transverse $\vec{j}_{\text{trans}}(\vec{r}, t)$ current densities we select

$$\vec{j}_{\text{long}}(\vec{r}, t) = \vec{j}_{\text{long},(0)}(\vec{r}) \exp\left(-\frac{(t-10.0)^2}{8}\right), \quad (3.3.32)$$

$$\vec{j}_{\text{trans}}(\vec{r}, t) = \vec{j}_{\text{trans},(0)}(\vec{r}) \exp\left(-\frac{(t-10.0)^2}{8}\right), \quad (3.3.33)$$

with

$$\vec{j}_{\text{long},(0)}(\vec{r}) = \begin{pmatrix} -x \\ -y \\ -z \end{pmatrix} \exp\left(\frac{-x^2-y^2-z^2}{2}\right), \quad (3.3.34)$$

$$\vec{j}_{\text{trans},(0)}(\vec{r}) = \begin{pmatrix} -y \\ x \\ 0 \end{pmatrix} \exp\left(\frac{-x^2-y^2-z^2}{2}\right). \quad (3.3.35)$$

To illustrate the spatial distribution of the current density we plot the x- and y-component of the transverse current $\vec{j}_{\text{trans},(0)}(\vec{r})$ in Figure 3.7. The z-component for the transverse current is zero and the shape of all components of the longitudinal current density are very similar to the transverse ones presented in Figure 3.7 and only differ in their orientation, so that we do not illustrate them. Using the same simulation parameters as in Sec. 3.3.1, we run the two longitudinal and transverse current simulations.

The results in Figure 3.8 for the longitudinal case agree with our previous considerations, where the current density causes only a localized field without any radiation. The plot sequence for a) with $t = 7.0$, b) with $t = 10.0$, and c) with $t = 30.0$ shows that the electric field increases in time without any outgoing signal.

In contrast, the transverse snapshot sequence in Figure 3.9 demonstrate a radial anti-symmetric wave form that propagates to the outside and leaves almost no localized field inside the simulation box. In panel a) at time $t = 16.0$ the wave is still inside the box, and almost outside the plot section at time $t = 25.0$ in panel b). Taking Eq. (3.3.19) for the longitudinal current density $\vec{j}_{\text{long}}(\vec{r}, t)$ gives the charge

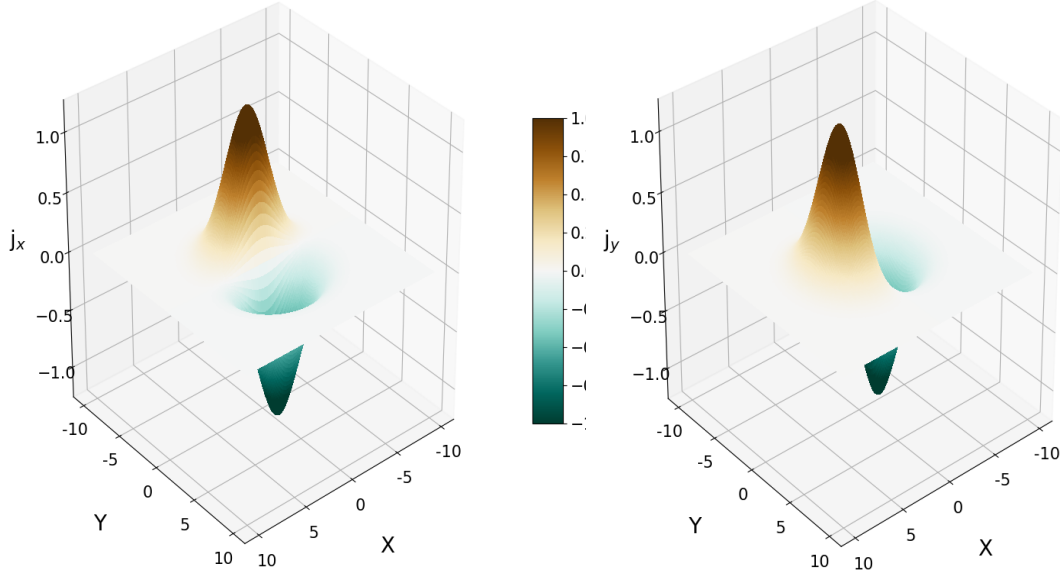


Figure 3.7: Spatial distribution of a transverse current density along the xy -plane. The figure on the right-hand side shows the x -component of the current density vector, whereas the figure on the left-hand side illustrates the y -component.

density with

$$\rho_{\text{long}}(\vec{r}, t) \approx \sqrt{2\pi} e^{-\frac{1}{2}(-x^2-y^2-z^2)} (-3 + x^2 + y^2 + z^2) \left[\text{Erf}\left(\frac{t-10.0}{2\sqrt{2}}\right) + 1 \right], \quad (3.3.36)$$

that corresponds to the electric field snapshots in Figure 3.8. In turn, the charge density for the transverse current density $\vec{j}_{\text{trans}}(\vec{r}, t)$ is constant for all three snapshots in Figure 3.9.

In a last plot in Figure 3.10, we evaluate the electric field, the magnetic field for different relevant directions, as well as the absolute value of the fields for the grid point $(5, 0, 0)$. Panel a) shows only the time-dependent part of the current pulse which follows the intensity behavior of the external current. In panel b) both graphs give the electric field in z -direction, whereas panel c) shows the corresponding magnetic field in the y -direction.

Comparing all four curves emphasizes the wave character of the transverse current propagation, where the electric field and the magnetic field are very similar in shape and magnitude for our selected unit system. The longitudinal current density causes only an electric field, which can be seen in panel e), where the absolute value of the magnetic field is plotted and returns zero for the longitudinal current run. In

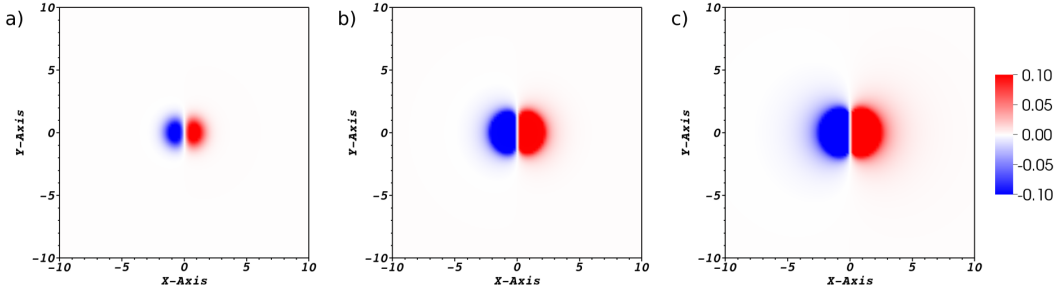


Figure 3.8: Snapshots of the electric field in z-direction for the longitudinal current density at times $t = 7.0$, $t = 10.0$ and $t = 30.0$.

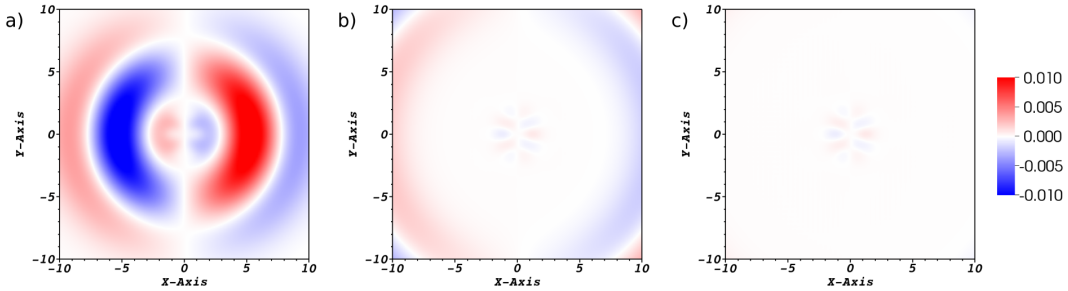


Figure 3.9: Snapshots of the electric field in z-direction for the transverse current density at times $t = 16.0$, $t = 25.0$ and $t = 30.0$.

addition, panel d) illustrates the absolute value of the electric field, which confirms that the main contribution of the electric field is polarized along the z-axis.

The decomposition of the electromagnetic field into longitudinal and transverse fields with different radiative features becomes an important ingredient when we consider later the electromagnetic fields in quantum electrodynamics (QED). In QED using Coulomb gauge, the longitudinal matter current density operator couples only to the quantized longitudinal field, whereas the transverse matter current density operator couples to the quantized transverse field. We focus on this aspect in more detail by using the longitudinal-transverse field decomposition in chapter 4.

3.4 Maxwell boundaries

To properly define different boundary conditions, we already introduced in Sec. 3.1.1 and illustrated in Figure 3.1 different regions in the simulation box, which we discuss here more in detail. The inner free Maxwell-propagation region obeys the physical Maxwell's equations, whereas the outer boundary region obeys specified Maxwell's equations to fulfill the appropriate simulation condition.

In the following sections we introduce two different schemes for absorbing bound-

aries to simulate open Maxwell systems, where outgoing Maxwell fields are damped with almost no reflections. For example in Sec. 3.3.1, we have shown an external current density in the box center that causes Maxwell fields which are moving to the box limits. In case of absorbing boundaries, we can use a much smaller simulation box to get the same results.

As a third boundary option, we show incident waves boundaries to simulate incident plane waves, which arise at the boundaries and propagate as free plane waves through the box, if the whole box describes vacuum.

In contrast, in presence of a linear medium inside the simulation box the elec-

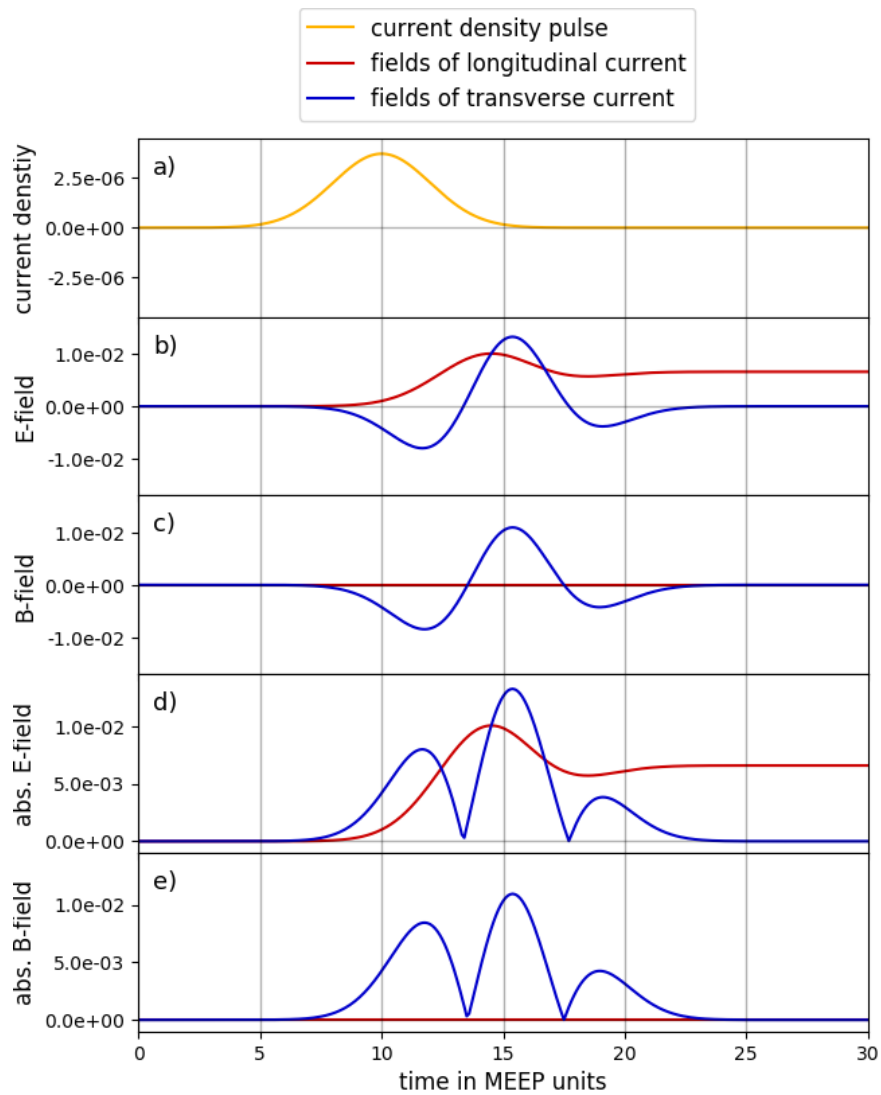


Figure 3.10: Electric and magnetic field reaction in z-direction for the longitudinal and transverse current density detected at point (5, 0, 0).

tromagnetic waves couple and scatter. To avoid further scatter and reflection effects at the box boundaries, we have to combine the incident waves boundaries with the absorbing boundaries, which we employ as another boundary option.

3.4.1 Absorbing boundaries by mask function

A simple method to implement and simulate absorbing boundaries is the mask absorption method, in which the Riemann-Silberstein vector is multiplied by a real mask function. The simulation box is split into two regions as shown in Figure 3.1, an inner free propagation region and an outer absorbing boundary region.

Consequently the mask function is always equal to one inside the free propagation region. The shape of the weight function in the outer boundary region has to be chosen such that it simulates absorption in a proper way. It is clear that the mask function has to be continuous at the transition from the edge to the inner region.

In addition, the mask function has to damp the Riemann-Silberstein vector to zero along the boundaries. To avoid almost all reflection and scatter effects in the free propagation region, the negative damping slope has to be smooth. A possible mask function $f_{\text{mask}}^{1\text{D}}(u)$ in one dimension that fulfills all that conditions is given by

$$f_{\text{mask}}^{1\text{D}}(u) = \begin{cases} 1 & \text{for } |u| \leq b_u \\ 1 - \sin\left(\frac{\pi|u-b_u|}{2|L_u-b_u|}\right)^2 & \text{for } |u| > b_u, \quad |u| \leq L_u, \end{cases} \quad (3.4.1)$$

where u represents one of the three possible dimension indices $u \in \{ 'x', 'y', 'z' \}$, and the length b_u denotes the limit of the inner free propagation box and L_u the outer simulation box limit. The total shape of the mask function $f_{\text{mask}}^{1\text{D}}(u)$ with box limits b_u and L_u is illustrated in Figure 3.11.

For numerical grids in more than one dimension, the total mask function is simply a product of all corresponding one-dimensional mask functions. Hence, the one-dimensional, the two-dimensional and three-dimensional mask functions $f_{\text{mask}}^{1\text{D}}(x)$, $f_{\text{mask}}^{2\text{D}}(x, y)$ and $f_{\text{mask}}^{3\text{D}}(x, y, z)$ are given by

$$f_{\text{mask}}^{1\text{D}}(x) = f_{\text{mask}}^{1\text{D}}(x), \quad (3.4.2)$$

$$f_{\text{mask}}^{2\text{D}}(x, y) = f_{\text{mask}}^{1\text{D}}(x) \cdot f_{\text{mask}}^{1\text{D}}(y), \quad (3.4.3)$$

$$f_{\text{mask}}^{3\text{D}}(x, y, z) = f_{\text{mask}}^{1\text{D}}(x) \cdot f_{\text{mask}}^{1\text{D}}(y) \cdot f_{\text{mask}}^{1\text{D}}(z). \quad (3.4.4)$$

A three-dimensional contour plot of a two-dimensional mask function $f_{\text{mask}}^{2\text{D}}(x, y)$ or a cut through a three-dimensional mask function $f_{\text{mask}}^{3\text{D}}(x, y, z)$ with constant z is shown in Figure 3.12.

It can be seen in this figure that due to the factorization of the mask function with corresponding one-dimensional mask functions, the overlap regions are continuous and smooth. Furthermore, the damping in the vertex regions is stronger than at the

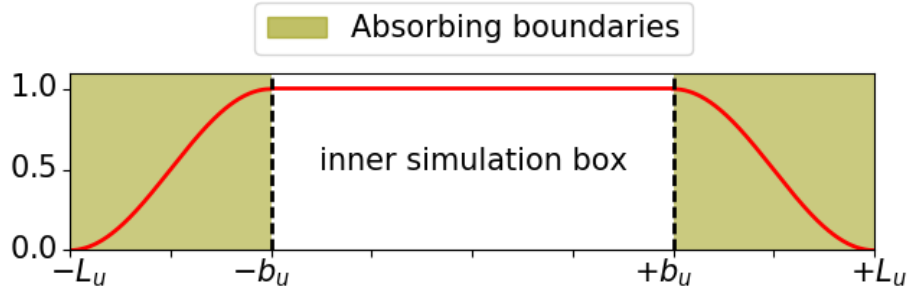


Figure 3.11: Mask function along a Cartesian axis $u \in \{ 'x', 'y', 'z' \}$ with its characteristic profile. Inside the inner simulation box limit $[-b_u, b_u]$ the mask function is equal to one, whereas the function decreases smoothly to zero in the mask boundary region $[-L_u, -b_u[$, and $] + b_u, +L_u]$. The decreasing function has a turning point and is point-symmetric to that point.

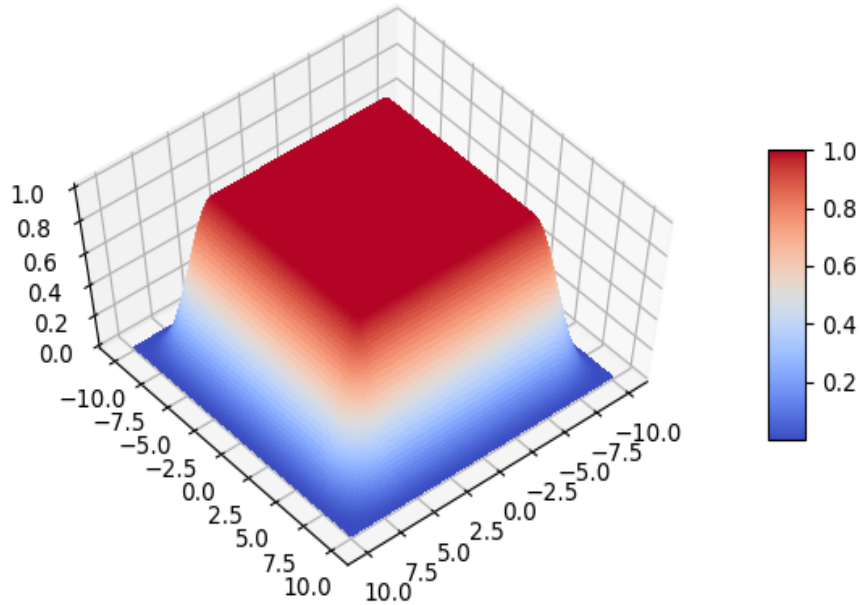


Figure 3.12: A three-dimensional contour plot of the mask function on the x-y plane. The inner plateau with the mask value equal to one marks the inner free Maxwell propagation region. The plot shows the smooth slope towards zero in the outer region and additionally the round corners at the overlapping x and y mask regions.

edges of the box, which avoids scatter effects especially in those more sensitive parts of the simulation box.

In case of a mask function as defined in Eq. (3.4.1), it is clear that only the distance of $|L_u - b_u|$ determines the shape of the function and therefore the ability to absorb the outgoing electromagnetic fields. Consequently, for larger absorbing boundary regions, the decreasing slope of the mask function is weaker and the accuracy of the simulated absorbing boundaries increases, which we see later in Figure 3.14 in Sec. 3.4.3.

3.4.2 Absorbing boundaries by perfectly matched layer

A more accurate method for open Maxwell systems is the perfectly matched layer (PML) absorbing boundary condition. We have implemented such a PML analogous to the Berènger layer for the Yee finite difference time domain algorithm [65, 87], but now modified for the Riemann-Silberstein Maxwell propagation.

The basic idea of the Berènger layer is to complement Maxwell's equations with an artificial lossy layer, which is described by a non-physical electric conductivity $\sigma_{\text{el}}(\vec{r})$ and a non-physical magnetic conductivity $\sigma_{\text{mag}}(\vec{r})$. These conductivities are defined such as to yield minimal reflections at the boundaries, but have no physical meaning otherwise.

The loss due to the conductivity parameters is linear in the corresponding $\vec{E}(\vec{r}, t)$ and $\vec{B}(\vec{r}, t)$. Therefore, the modified k-vector component of Faraday's and Ampère's laws without current density takes with Eq. (1.1.10) and Eq. (1.1.11) the form

$$\partial_t B_k(\vec{r}, t) = - \sum_{l,m} \varepsilon_{klm} \partial_l E_m(\vec{r}, t) - \sigma_{\text{mag}}(\vec{r}) B_k(\vec{r}, t), \quad (3.4.5)$$

$$\partial_t E_k(\vec{r}, t) = \frac{1}{\epsilon_0 \mu_0} \sum_{l,m} \varepsilon_{klm} \partial_l B_m(\vec{r}, t) - \sigma_{\text{el}}(\vec{r}) E_k(\vec{r}, t), \quad (3.4.6)$$

where ε_{klm} denotes the Levi-Civita tensor. We note here, that the PML is in principle not restricted to vacuum conditions but also valid for other homogeneous dielectric conditions. In other words, the Riemann-Silberstein PML that we have implemented also works in a linear medium, but with the constraint that $\epsilon(\vec{r})$ and $\mu(\vec{r})$, and consequently $c(\vec{r})$ are constant at the border and inside the boundaries for all time. According to Eq. (1.2.29) with the spatial constant medium parameters

$$\epsilon(\vec{r}) = \epsilon, \quad (3.4.7)$$

$$\mu(\vec{r}) = \mu \quad (3.4.8)$$

we obtain

$$\vec{\nabla} \epsilon = \vec{\nabla} \mu = 0, \quad c = \frac{1}{\sqrt{\epsilon \mu}}. \quad (3.4.9)$$

In this manner, the $\vec{K}_{\pm}(\vec{r})$ terms in Eq. (1.2.29) is equal to zero and only the $\sigma_{\text{mag}}(\vec{r})$ and $\sigma_{\text{el}}(\vec{r})$ terms $\sigma_{\text{el,mag}_{\pm}}(\vec{r})$ $\sigma_{\text{el,mag}_{\mp}}(\vec{r})$ remain.

For simplicity and since the form of the PML equations are equivalent for vacuum condition with ϵ_0 , μ_0 and in a linear medium for constant ϵ , μ at the border and inside the boundaries for all time, we drop the index "lm" of the Riemann-Silberstein vector $\vec{F}_{\text{lm},\pm}(\vec{r}, t)$

$$\vec{F}_{\text{lm},\pm}(\vec{r}, t) = \sqrt{\frac{\epsilon}{2}} \vec{E}(\vec{r}, t) \pm i \sqrt{\frac{1}{2\mu}} \vec{B}(\vec{r}, t) = \vec{F}_{\pm}(\vec{r}, t). \quad (3.4.10)$$

Using Eq. (1.2.29) without the $\vec{j}_{\text{free}}(\vec{r}, t)$ and $K_{\pm}(\vec{r}, t)$ terms or equivalently Eq. (3.4.5) and Eq. (3.4.6) combined into the Riemann-Silberstein representation yields

$$\begin{aligned} i\hbar \frac{\partial}{\partial t} \vec{F}_{\pm}(\vec{r}, t) &= \pm \hbar c \vec{\nabla} \times \vec{F}_{\pm}(\vec{r}, t) \\ &\quad - i\hbar \sigma_{\text{el}}(\vec{r}) \frac{1}{2} \left(\vec{F}_{+}(\vec{r}, t) + \vec{F}_{-}(\vec{r}, t) \right) \\ &\quad \mp i\hbar \sigma_{\text{mag}}(\vec{r}) \frac{1}{2} \left(\vec{F}_{+}(\vec{r}, t) - \vec{F}_{-}(\vec{r}, t) \right). \end{aligned} \quad (3.4.11)$$

Transforming Eqs. (1.1.6) - (1.1.2) to frequency domain, and using the Riemann-Silberstein vector in frequency space $\vec{F}_{\pm}(\vec{r}, \omega)$ with

$$\vec{F}_{\pm}(\vec{r}, \omega) = \int dt e^{i\omega t} \vec{F}_{\pm}(\vec{r}, t) \quad (3.4.12)$$

leads to the underlying Riemann-Silberstein Maxwell's equation for the k^{th} component in time-harmonic form [96, 97] of Eq. (3.4.6) and Eq. (3.4.5) for the absorbing layer

$$\begin{aligned} -\omega \hbar \vec{F}_{\pm,k}(\vec{r}, \omega) &= \mp \hbar c \sum_{l,m} \varepsilon_{klm} \partial_l \vec{F}_{\pm,m}(\vec{r}, \omega) \\ &\quad - i\hbar \frac{1}{2} \sigma_{\text{el}}(\vec{r}) \left(\vec{F}_{+,k}(\vec{r}, \omega) + \vec{F}_{-,k}(\vec{r}, \omega) \right) \\ &\quad \mp i\hbar \frac{1}{2} \sigma_{\text{mag}}(\vec{r}) \left(\vec{F}_{+,k}(\vec{r}, \omega) - \vec{F}_{-,k}(\vec{r}, \omega) \right), \end{aligned} \quad (3.4.13)$$

where the first term on the right-hand side describes the curl operation.

The principle of a PML is to propagate the respective field components in the absorbing boundary region which are necessary for a correct propagation inside the free Maxwell region, and to damp the remaining components without causing strong reflections back into the free Maxwell region. For this purpose, Berenger's method splits up Maxwell's equations for each direction in two equations which form the basis for the so-called split PML [98, 87, 65]. The field component in k -direction

is split into one component for l and one for m with $k \neq l \neq m$, so that the k^{th} component $\tilde{F}_{\pm}^k(\vec{r}, \omega)$ is given by

$$\tilde{F}_{\pm,k}(\vec{r}, \omega) = \tilde{F}_{\pm,k,(l)}(\vec{r}, \omega) + \tilde{F}_{\pm,k,(m)}(\vec{r}, \omega). \quad (3.4.14)$$

The field component $\tilde{F}_{\pm,k}$ is split such that the $\tilde{F}_{\pm,k,(l)}(\vec{r}, \omega)$ part is responsible for the field propagation parallel to direction l and accordingly $\tilde{F}_{\pm,k,(m)}(\vec{r}, \omega)$ parallel to direction m . In other words, there are two separate propagations which simulate only the free propagation along the corresponding direction. Thus, one propagation part could be where the field enters the PML region, while the other part is still in the free propagation box. We note here, that the vector component index is written without any parentheses, whereas the split direction is given inside parentheses, e.g., $\tilde{F}_{\pm,k,(l)}(\vec{r}, \omega)$ has the vector component k and the split direction (l) .

The damping of the fields is applied by the electric and magnetic conductivities $\sigma_{\text{el}}(\vec{r})$, $\sigma_{\text{mag}}(\vec{r})$ which are artificially modified and depend now also on the splitted direction, i.e., (l) direction for $\tilde{F}_{\pm,k,(l)}(\vec{r}, \omega)$ as well as the field direction k . In addition, each equation only contains one part of the two curl terms.

Applying all these previously considerations to the six components of the Maxwell's equations in Riemann-Silberstein form yield twelve relations for the PML. Explicitly, the two equations for the x component in Eq. (3.4.13) are

$$\begin{aligned} -\omega\hbar\tilde{F}_{\pm,x,(y)}(\vec{r}, \omega) &= \pm\hbar c\partial_y \left(\tilde{F}_{\pm,z,(x)}(\vec{r}, \omega) + \tilde{F}_{\pm,z,(y)}(\vec{r}, \omega) \right) \\ &\quad - i\hbar\frac{1}{2}\sigma_{\text{el},(y)}(\vec{r}) \left(\tilde{F}_{+,x,(y)}(\vec{r}, \omega) + \tilde{F}_{-,x,(y)}(\vec{r}, \omega) \right) \\ &\quad \mp i\hbar\frac{1}{2}\sigma_{\text{mag},(y)}(\vec{r}) \left(\tilde{F}_{+,x,(y)}(\vec{r}, \omega) - \tilde{F}_{-,x,(y)}(\vec{r}, \omega) \right), \end{aligned} \quad (3.4.15)$$

$$\begin{aligned} -\omega\hbar\tilde{F}_{\pm,x,(z)}(\vec{r}, \omega) &= \mp\hbar c\partial_z \left(\tilde{F}_{\pm,y,(x)}(\vec{r}, \omega) + \tilde{F}_{\pm,y,(z)}(\vec{r}, \omega) \right) \\ &\quad - i\hbar\frac{1}{2}\sigma_{\text{el},(z)}(\vec{r}) \left(\tilde{F}_{+,x,(z)}(\vec{r}, \omega) + \tilde{F}_{-,x,(z)}(\vec{r}, \omega) \right) \\ &\quad \mp i\hbar\frac{1}{2}\sigma_{\text{mag},(z)}(\vec{r}) \left(\tilde{F}_{+,x,(z)}(\vec{r}, \omega) - \tilde{F}_{-,x,(z)}(\vec{r}, \omega) \right), \end{aligned} \quad (3.4.16)$$

for the y component

$$\begin{aligned} -\omega\hbar\tilde{F}_{\pm,y,(z)}(\vec{r}, \omega) &= \pm\hbar c\partial_z \left(\tilde{F}_{\pm,x,(y)}(\vec{r}, \omega) + \tilde{F}_{\pm,x,(z)}(\vec{r}, \omega) \right) \\ &\quad - i\hbar\frac{1}{2}\sigma_{\text{el},(z)}(\vec{r}) \left(\tilde{F}_{+,y,(z)}(\vec{r}, \omega) + \tilde{F}_{-,y,(z)}(\vec{r}, \omega) \right) \\ &\quad \mp i\hbar\frac{1}{2}\sigma_{\text{mag},(z)}(\vec{r}) \left(\tilde{F}_{+,y,(z)}(\vec{r}, \omega) - \tilde{F}_{-,y,(z)}(\vec{r}, \omega) \right), \end{aligned} \quad (3.4.17)$$

$$\begin{aligned}
 -\omega\hbar\tilde{F}_{\pm,y,(x)}(\vec{r},\omega) &= \mp\hbar c\partial_x\left(\tilde{F}_{\pm,z,(x)}(\vec{r},\omega) + \tilde{F}_{\pm,z,(y)}(\vec{r},\omega)\right) \\
 &\quad - i\hbar\frac{1}{2}\sigma_{\text{el},(x)}(\vec{r})\left(\tilde{F}_{+,y,(x)}(\vec{r},\omega) + \tilde{F}_{-,y,(x)}(\vec{r},\omega)\right) \\
 &\quad \mp\hbar i\frac{1}{2}\sigma_{\text{mag},(x)}(\vec{r})\left(\tilde{F}_{+,y,(x)}(\vec{r},\omega) - \tilde{F}_{-,y,(x)}(\vec{r},\omega)\right),
 \end{aligned} \tag{3.4.18}$$

and for the z component

$$\begin{aligned}
 -\omega\hbar\tilde{F}_{\pm,z,(x)}(\vec{r},\omega) &= \pm\hbar c\partial_x\left(\tilde{F}_{\pm,y,(x)}(\vec{r},\omega) + \tilde{F}_{\pm,y,(z)}(\vec{r},\omega)\right) \\
 &\quad - i\hbar\frac{1}{2}\sigma_{\text{el},(x)}(\vec{r})\left(\tilde{F}_{+,z,(x)}(\vec{r},\omega) + \tilde{F}_{-,z,(x)}(\vec{r},\omega)\right) \\
 &\quad \mp i\hbar\frac{1}{2}\sigma_{\text{mag},(x)}(\vec{r})\left(\tilde{F}_{+,z,(x)}(\vec{r},\omega) - \tilde{F}_{-,z,(x)}(\vec{r},\omega)\right),
 \end{aligned} \tag{3.4.19}$$

$$\begin{aligned}
 -\omega\hbar\tilde{F}_{\pm,z,(y)}(\vec{r},\omega) &= \mp\hbar c\partial_y\left(\tilde{F}_{\pm,x,(y)}(\vec{r},\omega) + \tilde{F}_{\pm,x,(z)}(\vec{r},\omega)\right) \\
 &\quad - i\hbar\frac{1}{2}\sigma_{\text{el},(y)}(\vec{r})\left(\tilde{F}_{+,z,(y)}(\vec{r},\omega) + \tilde{F}_{-,z,(y)}(\vec{r},\omega)\right) \\
 &\quad \mp i\hbar\frac{1}{2}\sigma_{\text{mag},(y)}(\vec{r})\left(\tilde{F}_{+,z,(y)}(\vec{r},\omega) - \tilde{F}_{-,z,(y)}(\vec{r},\omega)\right).
 \end{aligned} \tag{3.4.20}$$

Similar to Berènger's split field PML derivation for the Yee-Algorithm, we want to include also in our case the frequency ω and the electric and magnetic conductivity σ_{el} and σ_{mag} in a factor multiplied by the corresponding split field [98, 87, 65] before we recombine the two split field equations. Using the two factors

$$\tilde{\eta}_{(l)}(\vec{r},\omega) = -\frac{i\omega(\sigma_{\text{el},(l)}(\vec{r}) + \sigma_{\text{mag},(l)}(\vec{r}) - 2i\omega)}{2(\sigma_{\text{el},(l)}(\vec{r}) - i\omega)(\sigma_{\text{mag},(l)}(\vec{r}) - i\omega)}, \tag{3.4.21}$$

$$\tilde{\xi}_{(l)}(\vec{r},\omega) = \frac{i\omega(\sigma_{\text{mag},(l)}(\vec{r}) - \sigma_{\text{el},(l)}(\vec{r}))}{2(\sigma_{\text{el},(l)}(\vec{r}) - i\omega)(\sigma_{\text{mag},(l)}(\vec{r}) - i\omega)}, \tag{3.4.22}$$

the system of the split equations in Eqs. (3.4.15) - (3.4.20) can be rearranged equivalently to

$$\begin{aligned}
 -\omega\hbar\tilde{F}_{\pm,x,(y)}(\vec{r},\omega) &= \pm\hbar c\tilde{\eta}_{(y)}(\vec{r},\omega)\partial_y\left(\tilde{F}_{\pm,z,(x)}(\vec{r},\omega) + \tilde{F}_{\pm,z,(y)}(\vec{r},\omega)\right) \\
 &\quad \pm\hbar c\tilde{\xi}_{(y)}(\vec{r},\omega)\partial_y\left(\tilde{F}_{\mp,z,(x)}(\vec{r},\omega) + \tilde{F}_{\mp,z,(y)}(\vec{r},\omega)\right),
 \end{aligned} \tag{3.4.23}$$

$$\begin{aligned}
 -\omega\hbar\tilde{F}_{\pm,x,(z)}(\vec{r},\omega) &= \mp\hbar c\tilde{\eta}_{(z)}(\vec{r},\omega)\partial_z\left(\tilde{F}_{\pm,y,(x)}(\vec{r},\omega) + \tilde{F}_{\pm,y,(z)}(\vec{r},\omega)\right) \\
 &\quad \mp\hbar c\tilde{\xi}_{(z)}(\vec{r},\omega)\partial_z\left(\tilde{F}_{\pm,y,(x)}(\vec{r},\omega) + \tilde{F}_{\pm,y,(z)}(\vec{r},\omega)\right)
 \end{aligned} \tag{3.4.24}$$

for the x component,

$$\begin{aligned}
 -\omega\hbar\tilde{F}_{\pm,y,(z)}(\vec{r},\omega) &= \pm\hbar c\tilde{\eta}_{(z)}(\vec{r},\omega)\partial_z\left(\tilde{F}_{\pm,x,(y)}(\vec{r},\omega) + \tilde{F}_{\pm,x,(z)}(\vec{r},\omega)\right) \\
 &\quad \pm\hbar c\tilde{\xi}_{(z)}(\vec{r},\omega)\partial_z\left(\tilde{F}_{\mp,x,(y)}(\vec{r},\omega) + \tilde{F}_{\mp,x,(z)}(\vec{r},\omega)\right),
 \end{aligned} \tag{3.4.25}$$

$$\begin{aligned}
 -\omega\hbar\tilde{F}_{\pm,y,(x)}(\vec{r},\omega) &= \mp\hbar c\tilde{\eta}_{(x)}(\vec{r},\omega)\partial_x\left(\tilde{F}_{\pm,z,(x)}(\vec{r},\omega) + \tilde{F}_{\pm,z,(y)}(\vec{r},\omega)\right) \\
 &\mp\hbar c\tilde{\xi}_{(x)}(\vec{r},\omega)\partial_x\left(\tilde{F}_{\pm,z,(x)}(\vec{r},\omega) + \tilde{F}_{\pm,z,(y)}(\vec{r},\omega)\right)
 \end{aligned} \tag{3.4.26}$$

for the y component, and

$$\begin{aligned}
 -\omega\hbar\tilde{F}_{\pm,z,(x)}(\vec{r},\omega) &= \pm\hbar c\tilde{\eta}_{(x)}(\vec{r},\omega)\partial_x\left(\tilde{F}_{\pm,y,(x)}(\vec{r},\omega) + \tilde{F}_{\pm,y,(z)}(\vec{r},\omega)\right) \\
 &\pm\hbar c\tilde{\xi}_{(x)}(\vec{r},\omega)\partial_x\left(\tilde{F}_{\mp,y,(x)}(\vec{r},\omega) + \tilde{F}_{\mp,y,(z)}(\vec{r},\omega)\right),
 \end{aligned} \tag{3.4.27}$$

$$\begin{aligned}
 -\omega\hbar\tilde{F}_{\pm,z,(y)}(\vec{r},\omega) &= \mp\hbar c\tilde{\eta}_{(y)}(\vec{r},\omega)\partial_y\left(\tilde{F}_{\pm,x,(y)}(\vec{r},\omega) + \tilde{F}_{\pm,x,(z)}(\vec{r},\omega)\right) \\
 &\mp\hbar c\tilde{\xi}_{(y)}(\vec{r},\omega)\partial_y\left(\tilde{F}_{\pm,x,(y)}(\vec{r},\omega) + \tilde{F}_{\pm,x,(z)}(\vec{r},\omega)\right)
 \end{aligned} \tag{3.4.28}$$

for the z component. Finally, adding each of the two Eqs. (3.4.23) - (3.4.24), Eqs. (3.4.26) - (3.4.25), Eqs. (3.4.27) - (3.4.28) and using Eq. (3.4.14) yields the PML equations in frequency domain for the Riemann-Silberstein representation

$$\begin{aligned}
 -\omega\hbar\begin{pmatrix} \tilde{F}_{+,k}(\vec{r},\omega) \\ \tilde{F}_{-,k'}(\vec{r},\omega) \end{pmatrix} &= \hbar c\begin{pmatrix} \sum_{l,m} \varepsilon_{klm}\tilde{\eta}_{(l)}(\vec{r},\omega)\partial_l\tilde{F}_{+,m}(\vec{r},\omega) \\ -\sum_{l',m'} \varepsilon_{klm}\tilde{\eta}_{(l')}(\vec{r},\omega)\partial_{l'}\tilde{F}_{-,m'}(\vec{r},\omega) \end{pmatrix} \\
 &+ \hbar c\begin{pmatrix} \hbar\sum_{l,m} \varepsilon_{klm}\tilde{\xi}_{(l)}(\vec{r},\omega)\partial_l\tilde{F}_{-,m}(\vec{r},\omega) \\ -\hbar\sum_{l',m'} \varepsilon_{k'l'm'}\tilde{\xi}_{(l')}(\vec{r},\omega)\partial_{l'}\tilde{F}_{+,m'}(\vec{r},\omega) \end{pmatrix}.
 \end{aligned} \tag{3.4.29}$$

In our PML implementation for simplicity, we do not introduce new correction terms in $\tilde{\eta}_{(l)}(\vec{r},\omega)$ or $\tilde{\xi}_{(l)}(\vec{r},\omega)$ to improve the PML and to reduce low-frequency reflections like it is commonly applied for the Yee algorithm [98, 87, 65]. While such extensions are possible in future refinements of our implementation, we found the simple form without correction terms already to provide good absorbance at the boundaries.

In principle, Eq. 3.4.29 describes the full PML equation for the Riemann-Silberstein representation of Maxwell's equations. The quantum mechanical like time-evolution propagation of Maxwell's fields that we introduced in this thesis can be applied in momentum space but of course also in position space. Since our first implementation in Octopus bases on real-space operations, we have to continue with several similar steps like in Ref. [98, 87, 65] for the FDTD method.

By back transforming Eq. (3.4.21) and Eq. (3.4.22) from frequency domain into

time domain, we arrive at

$$\begin{aligned} \int d\omega e^{-i\omega t} \tilde{\eta}_{(l)}(\vec{r}, \omega) &= \delta(t) - \frac{1}{2} \left(\sigma_{\text{el},(l)}(\vec{r}) e^{-\sigma_{\text{el},(l)}(\vec{r})t} + \sigma_{\text{mag},(l)}(\vec{r}) e^{-\sigma_{\text{mag},(l)}(\vec{r})t} \right) \Theta(t) \\ &= \delta(t) + \zeta_{(l)}(\vec{r}, t) \Theta(t), \end{aligned} \quad (3.4.30)$$

$$\begin{aligned} \int d\omega e^{-i\omega t} \tilde{\xi}_{(l)}(\vec{r}, \omega) &= -\frac{1}{2} \left(\sigma_{\text{el},(l)}(\vec{r}) e^{-\sigma_{\text{el},(l)}(\vec{r})t} - \sigma_{\text{mag},(l)}(\vec{r}) e^{-\sigma_{\text{mag},(l)}(\vec{r})t} \right) \Theta(t) \\ &= \xi_{(l)}(\vec{r}, t) \Theta(t). \end{aligned} \quad (3.4.31)$$

In analogy to the auxiliary functions $\tilde{\zeta}_{(l)}(\vec{r}, \omega)$ and $\tilde{\xi}_{(l)}(\vec{r}, \omega)$ in momentum space, we define two auxiliary functions $\zeta_{(l)}(\vec{r}, t)$ and $\xi_{(l)}(\vec{r}, t)$ in position space

$$\zeta_{(l)}(\vec{r}, t) = -\frac{1}{2} \left(\sigma_{\text{el},(l)}(\vec{r}) e^{-\sigma_{\text{el},(l)}(\vec{r})t} + \sigma_{\text{mag},(l)}(\vec{r}) e^{-\sigma_{\text{mag},(l)}(\vec{r})t} \right), \quad (3.4.32)$$

$$\xi_{(l)}(\vec{r}, t) = -\frac{1}{2} \left(\sigma_{\text{el},(l)}(\vec{r}) e^{-\sigma_{\text{el},(l)}(\vec{r})t} - \sigma_{\text{mag},(l)}(\vec{r}) e^{-\sigma_{\text{mag},(l)}(\vec{r})t} \right). \quad (3.4.33)$$

The electric conductivity $\sigma_{\text{el}}(\vec{r})$ and the magnetic conductivity $\sigma_{\text{mag}}(\vec{r})$ have to be chosen such that the reflection becomes minimal. As is well-known in FDTD [98, 87, 65], the relation between the electric conductivity $\sigma_{\text{el}}(\vec{r})$ and the magnetic conductivity $\sigma_{\text{mag}}(\vec{r})$ to minimize the reflection coefficient has to obey

$$\frac{\sigma_{\text{el},(l)}(\vec{r})}{\epsilon} = \frac{\sigma_{\text{mag},(l)}(\vec{r})}{\mu} \quad (3.4.34)$$

at the border between the free Maxwell simulation box and the absorbing boundaries.

Using this relation between the two conductivities, it is convenient to use only one conductivity with $\sigma(\vec{r}) = \sigma_{\text{el}}(\vec{r})$, and the updated forms of the expressions $\zeta_{(l)}(\vec{r}, t)$ and $\xi_{(l)}(\vec{r}, t)$ are

$$\zeta_{(l)}(\vec{r}, t) = -\frac{1}{2} \sigma_{(l)}(\vec{r}) e^{-\sigma_{(l)}(\vec{r})t} \left(1 + \frac{\mu}{\epsilon} e^{-(\mu/\epsilon - 1)\sigma_{(l)}(\vec{r})t} \right), \quad (3.4.35)$$

$$\xi_{(l)}(\vec{r}, t) = -\frac{1}{2} \sigma_{(l)}(\vec{r}) e^{-\sigma_{(l)}(\vec{r})t} \left(1 - \frac{\mu}{\epsilon} e^{-(\mu/\epsilon - 1)\sigma_{(l)}(\vec{r})t} \right). \quad (3.4.36)$$

As a result, the back transformation of Eq. (3.4.29) becomes

$$\begin{aligned}
 i\hbar c\partial_0 \begin{pmatrix} F_{+,k}(\vec{r}, t) \\ F_{-,k'}(\vec{r}, t) \end{pmatrix} &= \hbar c \begin{pmatrix} \sum_{l,m} \varepsilon_{klm} \left(\delta * \partial_l F_{+,m}(\vec{r}) \right) (t) \\ - \sum_{l',m'} \varepsilon_{k'l'm'} \left(\delta * \partial_{l'} F_{-,m'}(\vec{r}) \right) (t) \end{pmatrix} \\
 &+ \hbar c \begin{pmatrix} \sum_{l,m} \varepsilon_{klm} \left(\zeta_{(l)}(\vec{r}) * \partial_l F_{+,m}(\vec{r}) \right) (t) \\ - \sum_{l',m'} \varepsilon_{k'l'm'} \left(\zeta_{(l')}(\vec{r}) * \partial_{l'} F_{-,m'}(\vec{r}) \right) (t) \end{pmatrix} \\
 &+ \hbar c \begin{pmatrix} \sum_{l,m} \varepsilon_{klm} \left(\xi_{(l)}(\vec{r}) * \partial_l F_{-,m}(\vec{r}) \right) (t) \\ - \sum_{l',m'} \varepsilon_{k'l'm'} \left(\xi_{(l')}(\vec{r}) * \partial_{l'} F_{+,m'}(\vec{r}) \right) (t) \end{pmatrix}.
 \end{aligned} \tag{3.4.37}$$

which contains several convolutions in time. Whereas the first convolution on the right-hand side in Eq. (3.4.37) is simply

$$\left(\delta * \partial_l F_{\pm,m}(\vec{r}) \right) (t) = \int \delta(t - \tau) \partial_l F_{\pm,m}(\vec{r}, \tau) d\tau = \partial_l F_{\pm,m}(\vec{r}, t), \tag{3.4.38}$$

the remaining convolutions are explicitly given by

$$\left(\zeta_{(l)}(\vec{r}) * \partial_l F_{\pm,m}(\vec{r}) \right) (t) = \int_0^t \zeta_{(l)}(\vec{r}, t - \tau) \partial_l F_{\pm,m}(\vec{r}, \tau) d\tau, \tag{3.4.39}$$

$$\left(\xi_{(l)}(\vec{r}) * \partial_l F_{\pm,m}(\vec{r}) \right) (t) = \int_0^t \xi_{(l)}(\vec{r}, t - \tau) \partial_l F_{\pm,m}(\vec{r}, \tau) d\tau. \tag{3.4.40}$$

This completes the construction of the PML for our Riemann-Silberstein formulation when we use the curl operation in Eq. (1.1.26) with spin matrices to obtain

$$\begin{aligned}
 i\hbar c\partial_0 \begin{pmatrix} \vec{F}_+(\vec{r}, t) \\ \vec{F}_-(\vec{r}, t) \end{pmatrix} &= \hbar c \begin{pmatrix} \left(-i\vec{S} \cdot \vec{\nabla} \right) \vec{F}_+(\vec{r}, t) \\ \left(i\vec{S} \cdot \vec{\nabla} \right) \vec{F}_-(\vec{r}, t) \end{pmatrix} \\
 &+ \hbar c \begin{pmatrix} \int_0^t d\tau \left[-i \sum_k \zeta_{(k)}(\vec{r}, t - \tau) S_k \partial_k \right] \vec{F}_+(\vec{r}, \tau) \\ \int_0^t d\tau \left[i \sum_k \zeta_{(k)}(\vec{r}, t - \tau) S_k \partial_k \right] \vec{F}_-(\vec{r}, \tau) \end{pmatrix} \\
 &+ \hbar c \begin{pmatrix} \int_0^t d\tau \left[-i \sum_k \xi_{(k)}(\vec{r}, t - \tau) S_k \partial_k \right] \vec{F}_-(\vec{r}, \tau) \\ \int_0^t d\tau \left[i \sum_k \xi_{(k)}(\vec{r}, t - \tau) S_k \partial_k \right] \vec{F}_+(\vec{r}, \tau) \end{pmatrix}.
 \end{aligned} \tag{3.4.41}$$

Since we have already illustrated how to include a linear medium in the Riemann-Silberstein time-evolution in the previous sections, it becomes now straightforward to combine the PML with our existing implementation.

Adding the PML expressions to the Riemann-Silberstein Hamiltonian \mathcal{H} in Eq. (1.1.45) and using

$$\mathcal{F}(\vec{r}, t) = \begin{pmatrix} \vec{F}_+(\vec{r}, t) \\ \vec{F}_-(\vec{r}, t) \end{pmatrix}, \quad (3.4.42)$$

we arrive at a propagation scheme with perfectly matched layer boundaries

$$\mathcal{H}_{\text{PML}}(\vec{r}, t) = \mathcal{H}(\vec{r}, t) + \mathcal{G}(\vec{r}, t) \star \mathcal{F}(\vec{r}, t), \quad (3.4.43)$$

where the 6x6 PML operation $\mathcal{G}(\vec{r}, t) \star \mathcal{F}(\vec{r}, t)$ is given by

$$\begin{aligned} \mathcal{G}(\vec{r}, t) \star \mathcal{F}(\vec{r}, t) = & \left[\begin{pmatrix} 1 & 0 \\ 0 & -1 \end{pmatrix}_{2 \times 2} \otimes \left(-i\hbar c \int_0^t d\tau \sum_k [\zeta_{(k)}(\vec{r}, t - \tau) S_k \partial_k] \right)_{3 \times 3} \right] \mathcal{F}(\vec{r}, \tau) \\ & + \left[\begin{pmatrix} 0 & 1 \\ -1 & 0 \end{pmatrix}_{2 \times 2} \otimes \left(-i\hbar c \int_0^t d\tau \sum_k [\xi_{(k)}(\vec{r}, t - \tau) S_k \partial_k] \right)_{3 \times 3} \right] \mathcal{F}(\vec{r}, \tau). \end{aligned} \quad (3.4.44)$$

The left factor of the second Kronecker product in Eq. (3.4.44) has entries in the off-diagonal, and therefore the two Riemann-Silberstein vectors $\vec{F}_\pm(\vec{r}, t)$ always couple in the PML region.

In principle, the PML terms in Eq. (3.4.43) have to be calculated for each time step, which massively increases computational cost. However, taking a closer look at Eq. (3.4.39) and Eq. (3.4.40), we notice that the two functions $\zeta_{(k)}(\vec{r}, t - \tau)$ and $\xi_{(k)}(\vec{r}, t - \tau)$ contain exponential factors. Therefore it is possible to obtain a rather accurate approximation of the terms by using a recursive-convolution method [99] with finite time steps Δt . The recursive-convolution method allows to express integrals of the form

$$g(\vec{r}, t) = \int_0^t d\tau e^{-\alpha(\vec{r}, t - \tau)} f_{(1)}(\vec{r}, t - \tau) f_{(2)}(\vec{r}, \tau) \quad (3.4.45)$$

for discrete time $t = m\Delta t$

$$g(\vec{r}, m\Delta t) = \int_0^{m\Delta t} d\tau e^{-\alpha(\vec{r})(m\Delta t - \tau)} f_{(1)}(\vec{r}, m\Delta t - \tau) f_{(2)}(\vec{r}, \tau). \quad (3.4.46)$$

The method splits the integral into two, one with the integral limits from time $t = 0$ to time $t = (m - 1)\Delta t$ and an exponential prefactor, and one with the limits from

time $t = (m - 1)\Delta t$ to time $t = m\Delta t$

$$\begin{aligned}
 g(\vec{r}, m\Delta t) &= e^{-\alpha(\vec{r})\Delta t} \underbrace{\int_0^{(m-1)\Delta t} d\tau e^{-\alpha(\vec{r})((m-1)\Delta t - \tau)} f_{(1)}(\vec{r}, (m-1)\Delta t - \tau) f_{(2)}(\vec{r}, \tau)}_{g(\vec{r}, (m-1)\Delta t)} \\
 &+ \int_{(m-1)\Delta t}^{m\Delta t} d\tau e^{-\alpha(\vec{r})(m\Delta t - \tau)} f_{(1)}(\vec{r}, m\Delta t - \tau) f_{(2)}(\vec{r}, \tau) .
 \end{aligned} \tag{3.4.47}$$

The integral in the first term on the right-hand side is equivalent to the initial integral Eq. (3.4.45) form but for the discrete time $t = (m - 1)\Delta t$. Substituting $g((m - 1)\Delta t)$ into Eq. (3.4.47) leads to

$$g(\vec{r}, m\Delta t) = e^{-\alpha(\vec{r})\Delta t} g((m - 1)\Delta t) + \int_{(m-1)\Delta t}^{m\Delta t} d\tau e^{-\alpha(\vec{r})(m\Delta t - \tau)} f_{(1)}(\vec{r}, m\Delta t - \tau) f_{(2)}(\vec{r}, \tau) . \tag{3.4.48}$$

For finite yet sufficiently small time steps Δt , it can be assumed that the function $f_{(2)}(\vec{r}, \tau)$ in the last integral term on the right-hand side of Eq. (3.4.48) is constant. This allows to take $f_{(2)}(\vec{r}, (m - 1)\Delta t)$ outside of the integral. In the next step, we substitute $\alpha = \sigma$, and the functions $f_{(1)}(\vec{r}, t)$ and $f_{(2)}(\vec{r}, t)$ with the corresponding ones in Eq. (3.4.44)

$$f_{(1),\pm,l}(\vec{r}, t) = -\frac{1}{2}\sigma_{(l)}(\vec{r}) \left(1 \pm \frac{\mu}{\epsilon} e^{-(\mu/\epsilon - 1)\sigma_{(l)}(\vec{r})t} \right) , \tag{3.4.49}$$

$$f_{(2),\pm,l}(\vec{r}, t) = \partial_l F_{\pm,l}(\vec{r}, t) . \tag{3.4.50}$$

However, the above recursive convolution applied to Eq. (3.4.43) and Eq. (3.4.44) does not allow to express the term $\mathcal{G}(\vec{r}, t) \star \mathcal{F}(\vec{r}, t)$ in Eq. (3.4.43) as a matrix vector multiplication with an approximated matrix $\mathcal{G}(\vec{r}, t)$ and vector $\mathcal{F}(\vec{r}, t)$.

Nevertheless, it is possible to replace the whole $\mathcal{G}(\vec{r}, t) \star \mathcal{F}(\vec{r}, t)$ term by a 6x6 dimensional matrix, denoted as $\tilde{\mathcal{G}}$

$$\tilde{\mathcal{G}}(\vec{r}, m\Delta t) = i\hbar c_0 \begin{pmatrix} [\tilde{g}_{11}]_{kl}(\vec{r}, m\Delta t) & [\tilde{g}_{12}]_{kl}(\vec{r}, m\Delta t) \\ [\tilde{g}_{21}]_{kl}(\vec{r}, m\Delta t) & [\tilde{g}_{22}]_{kl}(\vec{r}, m\Delta t) \end{pmatrix} . \tag{3.4.51}$$

The matrix $\tilde{\mathcal{G}}(\vec{r}, m\Delta t)$ contains four 3x3 dimensional matrices. All four matrices are labeled by two indices in parentheses, i.e., \tilde{g}_{11} for the first upper left block, \tilde{g}_{12} for the upper right block, \tilde{g}_{21} for the lower left block, and \tilde{g}_{22} for the lower right block. Furthermore, each of these four matrices has three rows labeled by index 'k' and three columns labeled by index 'l'. They are defined recursively and depend on the current $t = m\Delta t$ and the previous time $t' = (m - 1)\Delta t$. With using Eqs. (3.4.44) - (3.4.50),

these recursive matrices are with matrix element labels k and l given by

$$\begin{aligned}
 [\tilde{g}_{11}]_{kl}(\vec{r}, m\Delta t) &= a_k(\vec{r})[\tilde{g}_{11}]_{kl}(\vec{r}, (m-1)\Delta t)\delta_{kl} - b_{+,k}\varepsilon^{qlp}\partial_p F_+(\vec{r}, m\Delta t)\delta_{kq}, \\
 [\tilde{g}_{12}]_{kl}(\vec{r}, m\Delta t) &= a_k(\vec{r})[\tilde{g}_{12}]_{kl}(\vec{r}, (m-1)\Delta t)\delta_{kl} - b_{+,k}\varepsilon^{qlp}\partial_p F_+(\vec{r}, m\Delta t)\delta_{kq}, \\
 [\tilde{g}_{21}]_{kl}(\vec{r}, m\Delta t) &= -a_k(\vec{r})[\tilde{g}_{21}]_{kl}(\vec{r}, (m-1)\Delta t)\delta_{kl} + b_{-,k}\varepsilon^{qlp}\partial_p F_-(\vec{r}, m\Delta t)\delta_{kq}, \\
 [\tilde{g}_{22}]_{kl}(\vec{r}, m\Delta t) &= -a_k(\vec{r})[\tilde{g}_{22}]_{kl}(\vec{r}, (m-1)\Delta t)\delta_{kl} + b_{-,k}\varepsilon^{qlp}\partial_p F_-(\vec{r}, m\Delta t)\delta_{kq}.
 \end{aligned} \tag{3.4.52}$$

The auxiliary variables $a_k(\vec{r})$ and $b_{\pm,k}(\vec{r})$ result from the last line of Eq. (3.4.48) after taking $f_{(2),\pm,k}(\vec{r}, (m-1)\Delta t)$ outside the integral. Hence, the factor $a_k(\vec{r})$ is the exponential function

$$a_k(\vec{r}) = e^{-\sigma_{(k)}(\vec{r})\Delta t}, \tag{3.4.53}$$

and $b_{\pm,k}(\vec{r})$ is the result of the integral

$$\begin{aligned}
 b_{\pm,k}(\vec{r}) &= \int_{(m-1)\Delta t}^{m\Delta t} d\tau e^{-\sigma_{(k)}(\vec{r})((m+1)\Delta t - \tau)} f_{(1),\pm,k}(\vec{r}, (m+1)\Delta t - \tau) \\
 &= \frac{1}{2}e^{-2\sigma_{(k)}(\vec{r})\Delta t} \left(1 - e^{\sigma_{(k)}(\vec{r})\Delta t}\right) \pm \frac{1}{2}e^{-2\frac{\mu}{c}\sigma_{(k)}(\vec{r})\Delta t} \left(1 - e^{\frac{\mu}{c}\sigma_{(k)}(\vec{r})\Delta t}\right).
 \end{aligned} \tag{3.4.54}$$

Collecting all steps, we can express the Maxwell Riemann-Silberstein Hamiltonian \mathcal{H}_{PML} from Eq. (3.4.43) in discretized form

$$\mathcal{H}_{\text{PML}}(\vec{r}, m\Delta t) = \mathcal{H} + \tilde{\mathcal{G}}(\vec{r}, m\Delta t). \tag{3.4.55}$$

With this definition it is then straightforward to insert the above PML expression $\mathcal{H}_{\text{PML}}(\vec{r}, m\Delta t)$ in the Maxwell propagator $\mathcal{U}(t, t_{(0)})$ of the numerical propagation equations in Eq. (5.3.3) or Eq. (5.3.4) to enable the simulation of open Maxwell systems via PML absorption.

In the last step, we have to determine the conductivity $\sigma_{(u)}(\vec{r})$ adequately to get an optimal PML. In FDTD, several useful profiles for the conductivity $\sigma_{(u)}(\vec{r})$ were found and we have chosen for our Riemann-Silberstein PML the FDTD polynomial grading profile which has the form [65]

$$\sigma_{(u)}(\vec{r}) = \begin{cases} \left(\frac{|r_u| - b_u}{L_u - b_u}\right)^q \sigma_{(u),\text{max}} & \text{for } x = u \\ 0 & \text{for } u \end{cases} \tag{3.4.56}$$

with direction index $u \in \{x, y, z\}$ that denotes one component of the position vector \vec{r} , i.e., $r_u = x$ for $u = x$, $r_u = y$ for $u = y$ or $r_u = z$ for $u = z$.

Furthermore, b_u and L_u denote the corresponding boundary dimensions in Fig. 3.1. The last variable $\sigma_{(u),\max}$ for the grading profile is determined by [65]

$$\sigma_{(u),\max} = -\frac{\epsilon(q+1)\ln(R(0))}{2\mu(L_u - b_u)}, \quad (3.4.57)$$

where the tolerated reflection error for normal angle incidence equal to zero can be set manually. The only parameter that we still have to determine is the exponent q in Eq. (3.4.56), which can only be done by a numerical screening.

In the following, we employ a test simulation of the PML with a series of different values for the exponent parameter q to get a proper value for q . Therefore, we use the same simulation setup as described in Sec. (3.3.1) also in MEEP units ($\epsilon = \mu = c = 1$), but select a smaller cubic simulation box with perfectly matched layers and a finite difference order of eight.

The total size of the box depends on the width of the absorbing boundaries since the inner simulation box is in all cases equally sized. Additionally, the grid spacing is always $\Delta x = \Delta y = \Delta z = 0.2$ and the simulation time $\Delta t = 0.1$. We employ a series of runs by using the external current density given in Eq. (3.3.7)

$$\vec{j}_{\text{ext},(4)}(\vec{r}, t) = \vec{j}_{\text{ext},(0)}(\vec{r}) \exp\left(-\frac{(t-10.0)^2}{8}\right) \cos(2.0(t-10.0)). \quad (3.4.58)$$

to compare the impact of the absorbing boundaries. The parameters except q , but including the absorbing width w_{ab} , that we change for each run are shown in Table 3.2.

variable	run 1	run 2	run 3	run 4	run 5	reference run
w_{ab}	0.5	1.0	1.5	2.0	2.5	4.0
L_x	10.5	11.0	11.5	12.0	12.5	54.0
L_y	10.5	11.0	11.5	12.0	12.5	54.0
L_z	10.5	11.0	11.5	12.0	12.5	54.0
b_x	10.0	10.0	10.0	10.0	10.0	50.0
b_y	10.0	10.0	10.0	10.0	10.0	50.0
b_z	10.0	10.0	10.0	10.0	10.0	50.0
$\Delta x, \Delta y, \Delta z$	0.2	0.2	0.2	0.2	0.2	0.2
finite difference order	8	8	8	8	8	8
exponential order	4	4	4	4	4	4
Δt	0.1	0.1	0.1	0.1	0.1	0.1
ϵ	1	1	1	1	1	1
μ	1	1	1	1	1	1
c	1	1	1	1	1	1

Table 3.2: Physical and simulation parameters of external current simulation for screening the parameters of the PML absorbing boundaries.

To evaluate the quality of the absorbing boundary, we apply a reference run with a box that is chosen so large ($L_x = L_y = L_z = 54.0$) that boundary effects do not arise. In the following the index i denotes the run number referring to Table 3.2, except the reference which denoted by an "ref" index.

First, we take a look at the energy inside the box. Since we know that the external current causes an electromagnetic wave that leaves the box, the electromagnetic energy should fall to zero when the wave reaches the boundaries. Therefore, we plot the quotient of the box energies $\langle E(t) \rangle$ at time $t_{(1)} = 14.7$ and $t_{(2)} = 40.0$ using Eq. (1.1.81) with the inner box limits

$$C_E = \frac{|\langle E_{(i)}(t_{(2)}) \rangle|}{|\langle E_{(i)}(t_{(1)}) \rangle|}. \quad (3.4.59)$$

According to Figure 3.5, time $t_{(1)}$ corresponds to the maximum box energy. Additionally, we evaluate the reflection coefficient based on the electric field at two grid points $\vec{r}_{(1)} = (8, 0, 0)$ and $\vec{r}_{(2)} = (8, 8, 0)$. In our case, we calculate the reflection coefficient via the energy density $u(t)$ using Eq. (1.1.79) at the corresponding point $\vec{r}_{(1)}$ respectively $\vec{r}_{(2)}$ and the reflection coefficient given by

$$R = \frac{\max |u_{(i)}(t) - u_{\text{ref}}(t)|}{\max |u_{\text{ref}}(t)|} \quad (3.4.60)$$

for the corresponding grid point and a maximum time of $t = 40.0$. Both variables, C_E and R , depending on the PML exponent parameter q is shown in Figure 3.13.

The impact of the PML does not simply increase with the width of the absorbing boundaries. The exponential factor q is more relevant for the absorbing efficiency. According to our five runs, the optimal setting for q is between two and three, and the width of the PML region or equivalently the number of grid points along the axis ($w_{\text{ab}}/\Delta x$, $w_{\text{ab}}/\Delta y$, $w_{\text{ab}}/\Delta z$) should be larger than seven.

3.4.3 Comparison of absorbing mask and perfectly matched layer boundaries

In this section, we compare the two different absorbing boundary schemes, the absorbing mask boundary and the perfectly matched layer. For this reason, we use the same simulation setup as for finding the optimal parameters for the PML in Sec. 3.4.2. Again, we simulate five runs plus one reference run for each absorbing scheme using the parameters given in Table 3.2 and calculate the energy coefficient C_E of Eq. (3.4.59) and reflection coefficient R of Eq. (3.4.59).

Besides the width of the absorbing mask, there is no other characteristic parameter. For the PML we select for the comparison the parameter $q = 2$, which corresponds to the minimum reflection effects according to Figure 3.13.

The comparison of C_E and R for both absorbing methods as function of the absorbing boundary width w_{ab} is illustrated in Figure 3.14. It reveals that in case of the absorbing mask an increasing boundary width does not improve significantly the

Relative reflection error of the perfectly matched layer

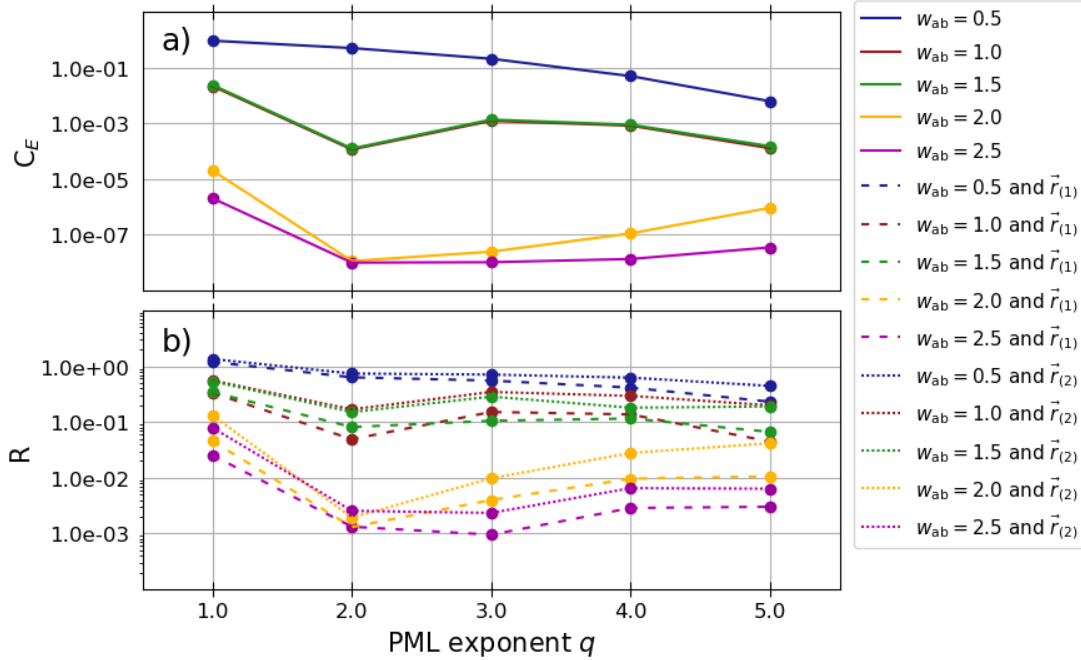


Figure 3.13: Relative variation of the energy and the electric field at two points for different parameters q . Panel a) shows the quotient of the Maxwell energy inside the box at time $t_{(2)} = 40.0$, when the energy should be approximately zero, and time $t_{(1)} = 14.7$, when the box energy reaches its maximum. Additionally, panel 2) gives the reflection coefficients at point $\vec{r}_{(1)}$ and $\vec{r}_{(2)}$.

result. The C_E -Factor stays almost constant, and the reflection constant R decreases slightly. In contrast, the PML absorbing improves all absorbing features for larger w_{ab} and becomes significantly better than the mask method. Only if the width w_{ab} is rather small, this behavior reverses.

3.4.4 Incident plane waves boundaries

Very common experimental setups to examine optical properties are based on disturbing a molecular system with various kinds of external electromagnetic pulses. In most cases, the used light pulse has a mathematically closed description and can be evolved in time analytically. For this situation, it is not necessary to chose such a large Maxwell simulation box so that the external light signal is completely inside the box. In addition, some analytical waves, i.g. plane waves, are in in principle only terminated parallel to their wavevector \vec{k} , but conceptually constant in space and periodic in time in the direction perpendicular to \vec{k} .

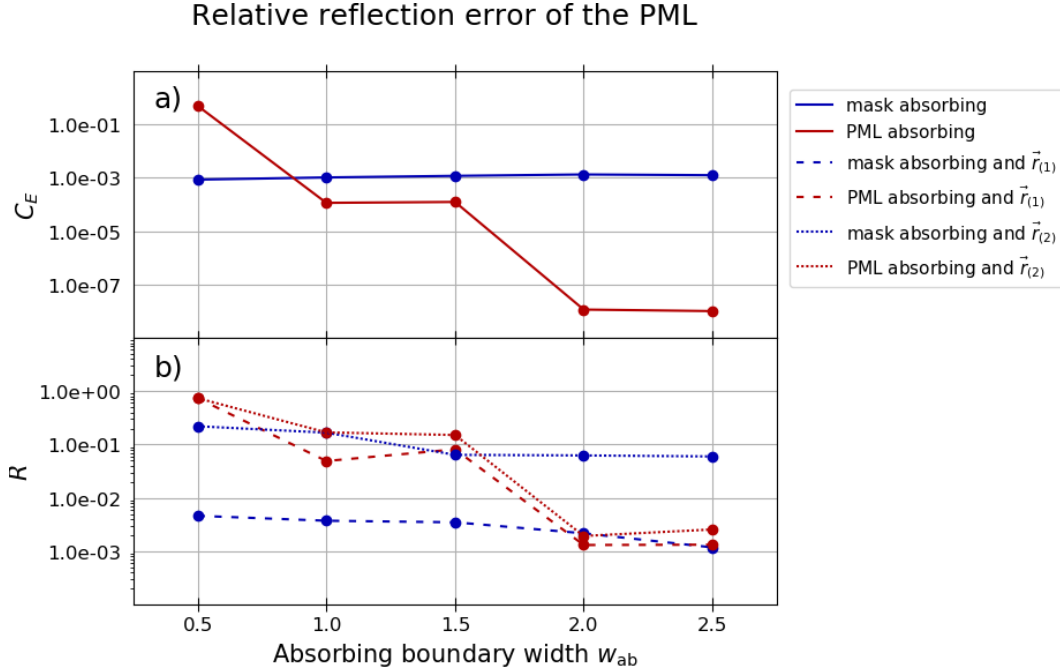


Figure 3.14: Comparison of absorbing mask and perfectly matched layer boundary conditions. Similar to Figure 3.13, the energy quotient of the box energy at $t_{(2)} = 40.0$ divided by the box energy at time $t_{(1)} = 14.7$ is plotted in panel a), and the reflection coefficients at $\vec{r}_{(1)}$ and $\vec{r}_{(2)}$ in panel b).

A convenient method to simulate such waves in the Maxwell simulation box can be obtained by using a boundary region as a frame where the grid point values are calculated via their analytical formula.

Figure 3.15 illustrates in a 2D cut the analytically calculated outer frame around the simulation box and a Gaussian shaped plane wave propagates parallel to the corresponding wavevector \vec{k} . All grid points which are inside the green frame boundary region are set by the analytical values of the plane wave function at the respective points. The number of necessary boundary grid points in each dimension is coupled to the given accuracy order of the spatial derivative operator. It is not sufficient to set only the points next to the box border, since we also have to take care of the discrete derivative operator and the corresponding stencil.

The two-dimensional stencil in Figure 3.2 shows that the spatial derivative of accuracy order n at the grid point $x_{(i),(j)}$ is determined by the point values of $x_{(i-n),(j)}, \dots, x_{(i+n),(j)}$ and $x_{(i),(j-n)}, \dots, x_{(i),(j+n)}$. Therefore, the width of the plane wave region has to be chosen, such that it contains n points in each direction.

A single analytical wave with wave vector \vec{k} and corresponding frequency ω can be expressed in terms of the six-component Riemann-Silberstein vector $\mathcal{F}(\vec{r}, t)$ that de-

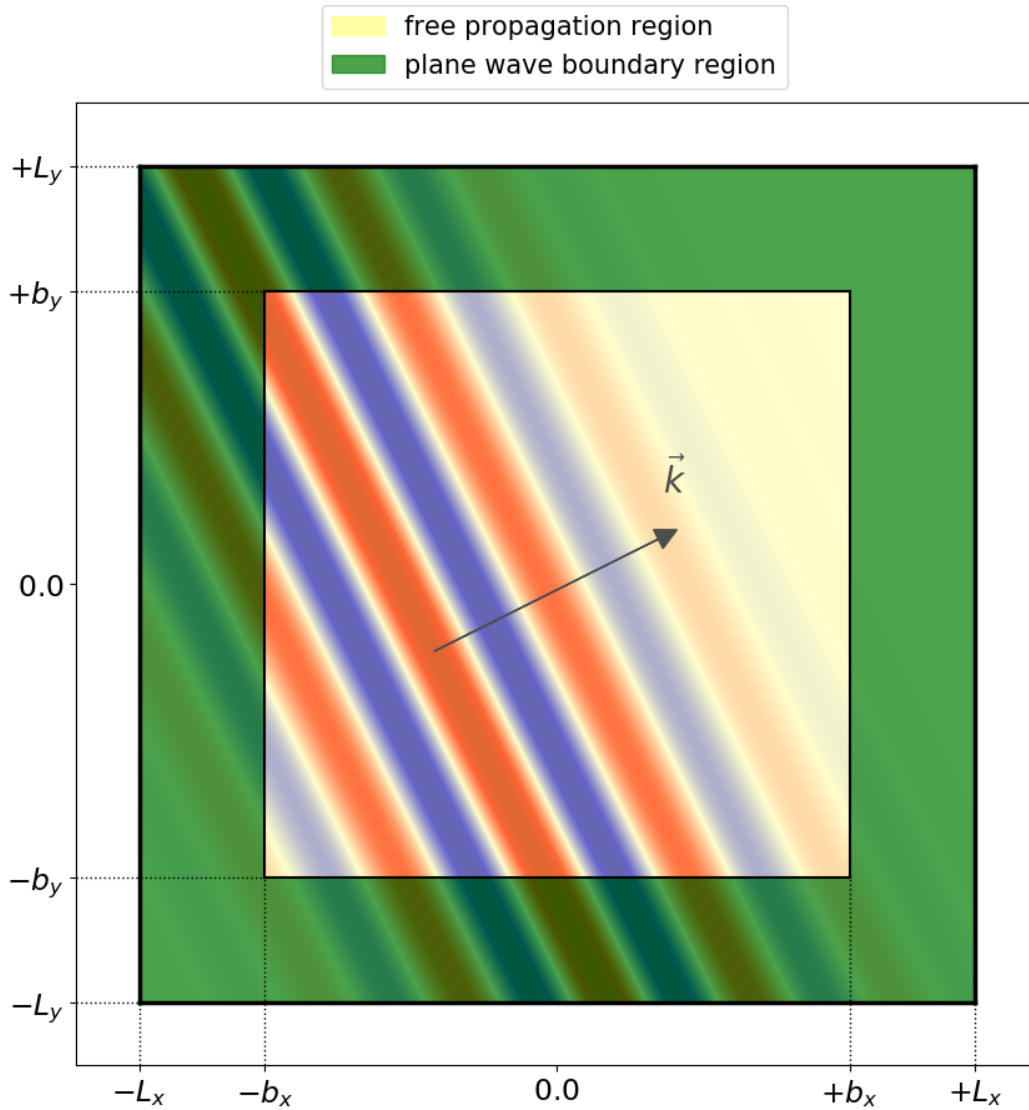


Figure 3.15: The green analytical waves region in this two-dimensional cut surrounds the free Maxwell propagation area to simulate incident waves and their propagation through the simulation box. The simulation box dimensions are denoted as L_x and L_y , and the inner free propagation box dimensions are b_x and b_y . The boundary width is determined by the size of the finite difference grid stencil. The figure shows schematically a Gaussian wave with wavevector \vec{k} propagating through the simulation box.

depends on the scalar propagation relation $(-\vec{k} \cdot \vec{r} - \omega t)$. In general, an arbitrary shaped analytical wave can be obtained by a superposition of different linear independent waves with

$$\mathcal{F}_{\text{pw}}(\vec{r}, t) = \sum_i \mathcal{F}_{\text{pw},(i)}(\vec{r}) \exp\left(i(\vec{k}_{(i)} \vec{r} - \omega_{(i)} t)\right), \quad (3.4.61)$$

where the i^{th} wave is represented by its wavevector $\vec{k}_{(i)}$ and frequency $\omega_{(i)}$ and by a Riemann-Silberstein vector $\mathcal{F}_{\text{pw},(i)}$ as initial vector.

In the following, we illustrate as example a simulation of two Gaussian light pulses, which enter the simulation box, interfere and leave the box. Specifically, we select the two electric field functions

$$\begin{aligned} \vec{E}_{\text{pw},(1)}(\vec{r}_{(1)}, t) = \\ E_{(1),(0),z} \vec{e}_z \cos\left(\vec{k}_{(1)} \cdot (\vec{r}_{(1)} - \vec{r}_{(1),(0)}) - c_0 |\vec{k}_{(1)}| t\right) \exp\left(-\frac{(\vec{r}_{(1)} - \vec{r}_{(1),(0)} - c_0 |\vec{k}_{(1)}| t)^2}{2w_{(1)}^2}\right), \end{aligned} \quad (3.4.62)$$

$$\begin{aligned} \vec{E}_{\text{pw},(2)}(\vec{r}_{(2)}, t) = \\ E_{(2),(0),z} \vec{e}_z \cos\left(\vec{k}_{(2)} \cdot (\vec{r}_{(2)} - \vec{r}_{(2),(0)}) - c_0 |\vec{k}_{(2)}| t\right) \exp\left(-\frac{(\vec{r}_{(2)} - \vec{r}_{(2),(0)} - c_0 |\vec{k}_{(2)}| t)^2}{2w_{(2)}^2}\right), \end{aligned} \quad (3.4.63)$$

with electric field amplitudes $E_{(0),(1),z}$ and $E_{(0),(2),z}$ and unit vector \vec{e}_z in z-direction. Both electric fields have only a polarization along the z-direction and the corresponding wavevectors

$$\vec{k}_{(1)} = \frac{\sqrt{2}}{2} \begin{pmatrix} 1 \\ -1 \\ 0 \end{pmatrix}, \quad \vec{k}_{(2)} = \frac{1}{2\sqrt{5}} \begin{pmatrix} -2 \\ -1 \\ 0 \end{pmatrix}. \quad (3.4.64)$$

with corresponding frequencies $\omega_1 = c_0 |\vec{k}_{(1)}|$ and $\omega_2 = c_0 |\vec{k}_{(2)}|$. They are shifted by the vectors $\vec{r}_{(1),(0)}$ and $\vec{r}_{(2),(0)}$ with

$$\vec{r}_{(1),(0)} = 25.0 \frac{\sqrt{2}}{2} \begin{pmatrix} -1 \\ 1 \\ 0 \end{pmatrix}, \quad \vec{r}_{(2),(0)} = 25.0 \frac{1}{\sqrt{5}} \begin{pmatrix} -2 \\ 1 \\ 0 \end{pmatrix}. \quad (3.4.65)$$

The Gaussian width for the first one is $w_{(1)} = 4.0$, the second one $w_{(2)} = 6.0$, and the field amplitudes are given by $E_{(0),(1),z} = 0.5$ and $E_{(0),(2),z} = 0.5$. The laser pulses propagate perpendicular to their wavevectors and since the electric-field polarization is oriented along the z-axis the corresponding magnetic fields have the form

$$\begin{aligned} \vec{B}_{\text{pw},(1)}(\vec{r}_{(1)}, t) = \\ \frac{E_{(1),(0),z}}{c_0} \vec{b}_{(1)} \cos\left(\vec{k}_{(1)} \cdot (\vec{r}_{(1)} - \vec{r}_{(1),(0)}) - c_0 |\vec{k}_{(1)}| t\right) \exp\left(-\frac{(\vec{r}_{(1)} - \vec{r}_{(1),(0)} - c_0 |\vec{k}_{(1)}| t)^2}{2w_{(1)}^2}\right), \end{aligned} \quad (3.4.66)$$

$$\vec{B}_{\text{pw},(2)}(\vec{r}_{(2)}, t) = \frac{E_{(2),(0),z}}{c_0} \vec{b}_{(2)} \cos\left(\vec{k}_{(2)} \cdot (\vec{r}_{(2)} - \vec{r}_{(2),(0)}) - c_0 |\vec{k}_{(2)}| t\right) \exp\left(-\frac{(\vec{r}_{(2)} - \vec{r}_{(2),(0)}) \cdot c_0 \vec{k}_{(2)} |t|}{2w_{(2)}^2}\right), \quad (3.4.67)$$

$$\vec{b}_{(1)} = \frac{1}{\sqrt{2}} \begin{pmatrix} -1 \\ -1 \\ 0 \end{pmatrix}, \quad \vec{b}_{(2)} = \frac{1}{\sqrt{5}} \begin{pmatrix} -1 \\ 2 \\ 0 \end{pmatrix}. \quad (3.4.68)$$

Using the electric and magnetic fields in Eqs. (3.4.62) - (3.4.63) and Eqs. (3.4.66) - (3.4.67), we can build the underlying Riemann-Silberstein vector $\mathcal{F}_{\text{pw}}(\vec{r}, t)$ for the superposition of the waves according to

$$\mathcal{F}_{\text{pw}}(\vec{r}, t) = \left(\begin{array}{l} \sqrt{\frac{\epsilon_0}{2}} \left(\vec{E}_{\text{pw},(1)}(\vec{r}, t) + \vec{E}_{\text{pw},(2)}(\vec{r}, t) \right) + i\sqrt{\frac{1}{2\mu_0}} \left(\vec{B}_{\text{pw},(1)}(\vec{r}, t) + \vec{B}_{\text{pw},(2)}(\vec{r}, t) \right) \\ \sqrt{\frac{\epsilon_0}{2}} \left(\vec{E}_{\text{pw},(1)}(\vec{r}, t) + \vec{E}_{\text{pw},(2)}(\vec{r}, t) \right) - i\sqrt{\frac{1}{2\mu_0}} \left(\vec{B}_{\text{pw},(1)}(\vec{r}, t) + \vec{B}_{\text{pw},(2)}(\vec{r}, t) \right) \end{array} \right). \quad (3.4.69)$$

This equation determines all Riemann-Silberstein values inside the plane waves boundaries region.

The remaining values inside the free propagation region are calculated by the homogeneous time-evolution Eq. (2.1.16), since we only consider a propagation in vacuum. As before, we use $\epsilon_0 = \mu_0 = c_0 = 1$ for the electromagnetic constants. The simulation box limits are $L_x = L_y = L_z = 10.0$ with spacing $\Delta x = \Delta y = \Delta z = 0.25$. We select a finite difference order of $n = 8$ and since the width w_{pw} of the plane waves boundaries are coupled to this order with $w_{\text{pw}} = n\Delta x = n\Delta y = n\Delta z$, the plane waves boundaries limits are given by $b_x = b_y = b_z = 8$. All simulation parameters are given in Table 3.3.

variable	MEEP units	variable	MEEP units
L_x	10.0	$k_{(1),x}$	0.707
L_y	10.0	$k_{(1),y}$	-0.707
L_z	10.0	$k_{(1),z}$	0.000
$\Delta x, \Delta y, \Delta z$	0.25	$E_{(1)(0),z}$	0.500
finite difference order	8	$w_{(1)}$	4.000
exponential order	4	$k_{(2),x}$	-0.447
Δt	0.144	$k_{(2),y}$	-0.223
ϵ_0	1	$k_{(2),z}$	0.000
μ_0	1	$E_{(2),(0),z}$	0.500
c_0	1	$w_{(2)}$	6.000

Table 3.3: Simulation parameters for the incident plane waves run with two interfering incident waves.

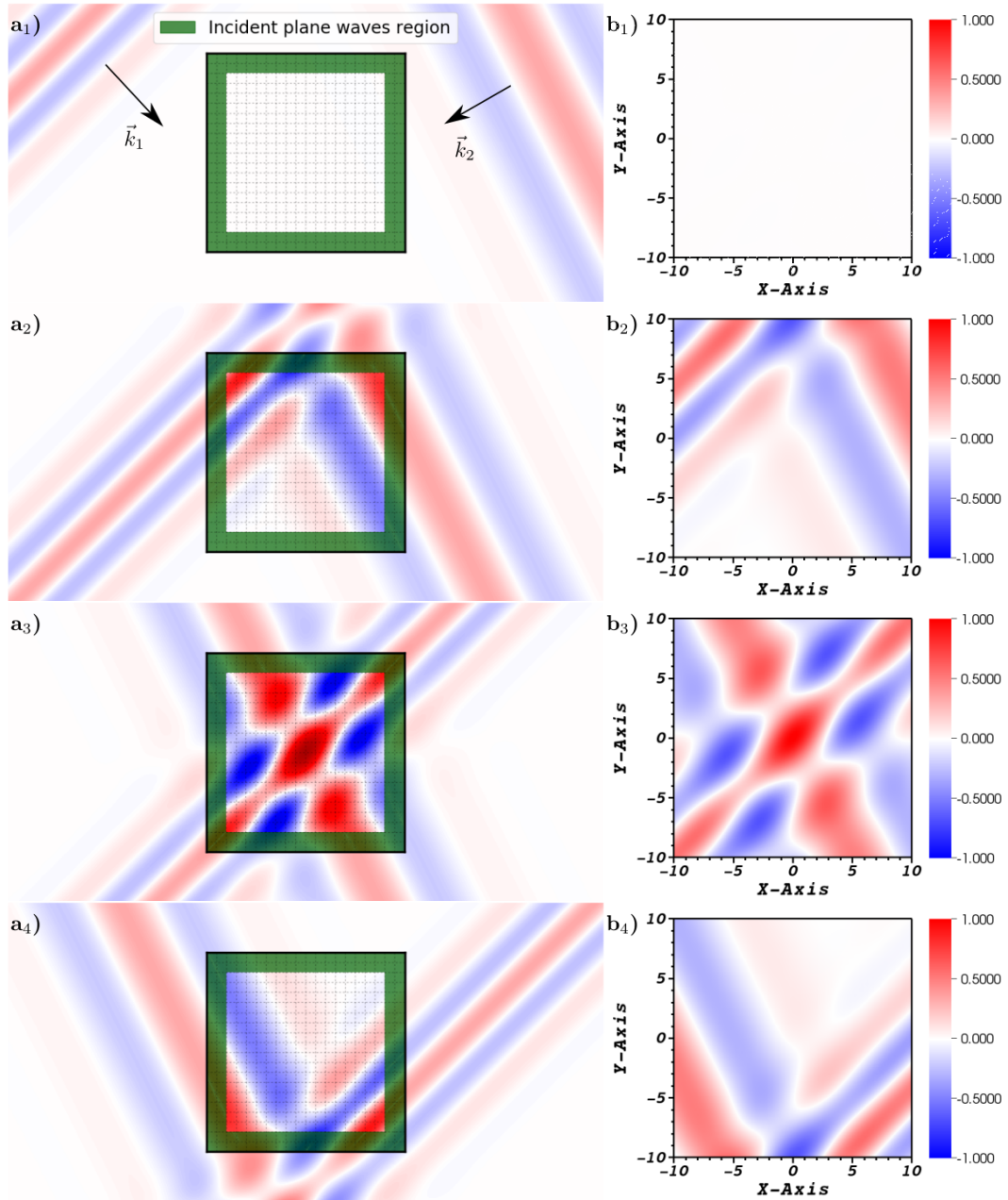


Figure 3.16: Incident plane waves simulation of two interfering plane waves. The panels a₁) - a₄) illustrate the box simulation scheme with the incident plane wave boundaries in green and the two Gaussian signals, which propagate into the direction of the box. On the right-hand side, denoted by b₁) - b₄), we show the two-dimensional cut of the simulation results. The four screenshots show relevant points in time, e.g., the two signals enter the box in a₂), b₂), their maximum interference in the middle of the box a₃), b₃), and when they leave the box again in a₄), b₄).

Two-dimensional snapshots of the electric field in z-direction in the xy-plane are illustrated in Figure 3.16. All panels denoted on the right-hand side of that figure, give the schematic setup of the simulation with a corresponding analytical calculation. The cut through the cubic simulation box is surrounded by the incident plane waves boundaries in green. In other words, the simulation box represents only a small section of the total environment and the boundaries ensure that the plane waves arise and propagate correctly through the box.

The figures $b_1)$ - $b_4)$ on the right-hand side show a cut through the simulation box which corresponds to the section in $a_1)$ - $a_4)$. In contrast to the left-hand side, the given contour shows the simulation output calculated by Octopus.

In $a_1)$ and $b_1)$, we display the initial Gaussian pulses at time $t_{(0)} = 0$. Since the significant signal amplitudes are located outside the simulation box, the Riemann-Silberstein vector inside the box and on the plane waves frame is almost zero.

After several time steps at time $t_{(1)} = 10.0$, in $a_2)$ and $b_2)$, the two Maxwell plane waves hit the simulation box. The plane waves region with the predetermined analytical values based on the given initial Maxwell plane waves ensure that the two electromagnetic signals arise at the border of the simulation box, when the significant signal amplitude reaches the box limits. The two plane waves propagate through the inner simulation region and start to interfere.

While one plane wave propagates from the upper left to the lower right side, and the other one in the opposite direction from the upper left to the lower right, the interference pattern moves from the upper to the lower box boundary. At the time $t_{(2)} = 25.0$, shown in $a_3)$ and $b_3)$, the electric field reaches a maximum of the two interfered plane waves, which is in the middle of the simulation box. Due to the linearity of Maxwell's equations, the two plane waves continue their propagation independently.

Finally, in $a_4)$ and $b_4)$, at time $t_{(3)} = 35.0$, both Maxwell plane waves passed the simulation box and are outside again, but contrary to the initial state in $a_1)$ and $b_1)$. The first Gaussian plane wave pulse with higher carrier frequency reached the lower right side and whereas the second Gaussian plane wave pulse with lower carrier frequency is in the lower left side. Without any Maxwell-matter coupling, the Maxwell fields return to zero inside the simulation box.

Comparing both cases, the analytical plotted figures ($a_1)$, $a_2)$, $a_3)$, $a_4)$) and the numerically calculated ones ($b_1)$, $b_2)$, $b_3)$, $b_4)$) show, that both propagation results agree very well. In the next section, we compare more quantitatively the difference and error between the exact analytical and numerical propagation of plane waves.

3.4.5 Numerical dispersion for plane waves propagation

In this section we evaluate our Riemann-Silberstein Maxwell-propagation method by benchmarking the numerical propagation with analytical wave solutions. As a simulation setup, we chose a Maxwell simulation box with incident plane waves boundaries where a Gaussian shaped wave is shifted outside the box and propagates

through the simulation box over time similar to Sec. 3.4.4. It can be assumed that the error between the numerical and exact propagation depends on the wavelength of the plane wave.

To get systematic results, we simulate a batch of different wavelengths λ for the Gaussian plane wave where we also couple the Gaussian width to the wavelength. The wavevector is set parallel to the x-axis and the polarization direction of the wave is chosen along the z-axis.

The analytical formula for the Gaussian plane wave electric field $\vec{E}_{\text{pw}}(\vec{r}, t)$ takes the form

$$\vec{E}_{\text{pw}}(\vec{r}, \vec{r}_{(0)}, t) = \vec{e}_z \exp\left(\frac{(x-x_{(0)})^2}{2\lambda^2}\right) \cos(2\pi/\lambda(x - x_{(0)}) - \omega t), \quad (3.4.70)$$

with corresponding magnetic field

$$\vec{B}_{\text{pw}}(\vec{r}, t) = -\vec{e}_y \frac{1}{c_0} \vec{E}_{\text{pw}}(\vec{r}, t), \quad (3.4.71)$$

which leads to the plane wave Riemann-Silberstein six-vector $\mathcal{F}_{\text{pw}}(\vec{r}, t)$

$$\mathcal{F}_{\text{pw}}(\vec{r}, t) = \begin{pmatrix} \sqrt{\frac{\epsilon_0}{2}} \vec{E}_{\text{pw}}(\vec{r}, t) + i\sqrt{\frac{1}{2\mu_0}} \vec{B}_{\text{pw}}(\vec{r}, t) \\ \sqrt{\frac{\epsilon_0}{2}} \vec{E}_{\text{pw}}(\vec{r}, t) - i\sqrt{\frac{1}{2\mu_0}} \vec{B}_{\text{pw}}(\vec{r}, t) \end{pmatrix}. \quad (3.4.72)$$

The shift parameter $x_{(0)}$ is set such that the Gaussian amplitude $\exp\left(\frac{(x-x_{(0)})^2}{2\lambda^2}\right)$ is lower than $1e^{-6}$ inside the whole simulation box. Consequently, we get two distinguished times, the first one t_{start} represents the time, where the Gaussian amplitude at the origin is lower than $1e^{-6}$ before the light pulse passes the box and in turn t_{end} gives the time, when the whole Gaussian amplitude is again lower than $1e^{-6}$ inside the box after the light pulse propagation. The outer dimensions of the parallelepiped simulation box is 35.0 in x-direction and 10 in y- and z-direction.

In addition to the wave length dependency for the numerical Riemann-Silberstein propagator, we examine the differences of our Maxwell simulation for two different grid spacings and four different finite difference orders for the spatial first derivative operation. Therefore, we perform a series of runs with different selected wavelengths. The wavelength with corresponding run number can be found in Table 3.5.

Since we evaluate the quality of the plane wave propagation we have to find a scalar variable that represent the variation between the exact analytical propagation and our numerical simulation. In a first step we have to take into account, that the wavelength dependency of Eq. (3.4.70) scales the length and time of the signal. Therefore, we map each Gaussian plane wave pulse to normalized times with $t_{\text{start}} \rightarrow 0$ and $t_{\text{end}} \rightarrow 1$. Consequently, each Gaussian pulse has the same shape and temporal scale.

variable	MEEP units
L_x	10.0
L_y	10.0
L_z	10.0
exponential order	4
Δt	0.144
ϵ_0	1
μ_0	1
c_0	1

Table 3.4: Simulation box and time parameters for the numerical dispersion run with an incident wave pulse.

run number	1	2	3	4	5	6	7	8	9
wavelength λ	1.0	2.0	3.0	4.0	5.0	10.0	15.0	20.0	25.0

run number	10	11	12	13	14	15	16	17
wavelength λ	30.0	35.0	40.0	45.0	50.0	100.0	500.0	1000.0

Table 3.5: Simulation box and time parameters for the numerical dispersion run with an incident wave pulse.

After that, we take the simulated and mapped Riemann-Silberstein vector $\mathcal{F}_{\text{map}}(\vec{r}, t, \lambda_{(i)})$ and the analytically calculated and mapped Riemann-Silberstein vector $\mathcal{F}_{\text{pw, map}}(\vec{r}, t, \lambda_{(i)})$ of run i and define the integral

$$var_{(i)} = \int_0^1 dt \sqrt{\left(\mathcal{F}_{\text{map}}(\vec{r}_0, t, \lambda_{(i)}) - \mathcal{F}_{\text{pw, map}}(\vec{r}_0, t, \lambda_{(i)}) \right)^2} \quad (3.4.73)$$

where \vec{r}_0 denotes the origin of the simulation box. The variance $var_{(i)}$ characterizes the numerical dispersion relation, which means it determines the error between the exact analytical and the calculated light pulse propagation since it depends on the wavelength λ .

In Figure 3.17 we plot in log-log scale the variance $var_{(i)}$ for all considered wavelengths from Table 3.5 and different finite difference orders and grid spacings. The plot reveals that the variance is rather significant for small wavelengths. This corresponds to the general feature of numerical grids that the resolution of waves are of low quality when the wavelength is near the same magnitude as the grid spacing. Therefore, the variance decreases for increasing wavelength and in most cases, a finer grid spacing leads to a smaller variance. Whereas the log-log graph of the 0.25 grid spacing shows a linear decrease, the variances for the 0.5 grid spacing increases for wavelengths larger than 50.0.

3.4.6 Incident waves boundaries plus absorbing boundaries

The incident waves boundaries simulate a signal that enters the simulation box. In contrast, the perfectly matched layer damps all outgoing electromagnetic fields. For our purpose, we want to combine both boundary condition.

We know, due to the analytical behavior of the incident waves, the incoming fields for all times. In addition, the outgoing electromagnetic signals should not cause any reflection at the boundaries. In the previous section, we have seen how the PML looks like only for the absorbing boundary condition. Hence, since we know how the undisturbed waves pass the simulation box, we can subtract the waves in the entire simulation box from the total disturbed field and apply the PML.

For proper incident waves with absorbing boundaries, we split the boundary region into two regions, one outer region for the incident waves frame, and an inner one for the PML as it is shown in figure FIG. (3.18). The limits of the inner boundary region are still represented by b_x, b_y, b_z , the outer boundaries are denoted by a_x, a_y, a_z and are located between the inner boundary region and the total box limits L_x, L_y, L_z .

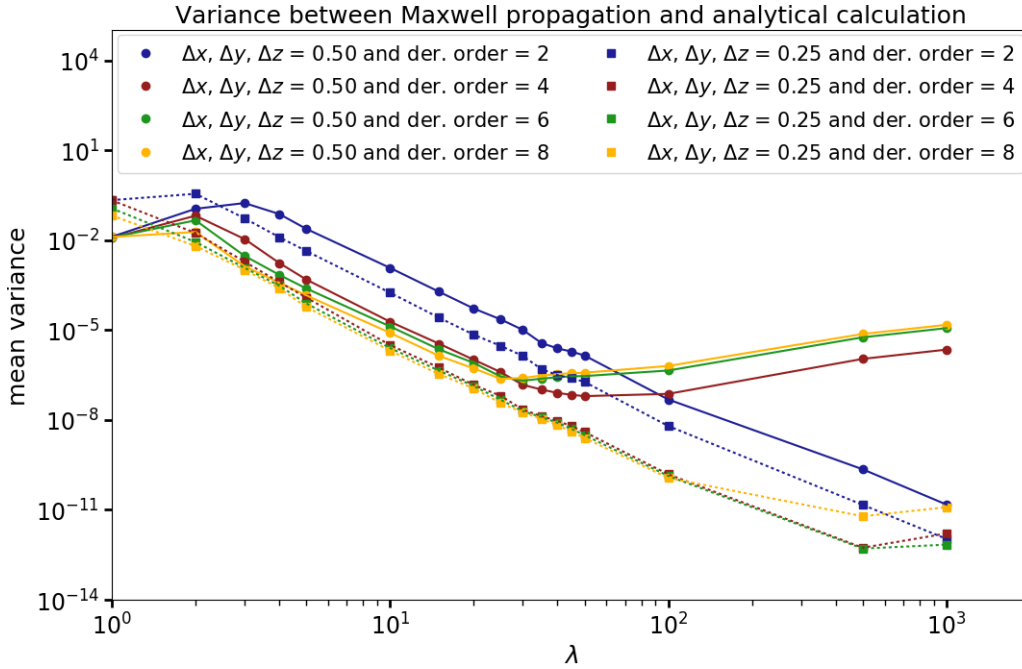


Figure 3.17: The graph of the numerical dispersion shows that the numerical accuracy depends on the wavelength of the propagated plane waves. Except the three graphs for grid spacing 0.5 and higher derivative accuracy order of $n = 2$, the accuracy of the free Maxwell plane wave propagation increases approximately linearly with the wavelength dispersion on a log-log scale. The excepted three graphs feature a knee around $\lambda = 25.0$ where the accuracy begins to decrease for higher wavelengths.

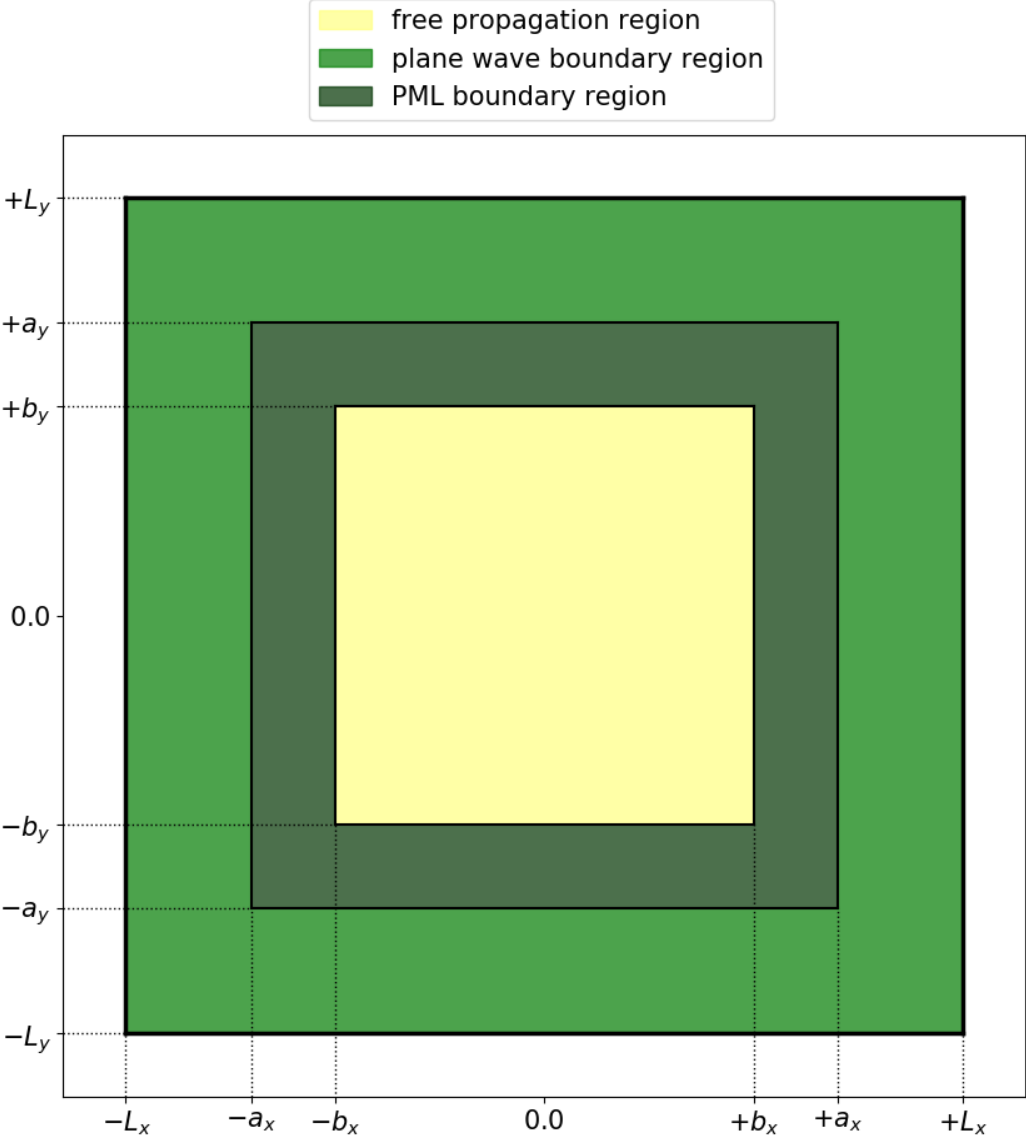


Figure 3.18: In the 2-dimensional cut of the simulation box with total dimensions L_x , and L_y , the boundary region is split into two subareas with analytical waves and PML boundary conditions. The outer boundaries with the limits L_x , b_x , and L_y , b_y are the analytical waves boundaries, whereas the inner boundaries determined by a_x , b_x , and a_y , b_y belong to the PML region.

Now, a combined waves plus PML step applies first a subtraction of the undisturbed waves. After that the PML acts on the remaining field. As a last step, the undisturbed waves are added again to the field.

We note, that there are two options to get the values of the incident waves which have to be subtracted. First, one can use simply the analytical values of the waves for the current time step. The second option requires a second auxiliary propagation which has to be performed concurrently with the full system propagation. In this case, the unperturbed wave propagation is calculated by the discretized Maxwell time-evolution operator.

This method avoids numerical reflection artefacts at the boundary due to the fact, that there is always a numerical error between the analytical waves and the numerically simulated ones.

3.5 Riemann-Silberstein Maxwell propagation for linear media

After introducing in the previous sections electromagnetic simulations based on the microscopic Maxwell's equations, we demonstrate in this section our implementation for electromagnetic field propagations in the presence of a linear medium. As set up we consider a laser pulse in vacuum that hits a simulation box which contains a linear medium which scatters the light pulse.

To describe the incident laser pulse, we take a simulation box with incident plane waves boundaries to propagate the light pulse starting outside the box and entering at the boundaries. Since we simulate an open system, we have to absorb the scattered light by the combined incident plane waves boundaries plus perfectly matched layer, which we introduced in Sec. 3.4.6.

A two-dimensional cut through the simulation box with corresponding relevant coordinates can be seen in Figure 3.19. The simulation box is similar to Figure 3.18, but in addition we include the perpendicular medium box centered at the origin. The corresponding box dimensions are determined by $l_{\text{lm},x}$, $l_{\text{lm},y}$, $l_{\text{lm},z}$, which is half of the box length in each direction. The medium box size parameters for the simulations that we present in the following are $l_{\text{lm},x} = l_{\text{lm},y} = l_{\text{lm},z} = 5.0$ and the total simulation box sizes are given by $L_x = L_y = L_z = 20.0$ with the grid spacing $\Delta x = \Delta y = \Delta z = 0.1$.

To obtain a high quality of electromagnetic field absorption at the boundaries, we chose an absorbing boundary width $w_{\text{ab}} = 4.2$. Furthermore, taking a derivative order of eight for the finite difference operation leads with the selected grid spacing to a width $w_{\text{pw}} = 0.8$. Hence, the total boundary width becomes $w_{\text{b}} = w_{\text{ab}} + w_{\text{pw}} = 5.0$ and the inner free simulation box area dimensions are $b_x = b_y = b_z = 15.0$.

Inside the medium box, the electric permittivity ϵ_{lm} and the magnetic permeability μ_{lm} differ from the vacuum constants ϵ_0 , μ_0 . We keep the electromagnetic

constants equal to one ($\epsilon_0 = \mu_0 = c_0 = 1$) as before in the previous sections and chose the corresponding medium values $\epsilon_{\text{lm}} = \mu_{\text{lm}} = 2.0$, and $c_{\text{lm}} = 0.5$. All necessary box and medium parameters are listed in Table 3.6 on the left-hand side.

The external laser pulse is given by the incident waves Eq. (3.4.61) parallel to the x-axis. Instead of a Gaussian shaped pulse like in Sec. 3.4.6, we select a cosinusoidally shaped pulse, which is given in closed form by

$$\vec{E}_{\text{pw}}(\vec{r}, t) = \vec{e}_z E_{(0),z} \cos\left(k_x(x - x_{(0)}) - \frac{2\pi}{\lambda} t\right) \cos\left(\frac{\pi(x - 2\xi - x_{(0)} - c_0 t)}{2\xi} + \pi\right) \theta\left(\xi - \frac{|k_x(x - x_{(0)}) - \frac{2\pi}{\lambda} t|}{|k_x|}\right) \quad (3.5.1)$$

and determines the electric field. The arising $\theta(x)$ denotes the usual Heaviside theta function. The wavevector \vec{k} has only a k_x component, the light pulse is shifted by $x_{(0)}$, and the pulse shift is determined by its characteristic width parameter ξ .

The orthogonal condition between electric field, magnetic field and electromagnetic wave yields for the magnetic field

$$\vec{B}_{\text{pw}}(\vec{r}, t) = -\vec{e}_y \frac{1}{c_0} \vec{E}_{\text{pw}}(\vec{r}, t). \quad (3.5.2)$$

Therefore the plane waves six-component Riemann-Silberstein vector $\mathcal{F}_{\text{pw}}(\vec{r}, t)$ takes the form

$$\mathcal{F}_{\text{pw}}(\vec{r}, t) = \begin{pmatrix} \sqrt{\frac{\epsilon_0}{2}} \vec{E}_{\text{pw}}(\vec{r}, t) + i\sqrt{\frac{1}{2\mu_0}} \vec{B}_{\text{pw}}(\vec{r}, t) \\ \sqrt{\frac{\epsilon_0}{2}} \vec{E}_{\text{pw}}(\vec{r}, t) - i\sqrt{\frac{1}{2\mu_0}} \vec{B}_{\text{pw}}(\vec{r}, t) \end{pmatrix}. \quad (3.5.3)$$

The corresponding laser parameters together with the medium parameters can be taken from the right-hand side of Table 3.6.

In case of an electromagnetic propagation with a linear medium, the underlying Maxwell's equations in Riemann-Silberstein representation are given by Eq. (1.2.37). Since we have no external current density, they take here the simpler form

$$i\hbar \frac{\partial}{\partial t} \mathcal{F}(\vec{r}, t) = \mathcal{H}_{\text{lm}}(\vec{r}, t) \mathcal{F}(\vec{r}, t), \quad (3.5.4)$$

where $\mathcal{H}_{\text{lm}}(\vec{r}, t)$ of Eq. (1.2.38) gives

$$\mathcal{H}_{\text{lm}}(\vec{r}, t) = \mathcal{H}_{\text{lm},(0)}(\vec{r}, t) + \mathcal{K}_{\text{lm}}(\vec{r}, t), \quad (3.5.5)$$

with

$$\mathcal{H}_{\text{lm},(0)}(\vec{r}, t) = \begin{pmatrix} 1 & 0 \\ 0 & 1 \end{pmatrix}_{2 \times 2} \otimes \left(-i\hbar c(\vec{r}, t) \vec{\nabla} \cdot \vec{\mathbf{S}} \right)_{3 \times 3}. \quad (3.5.6)$$

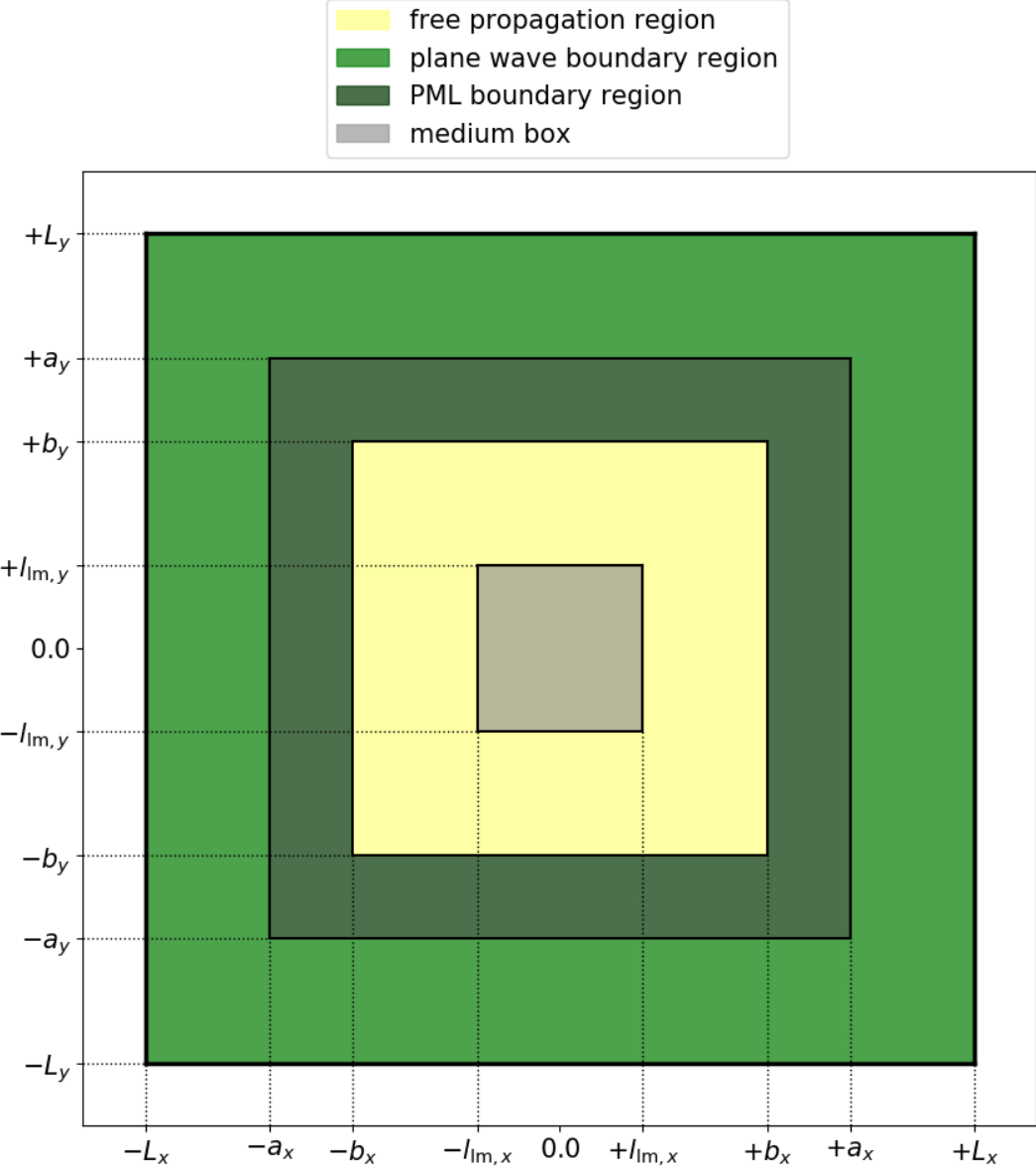


Figure 3.19: Simulation box illustration with a linear medium box in the center and combined incident waves and perfectly matched layer boundaries. The used parameters are equal to the ones of Figure 3.18. In addition we consider here the medium box limits l_x, l_y which correspond to half the length of the box.

variable	MEEP units	variable	MEEP units
L_x	20.0	k_x	0.628
L_y	20.0	$E_{(0),z}$	0.001
L_z	20.0	ξ	10.0
b_x	15.0	$x_{(0)}$	- 40.0
b_y	15.0	ϵ_0	1
b_z	15.0	μ_0	1
a_x	19.2	c_0	1
a_y	19.2	$l_{\text{lm},x}$	5.0
a_z	19.2	$l_{\text{lm},y}$	5.0
$\Delta x, \Delta y, \Delta z$	0.25	$l_{\text{lm},z}$	5.0
finite difference order	8	ϵ_{lm}	2.0
exponential order	4	μ_{lm}	2.0
Δt	0.144	c_{lm}	0.5

Table 3.6: Simulation parameters for the laser pulse run that hits a cubic linear medium box.

For our medium we take a linear medium constant in time without any losses. Therefore, the time derivatives of ϵ_{lm} and μ_{lm} as well as the electric and magnetic conductivity σ_{el} and σ_{mag} are equal to zero. Hence, the medium matrix function $\mathcal{K}_{\text{lm}}(\vec{r}, t)$ of the total $\mathcal{H}_{\text{lm}}(\vec{r}, t)$ simplifies with Eq. (1.2.40) to

$$\begin{aligned} \mathcal{K}_{\text{lm}}(\vec{r}, t) = & \begin{pmatrix} -1 & -1 \\ 1 & 1 \end{pmatrix}_{2 \times 2} \otimes \left(-i\hbar \frac{c(\vec{r}, t)}{4\epsilon(\vec{r}, t)} \left[\vec{\mathcal{S}} \cdot \left(\vec{\nabla} \epsilon(\vec{r}, t) \right) \right] \right)_{3 \times 3} \\ & + \begin{pmatrix} -1 & 1 \\ -1 & 1 \end{pmatrix}_{2 \times 2} \otimes \left(-i\hbar \frac{c(\vec{r}, t)}{4\mu(\vec{r}, t)} \left[\vec{\mathcal{S}} \cdot \left(\vec{\nabla} \mu(\vec{r}, t) \right) \right] \right)_{3 \times 3}. \end{aligned} \quad (3.5.7)$$

The six-dimensional Hamiltonian-like matrix $\mathcal{H}_{\text{lm}}(\vec{r}, t)$ determines the time-evolution, which is given by the time-evolution operator Eq. (2.3.6) for a constant linear medium

$$\mathcal{U}_{\text{lm}}(t, t_{(0)}) = \exp \left[-\frac{i}{\hbar} (t - t_{(0)}) \mathcal{H}_{\text{lm}}(\vec{r}) \right]. \quad (3.5.8)$$

Finally, we take this time evolution operator and use the recursive time-evolution Eq. (3.2.2) and adapt it for the present simulation, which leads to

$$\mathcal{F}_{\text{lm}}(\vec{r}, (m+1)\Delta t) = \mathcal{U}_{\text{lm}}((m+1)\Delta t, m\Delta t) \mathcal{F}_{\text{lm}}(\vec{r}, m\Delta t). \quad (3.5.9)$$

Based on the previous considerations, we run our Riemann-Silberstein implementation in Octopus and present some snapshots of the electric field motion. All figures have the same color table limits between -0.300 and $+0.300$ to ease the comparison of the presented electric fields. Figure 3.20 shows a sequence of electric fields for a

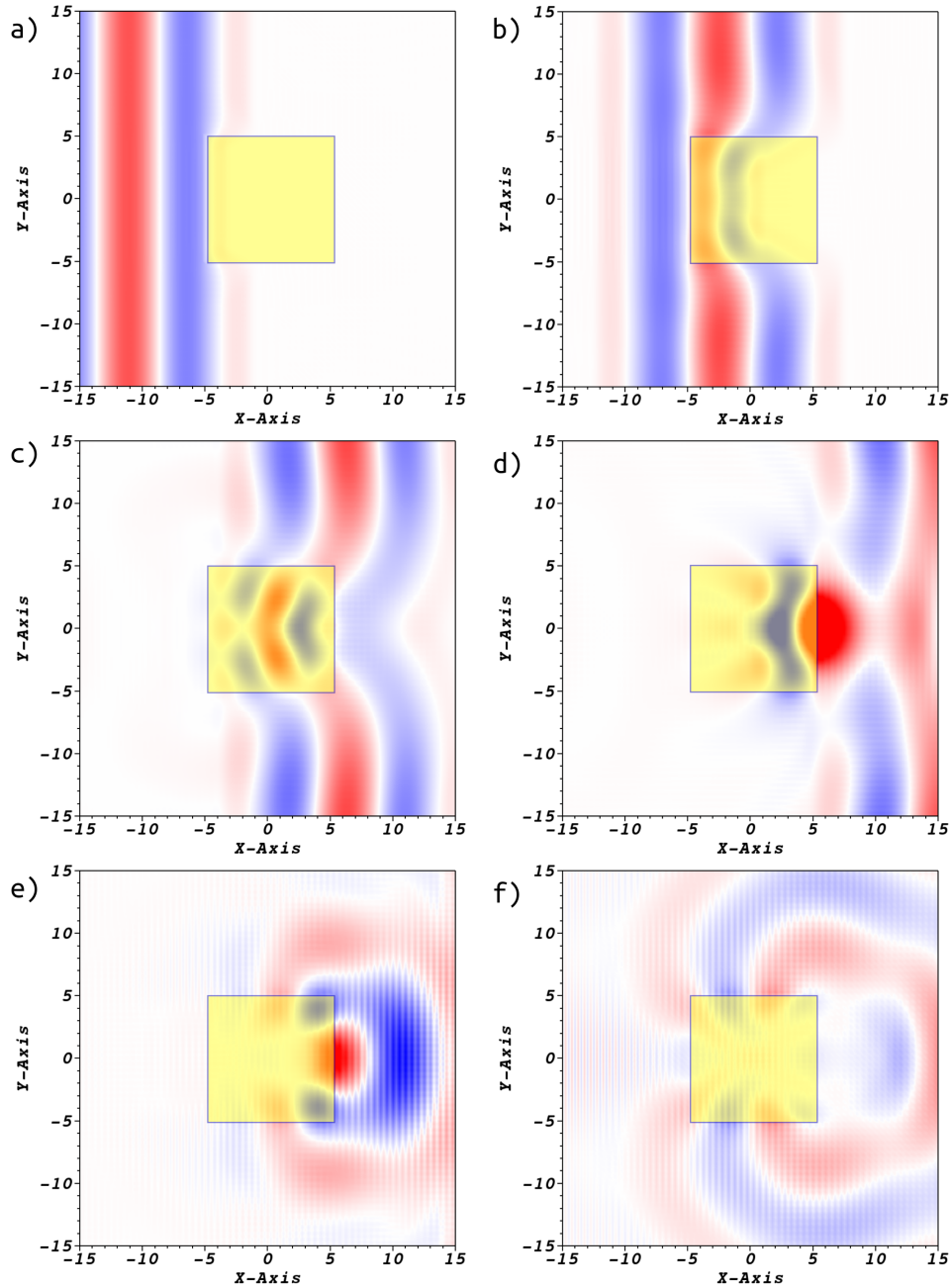


Figure 3.20: Sequence of the electric field simulated by a Riemann-Silberstein Maxwell propagation including a linear medium box. The snapshots were taken for a time interval of 6.0 starting at time $t = 20.0$. The light pulse has already entered the simulation box and hits the medium box in panel a). Following the propagation further in panel b) and c) shows the scattering effects of the medium. The incoming external signal plus the scattered and diffracted field causes a field enhancement, which is shown in panel d). The last two panels e) and f) show the emitted field radiation of the medium box.

time interval of 6.0 starting at time $t = 20.0$. At that time, the incident plane wave enters the simulation box and is reaching the beginning of the medium as can be seen in Figure 3.20 a).

Following the propagation further in panel b) at time $t = 26.0$, we can see the scattering effects of the medium. Due to the selected medium parameters, the speed of light is half compared to the speed of light in vacuum. Consequently, the wave front outside the medium box already passed the box, whereas the wave front inside passed one half of the box.

Shortly later in panel c) at time $t = 32.0$, the center of the external laser pulse passed the medium box. The wave front is dented around the box area and the light diffracts. The figure clearly visualizes the different wave lengths of the laser pulse inside the box, which corresponds to the dispersion rule for a linear medium $\lambda_{\text{lm}} = \lambda / \sqrt{\epsilon_{\text{lm}} \mu_{\text{lm}}}$.

The next snapshot in panel d) at time $t = 38.0$ demonstrates one consequence of the retarded light pulse propagation inside the medium box. When the light pulse passed through the box it interferes with the external diffracted light and here the maxima meet and cause a large electric field enhancement right outside the medium box. The electric field is more than three times larger compared to the incident pulse maximum. The same snapshot shows that the external laser left already half of the free Maxwell simulation area and hit the absorbing perfectly matched layer region.

The last two panels e) and f) at times $t = 44.0$ respectively $t = 50.0$ visualize the electric field reaction when the external laser left the simulation box. Due to the interaction with the medium, there is still a significant electric field inside the box which radiates and slowly decrease in time since the PML absorbs the outgoing field.

The present example of a Maxwell propagation with a linear medium demonstrates that the implemented code can handle arbitrary simulation box designs with a linear medium geometry. In addition to the medium parameters $\epsilon_{\text{lm}}(\vec{r})$, $\mu_{\text{lm}}(\vec{r})$ and $c_{\text{lm}}(\vec{r})$ that we used in the application, the implemented Riemann-Silberstein propagator also handles electric $\sigma_{\text{el}}(\vec{r})$ and magnetic conduction $\sigma_{\text{mag}}(\vec{r})$. These parameters are useful to setup mirrors, semi-transparent mirrors or perfect electric conductor mirrors, to simulate cavities or waveguides.

Up to now, we only considered matter as a classical linear medium which leads to helicity coupling for the six-component Riemann-Silberstein vector according to Sec. 1.2.4. The question how to replace the classical linear medium as well as the external current density by adequate quantum mechanical variables and proper coupling is discussed in the following chapters 4 - 6.

Chapter 4

Theoretical fundamentals of light-matter coupling

Quantum electrodynamics (QED) extends the classical electrodynamics that we considered in the previous chapters to a quantum field theory for coupled light-matter systems. In a non-relativistic setting, we use in the present chapter the Pauli equation to build a general Pauli-Fierz Hamiltonian for different species of charged particles which couple to the quantized electromagnetic field.

Based on this starting point, we discuss constructively the different levels of Hamiltonians, starting from a non-interacting many-particle Hamiltonian, then a Photon Hamiltonian coupled to a classical current, the longitudinal interaction Hamiltonian and the transverse interaction Hamiltonian. By combining these building blocks, we introduce a multi-species many-particle Hamiltonian for nuclei, electrons, and photons. For this Hamiltonian we establish a quantum electromagnetic density functional theory (QEDFT) for multi-species systems.

In the mean-field limit this density functional approach reduces to coupled Maxwell-Pauli-Kohn-Sham equations. In these equations the classical electromagnetic field is determined by the Maxwell's equations in Riemann-Silberstein representation taking the Kohn-Sham current density as the inhomogeneous Maxwell current term.

The novel Maxwell-Kohn-Sham equations with Pauli magnetization term are simplified in a last step by considering classical nuclei which obey Ehrenfest dynamics.

4.1 Relativistic covariant notation

In the previous chapters it was convenient to use standard vector notation to describe classical electrodynamics (ED) and non-relativistic quantum mechanics (QM). To extend our level of theory to quantum electrodynamics (QED), it is now beneficial to use additionally relativistic covariant notation.

In relativistic notation the position of the vector component indices matters. Upper and lower indices distinguish two vector types (co- and contravariant vectors)

that are connected by the Minkowski metric with the signature $g \equiv (+, -, -, -)$, and matrix form

$$g = g^{\mu\nu} = g_{\nu\mu} = \begin{pmatrix} 1 & 0 & 0 & 0 \\ 0 & -1 & 0 & 0 \\ 0 & 0 & -1 & 0 \\ 0 & 0 & 0 & -1 \end{pmatrix}. \quad (4.1.1)$$

A vector in relativistic theories is a four-component vector denoted with upper Greek indices. An arbitrary vector a^μ , respectively a_μ with $\mu = 0, 1, 2, 3$ is given by

$$a^\mu = \begin{pmatrix} a^0 \\ a^1 \\ a^2 \\ a^3 \end{pmatrix}, \quad a_\mu = \begin{pmatrix} a^0 \\ -a^1 \\ -a^2 \\ -a^3 \end{pmatrix}, \quad (4.1.2)$$

whereas a vector with roman indices, i.e., a^k with $k = 1, 2, 3$, is used in the following to represent only the three spatial dimensions

$$\vec{a} = \begin{pmatrix} a^1 \\ a^2 \\ a^3 \end{pmatrix}. \quad (4.1.3)$$

The contravariant counterpart of a^μ is denoted with lower indices a_μ . The corresponding four-gradient is defined as

$$\partial_\nu = \frac{\partial}{\partial x^\nu} = \begin{pmatrix} \frac{1}{c_0} \frac{\partial}{\partial t} \\ \frac{\partial}{\partial x} \\ \frac{\partial}{\partial y} \\ \frac{\partial}{\partial z} \end{pmatrix}, \quad \partial^\nu = \frac{\partial}{\partial x_\nu} = \begin{pmatrix} \frac{1}{c_0} \frac{\partial}{\partial t} \\ -\frac{\partial}{\partial x} \\ -\frac{\partial}{\partial y} \\ -\frac{\partial}{\partial z} \end{pmatrix}. \quad (4.1.4)$$

It is a standard convention to use the Einstein summation convention to sum over repeated upper and lower indices. In general, the contravariant version a^μ of a four-component covariant vector a_μ can be obtained per definition by

$$a^\mu = g^{\mu\nu} a_\nu. \quad (4.1.5)$$

Additionally to the full Minkowski metric $g_{\mu\nu}$, we define the corresponding spatial submatrix g_{kl} with $k = \{1, 2, 3\}$, $l = \{1, 2, 3\}$, and ϵ^{klm} the anti-symmetric Levi-Civita tensor.

The following table of equations summarizes the relations between the standard vector notation and the relativistic notation, where we use two four component vectors

a^μ , b^μ and a 3x3 matrix M_l^k

$$\vec{a} \equiv a^k, \quad (4.1.6)$$

$$M\vec{a} \equiv M_l^k a^l \quad (4.1.7)$$

$$\vec{a} \cdot \vec{b} \equiv -a^l b_l = -a_l b^l = -a^l b^m g_{ml}, \quad (4.1.8)$$

$$\vec{\nabla} a \equiv \partial_k a = -\partial^k a, \quad (4.1.9)$$

$$\vec{\nabla}^2 a \equiv -\partial_l \partial^l a, \quad (4.1.10)$$

$$\vec{\nabla} \cdot \vec{a} \equiv \partial_k a^k, \quad (4.1.11)$$

$$a_k = g_{kl} a^l \equiv -\vec{a}, \quad (4.1.12)$$

$$\vec{\nabla} \times \vec{a} \equiv -\varepsilon^{klm} \partial_l a_m, \quad (4.1.13)$$

$$\varepsilon_{klm} = \varepsilon^{abc} g_{ak} g_{bl} g_{cm}. \quad (4.1.14)$$

In Sec. (1.1.3), we introduced the curl operation in terms of spin-1 matrices, which appears on the right-hand side of Eq. (1.1.26). It is given by the scalar product $(\vec{\mathcal{S}} \cdot \vec{\nabla})$ of the spin matrices vector $\vec{\mathcal{S}}$ from Eq. (1.1.15) and the Nabla vector. This scalar product in relativistic notation takes the form

$$(\vec{\mathcal{S}} \cdot \vec{\nabla}) = \mathcal{S}^k \partial_k. \quad (4.1.15)$$

Hence, the k-component of the corresponding curl operation in terms of the spin-1 matrices in relativistic notation is with Eq. (4.1.13) expressed by

$$[\vec{\nabla} \times \vec{a}]^k = [-i(\mathcal{S} \cdot \vec{\nabla}) \vec{a}]^k = -i[\mathcal{S}^l \partial_l]^{km} a_m, \quad (4.1.16)$$

where k, m denote the matrix element indices.

In the following, to distinguish the covariant indices from other used indices we put the non-covariant indices in parenthesis.

4.2 Relativistic decomposition of spin particles and derivation of Maxwell's equations

Relativistic particles obey the energy-momentum relation

$$E^2 = m^2 c_0^2 + c_0^2 p_k p^k \quad (4.2.1)$$

for particles with mass like electrons and nuclei, and

$$E^2 = p^k p_k c_0^2 \quad (4.2.2)$$

for massless particles like photons. Substituting $E = i\hbar \frac{\partial}{\partial t}$ and $p^k = -i\hbar \partial_k = i\hbar \partial^k$ leads to the wave equations

$$\left(E^2 - c_0^2 p_k p^k - m^2 c_0^2 \right) \Psi(\vec{r}, t) = c_0^2 \left(-\frac{\hbar^2}{c_0^2} \partial_t^2 + \hbar^2 \partial^k \partial_k - m^2 c_0^2 \right) \Psi(\vec{r}, t) = 0, \quad (4.2.3)$$

and

$$\left(E^2 - c_0^2 p_k p^k\right) \Psi(\vec{r}, t) = c_0^2 \left(-\frac{\hbar^2}{c_0^2} \partial_t^2 + \hbar^2 \partial^k \partial_k\right) \Psi(\vec{r}, t) = 0. \quad (4.2.4)$$

Both equations are second order differential equations and in general their solutions are scalar plane wave functions and describe spinless particles. In Eq. (4.2.4) the particles are massless and the Klein-Gordon equation in Eq. (4.2.3) takes additionally particle masses into account. Due to the squared expressions in Eq. (4.2.4) and Eq. (4.2.3), both terms can be decomposed into

$$c_0^2 \left(-\frac{\hbar}{c_0} \partial_t + \hbar \partial^k - m\right) \left(-\frac{\hbar}{c_0} \partial_t - \hbar \partial_k + m\right) \Psi(\vec{r}, t) = 0. \quad (4.2.5)$$

and

$$c_0^2 \left(-\frac{\hbar}{c_0} \partial_t + \hbar \partial^k\right) \left(-\frac{\hbar}{c_0} \partial_t - \hbar \partial_k\right) \Psi(\vec{r}, t) = 0, \quad (4.2.6)$$

Considering different spin-types, the fundamental energy-momentum relation does not hold for scalar wave functions $\psi(\vec{r}, t)$, hence each type of spin requires a specific matrix algebra that transforms the corresponding second order differential equations into a first order differential equation.

Dirac used such an ansatz to describe free spin-1/2 particles in space with respect to the relativistic energy-momentum relation and introduced the well known γ matrices with [100]

$$\gamma^0 = \begin{pmatrix} \mathbb{1}_{(2)} & 0 \\ 0 & \mathbb{1}_{(2)} \end{pmatrix}, \quad \gamma^k = \begin{pmatrix} 0 & \sigma^k \\ -\sigma^k & 0 \end{pmatrix}. \quad (4.2.7)$$

The $\mathbb{1}_{(i)}$ denotes in general the i^{th} -dimensional identity matrix and σ^k are the three Pauli-matrices [100]

$$\sigma^0 = \begin{pmatrix} 1 & 0 \\ 0 & 1 \end{pmatrix}, \quad \sigma^1 = \begin{pmatrix} 0 & 1 \\ 1 & 0 \end{pmatrix}, \quad \sigma^2 = \begin{pmatrix} 0 & -i \\ i & 0 \end{pmatrix}, \quad \sigma^3 = \begin{pmatrix} 1 & 0 \\ 0 & -1 \end{pmatrix}. \quad (4.2.8)$$

The Pauli-matrices are related to each other by

$$\begin{aligned} \sigma^k \sigma^l &= \frac{1}{2} \left(\{ \sigma^k, \sigma^l \} + [\sigma^k, \sigma^l] \right) \\ &= \delta^{kl} \mathbb{1}_{(2)} - i \epsilon^{klj} \sigma_j. \end{aligned} \quad (4.2.9)$$

Due to the four-dimensional Dirac-matrices, the corresponding wave functions, i.e., $\Psi_{(4)}(\vec{r}, t)$, have four spinor components. In general $\Psi_{(i)}(\vec{r}, t)$ gives an i^{th} -dimensional spinor. The underlying relativistic energy-momentum relation is with Eq. (4.2.3) given by

$$\begin{aligned} &\left(\mathbb{1}_{(4)} E^2 - \mathbb{1}_{(4)} c_0^2 p_k p^k - \mathbb{1}_{(4)} m^2 c_0^2\right) \Psi_{(4)}(\vec{r}, t) \\ &= c_0^2 \left(-\mathbb{1}_{(4)} \frac{\hbar}{c_0^2} \partial_t^2 + \mathbb{1}_{(4)} \hbar \partial^k \partial_k - \mathbb{1}_{(4)} m^2\right) \Psi_{(4)}(\vec{r}, t) \\ &= 0. \end{aligned} \quad (4.2.10)$$

Using the Dirac-matrices leads to the decomposition of Eq. (4.2.10) [100]

$$c_0^2 \left(-\gamma_0 \frac{\hbar}{c_0} \partial_t + \hbar \gamma^k \partial_k - \mathbb{1}_{(4)} m \right) \left(-\gamma_0 \frac{\hbar}{c_0} \partial_t - \hbar \gamma^k \partial_k + \mathbb{1}_{(4)} m \right) \Psi_{(4)}(\vec{r}, t) = 0. \quad (4.2.11)$$

This decomposition of the basic relativistic wave function can also be applied to massless spin-1 particles, e.g., photons. Photon wave functions $\psi_3(\vec{r}, t)$ are three-dimensional and the energy-momentum relation takes with the three-dimensional identity operator $\mathbb{1}_{(3)}$ the form

$$\left(\mathbb{1}_{(3)} E^2 - \mathbb{1}_{(3)} c_0^2 p_k p^k \right) \Psi_{(3)}(\vec{r}, t) = \hbar^2 c_0^2 \left(\mathbb{1}_{(3)} \partial^k \partial_k - \mathbb{1}_{(3)} \frac{1}{c_0^2} \partial_t^2 \right) \Psi_{(3)}(\vec{r}, t) = 0. \quad (4.2.12)$$

The corresponding decomposition requires spin-1 matrices. We introduced them in Eq.(1.1.16) to express an identity operation for the curl, here given by their covariant notation

$$\mathbf{S}^1 = \begin{pmatrix} 0 & 0 & 0 \\ 0 & 0 & -i \\ 0 & i & 0 \end{pmatrix}, \quad \mathbf{S}^2 = \begin{pmatrix} 0 & 0 & i \\ 0 & 0 & 0 \\ -i & 0 & 0 \end{pmatrix}, \quad \mathbf{S}^3 = \begin{pmatrix} 0 & -i & 0 \\ i & 0 & 0 \\ 0 & 0 & 0 \end{pmatrix}. \quad (4.2.13)$$

Similar to the Pauli-matrices, the spin-1 matrices obey the following algebra

$$[\mathbf{S}^k, \mathbf{S}^l] = -i \epsilon^{klm} \mathbf{S}_m, \quad \vec{\mathbf{S}}^2 = \mathbb{1}_{(3)}. \quad (4.2.14)$$

Although, the spin-1 matrices and higher-order spin-matrices obey the same algebra as the spin-1/2 matrices, their decomposition cannot be written in a pure binomial form. We have to add an additional term as a side condition for the three-dimensional $\Psi_{(3)}(\vec{r}, t)$ wave functions. The spin-1 decomposition form has been considered in Ref. [69, 70], and is given by

$$\begin{aligned} & \hbar^2 c_0^2 \left(-\mathbb{1}_{(3)} \frac{1}{c_0} \partial_t + \mathbf{S}^k \partial_k \right) \left(-\mathbb{1}_{(3)} \frac{1}{c_0} \partial_t - \mathbf{S}^k \partial_k \right) \Psi_{(3)}(\vec{r}, t) \\ & + \hbar^2 c_0^2 \begin{pmatrix} \partial_1^2 & \partial_1 \partial_2 & \partial_1 \partial_3 \\ \partial_2 \partial_1 & \partial_2^2 & \partial_2 \partial_3 \\ \partial_3 \partial_1 & \partial_3 \partial_2 & \partial_3^2 \end{pmatrix} \Psi_{(3)}(\vec{r}, t) = 0, \end{aligned} \quad (4.2.15)$$

with \mathbf{S}^k from Eq. (1.1.16) and the relativistic scalar product of Eq. (4.1.8). The

corresponding complex conjugate of Eq. (4.2.15) is

$$\begin{aligned} \hbar^2 c_0^2 \left(-\mathbb{1}_{(3)} \frac{1}{c_0} \partial_t - \mathbf{S}^k \partial_k \right) \left(-\mathbb{1}_{(3)} \frac{1}{c_0} \partial_t + \mathbf{S}^k \partial_k \right) \Psi_{(3)}^*(\vec{r}, t) \\ + \hbar^2 c_0^2 \begin{pmatrix} \partial_1^2 & \partial_1 \partial_2 & \partial_1 \partial_3 \\ \partial_2 \partial_1 & \partial_2^2 & \partial_2 \partial_3 \\ \partial_3 \partial_1 & \partial_3 \partial_2 & \partial_3^2 \end{pmatrix} \Psi_{(3)}^*(\vec{r}, t) = 0. \end{aligned} \quad (4.2.16)$$

The two brackets inside the first terms of the left-hand side of Eq. (4.2.15) and Eq. (4.2.16) commute, so that both can be combined into one six-dimensional equation by

$$\begin{aligned} \hbar^2 c_0^2 \left(\left\{ \left[\left(\begin{pmatrix} 1 & 0 \\ 0 & 1 \end{pmatrix} \right)_{2 \times 2} \otimes \left(\mathbb{1}_{(3)} \frac{-1}{c_0} \partial_t \right)_{3 \times 3} + \left(\begin{pmatrix} 1 & 0 \\ 0 & -1 \end{pmatrix} \right)_{2 \times 2} \otimes \left(\mathbf{S}^k \partial_k \right)_{3 \times 3} \right] \right. \right. \\ \left. \left[\left(\begin{pmatrix} 1 & 0 \\ 0 & 1 \end{pmatrix} \right)_{2 \times 2} \otimes \left(\mathbb{1}_{(3)} \frac{-1}{c_0} \partial_t \right)_{3 \times 3} - \left(\begin{pmatrix} 1 & 0 \\ 0 & -1 \end{pmatrix} \right)_{2 \times 2} \otimes \left(\mathbf{S}^k \partial_k \right)_{3 \times 3} \right] \right\} \\ \left. + \left[\left(\begin{pmatrix} 1 & 0 \\ 0 & 1 \end{pmatrix} \right)_{2 \times 2} \otimes \begin{pmatrix} \partial_1^2 & \partial_1 \partial_2 & \partial_1 \partial_3 \\ \partial_2 \partial_1 & \partial_2^2 & \partial_2 \partial_3 \\ \partial_3 \partial_1 & \partial_3 \partial_2 & \partial_3^2 \end{pmatrix} \right]_{3 \times 3} \right) \begin{pmatrix} \Psi_{(3)}(\vec{r}, t) \\ \Psi_{(3)}^*(\vec{r}, t) \end{pmatrix} = 0. \end{aligned} \quad (4.2.17)$$

This equation holds if both terms are equal to zero independently, but other combinations are also possible [70]. The first term on the left-hand side of Eq. (4.2.17) is equal to zero, if either

$$\left[\left(\begin{pmatrix} 1 & 0 \\ 0 & 1 \end{pmatrix} \right)_{2 \times 2} \otimes \left(-\mathbb{1}_{(3)} \hbar \partial_t \right)_{3 \times 3} - \left(\begin{pmatrix} 1 & 0 \\ 0 & -1 \end{pmatrix} \right)_{2 \times 2} \otimes \left(c_0 \hbar \mathbf{S}^k \partial_k \right)_{3 \times 3} \right] \begin{pmatrix} \Psi_{(3)}(\vec{r}, t) \\ \Psi_{(3)}^*(\vec{r}, t) \end{pmatrix} = 0 \quad (4.2.18)$$

or

$$\left[\left(\begin{pmatrix} 1 & 0 \\ 0 & 1 \end{pmatrix} \right)_{2 \times 2} \otimes \left(-\mathbb{1}_{(3)} \hbar \partial_t \right)_{3 \times 3} + \left(\begin{pmatrix} 1 & 0 \\ 0 & -1 \end{pmatrix} \right)_{2 \times 2} \otimes \left(-c_0 \hbar \mathbf{S}^k \partial_k \right)_{3 \times 3} \right] \begin{pmatrix} \Psi_{(3)}(\vec{r}, t) \\ \Psi_{(3)}^*(\vec{r}, t) \end{pmatrix} = 0. \quad (4.2.19)$$

In Eq. (4.2.11), the corresponding spin-1/2 4-spinor wave function obeys the one particle relativistic equation of motion for a fermion.

As before, we consider Eq. (4.2.17) as the relativistic spin-1 equation of motion and $\Psi_{(3)}(\vec{r}, t)$ its one particle photon wave function. Comparing Eq. (4.2.18) with Eq. (1.1.47) shows that both are equivalent if the Riemann-Rilberstein vectors

$\vec{F}_+(\vec{r}, t)$, $\vec{F}_-(\vec{r}, t)$, and $\mathcal{F}(\vec{r}, t)$ correspond directly to the one photon wave function $\Psi_{(3)}(\vec{r}, t)$

$$\vec{F}_+(\vec{r}, t) = \Psi_{(3)}(\vec{r}, t), \quad \vec{F}_-(\vec{r}, t) = \Psi_{(3)}^*(\vec{r}, t), \quad \mathcal{F}(\vec{r}, t) = \begin{pmatrix} \Psi_{(3)}(\vec{r}, t) \\ \Psi_{(3)}^*(\vec{r}, t) \end{pmatrix}. \quad (4.2.20)$$

The term on the left-hand side of Eq. (4.2.18) multiplied by the imaginary unit leads to the combined Ampère's and Faraday's law in Riemann-Silberstein representation

$$\begin{aligned} & \left[\begin{pmatrix} 1 & 0 \\ 0 & 1 \end{pmatrix}_{2 \times 2} \otimes \begin{pmatrix} -\mathbb{1}_{(3)} i \hbar \partial_t \end{pmatrix}_{3 \times 3} + \begin{pmatrix} 1 & 0 \\ 0 & -1 \end{pmatrix}_{2 \times 2} \otimes \begin{pmatrix} -i c_0 \hbar \mathbf{S}^k \partial_k \end{pmatrix}_{3 \times 3} \right] \mathcal{F}(\vec{r}, t) \\ & = \left[\mathcal{H} - \mathbb{1}_{(6)} i \hbar \partial_t \right] \mathcal{F}(\vec{r}, t) = 0, \end{aligned} \quad (4.2.21)$$

with \mathcal{H} given in Eq. (1.1.45) which is expressed in relativistic notation by

$$\mathcal{H} = \begin{pmatrix} 1 & 0 \\ 0 & -1 \end{pmatrix}_{2 \times 2} \otimes \begin{pmatrix} i \hbar c_0 \delta(\vec{r} - \vec{r}') \delta(t - t') [\mathbf{S}^m \partial'_m] \end{pmatrix}_{3 \times 3}. \quad (4.2.22)$$

Considering the second terms on the left-hand side of Eq. (4.2.15) and Eq. (4.2.16), they describe a side condition for each equation. Both terms have to be equal to zero for all times and can be expressed in component notation by

$$\hbar^2 c_0^2 \begin{pmatrix} \partial_1^2 & \partial_1 \partial_2 & \partial_1 \partial_3 \\ \partial_2 \partial_1 & \partial_2^2 & \partial_2 \partial_3 \\ \partial_3 \partial_1 & \partial_3 \partial_2 & \partial_3^2 \end{pmatrix} \Psi_{(3)}(\vec{r}, t) = \partial_k \partial_l \Psi_{(3)}^l(\vec{r}, t), \quad (4.2.23)$$

$$\hbar^2 c_0^2 \begin{pmatrix} \partial_1^2 & \partial_1 \partial_2 & \partial_1 \partial_3 \\ \partial_2 \partial_1 & \partial_2^2 & \partial_2 \partial_3 \\ \partial_3 \partial_1 & \partial_3 \partial_2 & \partial_3^2 \end{pmatrix} \Psi_{(3)}^*(\vec{r}, t) = \partial_k \partial_l \Psi_{(3)}^{*l}(\vec{r}, t). \quad (4.2.24)$$

Using Eqs. (4.2.20) and defining the component vector notation for a six-component vector with

$$\mathcal{F}(\vec{r}, t) = \begin{pmatrix} \Psi_{(3)}^k(\vec{r}, t) \\ \Psi_{(3)}^{*k'}(\vec{r}, t) \end{pmatrix} = \begin{pmatrix} F_+^k \\ F_-^{*k'} \end{pmatrix}, \quad (4.2.25)$$

the two equations, Eq. (4.2.23) and Eq. (4.2.24), can be combined to a six-component vector by

$$\hbar^2 c_0^2 \begin{pmatrix} \partial_k \partial_l F_+^l(\vec{r}, t) \\ \partial_{k'} \partial_{l'} F_-^{l'}(\vec{r}, t) \end{pmatrix} = 0. \quad (4.2.26)$$

This equation holds if

$$\begin{pmatrix} \partial_l F_+^l(\vec{r}, t) \\ \partial_{l'} F_-^{l'}(\vec{r}, t) \end{pmatrix} = \mathcal{D} \cdot \mathcal{F}(\vec{r}, t) = 0 \quad (4.2.27)$$

where we use the six-component divergence operator \mathcal{D} in Eq. (1.1.41) and the dot product definition in Eq. (1.1.43).

We emphasize here, that we thus have derived the classical homogeneous Maxwell's equations starting with Dirac's decomposition Eq. (4.2.17) for the relativistic spin-1 energy-momentum relation and ending with the combination of the homogeneous Faraday's and Ampère's laws in Eq. (4.2.21) and the combination of the homogeneous Gauß laws in Eq. (4.2.27).

In contrast to the spin-1/2 particle wave function, where its spinor components refer to spin states, the spinor components of the photon wave function $\mathcal{F}(\vec{r}, t)$ refer to positive and negative helicity. The previous considerations can be repeated for arbitrary spins and particles with mass, but it is not always possible to find simple and physical side conditions.

4.3 Multi-species Hamiltonian

In this section, we build the total Hamiltonian of our multi species system coupled to an electromagnetic field four-vector potential $\hat{A}^\mu(\vec{r}, t)$. The total electric field consists of two parts, the internal field and an external field. The internal Maxwell field arises due to the presence of the charged particles of all N different species with elementary charge q , denoted as $\hat{A}_{\text{mat}}^\mu(\vec{r}, t)$ plus an external Maxwell field, described by its external classical vector potential $A_{\text{ext}}^\mu(\vec{r}, t)$. To construct the total Pauli-Fierz Hamiltonian of the multi-species system, we use the different parts of the multi-species Hamiltonian which are discussed in more detail in the Appendix A.

The underlying total four-current density $j_{\text{mat}}^\mu(\vec{r}, t)$ of the n different species system is a sum over all N species-specific four-current density $j_{\text{mat},(n)}^\mu(\vec{r}, t)$ of corresponding species n

$$j_{\text{mat}}^\mu(\vec{r}, t) = \sum_n^N j_{\text{mat},(n)}^\mu(\vec{r}, t) . \quad (4.3.1)$$

The zero component, respectively the total matter charge density $\rho_{\text{mat}}(\vec{r}, t)$ times the speed of light c_0 , reads according to Eq. (A.5.3)

$$\hat{j}_{\text{mat}}^0(\vec{r}, t) = c_0 \hat{\rho}_{\text{mat}}(\vec{r}, t) = \sum_{n=1}^N c_0 q_{(n)} \sum_s \hat{\Phi}_{(n)}^\dagger(\vec{r}, s, t) \hat{\Phi}_{(n)}(\vec{r}, s, t) \quad (4.3.2)$$

with spin states s , and the Fock space field operators for particle creation, $\hat{\Phi}^\dagger(\vec{r}, s)$, and annihilation, $\hat{\Phi}(\vec{r}, s)$. These operators follow the QED commutation rules, (+) for bosons and anti-commutation (−) for fermions [101]

$$\left[\hat{\Phi}(\vec{r}, s, t), \hat{\Phi}^\dagger(\vec{r}', s', t) \right]_{\pm} = \delta_{(ss')} \delta^3(\vec{r} - \vec{r}'). \quad (4.3.3)$$

The three-dimensional current density $j_{\text{mat}}^k(\vec{r}, t)$ is equivalent to Eq. (A.5.19). It can also be expressed as a sum of all N different current contributions of species n denoted as $j_{\text{mat},(i)}^k(\vec{r}, t)$ similar to Eq. (4.3.1), i.e., $\hat{j}_{\text{pmc},(n)}^k(\vec{r}, t)$ for the species-specific paramagnetic current, $\hat{j}_{\text{dmc},(n)}^k(\vec{r}, t)$ for the species-specific diamagnetic current, and $\hat{j}_{\text{mc},(n)}^k(\vec{r}, t)$ for the species-specific magnetic current contribution

$$\begin{aligned} j_{\text{mat}}^k(\vec{r}, t) &= \hat{j}_{\text{pmc}}^k(\vec{r}, t) + \hat{j}_{\text{dmc}}^k(\vec{r}, t) + \hat{j}_{\text{mc}}^k(\vec{r}, t) \\ &= \sum_n \hat{j}_{\text{pmc},(n)}^k(\vec{r}, t) + \sum_n \hat{j}_{\text{dmc},(n)}^k(\vec{r}, t) + \sum_n \hat{j}_{\text{mc},(n)}^k(\vec{r}, t), \end{aligned} \quad (4.3.4)$$

with paramagnetic current density from Eq. (A.5.20)

$$\begin{aligned} \hat{j}_{\text{pmc}}^k(\vec{r}, t) &= \sum_{n=1}^N \sum_s \frac{\hbar q(n)}{2M(n)\text{i}} \left[\left(\partial^k \hat{\Phi}_{(n)}^\dagger(\vec{r}, s, t) \right) \hat{\Phi}_{(n)}(\vec{r}, s, t) - \hat{\Phi}_{(n)}^\dagger(\vec{r}, s, t) \left(\partial^k \hat{\Phi}_{(n)}(\vec{r}, s, t) \right) \right] \\ &= \sum_n \hat{j}_{\text{pmc},(n)}^k(\vec{r}, t), \end{aligned} \quad (4.3.5)$$

diamagnetic current density from Eq. (A.5.21)

$$\begin{aligned} \hat{j}_{\text{dmc}}^k(\vec{r}, t) &= \sum_{n=1}^N -\frac{q(n)}{M(n)c_0^2} \hat{j}_{(n)}^0(\vec{r}, t) \hat{A}^k(\vec{r}, t) \\ &= \sum_n \hat{j}_{\text{dmc},(n)}^k(\vec{r}, t), \end{aligned} \quad (4.3.6)$$

and magnetization current density from Eq. (A.5.22)

$$\begin{aligned} \hat{j}_{\text{mc}}^k(\vec{r}, t) &= \sum_{n=1}^N \sum_{s,s'} -\varepsilon^{klm} \partial_l \hat{\Phi}_{(n)}^\dagger(\vec{r}, s, t) \left(\frac{\hbar q(n)}{2M(n)} [\mathbf{S}_{(n),m}]_{ss'} \right) \hat{\Phi}_{(n)}(\vec{r}, s', t) \\ &= \sum_n \hat{j}_{\text{mc},(n)}^k(\vec{r}, t). \end{aligned} \quad (4.3.7)$$

The expression $[\mathbf{S}_{(n),m}]_{ss'}$ gives with indices s, s' the corresponding matrix element of the spin matrix vector $\mathbf{S}_{(n),m}$ of species n . The total current density $j^\mu(\vec{r}, t)$ of the

considered system is the sum of the matter current density operator $\hat{j}_{\text{mat}}^\mu(\vec{r}, t)$ and an external current density $j_{\text{ext}}^\mu(\vec{r}, t)$

$$j^\mu(\vec{r}, t) = \hat{j}_{\text{mat}}^\mu(\vec{r}, t) + j_{\text{ext}}^\mu(\vec{r}, t) \quad (4.3.8)$$

The total four-vector potential of the entire system $\hat{A}^\mu(\vec{r}, t)$ also consists of the matter induced vector potential $\hat{A}_{\text{mat}}^\mu(\vec{r}, t)$ and an external vector potential $A_{\text{ext}}^\mu(\vec{r}, t)$

$$\hat{A}^\mu(\vec{r}, t) = \hat{A}_{\text{mat}}^\mu(\vec{r}, t) + A_{\text{ext}}^\mu(\vec{r}, t). \quad (4.3.9)$$

First, we start with the N -species kinetic Hamiltonian $\hat{H}_{\text{kin},(0)}(t)$ with Eq. (A.5.28) that determines the uncoupled kinetic energy of all N -species particles. It reads

$$\hat{H}_{\text{kin},(0)}(t) = \sum_{n=1}^N \int d^3r \frac{\hbar^2}{2M_{(n)}} \sum_s \hat{\Phi}_{(n)}^\dagger(\vec{r}, s, t) \partial_k \partial^k \hat{\Phi}_{(n)}(\vec{r}, s, t). \quad (4.3.10)$$

We continue by adding the interaction of the matter to the transverse electromagnetic field operator in Coulomb gauge. Coupling the particles to a vector-potential operator $\hat{A}^k(\vec{r}, t)$ modifies the previous uncoupled kinetic Hamiltonian to the general N -species kinetic Hamiltonian $\hat{H}_{\text{kin}}(t)$ according to Eq. (A.5.31)

$$\hat{H}_{\text{kin}}(t) = - \sum_{n=1}^N \int d^3r \frac{1}{2M_{(n)}} \sum_s \hat{\Phi}_{(n)}^\dagger(\vec{r}, s, t) \hat{P}_{(n),k}(\vec{r}, t) \hat{P}_{(n)}^k(\vec{r}, t) \hat{\Phi}_{(n)}(\vec{r}, s, t) \quad (4.3.11)$$

with the canonical momentum $\hat{P}_{(n)}^k(\vec{r}, t)$ of species type n of the form

$$\hat{P}_{(n)}^k(\vec{r}, t) = -i\hbar\partial^k + \frac{q_{(n)}}{c_0} \hat{A}^k(\vec{r}, t). \quad (4.3.12)$$

Next, we consider the interaction Hamiltonian $\hat{H}_{\text{int},\perp}(t)$ of an electromagnetic field operator $\hat{A}^k(\vec{r}, t)$ coupled to the matter, which is given in Eq. (A.5.26), i.e.,

$$\begin{aligned} \hat{H}_{\text{int},\perp}(t) = & - \sum_{n=1}^N \int d^3r \frac{i\hbar q_{(n)}}{2M_{(n)}c_0} \sum_{s,s'} \hat{\Phi}_{(n)}^\dagger(\vec{r}, s, t) \partial_k \hat{A}^k(\vec{r}, t) \hat{\Phi}_{(n)}(\vec{r}, s, t) \\ & - \sum_{n=1}^N \int d^3r \frac{i\hbar q_{(n)}}{2M_{(n)}c_0} \sum_{s,s'} \hat{\Phi}_{(n)}^\dagger(\vec{r}, s, t) \hat{A}_k(\vec{r}, t) \partial^k \hat{\Phi}_{(n)}(\vec{r}, s, t) \\ & + \sum_{n=1}^N \int d^3r \frac{q_{(n)}^2}{2M_{(n)}c_0^2} \sum_{s,s'} \hat{\Phi}_{(n)}^\dagger(\vec{r}, s, t) \hat{A}_k(\vec{r}, t) \hat{A}^k(\vec{r}, t) \hat{\Phi}_{(n)}(\vec{r}, s, t) \\ & + \sum_{n=1}^N \int d^3r \frac{\hbar q_{(n)}}{2M_{(n)}} \sum_{s,s'} \hat{\Phi}_{(n)}^\dagger(\vec{r}, s, t) [\mathbf{S}_{(n),k}]_{ss'} \hat{\Phi}_{(n)}(\vec{r}, s', t) \left(\frac{1}{c_0} \varepsilon^{klm} \partial_l \hat{A}_m(\vec{r}, t) \right). \end{aligned} \quad (4.3.13)$$

The last term on the right-hand side gives the Stern-Gerlach Hamiltonian term $\hat{H}_{\text{Stern}}(t)$

$$\hat{H}_{\text{Stern}}(t) = \sum_{n=1}^N \int d^3r \frac{\hbar q_{(n)}}{2M_{(n)}} \sum_{s,s'} \hat{\Phi}_{(n)}^\dagger(\vec{r}, s, t) [\mathbf{S}_{(n),k}]_{ss'} \hat{\Phi}_{(n)}(\vec{r}, s', t) \left(\frac{1}{c_0} \epsilon^{klm} \partial_l \hat{A}_m(\vec{r}, t) \right). \quad (4.3.14)$$

Comparing the two Hamiltonians $\hat{H}_{\text{kin}}(t)$ and $\hat{H}_{\text{kin}}(t)$ shows that we can add the zero Maxwell field kinetic Hamiltonian from $\hat{H}_{\text{kin},(0)}(t)$ Eq. (4.3.10) to the transverse interaction Hamiltonian $\hat{H}_{\text{int},\perp}(t)$ from Eq. (4.3.13). Therefore, we obtain $\hat{H}_{\text{kin,Stern}}(t)$, the sum of the general kinetic Hamiltonian $\hat{H}_{\text{kin}}(t)$ plus the Stern-Gerlach Hamiltonian term $\hat{H}_{\text{Stern}}(t)$.

$$\begin{aligned} \hat{H}_{\text{kin,Stern}}(t) &= \hat{H}_{\text{kin},(0)}(t) + \hat{H}_{\text{int},\perp}^{\perp}(t), \\ &= \hat{H}_{\text{kin}}(t) + \hat{H}_{\text{Stern}}(t). \end{aligned} \quad (4.3.15)$$

The longitudinal interaction Hamiltonian of the matter in Coulomb gauge couples only to the longitudinal electric field and depends according to Eq. (A.5.6) the zero component of the matter current density $j_{\text{mat}}^0(\vec{r}, t)$

$$\hat{H}_{\text{mat,int},\parallel}(t) = \frac{1}{2c_0^2} \int d^3r d^3r' w(\vec{r}, \vec{r}') \sum_{n,n'} : \hat{j}_{\text{mat},(n)}^0(\vec{r}, t) \hat{j}_{\text{mat},(n'),0}(\vec{r}', t) : , \quad (4.3.16)$$

with the Green's function that solves the Poisson equations

$$w(\vec{r}, \vec{r}') = -\frac{1}{\epsilon_0} G(\vec{r}, \vec{r}') = \frac{1}{4\pi\epsilon_0 |\vec{r} - \vec{r}'|}. \quad (4.3.17)$$

Additionally to the matter induced interaction to the electromagnetic field, we allow also coupling for a coupling to external variables, i.e., an external four-vector potential $A_{\text{ext}}^\mu(\vec{r}, t)$ and an external three-vector current density $j_{\text{ext}}^k(\vec{r}, t)$. As we discuss in the appendix Sec. (A.5.1), we discard the external charge density interaction to the photon field to avoid "double counting" same effects that arises due to the interaction of an external three-vector potential $A_{\text{ext}}^k(\vec{r}, t)$.

The transverse interaction Hamiltonian in Coulomb gauge $\hat{H}_{\text{int},\vec{j}_{\text{ext}},\perp}(t)$ of an external current density $j_{\text{ext}}^k(\vec{r}, t)$ to our total photon field $A^\mu(\vec{r}, t)$ of the system is equivalent to $\hat{H}_{\text{Ph},\vec{j}_{\text{ext}},\perp}(t)$ from Eq. (A.5.23), i.e.,

$$\hat{H}_{\text{int},\vec{j}_{\text{ext}},\perp}(t) = \frac{1}{c_0} \int d^3r j_{\text{ext}}^k(\vec{r}, t) \hat{A}_k(\vec{r}, t). \quad (4.3.18)$$

The longitudinal interaction Hamiltonian in Coulomb gauge $\hat{H}_{\text{int},A_{\text{ext}},\parallel}(t)$ of an external scalar potential $A_{\text{ext}}^0(\vec{r}, t)$ to the matter is represented by the last term of

Eq. (A.5.17) with

$$\hat{H}_{\text{int},A_{\text{ext}},\parallel}(t) = \sum_{n=1}^N \sum_s \int d^3r q_{(n)} A_{\text{ext},0}(\vec{r}, t) \hat{\Phi}_{(n)}^\dagger(\vec{r}, s, t) \hat{\Phi}_{(n)}(\vec{r}, s, t). \quad (4.3.19)$$

The free Photon-Hamiltonian $\hat{H}_{\text{Ph,free}}(t)$ for the electromagnetic field does not depend on N and is equal to Eq. (A.4.20)

$$\hat{H}_{\text{Ph,free}}(t) = \int d^3r : \hat{F}_{+,\perp,k}(\vec{r}, t) \hat{F}_{-,\perp}^k(\vec{r}, t) : . \quad (4.3.20)$$

Finally, adding all previously considered terms and summing over all different N species leads to the complete N -species Pauli-Fierz Hamiltonian \hat{H}_{Fierz} in Fock space

$$\begin{aligned} \hat{H}_{\text{Fierz}}(t) &= \hat{H}_{\text{mat,kin},(0)}(t) + \hat{H}_{\text{int},\perp}(t) + \hat{H}_{\text{int},\parallel}(t) + \hat{H}_{\text{Ph,free}}(t) + \hat{H}_{\text{int},\vec{j}_{\text{ext}},\perp}(t) + \hat{H}_{\text{int},A_{\text{ext}},\parallel}(t) \\ &= \hat{H}_{\text{mat,kin}}(t) + \hat{H}_{\text{Stern}}(t) + \hat{H}_{\text{int},\parallel}(t) + \hat{H}_{\text{Ph,free}}(t) + \hat{H}_{\text{int},\vec{j}_{\text{ext}},\perp}(t) + \hat{H}_{\text{int},A_{\text{ext}},\parallel}(t) \\ &= - \sum_{n=1}^N \int d^3r \frac{1}{2M_{(n)}} \sum_s \hat{\Phi}_{(n)}^\dagger(\vec{r}, s, t) \hat{P}_{(n),k}(\vec{r}, t) \hat{P}_{(n)}^k(\vec{r}, t) \hat{\Phi}_{(n)}(\vec{r}, s, t) \\ &\quad + \sum_{n=1}^N \int d^3r \frac{\hbar q_{(n)}}{2M_{(n)}} \sum_{s,s'} \hat{\Phi}_{(n)}^\dagger(\vec{r}, s, t) [\mathbf{S}_{(n),k}]_{ss'} \hat{\Phi}_{(n)}(\vec{r}, s', t) \left(\frac{1}{c_0} \epsilon^{klm} \partial_l \hat{A}_m(\vec{r}, t) \right) \\ &\quad + \frac{1}{2c_0^2} \int d^3r d^3r' w(\vec{r}, \vec{r}') \sum_{n,n'} : \hat{j}_{\text{mat},(n)}^0(\vec{r}, t) \hat{j}_{\text{mat},(n'),0}(\vec{r}', t) : \\ &\quad + \int d^3r : \hat{F}_{+,\perp,k}(\vec{r}, t) \hat{F}_{-,\perp}^k(\vec{r}, t) : + \frac{1}{c_0} \int d^3r j_{\text{ext}}^k(\vec{r}, t) \hat{A}_k(\vec{r}, t) \\ &\quad + \sum_{n=1}^N \sum_s \int d^3r q_{(n)} A_{\text{ext},0}(\vec{r}, t) \hat{\Phi}_{(n)}^\dagger(\vec{r}, s, t) \hat{\Phi}_{(n)}(\vec{r}, s, t) . \end{aligned} \quad (4.3.21)$$

Next, we discuss the Maxwell's equations of coupled electromagnetic fields. The inhomogeneous Maxwell's equations in Coulomb gauge and vector potential $A^\mu(\vec{r}, t)$ representation coupled to an external current density $j_{\text{ext}}^\mu(\vec{r}, t)$ are expressed in Eq. (A.4.16). Replacing the external current with system current density $j^\mu(\vec{r}, t)$ from Eq. (4.3.8) with external scalar potential $j_{\text{ext}}^0(\vec{r}, t) = 0$ leads to

$$(\partial_0^2 + \partial_l \partial^l) \hat{A}^k(\vec{r}, t) = \mu_0 c_0 \left(\hat{j}_{\text{mat}}^k(\vec{r}, t) + j_{\text{ext}}^k(\vec{r}, t) \right) - \partial^k \partial^0 \frac{1}{c_0} \int d^3r' w(\vec{r}, \vec{r}') \hat{j}_{\text{mat}}^0(\vec{r}', t) \quad (4.3.22)$$

Substituting the last term in Eq. (4.3.22) with the longitudinal current density Eq. (A.4.17), here in terms of the internal current density $j_{\text{mat}}^k(\vec{r}, t)$ and external current density $j_{\text{ext}}^k(\vec{r}, t)$ yields

$$\begin{aligned} (\partial_0^2 + \partial_l \partial^l) \hat{A}^k(\vec{r}, t) &= \mu_0 c_0 \hat{j}^k(\vec{r}, t) - \mu_0 c_0 \hat{j}_{\text{mat}, \parallel}^k(\vec{r}, t) \\ \Leftrightarrow (\partial_0^2 + \partial_l \partial^l) \hat{A}^k(\vec{r}, t) &= \mu_0 c_0 \left(\hat{j}_{\text{mat}}^k(\vec{r}, t) + j_{\text{ext}}^k(\vec{r}, t) \right) - \mu_0 c_0 \hat{j}_{\text{mat}, \parallel}^k(\vec{r}, t) \quad (4.3.23) \\ \Leftrightarrow (\partial_0^2 + \partial_l \partial^l) \hat{A}^k(\vec{r}, t) &= \mu_0 c_0 \left(\hat{j}_{\text{mat}, \perp}^k(\vec{r}, t) + j_{\text{ext}}^k(\vec{r}, t) \right). \end{aligned}$$

It determines the k -component of the vector potential $A^k(\vec{r}, t)$. The corresponding zero component of the four-vector potential $A^\mu(\vec{r}, t)$ is given by Eq. (A.5.14) and reads

$$A^0(\vec{r}, t) = \frac{1}{c_0} \int d^3 r' w(\vec{r}, \vec{r}') \left(j_{\text{mat}}^0(\vec{r}', t) + j_{\text{mat}}^0(\vec{r}', t) \right) + A_{\text{ext}}^0(\vec{r}, t), \quad (4.3.24)$$

According to appendix Sec. A.4, we can equivalently express the inhomogeneous Maxwell's equations, Eq. (4.3.22), in terms of the Riemann-Silberstein vector. Adapting Eqs. (A.4.21) - (A.4.24) with the total field vectors $\hat{F}_{\pm}^\mu(\vec{r}, t)$ and current density $\hat{j}^\mu(\vec{r}, t)$ leads to the underlying quantized Maxwell's equations in Riemann-Silberstein representation

$$i \hbar c_0 \partial_0 \hat{F}_{\pm}^k(\vec{r}, t) = \mp i \hbar c_0 \left(\mathbf{S}^l \partial_l \right)^{km} \hat{F}_{\pm, m}(\vec{r}, t) - i \frac{\hbar}{\sqrt{2\epsilon_0}} \left(\hat{j}_{\text{mat}}^k(\vec{r}, t) + j_{\text{ext}}^k(\vec{r}, t) \right), \quad (4.3.25)$$

$$\partial_k \hat{F}_{\pm}^k(\vec{r}, t) = \sqrt{\frac{1}{2\epsilon_0}} \hat{j}_{\text{mat}}^0(\vec{r}, t). \quad (4.3.26)$$

In principle, the N-species Pauli-Fierz Hamiltonian in Eq. (4.3.21) determines the non-relativistic light-matter system that consists of N different species. Since the Hamiltonian is described in Fock-space, the corresponding wave function $\Psi(\vec{r}, t)$ has no fixed particle number, for both particles with mass and for photons. Due to the arising infinite degrees of freedom, it is not possible to apply the common wave function-based Hamiltonian formalism to solve the problem. Even the constraint of a fixed particle number does not lead to a solution, since the photon degrees of freedom are still infinite.

However, to deal with such systems, one can also fix the photon particle number by describing few photon modes, e.g., in a photon cavity [48, 57]. Another possible way is to describe such a large number of photons with arbitrary modes, that their electromagnetic field expectation value becomes classical [101]. In this case, the corresponding vector potential becomes also classical. The matter system is still quantized, but trying to solve the many-body problem is very restricted to only few

particles since the degrees of freedom of all particles, which are coupled to each other, increase exponentially. One method to deal with such problems of large coupled many-particle systems is density functional theory (DFT) [66].

In recent work the standard density functional theory has been extended to quantum-electrodynamical density-functional theory (QEDFT). In the following section, we transform the N -species Pauli-Fierz Hamiltonian of Eq. (4.3.21) into a multi-species Hamiltonian of quantum-electrodynamical density-functional theory.

4.4 Quantum-electrodynamical density-functional theory for multi species

Many-body Schrödinger equations are not solvable for a large number of particles to obtain the corresponding wave functions due to their amount of degrees of freedom. To circumvent this situation, the common density functional formalism [66, 67] reduces the actual degrees of freedom by calculating all measurable observables \hat{O} in terms of an one particle density $n(\vec{r}, t)$ instead of the many-body wave functions. It describes the probability density to find a particle at position vector \vec{r} . In this section, we adapt the density functional method, which usually considered for only one species, to a multi species Quantum-electrodynamical density-functional theory.

Although we cannot determine the exact multi species many-body wave function $\Psi_{(\mathcal{N})}$ for the general Pauli-Fierz Hamiltonian Eq. (4.3.21) with practicable calculations, we start with its theoretical construction in Fock space. The number \mathcal{N} of all particles in the system is a sum of all $\mathcal{N}_{(n)}$ particles of each species n

$$\mathcal{N} = \sum_n^N \mathcal{N}_{(n)}. \quad (4.4.1)$$

The total system wave function $|\Psi_{(\mathcal{N})}\rangle$ with \mathcal{N} particles in total can be expressed as a Kronecker product of $N + 1$ species-specific wave functions $|\Psi_{(\mathcal{N}_{(n)})}\rangle$ with species particle number $\mathcal{N}_{(n)}$ plus the Photon wave function $|\Psi_{\text{Ph}}\rangle$

$$|\Psi_{(\mathcal{N})}\rangle = \underbrace{|\Psi_{(\mathcal{N}_{(1)})}\rangle \otimes \dots \otimes |\Psi_{(\mathcal{N}_{(n)})}\rangle \otimes \dots \otimes |\Psi_{(\mathcal{N}_{(N)})}\rangle}_{N \text{ species-specific wave functions}} \otimes |\Psi_{\text{Ph}}\rangle. \quad (4.4.2)$$

The total system wave function $|\Psi_{(\mathcal{N})}\rangle$ holds the normalization condition and only the scalar product of two different species waves functions is equal to zero, i.e., $\langle \Psi_{(\mathcal{N}_{(n)})} | \Psi_{(\mathcal{N}_{(n')})} \rangle = \delta_{nn'}$ and $\langle \Psi_{(\mathcal{N}_{(n)})} | \Psi_{\text{Ph}} \rangle = 0$

$$\langle \Psi_{(\mathcal{N})} | \Psi_{(\mathcal{N})} \rangle = \left(\prod_n^N \langle \Psi_{(\mathcal{N}_{(n)})} | \Psi_{(\mathcal{N}_{(n)})} \rangle \right) \cdot \langle \Psi_{\text{Ph}} | \Psi_{\text{Ph}} \rangle = 1, \quad (4.4.3)$$

$$\langle \Psi_{(\mathcal{N}_{(n)})} | \Psi_{(\mathcal{N}_{(n)})} \rangle = 1. \quad (4.4.4)$$

According to Ref. [102, 103, 104], a general species wave function $|\Psi_{(\mathcal{N}(n))}\rangle$ can be constructed in position representation by applying the species particle creation operator, i.e., $\hat{\Phi}_{(\mathcal{N}(n))}^\dagger(\vec{r}, s, t)$, $\mathcal{N}(n)$ times on the vacuum state $|0\rangle$

$$\begin{aligned} |\Psi_{(\mathcal{N}(n))}\rangle &= \sqrt{\frac{1}{\mathcal{N}(n)!}} \hat{\Phi}_{(\mathcal{N}(n))}^\dagger(\vec{r}_{(1(n))}, s_{(1(n))}, t) \dots \hat{\Phi}_{(\mathcal{N}(n))}^\dagger(\vec{r}_{(i(n))}, s_{(i(n))}, t) \dots \hat{\Phi}_{(\mathcal{N}(n))}^\dagger(\vec{r}_{(\mathcal{N}(n))}, s_{\mathcal{N}(n)}, t) |0\rangle \\ &= \left| \vec{r}_{(1(n))}, s_{(1(n))}; \dots; \vec{r}_{(i(n))}, s_{(i(n))}; \dots; \vec{r}_{(\mathcal{N}(n))}, s_{\mathcal{N}(n)}; t \right\rangle. \end{aligned} \quad (4.4.5)$$

Here, we labeled the pair of a particle position vector plus corresponding spin state with $(\vec{r}_{(i(n))}, s_{(i(n))})$ with a species specific particle index $i(n)$.

Next, we define the particle density $n_{(n)}(\vec{r}, t)$ of finding a particle of species n at position vector \vec{r} . The wave function $\mathcal{N}(n)$ -particle wave function depends on $3\mathcal{N}(n)$ coordinates. To obtain the particle density for a chosen species n , we have to integrate over all species and all position vectors starting with and sum up over all spin states except $\vec{r}_{(i(n))}, s_{(i(n))}$ of the requested species particle. Since all particles of one species are identical particles, we write the general position position vector and the corresponding particle spin state as $(\vec{r}, s) = (\vec{r}_{(i(n))}, s_{(i(n))})$ for any particle i of species n . Using the normalization condition of each species wave function from Eq. (4.4.4), the particle density of species n reads

$$n_{(n)}(\vec{r}, t) = \int d^3r_{(2(n))} \dots d^3r_{(\mathcal{N}(n))} \sum_s \left| \left\langle \Psi_{(\mathcal{N}(n))}(\vec{r}, s; \vec{r}_{(2(n))}, s_{(2(n))}; \dots; \vec{r}_{(\mathcal{N}(n))}, s_{(\mathcal{N}(n))}; t) \right\rangle \right|^2. \quad (4.4.6)$$

After defining the species-specific particle density, we can use the Hohenberg-Kohn theorem [105]. It indicates that there is a one-to-one correspondence between the ground state wave function $|\Psi_{(\mathcal{N}), (0)}\rangle$ from Eq. (4.4.2) expressed by the coordinates and the Kohn-Sham wave function $|\tilde{\Psi}_{(\mathcal{N}), (0)}[n_{(n)}(\vec{r}, t)]\rangle$ given in terms of the particle density $n_{(n)}(\vec{r}, t)$

$$\left| \Psi_{(\mathcal{N}), (0)}(\dots, (\vec{r}, s)_{(i(n))}, \dots, t) \right\rangle \rightarrow \left| \tilde{\Psi}_{(\mathcal{N}), (0)}[n_{(n)}(\vec{r}, t)] \right\rangle. \quad (4.4.7)$$

This means that all ground state observables \hat{O} , which are usually expressed in terms of $|\Psi_{(\mathcal{N}), (0)}(\dots, (\vec{r}, s)_{(i(n))}, \dots, t)\rangle$ with

$$\langle \hat{O} \rangle = \left\langle \Psi_{(\mathcal{N}), (0)}(\dots, (\vec{r}, s)_{(i(n))}, \dots, t) \left| \hat{O} \right| \Psi_{(\mathcal{N}), (0)}(\dots, (\vec{r}, s)_{(i(n))}, \dots, t) \right\rangle \quad (4.4.8)$$

can be also expressed in terms of the particle density $n_{(n)}(\vec{r}, t)$

$$\langle \hat{O} \rangle = \left\langle \tilde{\Psi}_{(\mathcal{N}), (0)}[n_{(n)}(\vec{r}, t)] \left| \hat{O} \right| \tilde{\Psi}_{(\mathcal{N}), (0)}[n_{(n)}(\vec{r}, t)] \right\rangle. \quad (4.4.9)$$

Consequently, the species current density $\vec{j}_{(n)}(\vec{r}, t)$ can be described in terms of $|\tilde{\Psi}_{(\mathcal{N}), (0)}[n_{(n)}(\vec{r}, t)]\rangle$. This gives us the opportunity to employ the Runge-Gross

theorem [106, 67], here on the non-relativistic level of the Pauli-Fierz Hamiltonian. The one-to-one correspondence using the Pauli-Fierz Hamiltonian for one species was proofed in Ref. [63, 107, 108], in that case for electrons.

Following the previously steps conceptually and expanding the proof by using properties of the total wave functions $|\Psi_{(\mathcal{N})}\rangle$, which solve the Schrödinger equation using the multi-species Hamiltonian of Eq. (4.3.21), leads to the corresponding proof for N species [63]. We note, the proof is based on the assumptions that the external vector potential $\vec{A}_{\text{ext}}(\vec{r}, t)$ is given in Coulomb gauge by

$$\partial_k A_{\text{ext}}^k(\vec{r}, t) = 0, \quad (4.4.10)$$

and the external current density has also to be transverse

$$\partial_k j_{\text{ext}}^k(\vec{r}, t) = 0. \quad (4.4.11)$$

This important one-to-one correspondence is the basis of constructing a Maxwell-Pauli-Kohn-Sham scheme in the next section.

4.5 Coupled Maxwell-Pauli-Kohn-Sham equations

In this section, we simplify our previous considered Maxwell-matter system which we described in so called "second quantization" with Fock spaces to only a "first quantization" semiclassical picture. A semiclassical description means, that the photon field become classical and in "first quantization" the matter particle number keeps constant.

As a first simplification makes the full system semiclassical (sc), since we change the photon field operators to classical electric field variables, i.e.,

$$\hat{A}^\mu(\vec{r}, t) \rightarrow A^\mu(\vec{r}, t), \quad \hat{F}_\pm^k(\vec{r}, t) \rightarrow F_\pm^k. \quad (4.5.1)$$

In other words, we use the mean-field approximation for the photon field, which indicates that the number of photons in the system is so large. In this manner, small changes of the total photon number are negligible.

The second issue needs more effort to discuss them here in greater detail. Hence, we only explain the basic idea and refer to the literature, e.g. in Ref. [101, 103, 104] for full deduction and exemplary consideration. In Fock space, the charged particle number of each species is not fixed and allows particle creation and annihilation. Therefore in the next simplification, we transforms the general Pauli-Fierz Hamiltonian in Fock space from Eq. (4.3.21) into a Hamiltonian with fixed particle (fp) number \mathcal{N} and fixed particle number $\mathcal{N}_{(n)}$ for each species. Mathematically, the fixed particle Hilbert space description of the full Maxwell-matter system is only a subset of the full Fock space. The many-body Fock state $|\Psi_{(\mathcal{N})}\rangle$ for all particles of the system can be expressed in position representation, given in Eq. (4.4.5), as well as in occupation-number representation (Fock space state). The projection of both

gives transformation coefficients [101, 103, 104], which are probability amplitudes, i.e., wave functions. In our case, we denote our proper transformation coefficient, respectively the \mathcal{N} -particle wave function $|\psi_{(\mathcal{N})}\rangle$. Furthermore according to the steps in Ref. [101, 103, 104], the Hamiltonian in Eq. (4.3.21) transforms to the fixed particle (fp) and semiclassical (sc) Hamiltonian $\hat{H}_{\text{Fierz,fp,sc}}(t)$

$$\begin{aligned} \hat{H}_{\text{Fierz,fp,sc}}(t) = & - \sum_{n=1}^N \frac{1}{2M_{(n)}} \sum_s \hat{P}_{\text{sc},(n),k}(\vec{r}, t) \hat{P}_{\text{sc},(n)}^k(\vec{r}, t) \\ & + \sum_{n=1}^N \frac{\hbar q_{(n)}}{2M_{(n)}} \sum_{s,s'} [\mathcal{S}_{(n),k}]_{ss'} \left(\frac{1}{c_0} \epsilon^{klm} \partial_l A_m(\vec{r}, t) \right) \\ & + \frac{1}{2c_0^2} \sum_{n,n'} \frac{q_{(n)}q_{(n')}}{4\pi\epsilon_0|\vec{r}-\vec{r}'|} + \sum_{n=1}^N q_{(n)} A_{\text{ext},0}(\vec{r}, t) \\ & + \int d^3r : F_{+,\perp,k}(\vec{r}, t) F_{-,\perp}^k(\vec{r}, t) : + \frac{1}{c_0} \int d^3r j_{\text{ext}}^k(\vec{r}, t) A_k(\vec{r}, t), \end{aligned} \quad (4.5.2)$$

with the canonical momentum coupled to a classical electromagnetic field $\hat{P}_{\text{sc},(n)}^k(\vec{r}, t)$

$$\hat{P}_{\text{sc},(n)}^k(\vec{r}, t) = -i\hbar\partial^k + \frac{q_{(n)}}{c_0} A^k(\vec{r}, t). \quad (4.5.3)$$

Explicitly solving for the wave function $|\psi_{(\mathcal{N})}\rangle$ of the generalized N -species Pauli-Fierz Hamiltonian in Eq. (4.5.2) is computationally not feasible. However, instead of solving the full problem, we can find an auxiliary effective non-interacting system $|\Phi_{(\mathbf{s}),(\mathcal{N})}\rangle$ with same number of particles and that has the same densities. In the following the index "s" represents the variables of this non-interacting system.

This so called Kohn-Sham construction [109, 110, 108, 111] exploits the previously discussed one-to-one correspondence in Sec. 4.4, which leads to a bijection between external and internal matter pairs

$$\left(A_{\text{ext},(\mathbf{s})}^\mu(\vec{r}, t), j_{\text{ext},(\mathbf{s})}^k(\vec{r}, t) \right) \leftrightarrow \left(j_{\text{mat}}^\mu(\vec{r}, t), A_{\text{mat}}^k(\vec{r}, t) \right). \quad (4.5.4)$$

Since the one-to-one correspondence also holds for the non-interacting system, we can find two mappings with

$$\begin{aligned} \left(j_{\text{mat}}^\mu(\vec{r}, t), A_{\text{mat}}^k(\vec{r}, t) \right) & \mapsto \left(A_{\text{mat}}^\mu(\vec{r}, t), j_{\text{ext}}^k(\vec{r}, t) \right), \\ \left(j_{\text{mat}}^\mu(\vec{r}, t), A_{\text{mat}}^k(\vec{r}, t) \right) & \mapsto \left(A_{\text{mat},(\mathbf{s})}^\mu(\vec{r}, t), j_{\text{ext},(\mathbf{s})}^k(\vec{r}, t) \right), \end{aligned} \quad (4.5.5)$$

which maps the internal matter variables $j_{\text{mat}}^\mu(\vec{r}, t)$ and $A_{\text{mat}}^k(\vec{r}, t)$ to external ones based on first the interacting species wave function $|\psi_{(\mathcal{N})}\rangle$ and second on the non-interacting wave function $|\Phi_{(\mathbf{s}),(\mathcal{N})}\rangle$. At this point, the extended Runge-Gross theorem for multi-species of Sec. 4.4 shows that the full coupled problem is equivalent

to the non-interacting problem using effective currents and potentials. This non-interacting Kohn-Sham picture includes an uncoupled photon field.

Instead of solving this photon field with infinitely many degrees of freedom, we equivalently use the classical inhomogeneous Maxwell's equations [108], since both descriptions, the classical field as well as the full quantized field lead per construction to the same internal matter vector potential $A_{\text{mat}}^k(\vec{r}, t)$. As a consequence, we select a non-interacting groundstate wave function $|\Phi_{(\mathbf{s}),(\mathcal{N}),0}\rangle$, which obeys [63, 107]

$$\left\langle \psi_{(\mathcal{N}),0} \left| \hat{j}_{\text{mat}}^0 \psi_{(\mathcal{N}),0} \right. \right\rangle = \left\langle \Phi_{(\mathbf{s}),(\mathcal{N}),0} \left| \hat{j}_{\text{mat}}^0 \Phi_{(\mathbf{s}),(\mathcal{N}),0} \right. \right\rangle. \quad (4.5.6)$$

Since this expectation value is equivalent to the initial matter charge density $j_{\text{mat}}^0(\vec{r}, t) = \rho_{\text{mat}}(\vec{r}, t)$ [63], this condition determines the initial Maxwell field by using the Gauß law.

Next, we consider the relations between the external current densities $j_{\text{ext}}^k(\vec{r}, t)$, $j_{\text{ext},(\mathbf{s})}^k(\vec{r}, t)$. Using the linearity of Maxwell's equations both mappings of the interacting external current density and the non-interacting current density are equal, and hence

$$j_{\text{ext}}^k(\vec{r}, t) \left[j_{\text{mat}}^\nu(\vec{r}, t), A_{\text{mat}}^l(\vec{r}, t) \right] = j_{\text{ext},(\mathbf{s})}^k(\vec{r}, t) \left[j_{\text{mat}}^\nu(\vec{r}, t), A_{\text{mat}}^l(\vec{r}, t) \right]. \quad (4.5.7)$$

Taking all previous considerations into account, we can follow the Kohn-Sham construction of Ref. [111], which requires the introduction of a mean-field exchange-correlation (mxc) potential $A_{\text{mxc}}(\vec{r}, t)$

$$A_{\text{mxc}}^\mu(\vec{r}, t) = A_{\text{ext},(\mathbf{s})}^\mu(\vec{r}, t) \left[j_{\text{mat}}^\nu(\vec{r}, t), A_{\text{ext}}^l(\vec{r}, t) \right] - A_{\text{ext}}^\mu(\vec{r}, t) \left[j_{\text{mat}}^\nu(\vec{r}, t), A_{\text{ext}}^l(\vec{r}, t) \right]. \quad (4.5.8)$$

The non-interacting potential $A_{\text{ext},(\mathbf{s})}^\mu$ is usually denoted as Kohn-Sham potential $A_{\text{KS}}^\mu(\vec{r}, t)$ and reads with Eq. (4.5.8)

$$A_{\text{KS}}^\mu(\vec{r}, t) = A_{\text{mxc}}^\mu(\vec{r}, t) + A_{\text{ext}}^\mu(\vec{r}, t). \quad (4.5.9)$$

We emphasize here, that in case of having an exact mean-field exchange-correlation potential $A_{\text{mxc}}(\vec{r}, t)$, the solution of the coupled MPKS problem leads to the exact internal matter pair $(j_{\text{mat}}^\mu(\vec{r}, t), A_{\text{mat}}^k(\vec{r}, t))$ for a given generalized Pauli-Fierz Hamiltonian $\hat{H} [A_{\text{ext}}^\mu(\vec{r}, t), j_{\text{ext}}^k(\vec{r}, t)]$.

The initial auxiliary total wave function $|\Phi_{(\mathbf{s}),(\mathcal{N})}\rangle$ of \mathcal{N} particles can be separated into N species-specific $\mathcal{N}_{(n)}$ -particle wave functions $|\Phi_{(\mathbf{s}),(\mathcal{N}_{(n)})}\rangle$ since all wave functions describe non-interacting particles and $|\Phi_{(\mathbf{s}),(\mathcal{N})}\rangle$ is a product of all $|\Phi_{(\mathbf{s}),(\mathcal{N}_{(n)})}\rangle$

$$|\Phi_{(\mathbf{s}),(\mathcal{N})}\rangle = \prod_n^N |\Phi_{(\mathbf{s}),(\mathcal{N}_{(n)})}\rangle, \quad (4.5.10)$$

and again $|\Phi_{(\mathbf{s}),(\mathcal{N}_{(n)})}(\vec{r}, t)\rangle$ is a product of $\mathcal{N}_{(n)}$ non-interacting particles wave functions $\phi_{(n),(i)}(\vec{r}, t)$, so called Kohn-Sham orbitals, of species n and orbital index i

$$|\Phi_{(\mathbf{s}),(\mathcal{N}_{(n)})}(\vec{r}_{1(n)}, \mathbf{s}_{1(n)}; \dots; \vec{r}_{i(n)}, \mathbf{s}_{i(n)}; \dots; \vec{r}_{\mathcal{N}_{(n)}}, \mathbf{s}_{\mathcal{N}_{(n)}}; t)\rangle = \prod_i^{\mathcal{N}_{(n)}} \phi_{(n),(i)}(\vec{r}_{i(n)}, \mathbf{s}_{i(n)}, t). \quad (4.5.11)$$

In the non-interacting picture all particle-particle interaction are represented by an external Kohn-Sham potential $A_{\text{KS}}(\vec{r}, t)$ and we employ the Kohn-Shame scheme [109, 110, 108, 111]. After reducing the semiclassical Pauli-Fierz Hamiltonian in Eq. (4.5.2) in a one-particle Hamiltonian, the corresponding auxiliary Maxwell-Pauli-Kohn-Sham (MPKS) equation takes the form

$$\begin{aligned} i\partial_t \phi_{(n),(i)}(\vec{r}_{i(n)}, \mathbf{s}_{i(n)}, t) &= \hat{\mathcal{P}}_{(n),k}(\vec{r}_{i(n)}, t) \hat{\mathcal{P}}_{(n)}^k(\vec{r}_{i(n)}, t) \phi_{(n),(i)}(\vec{r}_{i(n)}, \mathbf{s}_{i(n)}, t) \\ &\quad - qA_{\text{KS}}^0(\vec{r}, t) \phi_{(n),(i)}(\vec{r}_{i(n)}, \mathbf{s}_{i(n)}, t) \\ &\quad + \frac{q\hbar}{2M_{(n)}c_0} \mathbf{S}_{(n),k} \varepsilon^{klm} \partial_l A_{\text{KS}}^m(\vec{r}, t) \phi_{(n),(i)}(\vec{r}_{i(n)}, \mathbf{s}_{i(n)}, t), \end{aligned} \quad (4.5.12)$$

with the canonical momentum

$$\hat{\mathcal{P}}_{(n)}^k(\vec{r}_{i(n)}, t) = -i\hbar \partial_{i(n)}^k - \frac{q(n)}{c_0} A_{\text{KS}}^k(\vec{r}_{i(n)}, t). \quad (4.5.13)$$

The MPKS equation describes the Schrödinger equation with Pauli term for non-interacting one-particle Kohn-Sham orbitals $\phi_{(n),(i)}(\vec{r}_{i(n)}, \mathbf{s}_{i(n)}, t)$.

Depending on bosonic or fermionic species type, the corresponding wave function $\Phi_{(\mathbf{s}),(\mathcal{N}_{(n)})}$ from Eq. (4.5.11) has to be symmetric or anti-symmetric. Tensor products of Slater determinants and permanents obey the corresponding feature. In case of bosons, the corresponding symmetric wave function of \mathcal{N} particles of species n is a normalized permanent [112]

$$\begin{aligned} &|\Phi_{(\mathbf{s}),(\mathcal{N}_{(n)}),\text{sym}}(\vec{r}_{1(n)}, \mathbf{s}_{1(n)}; \dots; \vec{r}_{i(n)}, \mathbf{s}_{i(n)}; \dots; \vec{r}_{\mathcal{N}_{(n)}}, \mathbf{s}_{\mathcal{N}_{(n)}}; t)\rangle = \\ &\quad \left\{ \sqrt{\frac{1}{\mathcal{N}_{(n)}! \prod_i m_{(i)}!}} \right\} \sum_p \left(\prod_i \phi_{(n)}(\vec{r}_{p(i(n))}, \mathbf{s}_{p(i(n))}, t) \right), \end{aligned} \quad (4.5.14)$$

with permutations p acting on $\mathcal{N}_{(n)}$ particles. The first product symbol \prod multiplies the factorial m_i , the quantity for the number of times each single particle orbital states i appears in the state, the second product symbol multiplies all $\mathcal{N}_{(n)}$ permuted particle orbitals and all possible permutations are summed up by the \sum symbol. The fermion wave function is antisymmetrized by the normalized Slater determinant

with [112]

$$\begin{aligned} & \left| \Phi_{(\mathbf{s}), (\mathcal{N}_{(n)})}^{\text{a-sym}}(\vec{r}_{(1(n))}, \mathcal{S}_{(1(n))}; \dots; \vec{r}_{(i(n))}, \mathcal{S}_{(i(n))}; \dots; \vec{r}_{(\mathcal{N}_{(n)})}, \mathcal{S}_{(\mathcal{N}_{(n)})}, t) \right\rangle = \\ & \sqrt{\frac{1}{\mathcal{N}!}} \sum_p \text{sgn}(p) \left(\prod_i \phi_{(n)}(\vec{r}_{(p(i(n)))}, \mathcal{S}_{p(i(n))}, t) \right), \end{aligned} \quad (4.5.15)$$

where $\text{sgn}(p)$ denotes the sign of each permutation. The Kohn-Sham orbitals are spin-dependent according to their species spin and represented by the index $s_{(n)}$.

From Eq. (4.4.8), Eq. (4.4.9) and the one-one-correspondence Eq. (4.5.4), we know that for the ground state we have

$$\left\langle \psi_{(\mathcal{N}), (0)} \left| \hat{j}_{\text{mat}}^\mu \right| \psi_{(\mathcal{N}), (0)} \right\rangle = \left\langle \Phi_{(\mathbf{s}), (\mathcal{N}), (0)} \left| \hat{j}_{\text{mat}}^\mu \right| \Phi_{(\mathbf{s}), (\mathcal{N}), (0)} \right\rangle, \quad (4.5.16)$$

which gives the initial classical current density. However, in general for arbitrary excited states the classical exact current density cannot be obtained by the non-interacting state $|\Phi_{(\mathbf{s}), (\mathcal{N})}\rangle$. In principle, the current density has to be described by current density functionals [113], which is not included in our implementation. Nevertheless, we approximate the exact current density by taking the non-interacting wave functions $|\Phi_{(\mathbf{s}), (\mathcal{N})}\rangle$ to get $j_{\text{mat}}^\mu(\vec{r}, t)$ also beyond the ground state.

Taking the operator valued Maxwell's equations from Eq. (4.3.23) classically, turns to the classical Maxwell's equation in terms of the total vector potential $A^\mu(\vec{r}, t)$ of the system

$$(\partial_0^2 + \partial_l \partial^l) A^k(\vec{r}, t) = \mu_0 c_0 \left(j_{\text{mat}, \perp}^k(\vec{r}, t) + j_{\text{ext}}^k(\vec{r}, t) \right). \quad (4.5.17)$$

Consequently, the operator valued Riemann-Silberstein Maxwell's Eqs. (4.3.25) - (4.3.26) become classical equations with

$$i\hbar c_0 \partial_0 F_{\pm}^k(\vec{r}, t) = \mp i\hbar c_0 \left[\mathbf{S}^l \partial_l \right]^{km} F_{\pm, m}(\vec{r}, t) - i \frac{\hbar}{\sqrt{2\epsilon_0}} \left(j_{\text{mat}}^k(\vec{r}, t) + j_{\text{ext}}^k(\vec{r}, t) \right), \quad (4.5.18)$$

$$\partial_k F_{\pm}^k(\vec{r}, t) = \sqrt{\frac{1}{2\epsilon_0}} j_{\text{mat}}^0(\vec{r}, t), \quad (4.5.19)$$

which determines the classical electromagnetic field of the total system.

We emphasize here, that only the two coupled systems together, i.e., the electron-nucleus system and the photon field, without external fields are invariant with respect to the total momentum and total angular momentum of the coupled matter-photon system [62]. Consequently, translating or rotating only the matter system breaks this symmetry.

Due to the Kohn-Sham potential $A_{\text{KS}}^\mu(\vec{r}, t)$ used in Eq. (4.5.12) and the physical total potential $A^\mu(\vec{r}, t)$ in Eq. (4.5.17), we have in principle to find a relation between those two potentials.

At this point we note that we have quite some freedom in establishing the mappings as well as the MPKS systems. For instance, we can look at each individual particle-species' internal current and find that also each species' internal current can be used to establish a mapping individually. We could then (unphysically) assume that each species sees a different external field and then establish purpose built $A_{\text{mxc}}^\mu(\vec{r}, t)$.

Building the complete mxc potentials step by step could lead to an easier established and more accurate approximation for the mxc potentials. We do not discuss this issue in this work, but try to find a first approximation to simplify the MPKS construction, because even solving the coupled generalized Pauli-Fierz problem in terms of single-particle equations.

Furthermore, for the initial states, which can be determined from a ground-state reformulation of the generalized Pauli-Fierz problem following Ref. [50], it is often beneficial to make the Born-Oppenheimer approximation and treat the nuclei semi-classically.

The zero component of the Kohn-Sham vector potential $A_{\text{KS}}^0(\vec{r}, t)$ depend on the exchange-correlation potential $A_{\text{xc}}^0(\vec{r}, t)$. It combines the exchange interaction with the correlation interaction. The exchange interaction describes the energy that arises due to the exchange symmetry (symmetric or antisymmetric wave functions), when identical particle are exchanged compared to non-identical particle, whereas the particle correlation gives the interaction between electrons [114, 66]. Hence, $A_{\text{KS}}^0(\vec{r}, t)$ reads with $A^0(\vec{r}, t) = A_{\text{mat}}^0(\vec{r}, t) + A_{\text{ext}}^0(\vec{r}, t)$

$$\begin{aligned} A_{\text{KS}}^0(\vec{r}, t) &= A_{\text{mxc}}^0(\vec{r}, t) + A_{\text{ext}}^0(\vec{r}, t) \\ &= A_{\text{mat}}^0(\vec{r}, t) + A_{\text{ext}}^0(\vec{r}, t) + A_{\text{xc}}^0(\vec{r}, t). \end{aligned} \quad (4.5.20)$$

Since finding $A_{\text{mxc}}^k(\vec{r}, t)$ with Eq. (4.5.8) is a non-trivial problem, we use later in the applications the mean-field approximation $A_{\text{mxc}}^k(\vec{r}, t) \approx A_{\text{mat}}^k(\vec{r}, t)$ and the total vector potential of the system $A^k(\vec{r}, t) = A_{\text{mat}}^k(\vec{r}, t) + A_{\text{ext}}^k(\vec{r}, t)$

$$\begin{aligned} A_{\text{KS}}^k(\vec{r}, t) &= A_{\text{mxc}}^k(\vec{r}, t) + A_{\text{ext}}^k(\vec{r}, t) \\ &\approx A_{\text{mat}}^k(\vec{r}, t) + A_{\text{ext}}^k(\vec{r}, t) = A^k(\vec{r}, t). \end{aligned} \quad (4.5.21)$$

4.6 Classical limit for Nuclei

In general, nuclei consists of protons and neutrons, which have almost the same mass as protons. The fact that nuclei are much heavier than the electrons leads to very different time scales of motion, which means that the electrons are significantly faster than the nuclei. This feature is usually exploited by treating the nuclei classical. Although there are more advanced alternatives, e.g., factorization of electron-nuclear wave functions [33, 34], we illustrate in the present section how to simplify our MPKS scheme by describing the nuclei classically.

As a first step, we neglect the Stern-Gerlach term, since this term is suppressed with respect to the other fields by $1/M_{(n)}$. Now, we express the spatial orbitals in polar representation

$$\phi_{(n),(i)}(\vec{r}, t) = |\phi_{(n),(i)}(\vec{r}, t)| e^{(i/\hbar)S_{(n),(i)}(\vec{r}, t)}, \quad (4.6.1)$$

and substitute Eq. (4.6.1) into the MPKS Eq. (4.5.12). Here, $S_{(n),(i)}(\vec{r}, t)$, not as a bold symbol to distinguish from the spin matrices vector \mathbf{S}^k which we used in the previous sections, denotes the phase of the polar representation. After dropping the last term (Stern-Gerlach term), we find a Hamilton-Jacobi-type equation for $S_{(n),(i)}(\vec{r}, t)$ [115]

$$\begin{aligned} \partial_t S_{(n),(i)}(\vec{r}, t) &= \frac{\left(\partial_l S_{(n),(i)}(\vec{r}, t) + \frac{q_{(n)}}{c_0} A_{\text{KS},l}(\vec{r}, t) \right) \left(\partial^l S_{(n),(i)}(\vec{r}, t) + \frac{q_{(n)}}{c_0} A_{\text{KS}}^l(\vec{r}, t) \right)}{2M_{(n)}} \\ &\quad - q_{(n)} A_{\text{KS}}^0(\vec{r}, t) + \frac{\hbar^2}{2M_{(n)}} \frac{\partial_l \partial^l |\phi_{(n),(i)}(\vec{r}, t)|}{|\phi_{(n),(i)}(\vec{r}, t)|}. \end{aligned} \quad (4.6.2)$$

In a next step, we express the classical observables by their quantum variables. Starting with the matter current $\tilde{j}_{\text{mat}}(\vec{r}, t)$ from Eq. (4.3.4) without the magnetization current $j_{\text{mc}}^k(\vec{r}, t)$

$$\tilde{j}_{\text{mat}}^k(\vec{r}, t) = j_{\text{pmc}}^k(\vec{r}, t) + j_{\text{dmc}}^k(\vec{r}, t) \quad (4.6.3)$$

$$= \sum_n^N j_{\text{pmc},(n),(i)}^k(\vec{r}, t) + \sum_n^N j_{\text{dmp},(n),(i)}^k(\vec{r}, t), \quad (4.6.4)$$

where $j_{\text{pmc},(n),(i)}^k(\vec{r}, t)$ represents the paramagnetic current density of species n and Kohn-Sham orbital i , and $j_{\text{dmc},(n),(i)}^k(\vec{r}, t)$ the corresponding diamagnetic current density. After replacing the creation and annihilation operators $\hat{\psi}(\vec{r}, t)$ and $\hat{\psi}^\dagger(\vec{r}, t)$ with the Kohn-Sham wave function $\phi_{(n),(i)}(\vec{r}, t)$ and $\phi_{(n),(i)}^\dagger(\vec{r}, t)$ of species n and orbital index i , both current densities are given by

$$\hat{j}_{\text{pmc},(n),(i)}^k(\vec{r}, t) = \frac{\hbar q_{(n)}}{2M_{(n)}i} \left[\left(\partial^k \phi_{(n),(i)}^\dagger(\vec{r}, s, t) \right) \hat{\phi}_{(n)}(\vec{r}, s, t) - \hat{\phi}_{(n)}^\dagger(\vec{r}, s, t) \left(\partial^k \phi_{(n),(i)}(\vec{r}, s, t) \right) \right], \quad (4.6.5)$$

$$\hat{j}_{\text{dmc},(n),(i)}^k(\vec{r}, t) = -\frac{q_{(n)}}{M_{(n)}c_0^2} \hat{j}_{(n)}^0(\vec{r}, t) \hat{A}^k(\vec{r}, t). \quad (4.6.6)$$

We find with Eq. (4.6.1) plus the two corresponding current density Eqs. (4.6.5) - (4.6.6) for the current density contribution $j_{\text{mat},(n),(i)}^k(\vec{r}, t)$ of species n and orbital i

the expression

$$\begin{aligned}
 j_{\text{mat},(n),(i)}^k(\vec{r}, t) &= j_{\text{pmc},(n),(i)}^k(\vec{r}, t) + j_{\text{dmc},(n),(i)}^k(\vec{r}, t) \\
 &= \frac{q_{(n)}}{M_{(n)}} |\phi_{(n),(i)}(\vec{r}, t)| \vec{\nabla} S_{(n),(i)}(\vec{r}, t) - \frac{q_{(n)}^2}{M_{(n)}c_0} A_{\text{KS}}^k(\vec{r}, t) |\phi_{(n),(i)}(\vec{r}, t)|.
 \end{aligned} \tag{4.6.7}$$

Furthermore, the total velocity field becomes

$$v_{(n),(i)}^k(\vec{r}, t) = \frac{j_{\text{mat},(n),(i)}^k(\vec{r}, t)}{q_{(n)} |\phi_{(n),(i)}(\vec{r}, t)|} = \frac{1}{M_{(n)}} \left(-\partial^k S_{(n),(i)}(\vec{r}, t) - \frac{q_{(n)}}{c_0} A_{\text{KS}}^k(\vec{r}, t) \right), \tag{4.6.8}$$

and accordingly we can define the total momentum field $\vec{p}_{(n),(i)}(\vec{r}, t) = M_{(n)}\vec{v}_{(n),(i)}(\vec{r}, t)$. Next, we take the classical limit $\hbar \rightarrow 0$ for the nuclei, and the quantum-potential contribution (last term) in Eq. (4.6.2) goes to zero. The remaining terms can be expressed by

$$\begin{aligned}
 \partial_t S_{(n),(i)}(\vec{r}, t) &= - \left(v_{(n),(i)}^l(\vec{r}, t) \partial_l \right) p_{(n),(i)}^k(\vec{r}, t) \\
 &\quad - q_{(n)} A_{\text{KS}}^0(\vec{r}, t) \\
 &\quad - \frac{q_{(n)}}{M_{(n)}} \varepsilon^{klm} p_{(n),(i),l}(\vec{r}, t) \times B_{\text{KS},m}(\vec{r}, t),
 \end{aligned} \tag{4.6.9}$$

where

$$B_{\text{KS}}^k(\vec{r}, t) = -\frac{1}{c_0} \varepsilon^{klm} \partial_l A_{\text{KS},m}(\vec{r}, t). \tag{4.6.10}$$

Next, we add the partial time-derivative of the Kohn-Sham vector potential to both sides and define the total derivative for a co-moving reference frame that moves with the velocity field $\vec{v}_{(n),(i)}$ with

$$\dot{p}_{(n),(i)}^k(\vec{r}, t) = \partial_t p_{(n),(i)}^k(\vec{r}, t) + \left(v_{(n),(i)}^l(\vec{r}, t) \partial_l \right) p_{(n),(i)}^k(\vec{r}, t). \tag{4.6.11}$$

Using both, turns Eq. (4.6.11) into the classical Lorentz equation

$$\dot{p}_{(n),(i)}^k(\vec{r}, t) = q_{(n)} \varepsilon^{klm} v_{(n),(i),l}(\vec{r}, t) B_{\text{KS},m}(\vec{r}, t) + q_{(n)} E_{\text{KS}}^k(\vec{r}, t). \tag{4.6.12}$$

We exploit here that in Coulomb gauge, the transverse electric field $E_{\text{KS},\perp}^k(\vec{r}, t)$ and longitudinal electric field $E_{\text{KS},\parallel}^k(\vec{r}, t)$

$$E_{\text{KS}}^k(\vec{r}, t) = E_{\text{KS},\perp}^k(\vec{r}, t) + E_{\text{KS},\parallel}^k(\vec{r}, t) \tag{4.6.13}$$

can be obtained from $A_{\text{KS}}^\mu(\vec{r}, t)$ according to Eqs. (A.1.15) - (A.1.16) with

$$-\partial_0 A_{\text{KS}}^k(\vec{r}, t) = E_{\text{KS},\perp}^k(\vec{r}, t) \quad (4.6.14)$$

and

$$\partial^k A_{\text{KS}}^0(\vec{r}, t) = E_{\text{KS},\parallel}^k(\vec{r}, t) . \quad (4.6.15)$$

Similar to Sec. (4.5), we use here the mean-field approach for the Kohn-Sham four-vector potential $A_{\text{KS}}^\mu(\vec{r}, t)$ in Eqs. (4.5.20) - (4.5.21) to express the Kohn-Sham electric fields $E_{\text{KS},\parallel}^k(\vec{r}, t)$ and $E_{\text{KS},\perp}^k(\vec{r}, t)$.

Finally, the time derivative Eq. (4.6.12) of the momentum, the classical Lorentz force equation, can be solved by the method of characteristics, i.e., we can follow a specific classical trajectory that starts at $\vec{r}_{(n),(i)}(t_0)$ and $\vec{p}_{(n),(i)}(t_0)$. The initial wave function then gives us the initial distribution of these trajectories.

Chapter 5

Maxwell-Pauli-Kohn-Sham propagation on a three-dimensional grid

In chapter 4, we introduced a theory to describe molecular many-body systems in terms of a density-functional theory based on quantum electrodynamics (QED). Furthermore, we argued why a full QED calculation is not feasible for large systems. As a consequence, we first assume slowly moving particles (Pauli description) and a semiclassical description of the Maxwell fields. In this way, we have two coupled systems, the quantum mechanical Kohn-Sham system and the classical Maxwell system.

Usually the semiclassical picture is simplified further by considering only the electromagnetic field-to-matter coupling, but no back reaction, i.e., matter does not influence the transverse electric field. In this case, the Maxwell field has an external component and a purely longitudinal internal component. The external field interacts with the matter, i.e., induces electric currents and charge motion inside the matter, but the matter does not act back on the transverse degrees of the electric field. Thus, the external electromagnetic field propagates freely.

In this approximation, the total electromagnetic field is a superposition of the external field and the internal field is purely longitudinal due to the Coulomb interaction. This approach is valid for many cases, especially small systems. But the influence of the external electric field can be large enough to induce a significant back-reaction of matter such that an effective screening or polarization appears. This happens when significant currents are present in the system. Hence, the backward coupling of matter to light becomes important.

In the chapters 1 - 3, we introduced the Riemann-Silberstein formalism of Maxwell fields and developed a numerical propagation scheme to solve inhomogeneous Maxwell equations in a similar manner as is done in quantum mechanics for the time-dependent Schrödinger equation. We can use the same time-evolution method for the propagation of Kohn-Sham orbitals. We consider the electrons as the only quantum me-

chanical species, which we described in chapter 4. The nuclei are treated as classical particles, which obey the Ehrenfest equations [116].

In this chapter, we introduce our full coupled Ehrenfest-Maxwell-Pauli-Kohn-Sham system. Therefore, we use the Kohn-Sham charge and current density as the inhomogeneity. We use them to adapt the microscopic Riemann-Silberstein Maxwell's equation, such that these quantum-mechanical based variables couple to the classical electromagnetic field. In turn, we use the 'minimal coupling' for the electromagnetic field to matter coupling.

Additionally, we transform the Kohn-Sham Hamiltonian with the Power-Zienau-Woolley transformation to get a gauge independent light-matter coupling in terms of the electromagnetic field variables instead of the gauge dependent vector potential. The electric multipole interaction terms in turn require only transverse components of the electromagnetic field, which we obtain by a Helmholtz decomposition by solving a Poisson equation for each field dimension. Our full propagation on two separated coupled grids leads to various combination possibilities for the different grids which we introduce. Furthermore, the different physical length and time scales for light and matter demand a multi-scale consideration in space and time.

In order to solve the coupled Maxwell-Kohn-Sham propagation, we describe a efficient self-consistent propagation scheme. In the final part of this chapter, we consider the Maxwell-matter system as an open quantum system and introduce electromagnetic detectors to measure directly the outgoing electromagnetic field.

5.1 Riemann-Silberstein Maxwell's equations with Kohn-Sham current density

In Sec. 1.1.5 we have introduced the microscopic Riemann-Silberstein Maxwell's equations and the six-component vector $\mathcal{F}(\vec{r}, t)$. They describe the Maxwell fields in vacuum in the presence of a charge density $\rho(\vec{r}, t)$ and a current density $\vec{j}(\vec{r}, t)$, which are represented in the Riemann-Silberstein description by $\mathcal{Q}(\vec{r}, t)$ from Eq. (1.1.40) and by $\mathcal{J}(\vec{r}, t)$ from Eq. (1.1.46). Since we want to describe coupled Maxwell-Kohn-Sham systems, we apparently have to express the classical variables $\mathcal{Q}(\vec{r}, t)$ and $\mathcal{J}(\vec{r}, t)$ in Eq. (1.1.42) and Eq. (1.1.44) in terms of the corresponding quantum-mechanical Kohn-Sham expectation values. All Kohn-Sham variables for the selected species n depend on the Kohn-Sham density $n_{(n,i)}(\vec{r}, s_{(n)})$. We describe the Riemann-Silberstein variables $\mathcal{Q}(\vec{r}, t)$ and $\mathcal{J}(\vec{r}, t)$ in terms of the corresponding Kohn-Sham variables. Especially the Riemann-Silberstein current density $\mathcal{J}(\vec{r}, t)$ can be separated into several terms which we discuss in the following.

According to Sec. 4.5 each species is described by auxiliary one-particle Kohn-Sham orbitals $\phi_{(n,i)}(\vec{r}, s_{(n)})$ and the particle density $n_{(n,i)}(\vec{r}, s_{(n)})$ is given by

$$n_{(n,i)}(\vec{r}, s_{(n)}) = |\phi_{(n,i)}(\vec{r}, s_{(n)})|^2. \quad (5.1.1)$$

Using Eq. (A.5.3) with the Kohn-Sham wave functions leads to $j^0(\vec{r})$

$$j^0(\vec{r}, t) = \sum_{n=1}^N c_0 q(n) \sum_i^{I(n)} \sum_{s(n)} n_{(n,i)}(\vec{r}, s(n), t). \quad (5.1.2)$$

With the Riemann-Silberstein charge density Eq. (1.1.40), $\mathcal{Q}(\vec{r}, t)$ reads

$$\mathcal{Q}(\vec{r}, t) = \begin{pmatrix} 1 \\ 1 \end{pmatrix}_{2 \times 1} \otimes \left(\frac{1}{c_0 \sqrt{2\epsilon_0}} j^0(\vec{r}, t) \right)_{1 \times 1}. \quad (5.1.3)$$

Referring appendix A.4 and A.5 in case of no external electromagnetic field, only the Riemann-Silberstein charge density $\mathcal{Q}(\vec{r}, t)$ causes a purely longitudinal electric field and Eq. (1.1.42) holds

$$\mathcal{D} \cdot \mathcal{F}(\vec{r}, t) = \mathcal{Q}(\vec{r}, t). \quad (5.1.4)$$

Later in Sec. 6 we obtain the initial Riemann-Silberstein longitudinal electric field from the quantum mechanical groundstate charge density of the matter system.

For the Riemann-Silberstein current density in terms of the k-component of the quantum-mechanical four-vector current density $j^\mu(\vec{r}, t)$ we have to follow some considerations, starting with Eq. (A.5.19) plus an external current $j_{\text{ext}}^k(\vec{r}, t)$

$$j^k(\vec{r}, t) = j_{\text{pmc}}^k(\vec{r}, t) + j_{\text{dmc}}^k(\vec{r}, t) + j_{\text{mc}}^k(\vec{r}, t) + j_{\text{ext}}^k(\vec{r}, t). \quad (5.1.5)$$

The paramagnetic current $j_{\text{pmc}}^k(\vec{r}, t)$, the diamagnetic current $j_{\text{dmc}}^k(\vec{r}, t)$, and the magnetization current $j_{\text{mc}}^k(\vec{r}, t)$ in terms of the Kohn-Sham orbitals are explicitly given by

$$\begin{aligned} j_{\text{pmc}}^k(\vec{r}, t) = & \sum_{n=1}^N \frac{\hbar q(n)}{i2M(n)} \sum_i^{I(n)} \sum_{s(n)} \left[\left(\partial^k \phi_{(n,i)}^\dagger(\vec{r}, s(n), t) \right) \phi_{(n,i)}(\vec{r}, s(n), t) \right] \\ & - \sum_{n=1}^N \frac{\hbar q(n)}{i2M(n)} \sum_i^{I(n)} \sum_{s(n)} \left[\phi_{(n,i)}^\dagger(\vec{r}, s(n), t) \left(\partial^k \phi_{(n,i)}(\vec{r}, s(n), t) \right) \right], \end{aligned} \quad (5.1.6)$$

$$j_{\text{dmc}}^k(\vec{r}, t) = - \sum_{n=1}^N \frac{q(n)^2}{M(n)c_0} \left[\sum_i^{I(n)} \sum_{s(n)} n_{(n,i)}(\vec{r}, s(n), t) \right] A^k(\vec{r}, t), \quad (5.1.7)$$

$$j_{\text{mc}}^k(\vec{r}, t) = - \sum_{n=1}^N \left[\sum_i^{I(n)} \sum_{s(n)} \varepsilon^{klm} \partial_l \phi_{(n,i)}^\dagger(\vec{r}, s(n), t) \left(\frac{q(n)\hbar}{2M(n)} \mathbf{S}_m^{(n)} \right) \phi_{(n,i)}(\vec{r}, s(n), t) \right]. \quad (5.1.8)$$

All three current contributions depend on the particle charge $q_{(n)}$, particle mass $M_{(n)}$, and the single-particle wave functions. While the paramagnetic current and magnetization current do not depend explicitly on the Maxwell field, the diamagnetic current depend on the vector potential $A^k(\vec{r}, t)$.

According to Eq. (1.1.44), the corresponding microscopic Maxwell's Ampère's and Faraday's equation in Riemann-Silberstein representation coupled to quantum mechanical Kohn-Sham current density (5.1.7) - (5.1.8) can be expressed as

$$i\hbar \frac{\partial}{\partial t} \mathcal{F}(\vec{r}, t) = \mathcal{H}\mathcal{F}(\vec{r}, t) - i\hbar \mathcal{J}(\vec{r}, t), \quad (5.1.9)$$

where $\mathcal{J}(\vec{r}, t)$ represents the total quantum mechanical current density $j^k(\vec{r}, t)$ (Kohn-Sham current density plus external current density) from Eq. (5.1.5) with

$$\mathcal{J}(\vec{r}, t) = \begin{pmatrix} 1 \\ 1 \end{pmatrix}_{2 \times 1} \otimes \begin{pmatrix} j^k \end{pmatrix}_{3 \times 1}. \quad (5.1.10)$$

Since the diamagnetic current depends directly on the Riemann-Silberstein six-vector $\mathcal{F}(\vec{r}, t)$, it is convenient to separate the $\mathcal{J}_{\text{dmc}}(\vec{r}, t)$ from the remaining total current density $\mathcal{J}(\vec{r}, t)$ with

$$\mathcal{J}(\vec{r}, t) = \mathcal{J}_{\text{dmc}}(\vec{r}, t) + \mathcal{J}_{\text{loc}}(\vec{r}, t) \quad (5.1.11)$$

$$i\hbar \frac{\partial}{\partial t} \mathcal{F}(\vec{r}, t) = \mathcal{H}\mathcal{F}(\vec{r}, t) - i\hbar \mathcal{J}_{\text{dmc}}(\vec{r}, t) - i\hbar \mathcal{J}_{\text{loc}}(\vec{r}, t). \quad (5.1.12)$$

Here, the paramagnetic current $j_{\text{pmc}}^k(\vec{r}, t)$, the magnetization current $j_{\text{mc}}^k(\vec{r}, t)$ and the external current $j_{\text{ext}}^k(\vec{r}, t)$ contributions are expressed as a local Riemann-Silberstein current density $\mathcal{J}_{\text{loc}}(\vec{r}, t)$ with Eq. (1.1.46)

$$\mathcal{J}_{\text{loc}}(\vec{r}, t) = \frac{1}{\sqrt{2\epsilon_0}} \begin{pmatrix} 1 \\ 1 \end{pmatrix}_{2 \times 1} \otimes \begin{pmatrix} j_{\text{pmc}}^k(\vec{r}, t) + j_{\text{mc}}^k(\vec{r}, t) + j_{\text{ext}}^k(\vec{r}, t) \end{pmatrix}_{3 \times 1}, \quad (5.1.13)$$

because the corresponding currents Eq. (5.1.7) and Eq. (5.1.8) are local in space and time. The corresponding Riemann-Silberstein vector $\mathcal{J}_{\text{dmc}}(\vec{r}, t)$ of the diamagnetic current takes the form

$$\mathcal{J}_{\text{dmc}}(\vec{r}, t) = \frac{1}{\sqrt{2\epsilon_0}} \begin{pmatrix} 1 \\ 1 \end{pmatrix}_{2 \times 1} \otimes \begin{pmatrix} j_{\text{dmc}}^k(\vec{r}, t) \end{pmatrix}_{3 \times 1}. \quad (5.1.14)$$

The vector potential $A^k(\vec{r}, t)$ can be expressed in two ways using the Riemann-Silberstein six-vector $\mathcal{F}(\vec{r}, t)$ and thus also $\mathcal{J}_{\text{dmc}}(\vec{r}, t)$, which we show separately in the following.

First, we discuss the non-local in space description by using the relation between the vector potential $A^k(\vec{r}, t)$ and the magnetic field of Eq. (A.1.10). After solving for $A^k(\vec{r}, t)$, we obtain [75, 80]

$$\begin{aligned} A^k(\vec{r}, t) &= -c_0 \int d^3r' \frac{\varepsilon^{klm} \partial'_l B_m(\vec{r}', t)}{4\pi|\vec{r} - \vec{r}'|} \\ &= ic_0 \underbrace{\sqrt{\frac{\mu_0}{2}} \int d^3r' \frac{\varepsilon^{klm} \partial'_l}{4\pi|\vec{r} - \vec{r}'|} \left(F_{+,m}(\vec{r}', t) - F_{-,m}(\vec{r}', t) \right)}_{\text{Solution of poisson equation}}. \end{aligned} \quad (5.1.15)$$

The integral operation in Eq. (5.1.15) is a simple Poisson equation. Efficient methods exists to solve the Poisson equation which makes this equation easy to handle. Due to the vector potential, the diamagnetic current density for $\mathcal{J}_{\text{dmc},s}(\vec{r}, t)$ includes an integration over space and uses the six-vector Riemann-Silberstein Eq. (1.1.38) as well as the spin matrices representation Eq. (1.1.26) for the curl. Hence, $\mathcal{J}_{\text{dmc},s}(\vec{r}, t)$ takes the form

$$\mathcal{J}_{\text{dmc},s}(\vec{r}, t) = \left[\begin{pmatrix} 1 & -1 \\ 1 & -1 \end{pmatrix}_{2 \times 2} \otimes \left(\int d^3r' \frac{1}{2} \sqrt{\frac{\mu_0}{\epsilon_0}} \frac{\kappa(\vec{r}, t)}{|4\pi\vec{r} - \vec{r}'|} \mathbf{S}^m \partial'_m \right)_{3 \times 3} \right] \mathcal{F}(\vec{r}', t) \quad (5.1.16)$$

with function $\kappa_s(\vec{r}, t)$

$$\kappa(\vec{r}, t) = \sum_{n=1}^N \frac{q_{(n)}^2}{M_{(n)}} \left[\sum_{i=1, s_{(n)}}^{I_{(n)}} n_{(n,i)}(\vec{r}, s_{(n)}, t) \right], \quad (5.1.17)$$

that contains the matter mass and corresponding charge density. Since the diamagnetic current term $\mathcal{J}_{\text{dmc}}(\vec{r}, t)$ depends on the Riemann-Silberstein vector $\mathcal{F}(\vec{r}, t)$ according to Eq. (5.1.16), Eq. (5.1.12) can be written as

$$\begin{aligned} i\hbar \frac{\partial}{\partial t} \mathcal{F}(\vec{r}, t) &= \int_{t(0)}^t d^3r' \int dt' \delta(\vec{r} - \vec{r}') \delta(t - t') \mathcal{H} \mathcal{F}(\vec{r}', t') \\ &\quad + \int_{t(0)}^t d^3r' \int dt' \tilde{\mathcal{K}}_{\mathcal{J}_{\text{dmc},s}}(\vec{r}, \vec{r}', t, t') \mathcal{F}(\vec{r}', t') \\ &\quad - i\hbar \mathcal{J}_{\text{loc}}(\vec{r}, t). \end{aligned} \quad (5.1.18)$$

Here, we use a double integral over space and time and two corresponding delta functions, $\delta(\vec{r} - \vec{r}')$ and $\delta(t - t')$ to express the $\mathcal{H} \mathcal{F}(\vec{r}, t)$ term and the diamagnetic current density $\mathcal{J}_{\text{dmc}}(\vec{r}, t)$ of Eq. (5.1.12). In this form, we can define three auxiliary 6x6 dimensional matrices as integral kernels, $\tilde{\mathcal{H}}(\vec{r}, \vec{r}', t, t')$ for the Riemann-Silberstein Hamiltonian operation and $\tilde{\mathcal{K}}_{\mathcal{J}_{\text{dmc},s}}(\vec{r}, \vec{r}', t, t')$ for the diamagnetic current

density term. To show that the corresponding operations can be in principle non-local in space and time depend on four variables, the two position vectors \vec{r} , \vec{r}' , and the two times t , t' . The first one, $\tilde{\mathcal{H}}(\vec{r}, \vec{r}', t, t')$, contains the Riemann-Silberstein Hamiltonian \mathcal{H} explicitly given in Eq. (4.2.22) and the two delta functions

$$\begin{aligned} \tilde{\mathcal{H}}(\vec{r}, \vec{r}', t, t') &= \delta(\vec{r} - \vec{r}')\delta(t - t')\mathcal{H} \\ &= \begin{pmatrix} 1 & 0 \\ 0 & -1 \end{pmatrix}_{2 \times 2} \otimes \begin{pmatrix} -i\hbar c_0 \delta(\vec{r} - \vec{r}')\delta(t - t') [\mathbf{S}^m \partial'_m] \end{pmatrix}_{3 \times 3}. \end{aligned} \quad (5.1.19)$$

To shorten the full integral equation for $\mathcal{H}\mathcal{F}(\vec{r}, t)$, we introduce a new denotation $\mathcal{H} \star \mathcal{F}(\vec{r}, t)$ defined as

$$\mathcal{H} \star \mathcal{F}(\vec{r}, t) := \int_{t(0)}^t d^3r' \int dt' \tilde{\mathcal{H}}(\vec{r}, \vec{r}', t, t') \mathcal{F}(\vec{r}', t') = \mathcal{H}\mathcal{F}(\vec{r}, t). \quad (5.1.20)$$

In a similar way to the matrix integral kernel $\tilde{\mathcal{H}}(\vec{r}, \vec{r}', t, t')$, we define a 6x6 dimensions matrix integral kernel $\tilde{\mathcal{K}}_{\mathcal{J}_{\text{dmc},s}}(\vec{r}, \vec{r}', t, t')$ with

$$\tilde{\mathcal{K}}_{\mathcal{J}_{\text{dmc},s}}(\vec{r}, \vec{r}', t, t') = \begin{pmatrix} 1 & -1 \\ 1 & -1 \end{pmatrix}_{2 \times 2} \otimes \begin{pmatrix} -i\hbar \frac{1}{2} \sqrt{\frac{\mu_0}{\epsilon_0}} \delta(t - t') \kappa(\vec{r}, t) \frac{\mathbf{S}^m \partial'_m}{4\pi|\vec{r} - \vec{r}'|} \end{pmatrix}_{3 \times 3}. \quad (5.1.21)$$

Again, we introduce for the integral operations a short denotation $\mathcal{K}_{\mathcal{J}_{\text{dmc},s}} \star \mathcal{F}(\vec{r}, t)$

$$\mathcal{K}_{\mathcal{J}_{\text{dmc},s}} \star \mathcal{F}(\vec{r}, t) := \int_{t(0)}^t d^3r' \int dt' \tilde{\mathcal{K}}_{\mathcal{J}_{\text{dmc},s}}(\vec{r}, \vec{r}', t, t') \mathcal{F}(\vec{r}', t'). \quad (5.1.22)$$

Now, both double integral terms on the right hand side of Eq. (5.1.29) can be combined into one. In this manner, since both terms depend on the Riemann-Silberstein six-vector $\mathcal{F}(\vec{r}', t')$, the diamagnetic current contribution $\tilde{\mathcal{K}}_{\mathcal{J}_{\text{dmc},s}}(\vec{r}, \vec{r}', t, t')$ becomes part of a modified Maxwell Hamiltonian kernel $\tilde{\mathcal{H}}_{\mathcal{J}_{\text{dmc},s}}(\vec{r}, \vec{r}', t, t')$

$$\tilde{\mathcal{H}}_{\mathcal{J}_{\text{dmc},s}}(\vec{r}, \vec{r}', t, t') = \tilde{\mathcal{H}}(\vec{r}, \vec{r}', t, t') + \tilde{\mathcal{K}}_{\mathcal{J}_{\text{dmc},s}}(\vec{r}, \vec{r}', t, t'). \quad (5.1.23)$$

Finally, Eq. (5.1.18) is equivalent to

$$i\hbar \frac{\partial}{\partial t} \mathcal{F}(\vec{r}, t) = \mathcal{H}_{\mathcal{J}_{\text{dmc},s}} \star \mathcal{F}(\vec{r}, t) - i\hbar \mathcal{J}_{\text{loc}}(\vec{r}, t) \quad (5.1.24)$$

with the short integral denotation

$$\mathcal{H}_{\mathcal{J}_{\text{dmc},s}} \star \mathcal{F}(\vec{r}, t) = \int_{t(0)}^t d^3r' \int dt' \tilde{\mathcal{H}}_{\mathcal{J}_{\text{dmc},s}}(\vec{r}, \vec{r}', t, t') \mathcal{F}(\vec{r}', t'). \quad (5.1.25)$$

The second way to express $\mathcal{J}_{\text{dmc}}(\vec{r}, t)$ uses the relation between electric field and vector plus scalar potential from Eq. (A.1.9). In Coulomb gauge with $\partial_k \vec{A}^k(\vec{r}, t) = 0$, it can be reduced to [75, 80]

$$\begin{aligned}
 E^k(\vec{r}, t) &= -\partial^k \Phi(\vec{r}, t) - \frac{1}{c_0} \frac{\partial}{\partial t} A^k(\vec{r}, t) \\
 \Leftrightarrow E_{\perp}^k(\vec{r}, t) + E_{\parallel}^k(\vec{r}, t) &= -\partial^k \Phi(\vec{r}, t) - \frac{1}{c_0} \frac{\partial}{\partial t} A^k(\vec{r}, t) \\
 \Leftrightarrow E_{\perp}^k(\vec{r}, t) &= -\frac{1}{c_0} \frac{\partial}{\partial t} A^k(\vec{r}, t).
 \end{aligned} \tag{5.1.26}$$

Hence, we have to split the electric field in its transverse $\vec{E}_{\perp}(\vec{r}, t)$ and longitudinal $\vec{E}_{\parallel}(\vec{r}, t)$ components. We use the general vector field properties [117] that the gradient of a scalar field is always a longitudinal vector, i.e, $E_{\parallel}^k(\vec{r}, t) = -\partial^k \Phi(\vec{r}, t)$ and $A^k(\vec{r}, t)$ is purely transverse due to the Coulomb gauge condition. The last expression in Eq. (5.1.26) after replacing $\vec{E}_{\perp}(\vec{r}, t)$ by the corresponding Riemann-Silberstein Eq. (1.1.6) and integrating over time from time $t_{(0)}$ to time t leads to

$$A^k(\vec{r}, t) = -c_0 \sqrt{\frac{1}{2\epsilon_0}} \int_{t_{(0)}}^t dt' \left(F_{+}^k(\vec{r}, t') + F_{-}^k(\vec{r}, t') \right)_{\perp} + A^k(\vec{r}, t_{(0)}). \tag{5.1.27}$$

Here, the initial vector potential is $A^k(\vec{r}, t_{(0)})$. The vector potential Eq. (5.1.27) results with Eq. (5.1.7) and Eq. (1.1.38) in an integration over time expression for the diamagnetic current density $\mathcal{J}_{\text{dmc},t}(\vec{r}, t)$

$$\begin{aligned}
 \mathcal{J}_{\text{dmc},t}(\vec{r}, t) &= \left[\begin{pmatrix} 1 & 1 \\ 1 & 1 \end{pmatrix}_{2 \times 2} \otimes \begin{pmatrix} 1 \\ 2\epsilon_0 \kappa(\vec{r}, t) \mathbb{1}_3 \end{pmatrix}_{3 \times 3} \right] \mathcal{F}(\vec{r}, t') \\
 &\quad - \begin{pmatrix} 1 \\ 1 \end{pmatrix}_{2 \times 1} \otimes \left(\sqrt{\frac{\mu_0}{2}} \kappa(\vec{r}, t) A^k(\vec{r}, t_{(0)}) \right)_{3 \times 3}.
 \end{aligned} \tag{5.1.28}$$

Using the time integrated Eq. (5.1.28) instead of the space integrated Eq. (5.1.16) Eq. (5.1.12) can also be written as

$$\begin{aligned}
 i\hbar \frac{\partial}{\partial t} \mathcal{F}(\vec{r}, t) &= \int d^3 r' \int_{t_{(0)}}^t dt' \delta(\vec{r} - \vec{r}') \delta(t - t') \mathcal{H} \mathcal{F}(\vec{r}', t') \\
 &\quad + \int d^3 r' \int_{t_{(0)}}^t dt' \tilde{\mathcal{K}}_{\mathcal{J}_{\text{dmc},t}}(\vec{r}, \vec{r}', t, t') \mathcal{F}(\vec{r}', t') \\
 &\quad - i\hbar \mathcal{J}_{\text{loc}}(\vec{r}, t) - i\hbar \mathcal{J}_{\mathcal{A}}(\vec{r}, t, t_{(0)}).
 \end{aligned} \tag{5.1.29}$$

The initial vector potential term, the second term on the right-hand side of Eq. (5.1.29), can be seen as a current contribution term $\mathcal{J}_{\mathcal{A}}(\vec{r}, t, t_{(0)})$ with

$$\mathcal{J}_{\mathcal{A}}(\vec{r}, t, t_{(0)}) = \sqrt{\frac{\mu_0}{2}} \kappa(\vec{r}, t) \mathcal{A}(\vec{r}, t_{(0)}) . \quad (5.1.30)$$

The six-vector $\mathcal{A}(\vec{r}, t)$ denotes the Riemann-Silberstein expression for the vector potential $\vec{A}(\vec{r}, t)$ with

$$\mathcal{A}(\vec{r}, t) = \left[\left(\begin{array}{c} 1 \\ 1 \end{array} \right)_{2 \times 1} \otimes \left(\begin{array}{c} \mathbb{1}_3 \end{array} \right)_{3 \times 1} \right] \vec{A}(\vec{r}, t) . \quad (5.1.31)$$

The two Riemann-Silberstein currents $\mathcal{J}_{\text{loc}}(\vec{r}, t)$ and $\mathcal{J}_{\mathcal{A}}(\vec{r}, t, t_{(0)})$, the last two terms on the right-hand side of Eq. (5.1.29), can be combined to one effective current density $\mathcal{J}_{\text{loc}, \mathcal{A}}(\vec{r}, t, t_{(0)})$

$$\mathcal{J}_{\text{loc}, \mathcal{A}}(\vec{r}, t, t_{(0)}) = \mathcal{J}_{\text{loc}}(\vec{r}, t) + \mathcal{J}_{\mathcal{A}}(\vec{r}, t, t_{(0)}) . \quad (5.1.32)$$

Analogous to Eq. (5.1.21), the corresponding integral kernel $\tilde{\mathcal{K}}_{\mathcal{J}_{\text{dmc}, t}}(\vec{r}, \vec{r}', t, t')$ for the non-local in space case reads

$$\tilde{\mathcal{K}}_{\mathcal{J}_{\text{dmc}, t}}(\vec{r}, \vec{r}', t, t') = \left(\begin{array}{cc} 1 & 1 \\ 1 & 1 \end{array} \right)_{2 \times 2} \otimes \left(-i\hbar \frac{1}{2\epsilon_0} \kappa(\vec{r}, t) \mathbb{1}_3 \right)_{3 \times 3} . \quad (5.1.33)$$

The shorten integral denotation for the second term on the right-hand side of Eq. (5.1.29) is

$$\mathcal{K}_{\mathcal{J}_{\text{dmc}, s}} \star \mathcal{F}(\vec{r}, t) := \int d^3 r' \int_{t_{(0)}}^t dt' \tilde{\mathcal{K}}_{\mathcal{J}_{\text{dmc}, s}}(\vec{r}, \vec{r}', t, t') \mathcal{F}(\vec{r}', t') . \quad (5.1.34)$$

Similar to the previously discussed non-local in space consideration, the diamagnetic current kernel for the non-local in time integration $\tilde{\mathcal{K}}_{\mathcal{J}_{\text{dmc}, s}}(\vec{r}, \vec{r}', t, t')$ can be added to the Hamiltonian kernel $\tilde{\mathcal{H}}(\vec{r}, \vec{r}', t, t')$

$$\tilde{\mathcal{H}}_{\mathcal{J}_{\text{dmc}, t}}(\vec{r}, \vec{r}', t, t') = \tilde{\mathcal{H}}(\vec{r}, \vec{r}', t, t') + \tilde{\mathcal{K}}_{\mathcal{J}_{\text{dmc}, t}}(\vec{r}, \vec{r}', t, t') . \quad (5.1.35)$$

In this manner, the two first terms on the right-hand side of Eq. (5.1.29) can be written as

$$\mathcal{H}_{\mathcal{J}_{\text{dmc}, t}} \star \mathcal{F}(\vec{r}, t) := \int d^3 r' \int_{t_{(0)}}^t dt' \tilde{\mathcal{H}}_{\mathcal{J}_{\text{dmc}, t}}(\vec{r}, \vec{r}', t, t') \mathcal{F}(\vec{r}', t') . \quad (5.1.36)$$

Finally, the complete Ampère's and Faraday's Maxwell's in Riemann-Silberstein representation with microscopic quantum mechanical current densities Eq. (5.1.9) can be expressed in a short form. It can be expressed non-local in space with Eq. (5.1.25)

$$i\hbar \frac{\partial}{\partial t} \mathcal{F}(\vec{r}, t) = \mathcal{H}_{\mathcal{J}_{\text{dmc},s}} \star \mathcal{F}(\vec{r}, t) - i\hbar \mathcal{J}_{\text{loc}}(\vec{r}, t). \quad (5.1.37)$$

or non-local in time with Eq. (5.1.36) and Eq. (5.1.32)

$$i\hbar \frac{\partial}{\partial t} \mathcal{F}(\vec{r}, t) = \mathcal{H}_{\mathcal{J}_{\text{dmc},t}} \star \mathcal{F}(\vec{r}, t) - i\hbar \mathcal{J}_{\text{loc},\mathcal{A}}(\vec{r}, t, t_{(0)}). \quad (5.1.38)$$

The non-local Hamiltonian operations $\mathcal{H}_{\mathcal{J}_{\text{dmc},s}} \star \mathcal{F}(\vec{r}, t)$ and $\mathcal{H}_{\mathcal{J}_{\text{dmc},t}} \star \mathcal{F}(\vec{r}, t)$ in this expression require some adaptations for the real-time propagation, which is the subject of the next section.

In future publications, we will examine the relation between the coupling in a linear medium determined by $\mathcal{K}_{\text{lm}}(\vec{r})\mathcal{F}_{\text{lm}}(\vec{r}, t)$ using $\mathcal{K}_{\text{lm}}(\vec{r})$ from Eq. (1.2.40) and $\mathcal{K}_{\text{dmc},s} \star \mathcal{F}(\vec{r}, t)$ from Eq. (5.1.21) respectively $\mathcal{K}_{\text{dmc},t} \star \mathcal{F}(\vec{r}, t)$ from Eq. (5.1.33). In all three cases the two helicity Riemann-Silberstein vectors $\vec{F}_+(\vec{r}, t)$ and $\vec{F}_-(\vec{r}, t)$ couple each other.

5.2 Riemann-Silberstein Maxwell propagation coupled to the Kohn-Sham current density

In the previous section, we expressed in Eq. (5.1.37) respectively in Eq. (5.1.38) the Ampère's and Faraday's law as an inhomogeneous Schrödinger-like equation in the Riemann-Silberstein formalism. To get a general expression for the Riemann-Silberstein time-propagation with quantum-mechanical current density, we start with the inhomogeneous time-evolution Eq. (2.2.14). According to Sec. 5.1, the diamagnetic current density $\mathcal{J}_{\text{dmc}}(\vec{r}, t)$ modifies the Maxwell Hamiltonian

$$\mathcal{H}\mathcal{F}(\vec{r}, t) \rightarrow \mathcal{H}_{\mathcal{J}_{\text{dmc},s/t}} \star \mathcal{F}(\vec{r}, t). \quad (5.2.1)$$

Here, $\mathcal{H}_{\mathcal{J}_{\text{dmc},s/t}}$ denotes one of the two diamagnetic current Hamiltonians, $\mathcal{H}_{\mathcal{J}_{\text{dmc},s}}$ from Eq. (5.1.25) or $\mathcal{H}_{\mathcal{J}_{\text{dmc},t}}$ from Eq. (5.1.36). Consequently we have to adapt the first time-evolution operator in Eq. (2.2.14) with the two Riemann-Silberstein representations of a Maxwell system coupled to a Kohn-Sham current density, i.e., Eq. (5.1.37) or Eq. (5.1.38), to

$$\mathcal{U}(t, t_{(0)})\mathcal{F}(\vec{r}, t_{(0)}) \rightarrow \mathcal{U}_{\mathcal{J}_{\text{dmc},s/t}} \star (t, t_{(0)})\mathcal{F}(\vec{r}, t_{(0)}). \quad (5.2.2)$$

After that, we adapt the total inhomogeneous time-evolution from Eq. (2.2.14)

$$\mathcal{F}(\vec{r}, t) = \mathcal{U}(t, t_{(0)})\mathcal{F}(\vec{r}, t_{(0)}) - \int_{t_{(0)}}^t d\tau \mathcal{U}(t, \tau) \mathcal{J}(\vec{r}, \tau) \quad (5.2.3)$$

to the proper time-evolution with local current density $\mathcal{J}_{\text{loc}}(\vec{r}, t)$ and use Eq. (5.2.2). Therefore, we obtain

$$\mathcal{F}(\vec{r}, t) = \mathcal{U}_{\mathcal{J}_{\text{dmc}}}(t, t_{(0)}) \star \mathcal{F}(\vec{r}, t_{(0)}) - \int_{t_{(0)}}^t d\tau \mathcal{U}(t, \tau) \mathcal{J}_{\text{loc}}(\vec{r}, \tau). \quad (5.2.4)$$

First, we determine the $\mathcal{U}_{\mathcal{J}_{\text{dmc}}}(t, t_{(0)}) \star \mathcal{F}(\vec{r}, t_{(0)})$ operation, we set $\mathcal{J}_{\text{loc}}(\vec{r}, t)$ equal to zero and a non-zero. The two Riemann-Silberstein equations, Eq. (5.1.37) and Eq. (5.1.38), that couples the quantum mechanical current density to the Maxwell fields, become homogeneous

$$i\hbar \frac{\partial}{\partial t} \mathcal{F}(\vec{r}, t) = \mathcal{H}_{\mathcal{J}_{\text{dmc},s/t}} \star \mathcal{F}(\vec{r}, t), \quad (5.2.5)$$

Here, $\mathcal{H}_{\mathcal{J}_{\text{dmc},s/t}} \star \mathcal{F}(\vec{r}, t)$ denotes the two different possible Maxwell Hamiltonian operations $\mathcal{H}_{\mathcal{J}_{\text{dmc},s}} \star \mathcal{F}(\vec{r}, t)$ from Eq. (5.1.25) and $\mathcal{H}_{\mathcal{J}_{\text{dmc},t}} \star \mathcal{F}(\vec{r}, t)$ from Eq. (5.1.36). The corresponding time-evolution operation $\mathcal{U}_{\mathcal{J}_{\text{dmc}}}(t, t_{(0)}) \star \mathcal{F}(\vec{r}, t_{(0)})$, that propagates the Maxwell's fields from a given time $t_{(0)}$ to t similar to chapter 2, considers the integral kernels $\tilde{\mathcal{H}}_{\mathcal{J}_{\text{dmc},s}}(\vec{r}, \vec{r}', t, t')$ from Eq. (5.1.23) or $\tilde{\mathcal{H}}_{\mathcal{J}_{\text{dmc},t}}(\vec{r}, \vec{r}', t, t')$ from Eq. (5.1.35). Analogous to the time-evolution operator in quantum mechanics, the corresponding one $\mathcal{U}_{\mathcal{J}_{\text{dmc}}}(t, t_{(0)})$ includes the $\mathcal{H}_{\mathcal{J}_{\text{dmc},s/t}} \star \mathcal{F}(\vec{r}, t)$ operations in Eq. (5.1.25) respectively Eq. (5.1.36). Taking this into account, we express the time-evolution operation to propagate a Riemann-Silberstein vector from time $t_{(0)}$ to t by

$$\mathcal{F}(\vec{r}, t) = \mathcal{U}_{\mathcal{J}_{\text{dmc}}}(t, t_{(0)}) \star \mathcal{F}(\vec{r}, t_{(0)}). \quad (5.2.6)$$

The time-evolution operation has to obey the group composition laws known from quantum mechanics [118]

$$1.) \quad \mathcal{U}_{\mathcal{J}_{\text{dmc}}}^\dagger(t, t_{(0)}) \star \mathcal{U}_{\mathcal{J}_{\text{dmc}}}(t, t_{(0)}) \star \mathcal{F}(\vec{r}, t_{(0)}) = \mathcal{F}(\vec{r}, t_{(0)}), \quad (5.2.7)$$

$$2.) \quad \lim_{t \rightarrow t_{(0)}} \mathcal{U}_{\mathcal{J}_{\text{dmc}}}(t, t_{(0)}) \star \mathcal{F}(\vec{r}, t_{(0)}) = \mathcal{F}(\vec{r}, t_{(0)}), \quad (5.2.8)$$

$$3.) \quad \mathcal{U}_{\mathcal{J}_{\text{dmc}}}(t_2, t_{(0)}) = \mathcal{U}_{\mathcal{J}_{\text{dmc}}}(t_2, t_1) \star \mathcal{U}_{\mathcal{J}_{\text{dmc}}}(t_1, t_{(0)}) \star \mathcal{F}(\vec{r}, t_{(0)}). \quad (5.2.9)$$

Let us first consider the homogeneous case. The operator $\mathcal{U}_{\mathcal{J}_{\text{dmc}}}(t, t_{(0)})$ should then obey the infinitesimal time evolution equation

$$\mathcal{U}_{\mathcal{J}_{\text{dmc}}}(t_{(0)} + dt) \star \mathcal{F}(\vec{r}, t_{(0)}) = \mathcal{F}(\vec{r}, t_{(0)}) + \frac{i}{\hbar} dt \mathcal{H}_{\mathcal{J}_{\text{dmc}}}(\vec{r}, t_{(0)}) \star \mathcal{F}(\vec{r}, t_{(0)}) \quad (5.2.10)$$

Applying Eq. (5.2.10) serial for many infinitesimal time-evolutions leads to a series expansion for the time evolution operation $\mathcal{U}_{\text{dmc}}(t, t_{(0)}) \star \mathcal{F}(\vec{r}, t_{(0)})$ very similar our discussion in Sec. 2.3 for the linear medium propagation. With the time ordering

operator $\hat{\mathcal{T}}$ and the Dyson series time symmetric considerations from ref. [83], we obtain

$$\begin{aligned} & \mathcal{U}_{\mathcal{J}_{\text{dmc}}}(t, t_{(0)}) \star \mathcal{F}(\vec{r}, t_{(0)}) = \\ & \mathcal{F}(\vec{r}, t_{(0)}) + \sum_{k=1}^{\infty} \frac{1}{k!} \left(\frac{i}{\hbar} \right)^k \hat{\mathcal{T}} \prod_{p=1}^k \int_{t_{(0)}}^t d\tau_{(p)} \int d^3 r_{(p)} \int_{t_{(0)}}^{\tau_{(p)}} dt_{(p)} \tilde{\mathcal{H}}_{\mathcal{J}_{\text{dmc},s/t}}(\vec{r}_{(p-1)}, \vec{r}_{(p)}, t_{(p)}, t_{(0)}) \mathcal{F}(\vec{r}_{(p)}, t_{(0)}), \end{aligned} \quad (5.2.11)$$

where we used Eq. (5.1.25) respectively Eq. (5.1.36), $\vec{r}_{(0)} = \vec{r}$, and $\hat{\mathcal{T}}$ the time-ordering operator such that earlier times go to the right.

For the simplest case, where the paramagnetic current $j_{\text{pmc}}^k(\vec{r}, t)$, the diamagnetic current $j_{\text{dmc}}^k(\vec{r}, t)$, the magnetization current $j_{\text{mc}}^k(\vec{r}, t)$, and $j_{\text{ext}}^k(\vec{r}, t)$ are equal to zero, we obtain with Eq. (5.1.5), Eq. (5.1.13) and Eq.(5.1.14)

$$\left. \begin{aligned} j_{\text{dmc}}^k(\vec{r}, t) &= 0 \\ j_{\text{pmc}}^k(\vec{r}, t) &= 0 \\ j_{\text{mc}}^k(\vec{r}, t) &= 0 \\ j_{\text{ext}}^k(\vec{r}, t) &= 0 \end{aligned} \right\} \left. \begin{aligned} \mathcal{J}_{\text{dmc}}(\vec{r}, t) &= 0 \\ \mathcal{J}_{\text{loc}}(\vec{r}, t) &= 0 \end{aligned} \right\} \mathcal{J}(\vec{r}, t) = 0. \quad (5.2.12)$$

The corresponding time evolution equation in (5.2.11) reduces and the underlying Riemann-Silberstein Maxwell's time-evolution equation in (5.2.5) becomes

$$i\hbar \frac{\partial}{\partial t} \mathcal{F}(\vec{r}, t) = \mathcal{H} \mathcal{F}(\vec{r}, t), \quad (5.2.13)$$

which is equivalent to Eq. (2.1.2) with \mathcal{H} from Eq. (4.2.22). The corresponding time-evolution equation is given in Eq. (2.1.16), i.e,

$$\mathcal{F}(\vec{r}, t) = \mathcal{U}(t, t_{(0)}) \mathcal{F}(\vec{r}, t_{(0)}), \quad (5.2.14)$$

$$\mathcal{U}(t, t_{(0)}) = \exp \left[-\frac{i}{\hbar} \mathcal{H}(t - t_{(0)}) \right]. \quad (5.2.15)$$

In a second step, we consider non-zero current densities $\mathcal{J}_{\text{dmc}}(\vec{r}, t)$ and $\mathcal{J}_{\text{loc}}(\vec{r}, t)$ with $\mathcal{J}(\vec{r}, t) = \mathcal{J}_{\text{dmc}}(\vec{r}, t) + \mathcal{J}_{\text{loc}}(\vec{r}, t)$ and start with Eq. (5.1.9). In this case, the Riemann-Silberstein Maxwell's equation takes

$$\frac{\partial}{\partial t} \mathcal{F}(\vec{r}, t) = -\frac{i}{\hbar} \mathcal{H} \mathcal{F}(\vec{r}, t) - \mathcal{J}(\vec{r}, t). \quad (5.2.16)$$

We already discussed the corresponding time-evolution equation for an inhomogeneous Schrödinger equation in Sec. (2.2). It has the following form also given in Eq. (2.2.14)

$$\mathcal{F}(\vec{r}, t) = \mathcal{U}(t, t_{(0)}) \mathcal{F}(\vec{r}, t_{(0)}) - \int_{t_{(0)}}^t d\tau \mathcal{U}(t, \tau) \mathcal{J}(\vec{r}, \tau). \quad (5.2.17)$$

including all quantum-mechanical current densities of Eqs. (5.1.7) - (5.1.8). If we consider the separation of $\mathcal{J}(\vec{r}, t)$ with Eq. (5.1.11), we can rewrite Eq. (5.2.17) as

$$\mathcal{F}(\vec{r}, t) = \mathcal{U}(t, t_{(0)})\mathcal{F}(\vec{r}, t_{(0)}) - \int_{t_{(0)}}^t d\tau \mathcal{U}(t, \tau) \mathcal{J}_{\text{dmc}}(\vec{r}, \tau) - \int_{t_{(0)}}^t d\tau \mathcal{U}(t, \tau) \mathcal{J}_{\text{loc}}(\vec{r}, \tau). \quad (5.2.18)$$

The first two terms of the right-hand side of this equation are equivalent to Eq. (5.2.6). Hence, we can find for Eq. (5.2.17) the equivalent expression

$$\mathcal{F}(\vec{r}, t) = \mathcal{U}_{\mathcal{J}_{\text{dmc}}}(t, t_{(0)}) \star \mathcal{F}(\vec{r}, t_{(0)}) - \int_{t_{(0)}}^t d\tau \mathcal{U}(t, \tau) \mathcal{J}_{\text{loc}}(\vec{r}, \tau), \quad (5.2.19)$$

which is our requested general form of a time-evolution equation with quantum-mechanical current.

In Sec. 2.4 we have shown that the Maxwell Gauß laws as side conditions hold during the time-propagation. This property is also given for the microscopic time-evolution Eq. (5.2.17) and the equivalent Eq. (5.2.19). To show this we apply the \mathcal{D} operator from Eq. (1.1.41) on Eq. (5.2.17) to get $\mathcal{D} \cdot \mathcal{F}(\vec{r}, t)$ with

$$\mathcal{D} \cdot \mathcal{F}(\vec{r}, t) = \mathcal{D} \cdot \mathcal{U}(t, t_{(0)})\mathcal{F}(\vec{r}, t_{(0)}) - \int_{t_{(0)}}^t d\tau \mathcal{D} \cdot \mathcal{U}(\tau, t_{(0)}) \mathcal{J}(\vec{r}, \tau). \quad (5.2.20)$$

The current density $\mathcal{J}(\vec{r}, t)$ is classical, and the $\mathcal{U}(t, t_{(0)})$ Eq. (5.2.15) and its containing Hamiltonian \mathcal{H} from Eq. (4.2.22) is equivalent to the one considered in Sec. 2.4. Consequently, we can directly conclude that the Gauß side condition for the electromagnetic fields hold, if it holds for the initial Riemann-Silberstein vector. Furthermore, since Eq. (5.2.17) and Eq. (5.2.19) are equivalent, the conservation of the Gauß is also valid for Eq. (5.2.19).

5.3 Discretized time-evolution and Time-reversal symmetry of the Maxwell system

In Sec. 3.2, the discretized time-evolution equation is introduced in Eq. (3.2.2). Based on the time-evolution Eq. (5.2.19) coupled to Kohn-Sham current densities, the discretized time-evolution takes the recursive form

$$\mathcal{F}(\vec{r}, (m+1)\Delta t) = \mathcal{U}_{\mathcal{J}_{\text{dmc}}}((m+1)\Delta t, m\Delta t) \star \mathcal{F}(\vec{r}, m\Delta t) - \int_{m\Delta t}^{(m+1)\Delta t} d\tau \mathcal{U}(\tau, m\Delta t) \mathcal{J}_{\text{loc}}(\vec{r}, \tau). \quad (5.3.1)$$

Using this equation, the six-component Riemann-Silberstein vector $\mathcal{F}(\vec{r}, m\Delta t)$ at the discrete time $m\Delta t$ with $m \in \mathbb{N}$, evolves the system for a small time step Δt to time $(m+1)\Delta t$. Unfortunately this direct propagation scheme breaks the fundamental time-symmetry of the system.

The Pauli-Fierz Hamiltonian Eq. (4.5.2), describing the full coupling Maxwell-Matter system, and the corresponding Maxwell-Kohn-Sham equation are in principle symmetric under a time reversal transformation $t \rightarrow -t$. This constraint is only strictly given, if we consider the whole coupled Maxwell-matter system where both systems influence each other. Considering only forward coupling breaks the symmetry. Consequently, in the time-evolution step for full Maxwell-matter coupling, the time-evolution equation has to obey the property that a reverse time step from $\mathcal{F}(\vec{r}, m\Delta t)$ leads again to the previous result $\mathcal{F}(\vec{r}, (m-1)\Delta t)$. In general, this constraint is not fulfilled for simple time evolution steps. However, we can construct a numerical time-evolution equation based on the enforced time-reversal symmetry (ETRS) [119] for quantum mechanic systems. The underlying condition requires that a propagation forward starting from $\mathcal{F}(\vec{r}, m\Delta t)$ with $\Delta t/2$ and one backwards starting from $\mathcal{F}(\vec{r}, (m+1)\Delta t)$ with $\Delta t/2$ has to give the same value of $\mathcal{F}(\vec{r}, (m+1/2)\Delta t)$. A modified numerical recursive time-evolution equation for ETRS based on Eq. (3.2.2) takes the form

$$\begin{aligned} \mathcal{F}(\vec{r}, (m+1)\Delta t) &= \mathcal{U}_{\mathcal{J}_{\text{dmc}}}((m+1)\Delta t, m\Delta t) \star \mathcal{F}(\vec{r}, t) \\ &\quad - \int_{m\Delta t}^{(m+\frac{1}{2})\Delta t} d\tau \mathcal{U}(m\Delta t, \tau) \mathcal{J}_{\text{loc}}(\vec{r}, \tau) + \int_{m\Delta t}^{(m+\frac{1}{2})\Delta t} d\tau \mathcal{U}((m+1)\Delta t, \tau) \mathcal{J}_{\text{loc}}(\vec{r}, \tau) . \end{aligned} \quad (5.3.2)$$

The included integrals can be approximated by trapezoidal rule so that the numerical time-evolution equations take the explicit forms

$$\begin{aligned} \mathcal{F}(\vec{r}, (m+1)\Delta t) &\approx \mathcal{U}_{\mathcal{J}_{\text{dmc}}}((m+1)\Delta t, m\Delta t) \star \mathcal{F}(\vec{r}, m\Delta t) \\ &\quad - \frac{\Delta t}{2} \mathcal{U}((m+1)\Delta t, m\Delta t) \mathcal{J}_{\text{loc}}(\vec{r}, (m+1)\Delta t) \\ &\quad - \frac{\Delta t}{2} \mathcal{J}_{\text{loc}}(\vec{r}, m\Delta t) , \end{aligned} \quad (5.3.3)$$

for the simple direct propagation Eq. (5.3.1), and

$$\begin{aligned} \mathcal{F}(\vec{r}, (m+1)\Delta t) &\approx \mathcal{U}_{\mathcal{J}_{\text{dmc}}}((m+1)\Delta t, m\Delta t) \star \mathcal{F}(\vec{r}, m\Delta t) \\ &\quad - \frac{\Delta t}{4} \mathcal{U}((m+1)\Delta t, m\Delta t) \mathcal{J}_{\text{loc}}(\vec{r}, m\Delta t) \\ &\quad - \frac{\Delta t}{4} \mathcal{U}((m+1)\Delta t, (m+1/2)\Delta t) \mathcal{J}_{\text{loc}}(\vec{r}, (m+1/2)\Delta t) \\ &\quad - \frac{\Delta t}{4} \mathcal{J}_{\text{loc}}(\vec{r}, (m+1)\Delta t) \\ &\quad - \frac{\Delta t}{4} \mathcal{U}(m\Delta t, (m+1/2)\Delta t) \mathcal{J}_{\text{loc}}(\vec{r}, (m+1/2)\Delta t) \end{aligned} \quad (5.3.4)$$

for the ETRS propagation Eq. (5.3.2).

5.4 Discretized time-evolution and Time-reversal symmetry of the matter system

In contrast to our novel quantum mechanical like time-evolution equation for the six-component Maxwell-Riemann-Silberstein vector in chapter 2, various types of time-evolution schemes for Kohn-Sham orbitals are considered in the literature [119, 120] and implemented in quantum mechanical computer programs like octopus. In the present work, we use consistently the ETRS time-evolution method for both, matter and Maxwell, propagations. According to Eq. (4.5.12), the one-particle Maxwell-Pauli-Kohn-Sham (MPKS) Hamiltonian $\hat{h}_{\text{MPKS},(n)}(\vec{r}, t)$ for a species n with position vector \vec{r} takes the form

$$\begin{aligned} \hat{h}_{\text{MPKS},(n)}(\vec{r}, t) = & -\frac{1}{2M_{(n)}} \tilde{\mathcal{P}}_{(n)}^k(\vec{r}, t) \tilde{\mathcal{P}}_{(n),k}(\vec{r}, t) + q_{(n)} A_{\text{KS}}^0(\vec{r}, t) \\ & - \frac{\hbar q_{(n)}}{2M_{(n)} c_0} \mathbf{S}_{(n),k} \left[\epsilon^{klm} \partial_l A_{\text{KS},m}(\vec{r}, t) \right], \end{aligned} \quad (5.4.1)$$

where the canonical momentum is given by

$$\tilde{\mathcal{P}}_{(n)}^k(\vec{r}, t) = -i\hbar\partial^k + \frac{q_{(n)}}{c_0} A_{\text{KS}}^k(\vec{r}, t). \quad (5.4.2)$$

The total non-interacting many-body MPKS Hamiltonian $\hat{H}_{\text{MPKS},(n)}(t)$ is the sum over all N species and all $\mathcal{N}_{(n)}$ one-particle Hamiltonians $\hat{h}_{\text{MPKS},(n)}(\vec{r}, t)$ of species n with corresponding particle position vector $\vec{r}_{(i_{(n)})}$

$$\hat{H}_{\text{MPKS}}(t) = \sum_n^N \sum_{i_{(n)}}^{\mathcal{N}_{(n)}} \hat{h}_{\text{MPKS},(n)}(\vec{r}_{(i_{(n)})}, t). \quad (5.4.3)$$

The time evolution equation from starting time $t_{(0)}$ to time t contains the Kohn-Sham orbitals $\phi_{(n),(i)}(\vec{r}, t)$ for one species particle, that we introduced in Eq. (4.5.11), and is given by

$$\phi_{(n),(i)}(\vec{r}, t) = \hat{u}_{\text{MPKS},(n)}(t, t_{(0)}) \phi_{(n),(i)}(\vec{r}, t_{(0)}). \quad (5.4.4)$$

The corresponding time-ordered ($\hat{\mathcal{T}}$ MPKS time evolution operator $\hat{u}_{\text{MPKS},(n)}(t, t_{(0)})$ takes with the time-dependent one-particle MPKS Hamiltonian $\hat{h}_{\text{MPKS},(n)}(\vec{r}, t)$ in Eq. (5.4.1) the form [82, 83]

$$\hat{u}_{\text{MPKS},(n)}(\vec{r}, t, t_{(0)}) = \hat{\mathcal{T}} \exp \left[-i \int_{t_{(0)}}^t d\tau \hat{h}_{\text{MPKS},(n)}(\vec{r}, \tau) \right]. \quad (5.4.5)$$

For a non-interacting particle system, the full time evolution operator Eq. (5.4.5) is a Kronecker product (\otimes) of $\mathcal{N}_{(n)}$ occupied Kohn-Sham orbitals for species n

$$\hat{U}_{(n)}(t, t_{(0)}) = \otimes_{i=1}^{\mathcal{N}_{(n)}} \hat{u}_{\text{MPKS},(n)}(\vec{r}_{(i_{(n)})}, t, t_{(0)}) . \quad (5.4.6)$$

The total Kohn-Sham wave function $|\Phi_{(s),(n)}\rangle$ of species n from Eq. (4.5.11) evolves in time by

$$|\Phi_{(s),(n)}(t)\rangle = \hat{U}_{(n)}(t, t_{(0)}) |\Phi_{(s),(n)}(t_{(0)})\rangle , \quad (5.4.7)$$

The evolution operators do not need to be (anti-)symmetrized, since the symmetry of the initial state is preserved.

We use for both subsystems, light and matter, the same propagation scheme and construct also a numerical enforced-time-reversal-symmetry propagation for the Kohn-Sham orbitals. The numerical ETRS time-evolution equation for the $(m+1)\Delta t$ time step from current time $m\Delta t$ for the total Kohn-Sham system reads

$$|\Phi_{(s),(n)}((m+1)\Delta t)\rangle = \hat{U}_{(n)}((m+1)\Delta t, m\Delta t) |\Phi_{(s),(n)}(m\Delta t)\rangle . \quad (5.4.8)$$

According to the full many-body Hamiltonian splitting as a sum of one-particle Hamiltonians in Eq. (5.5.1) and the corresponding time-evolution operator splitting as a product of one-particle time-evolution operators in Eq. (5.4.6), the full time-evolution is based on the time-evolution of each species-specific Kohn-Sham orbital $\phi_{(n),(i)}(\vec{r}_{(i_{(n)})}, m\Delta t)$. Therefore, the time-evolution of the full Kohn-Sham state from Eq. (5.4.6) can be obtained by the one-particle time-evolution for each particle and species

$$\phi_{(n),(i)}(\vec{r}_{(i_{(n)})}, (m+1)\Delta t) = \hat{u}_{\text{MPKS,ETRS},(n)}((m+1)\Delta t, m\Delta t) \phi_{(n),(i)}(\vec{r}_{(i_{(n)})}, m\Delta t) \quad (5.4.9)$$

with the corresponding ETRS time-evolution operator for species n [119]

$$\begin{aligned} \hat{u}_{\text{MPKS,ETRS},(n)}((m+1)\Delta t, m\Delta t) = \\ \exp\left[-i\frac{\Delta t}{2}\hat{h}_{\text{MPKS},(n)}((m+1)\Delta t)\right] \exp\left[-i\frac{\Delta t}{2}\hat{h}_{\text{MPKS},(n)}(m\Delta t)\right] . \end{aligned} \quad (5.4.10)$$

Similar to the Maxwell time-evolution, the time step parameter Δt has to yield to a stable and quite accurate propagation. In contrast to the Maxwell system, there is no CFL criterion for the Kohn-Sham evolution since in our non-relativistic approximation the speed of matter waves is not capped by a fixed velocity. However, for our applications we have a non-relativistic low energy region for the electrons in mind for which the Kohn-Sham orbitals motion is much slower than the speed of light. Hence, the maximum Δt is in most cases much larger than the one for the Maxwell fields. We focus on this issue later in Sec. 5.6 when we discuss different propagation levels.

5.5 Kohn-Sham interaction Hamiltonian

The electromagnetic field interaction with matter is in principle described by extending the Dirac equation with the full minimal coupling term. The full minimal coupling takes both, the Lorentz- and gauge-invariance into account. The non-relativistic MPKS approach of Sec. 4.3 breaks this symmetry. However, it is still an accurate approximation for particles in a low energy limit. Higher order extension of the Pauli-Fierz Hamiltonian exists that consider relativistic corrections. But for most applications, the MPKS approach leads to sufficiently accurate results.

In this section, we derive the multipole expansion as one possible approximation, which gives in first order the most commonly used Maxwell-to-matter interaction term, the dipole approximation. We introduce additionally electric quadrupole and magnetic dipole coupling to investigate later effects beyond the dipole coupling to show the influence of this approximation.

5.5.1 Full minimal coupling

The full minimal coupling was applied by substituting the canonical momentum transformation Eq. (A.2.1) into the Dirac Eq. (4.2.10). Based on the Pauli and QEDFT approaches, we get the full minimal coupling Kohn-Sham Hamiltonian from Eq. (5.4.1). Next, we separate the Hamiltonian into a kinetic Hamiltonian $\hat{H}_{\text{kin}}(t)$ and an interaction Hamiltonian $\hat{H}_{\text{int}}(t)$ which includes Maxwell and matter variables

$$\begin{aligned} \hat{H}_{\text{MPKS},(n)}(t) &= \hat{H}_{\text{MPKS,kin},(n)}(t) + \hat{H}_{\text{MPKS,int},(n)}(t) \\ &= \sum_i^{\mathcal{N}_{(n)}} \hat{h}_{\text{MPKS,kin},(n)}(\vec{r}_{(i_{(n)})}, t) + \sum_i^{\mathcal{N}_{(n)}} \hat{h}_{\text{MPKS,int},(n)}(\vec{r}_{(i_{(n)})}, t), \end{aligned} \quad (5.5.1)$$

where the kinetic piece is given by

$$\hat{h}_{\text{MPKS,kin},(n)}(\vec{r}_{(i_{(n)})}) = \frac{\hbar^2}{2M_{(n)}} \partial_{(i_{(n)})}^k \partial_{(i_{(n)})},k}, \quad (5.5.2)$$

and the light-matter coupling is contained in

$$\begin{aligned} \hat{h}_{\text{MPKS,int},(n)}(\vec{r}_{(i_{(n)})}, t) &= -\frac{i\hbar q_{(n)}}{M_{(n)}} A_{\text{KS}}^k(\vec{r}_{(i_{(n)})}, t) \partial_k + \frac{q_{(n)}^2}{2M_{(n)}} A_{\text{KS}}^k(\vec{r}_{(i_{(n)})}, t) A_{\text{KS},k}(\vec{r}_{(i_{(n)})}, t) \\ &\quad + q_{(n)} A_{\text{KS}}^0(\vec{r}_{(i_{(n)})}, t) - \frac{q_{(n)} \hbar}{2M_{(n)} c_0} \sigma_k \epsilon^{klm} \partial_l A_{\text{KS},m}(\vec{r}_{(i_{(n)})}, t). \end{aligned} \quad (5.5.3)$$

From Sec. 4.5 we know that we get the physical total vector potential $A^k(\vec{r}, t)$ with the Riemann-Silberstein propagation. Finding accurate approximations for the corresponding Kohn-Sham potential $A_{\text{KS}}^k(\vec{r}, t)$ is one aspect for future work. As a first approximation for $A_{\text{KS}}^k(\vec{r}, t)$, we use here Eq. (4.5.21). The mean field vector potential $A^k(\vec{r}, t)$ is determined by the Riemann-Silberstein vector via Eq. (5.1.15).

We note here, that the total vector potential especially the scalar potential component $A_{\text{KS}}^0(\vec{r}, t)$, given in Eq. (4.5.20), in principle includes all electronic and nuclear potentials.

5.5.2 Multipole expansion

In many applications, the correct full minimal coupling is expensive to calculate or not needed since the length scales of matter and radiation differ vastly. Therefore, the minimal coupling is often approximated by a multipole expansion using the electric and magnetic fields variables. As is well-known, the ubiquitous electric dipole approximation is equivalent to the lowest order term of the multipole expansion. In the following, we briefly summarize the derivation of the multipole expansion based on the Power-Zienau-Woolley transformation (cf. chapter 5.2 of Ref. [121]) and adapt it to the present Maxwell-Pauli-Kohn-Sham case. As first step, we introduce the polarization species-specific $\vec{P}_{(n)}(\vec{r})$ of species n as the sum over all considered species particles i

$$\vec{P}_{(n)}(\vec{r}) = \frac{q(n)}{c_0} \sum_i \vec{r}_{(i(n))} \int_0^1 \delta(\vec{r} - \alpha \vec{r}_{(i(n))}) d\alpha. \quad (5.5.4)$$

In Coulomb gauge with $\vec{\nabla} \cdot \vec{A}_{\text{KS}} = 0$, the vector potential is always transverse and hence the unitary Power-Zienau-Woolley transformation $\hat{U}_{\text{PZW},(n)}$ is defined by

$$\begin{aligned} \hat{U}_{\text{PZW},(n)} &= \exp \left[\frac{i}{\hbar} \int d^3r \vec{P}_{(n),\perp}(\vec{r}) \cdot \vec{A}_{\text{KS}}(\vec{r}) \right] \\ &= \exp \left[\frac{iq(n)}{\hbar} \sum_i^{\mathcal{N}_{(n)}} \int_0^1 \vec{r}_{(i(n))} \cdot \vec{A}_{\text{KS}}(\alpha \vec{r}_{(i(n))}) d\alpha \right]. \end{aligned} \quad (5.5.5)$$

Next, we transform the MPKS Hamiltonian $\hat{H}_{\text{MPKS},(n)}$ from Eq. (5.5.1) using $\hat{U}_{\text{PZW},(n)}$ into

$$\hat{H}'_{\text{MPKS},(n)} = \hat{U}_{\text{PZW},(n)}^{-1} \hat{H}_{\text{MPKS},(n)} \hat{U}_{\text{PZW},(n)} \quad (5.5.6)$$

According to the Power-Zienau-Woolley transformation, the corresponding Kohn-Sham wave function $|\Phi'_{(\mathbf{s}), (n)}\rangle$ starting with the one $|\Phi_{(\mathbf{s}), (n)}\rangle$ from Sec. (4.4) are given by

$$\begin{aligned} |\Phi'_{(\mathbf{s}), (n)}\rangle &= \hat{U}_{\text{PZW},(n)}^{-1} |\Phi_{(\mathbf{s}), (n)}\rangle \\ &= \prod_i^{\mathcal{N}_{(n)}} \phi'_{(n), (i)}(\vec{r}_{(i(n))}, s_{(i(n))}, t). \end{aligned} \quad (5.5.7)$$

Here, $\phi'_{(n), (i)}(\vec{r}_{(i(n))}, s_{(i(n))}, t)$ represents the Power-Zienau-Woolley transformed Kohn-Sham orbital i of species n of the initial ones introduced in Eq. (4.5.11). In the same

way as in Eqs. (4.5.11) - (4.5.11), the transformed wave functions $|\Phi'_{(s)(n)}\rangle$ can be build symmetric and anti-symmetric.

Next, we transform the nabla operator of particle i

$$\hat{U}_{\text{PZW},(n)}^{-1} \vec{\nabla}_{(i(n))} \hat{U}_{\text{PZW}} = \vec{\nabla}_{(i(n))} + \frac{iq(n)}{\hbar c_0} \int_0^1 \left(\vec{\nabla}_{(i(n))} \vec{r}_{(i(n))} \cdot \vec{A}_{\text{KS}}(\alpha \vec{r}_{(i(n))}, t) d\alpha \right). \quad (5.5.8)$$

Finally, applying the transformed Power-Zienau-Wolley Hamiltonian $\hat{H}'_{\text{MPKS},(n)}$ from Eq. (5.5.6) to the transformed wave functions $|\Phi'_{(s)(n)}\rangle$ leads to the transformed Power-Zienau-Woolley Kohn-Sham equation

$$\begin{aligned} i\hbar \partial_t \phi'_{(n),(i)}(\vec{r}, s(n), t) = & \frac{1}{2M(n)} \left(-i\hbar \vec{\nabla} + \frac{q(n)}{c_0} \int_0^1 \alpha \vec{r} \times \vec{B}_{\text{KS}}(\alpha \vec{r}, t) d\alpha \right)^2 \phi'_{(n),(i)}(\vec{r}, s(n), t) \\ & + q(n) A_{\text{KS}}^0(\vec{r}, t) \phi'_{(n),(i)}(\vec{r}, s(n), t) \\ & + q(n) \int_0^1 \vec{r} \cdot \vec{E}_{\text{KS},\perp}(\alpha \vec{r}, t) d\alpha \phi'_{(n),(i)}(\vec{r}, s(n), t) \\ & - \frac{q(n)\hbar}{2M(n)} \vec{S}^{(n)} \cdot \vec{B}_{\text{KS}}(\vec{r}, s(n), t) \phi'_{(n),(i)}(\vec{r}, s(n), t). \end{aligned} \quad (5.5.9)$$

Rewriting the transformed Hamiltonian of the previous equation leads to the multipole expansion of the Kohn-Sham Hamiltonian with

$$\hat{H}'_{\text{MPKS},(n)} = \hat{H}_{\text{MPKS,kin},(n)} + \underbrace{\hat{H}_{\text{MPKS,ED},(n)} + \hat{H}_{\text{MPKS,MD},(n)} + \hat{H}_{\text{MPKS,EQ},(n)} + \dots}_{\hat{H}_{\text{MPKS,int},(n)}}, \quad (5.5.10)$$

where the kinetic Hamiltonian $\hat{H}_{\text{MPKS,kin},(n)}$ is given in Eq. (5.5.2). The remaining multipole terms until second order are the electric dipole term $\hat{H}_{\text{MPKS}}^{\text{ED},(n)}$

$$\hat{h}_{\text{MPKS,ED}}(\vec{r}, \vec{r}_0) = e \vec{r} \cdot \vec{E}_{\perp}(\vec{r}_0) \quad (5.5.11)$$

$$\hat{H}_{\text{MPKS,ED},(n)} = \sum_i \hat{h}_{\text{MPKS,ED}}(\vec{r}_{(i(n))}, \vec{r}_0), \quad (5.5.12)$$

the magnetic dipole term $\hat{H}_{\text{MPKS,MD},(n)}$

$$\hat{h}_{\text{MPKS,MD}}(\vec{r}, \vec{r}_0) = \left(-i \frac{e\hbar}{2m} \vec{B}(\vec{r}_0) \cdot (\vec{r} \times \vec{\nabla}) \right) \quad (5.5.13)$$

$$\hat{H}_{\text{MPKS,MD},(n)} = \sum_i \hat{h}_{\text{MPKS,MD}}(\vec{r}_{(i(n))}, \vec{r}_0), \quad (5.5.14)$$

and the electric quadrupole term $\hat{H}_{\text{MPKS,EQ},(n)}$

$$\hat{h}_{\text{MPKS,EQ}}(\vec{r}, \vec{r}_{(0)}) = \frac{1}{2} e \left(\vec{r} \cdot \vec{\nabla} \right) \vec{r} \cdot \left(\vec{E}_{\perp}(\vec{r}) \right) \Big|_{\vec{r}=\vec{r}_{(0)}} \quad (5.5.15)$$

$$\hat{H}_{\text{MPKS,EQ},(n)} = \sum_i \hat{h}_{\text{MPKS,EQ}}(\vec{r}_{(i_n)}, \vec{r}_{(0)}) . \quad (5.5.16)$$

They are all expanded around the expansion point $\vec{r}_{(0)}$, which can be chosen in good approximation either as center of mass or center of charge of the matter system. We note here, that we employed the Power-Zienau-Woolley transformation on classical Kohn-Sham fields. For quantized fields, the result differ and a usual Taylor expansion is not applicable [5, 122, 62].

5.5.3 Transverse Riemann-Silberstein vector calculation

The Power-Zienau-Woolley transformed Hamiltonian results in Maxwell-matter coupling in terms of the electric and magnetic field. Whereas the magnetic dipole term depends on the total magnetic field, the electric dipole and quadrupole terms depend only on the transverse component of the electric field. Consequently, we have to decompose the Riemann-Silberstein vector into its transverse and longitudinal components. In general, the Helmholtz-decomposition [117] formula for the Riemann-Silberstein vector is given by

$$\vec{F}_{\pm,\perp}(\vec{r}, t) = \vec{\nabla} \times \underbrace{\int_V d^3 r' \frac{\vec{\nabla}_{\vec{r}'} \times \vec{F}_{\pm}(\vec{r}', t)}{4\pi |\vec{r} - \vec{r}'|}}_{\text{Solution of poisson equation}} - \frac{1}{4\pi} \oint_S dS' \vec{n} \times \frac{\vec{F}_{\pm}(\vec{r}', t)}{4\pi |\vec{r} - \vec{r}'|}, \quad (5.5.17)$$

where V gives the volume of the considered system, S the corresponding surface and dS' gives the infinitesimal surface area at position vector \vec{r}' . The first term on the right-hand side of Eq. (5.5.17) can be computed efficiently by a Poisson solver since it is the solution of the Poisson equation. Octopus provides several effective Poisson solvers [93, 123] to obtain Kohn-Sham potentials for matter systems, which we adapt here for the Riemann-Silberstein decomposition. The second integral in Eq. (5.5.17) is a surface integral which is necessary, if the Riemann-Silberstein vector does not vanish at the simulation box boundaries. Since the Riemann-Silberstein vector in the multipole expansion Hamiltonian in Eq. (5.5.10) does only depend on the expansion point \vec{r}_0 of the multipole expansion and its corresponding Riemann-Silberstein vector inside the box, it is sufficient to calculate the values of the surface integral only for the stencil points that correspond to the expansion center \vec{r}_0 of the multipole expansion. This reduces the computational cost for the boundary term significantly.

Note, that in principle the field decomposition of coupled Maxwell-matter systems can be achieved by calculating the longitudinal electric field caused by the Kohn-Sham orbitals of all species. But some of the simulations for large matter systems that we have performed have shown instabilities after a long time of propagation.

Therefore, we decompose the field for each time step when it couples to the matter to avoid small errors, which possibly result in an incorrect simulation run.

5.6 Maxwell-Kohn-Sham multi-scale implementation

Up to now, we have seen in the previous sections that both physical systems, matter and Maxwell, can be expressed mathematically very similar. Both can be propagated in time by a Schrödinger-like equation. Nevertheless some fundamental differences require different physical parameters to simulate each system properly, especially for length and time scale. Some examples are molecular systems interacting with infrared, optical or ultraviolet laser pulses. In all cases, the matter wave functions are localized in a small volume compared to the laser field. Additionally, the wave functions fluctuate rather strongly, whereas typical experiments show that the Maxwell fields reaction is often smoother. The length scale difference of Maxwell radiation and matter motion can differ by about some orders of magnitude. Although our implementation is not restricted to such simulations, we introduce some grid types which are especially designed for laser-molecule interactions.

5.6.1 Multi-grid types

In Figure 5.1, we illustrate different kinds of combined matter and Maxwell grids, and consider without loss of generality only matter grid spacings smaller or equal to the Maxwell grid spacing. In principle, our implementation can also reverse this grid relation to simulate high frequency Maxwell signals, e.g., x-rays.

The grids in Figure 5.1 a) and b) represent equal sized grid for both systems. In general, the Maxwell grid points do not necessarily have to lie on the top of a matter grid point, illustrated in a). For both grid types a) or b), it is not possible to use the grid point values directly in the respective coupling terms of the propagation equations. For example, the finer matter grid points have to be sorted in clusters which map to the next nearest Maxwell grid point and different methods to get the weighted mean value yield the coupling value for that Maxwell point. Vice versa, a Taylor series extrapolation of the Maxwell values can be used to obtain the coupling values for the matter points. These grid types of equally sized dimensions are well suited to simulate periodic systems.

The two schemes in Figure 5.1 c) and d) show matter grid types, in first case without common grid points, and in second case with common grid points, but compared to the previous grids with smaller dimensions for the matter grid than for the Maxwell one. As before, the values for the corresponding coupling terms have to be calculated by weighted mean and interpolation. Those grid types can describe efficiently bound molecules and nanoparticles, especially when focussing on electromagnetic far-fields. In case of near field effects, where the electromagnetic field fluctuation correlate strongly with the matter wave functions, it is consequently a good choice to select the same grid spacings for both grids and to place matter and Maxwell grid points on top of each other as shown in Figure 5.1 e) and f). In this case, the values for

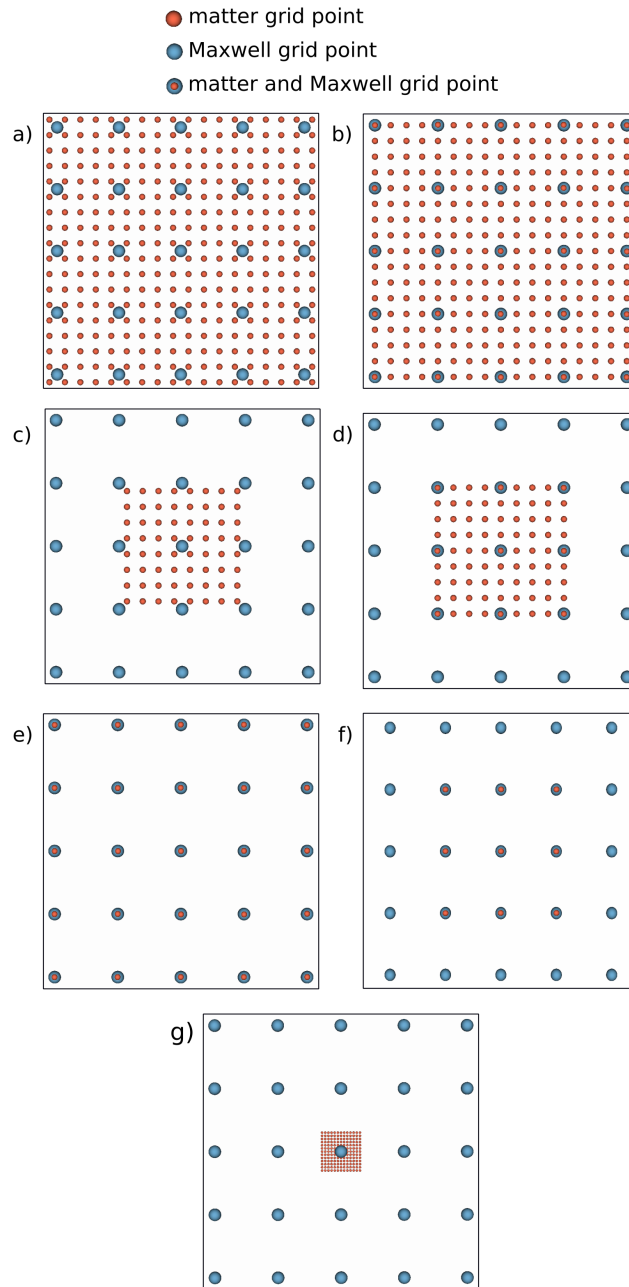


Figure 5.1: An overview over some multiscale grid types. The red dots represent grid points for the Kohn-Sham wave functions and the blue dots show the grid point for the Maxwell field variables. In most relevant applications, the Kohn-Sham grid is finer than the Maxwell grid, like in a), b), c), d), and g). The grid types e) and f) represent special cases, where both grids lie on top of each other, but they are not necessarily of same size which is given in f). Only the equal sized grids in a), b), and e) are suitable for periodic systems, whereas the remaining types describe proper bound non-periodic systems.

both respective coupling terms can be obtained directly from the field point at the respective grid point. Besides the near-field simulation, the grid type f) with larger Maxwell grid dimensions is suited to study the onset of the electromagnetic far-field and allows to define electromagnetic detectors at the box boundaries.

The last grid type in Figure 5.1 g) illustrates the case, where the matter grid is chosen much finer than the Maxwell grid. Only one Maxwell grid point lies in the middle of the matter grid. Here, it is assumed that the Maxwell field is approximately constant for all matter grid points. Vice versa, the coupling value for the Maxwell grid is obtained by the mean value of all matter points.

5.6.2 Multi-scales in time

After setting up the two spatial system grids and their different length scales, we focus in this section on the different time scales. The different scales for matter and radiation in time require a more detailed consideration about the propagation time steps of each subsystem.

In principle, it is possible to chose identical parameters with the condition that both propagators have to run stable in time, but this is for most physical cases not the most efficient choice. According to the underlying Maxwell Hamiltonian-like operator in H_{Mx} Eq. (1.1.31), which forms the 6x6 \mathcal{H} operator in Eq. (1.1.45) for the Maxwell propagation, the gradient operation is multiplied by the speed of light c_0 (roughly 137 in atomic units). This factor imposes the speed for the electromagnetic waves on the grid.

On the other hand, the matter Hamiltonian in our non-relativistic Pauli limit is lacking the factor of c_0 and yields a much smaller spectral range of the maximum and minimum eigenvalue of the Hamiltonian. Consequently, the underlying time step variables have to propagate "fast" photon motion and "slow" motion of matter. This results in a much smaller maximum time step $\Delta t_{\text{KS,max}}$ for the Maxwell propagation compared to the maximum time step of the matter $\Delta t_{\text{KS,max}}$.

A similar situation of different physical time scales is already known in electron-nuclear dynamics, where the large nuclear mass leads to a rather slow motion of the nuclei compared to the faster motion of the lighter electrons. Now, the propagation of the Maxwell fields also with electron-nuclear dynamics adds a third timescale. In our numerical time-stepping scheme, we exploit the different time scales explicitly to increase the computational efficiency.

Several test simulations that we have performed have shown, that the coupled propagation of nuclei, electrons and Maxwell fields keeps relatively accurate, stable and converged, if we perform several Maxwell propagation steps Δt_{Mx} as intermediate steps between the Kohn-Sham propagation steps Δt_{KS} and Ehrenfest steps for the nuclei. We select the Kohn-Sham time steps $\Delta t_{\text{KS}} < \Delta t_{\text{KS,max}}$ as the basic time step parameter for the entire MPKS system. The number $N_{\text{Mx-steps}}$ of intermediate Maxwell steps is automatically chosen such that

$$\Delta t_{\text{KS}} \leq N_{\text{Mx-steps}} \Delta t_{\text{Mx,CFL}} , \quad (5.6.1)$$

where $\Delta t_{\text{Mx,CFL}}$ denotes the Courant time step given in Eq. (3.2.6).

Performing these intermediate Maxwell time steps, assumes that the intermediate Maxwell propagation between the $m\Delta_{\text{KS}}$ time step and the following $(m+1)\Delta_{\text{KS}}$ time step does not affect the matter propagation significantly. Therefore, the current density for the corresponding i^{th} is approximated by the linear expansion

$$\mathcal{J}_{\text{loc}}(\vec{r}, m\Delta t_{\text{KS}} + i\Delta t_{\text{Mx}}) = \mathcal{J}_{\text{loc}}(\vec{r}, m\Delta t_{\text{KS}}) + \left[\frac{\mathcal{J}_{\text{loc}}(\vec{r}, (m+1)\Delta t_{\text{KS}}) - \mathcal{J}_{\text{loc}}(\vec{r}, m\Delta t_{\text{KS}})}{N_{\text{Mx-steps}}} \right] i. \quad (5.6.2)$$

The recursive ETRS time-evolution equation for the i^{th} step then takes with Eq. (5.3.4) the form

$$\begin{aligned} \mathcal{F}(\vec{r}, t_{(m),(i+1)}) &\approx \mathcal{U}_{\mathcal{J}_{\text{dmc}}}(t_{(m),(i+1)}, t_{(m),(i)}) \star \mathcal{F}(\vec{r}, t_{(m),(i)}) \\ &- \frac{\Delta t_{\text{Mx}}}{4} \mathcal{U}(t_{(m),(i+1)}, t_{(m),(i)}) \mathcal{J}_{\text{loc}}(\vec{r}, t_{(m),(i)}) \\ &- \frac{\Delta t_{\text{Mx}}}{4} \mathcal{U}(t_{(m),(i+1)}, t_{(m),(i+1/2)}) \mathcal{J}_{\text{loc}}(\vec{r}, t_{(m),(i+1/2)}) \\ &- \frac{\Delta t_{\text{Mx}}}{4} \mathcal{U}(t_{(m),(i)}, t_{(m),(i+1/2)}) \mathcal{J}_{\text{loc}}(\vec{r}, t_{(m),(i+1/2)}) \\ &- \frac{\Delta t_{\text{Mx}}}{4} \mathcal{J}_{\text{loc}}(\vec{r}, t_{(m),(i)}) \end{aligned} \quad (5.6.3)$$

with

$$\begin{aligned} t_{(m),(i)} &= m\Delta t_{\text{KS}} + i\Delta t_{\text{Mx}}, \\ t_{(m),(i+1)} &= m\Delta t_{\text{KS}} + (i+1)\Delta t_{\text{Mx}}, \\ t_{(m),(i+1/2)} &= m\Delta t_{\text{KS}} + (i+1/2)\Delta t_{\text{Mx}}. \end{aligned} \quad (5.6.4)$$

To reduce computational cost even further, we can assume in most cases that the last for inhomogeneity terms in Eq. (5.6.3) are approximately constant for all intermediate time steps during the time interval Δt_{KS} . Thus, we use in this case for all occurring $\mathcal{J}_{\text{loc}}(\vec{r}, t)$ in Eq. (5.6.3) the arithmetic mean of $\mathcal{J}_{\text{loc}}(\vec{r}, m\Delta t)$, and $\mathcal{J}_{\text{loc}}(\vec{r}, (m+1)\Delta t)$ which reduces the amount of necessary computational expensive \mathcal{U} operations. These considered approximations to the full time-evolution requires always a check of convergence for a given application.

5.6.3 Finite difference operators and parallelization strategy

The previously introduced grids provide the basis to express approximately the matter wave functions and the Maxwell field variables. In addition, the grid point values determine the spatial derivatives of both systems. In Sec. 5.3 and Sec. 5.4, we show both time-evolution equations, which we use to propagate the corresponding system. Their underlying time-evolution operations depend on first-order spatial derivatives in case of the Maxwell fields and second-order spatial derivatives in case of the matter wave functions. We obtain both operations with the finite-difference method [89, 90, 91]. Since we introduce and consider mainly the Maxwell field propagation the present work, which have a Schrödinger-like form, but with first-order

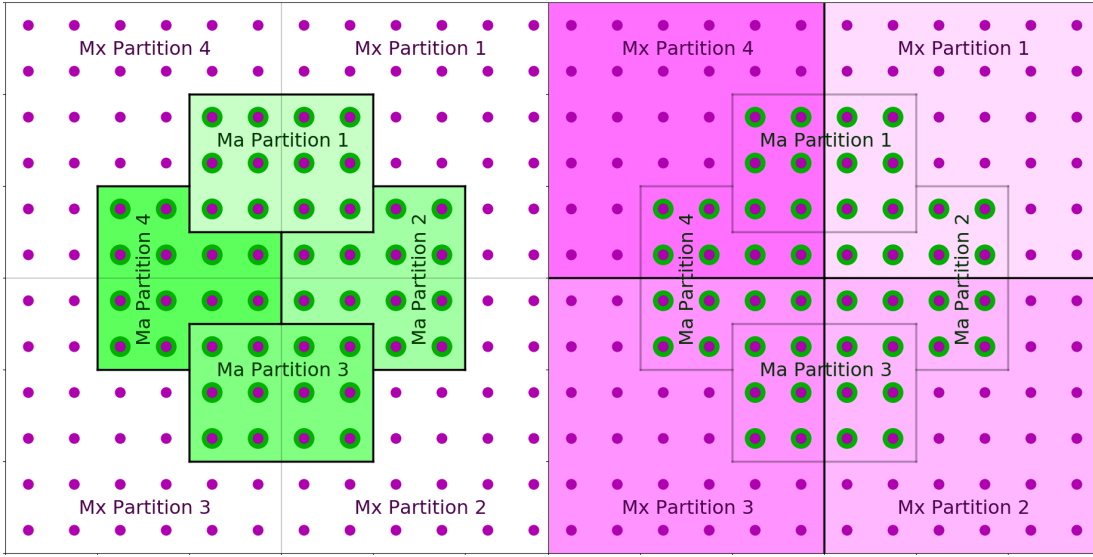


Figure 5.2: Domain parallelization of matter and Maxwell grid. Both schematic drawings show the same two matter and Maxwell grids, and represent grid type f) in Figure (5.1). The matter grid points are bold green dots, and the Maxwell grid points are the smaller purple dots. The left one emphasize partition of the matter grid, and the right one the partition of the Maxwell grid. Both grid partitions have common points with more than one other partition, since each division is independent from each other.

derivatives, we introduce the first derivative finite-difference stencil in Sec. 3.1. The second derivatives, which we need for the kinetic operator of the Pauli-Fierz Hamiltonian, are established and discussed in literature [93, 123]. Finite difference routines for first and second derivatives for selectable accuracy order are implemented in octopus [123].

We also considered in Sec. 3.1 the parallelization scheme for the Maxwell propagation. In case of coupled Maxwell-matter simulations, we speed up the time-evolution by using additionally a parallel propagation scheme for the matter. Octopus provides an optimized parallelization in domains and in "states" or "orbitals/k-points" [93]. Since the Riemann-Silberstein vector is always a six-dimensional vector whose components are considered as six states in the routines of the code, parallelization in states is not so effective in this case.

As already described in Sec. 3.1, Octopus has to share the values from some grid points of the grid partition and share them with other partitions to get the correct derivative operations. This technique is illustrated in Figure 3.3 for the Maxwell grid. Furthermore, this communication of shared data has to be expanded now. Both system grids could vary in size, grid points and they are partitioned independently from each other. As a consequence, the point mapping between the grids leads in general to a mapping between different partitions.

Figure 5.6.3 illustrates an example for such a partitioning of a Maxwell-matter system. The matter grid points are marked with large dots and divided into four domains also highlighted in green on the left in Figure 5.6.3. The Maxwell grid partitions with their grid points are plotted and highlighted in purple on the right in Figure 5.6.3. It can be seen in both figures, that the matter grid points of partition 1 maps on Maxwell partitions 1 and 4. On the other hand, the Maxwell partition 1 has common grid points with the matter partitions 1 and 2. We have implemented a mapping, that considers the parallelization in domains of each grid and arranges the necessary data shares to get the right coupling values from the respective other subsystem.

5.6.4 Predictor-corrector method

Previously, in Sec. 5.3 and Sec. 5.4 we described the two propagation schemes for matter and electromagnetic fields separately. In the following, we show a predictor-corrector method that enforces a self-consistent propagation of the system.

5.6.5 Forward coupling

In most studies in the literature, light-matter coupling is restricted to forward Maxwell-matter coupling. The electromagnetic fields influence the matter, but the induced back-reaction due to charge motion does not influence the propagation of the electromagnetic fields. In only forward coupling simulations, the external electromagnetic field propagates without any perturbation by the matter and is calculated separately either analytically or numerically. Such a propagation scheme for one time step is illustrated on the left-hand side in Figure 5.3.

According to the time-evolution operator in Eq. (5.4.10), the operator depends on the Hamiltonian operator at the future time $t = (m+1)\Delta t_{\text{KS}}$. This future Hamiltonian is not only determined by the external Maxwell fields but also by the motions of the ions and electrons and their interactions. Therefore, it is necessary to apply a predictor corrector cycle for the matter propagation. In a first step, the future Hamiltonian is estimated by an extrapolation [124] and the calculated time propagation returns an estimated Kohn-Sham potential which is again used for an updated extrapolation of the Hamiltonian. These steps are repeated until the absolute value of the variance of two subsequently Kohn-Sham potentials falls below a small threshold value. For our calculations, we set a threshold value of $1e^{-6}$ in atomic units for the potential variance and adjust the time step Δt_{KS} for the propagation so that the matter system is converged in at least two iterations if the system is only disturbed very weakly by the external field. During the full run and stronger perturbations, we notice that the number of iterations is barely larger than five.

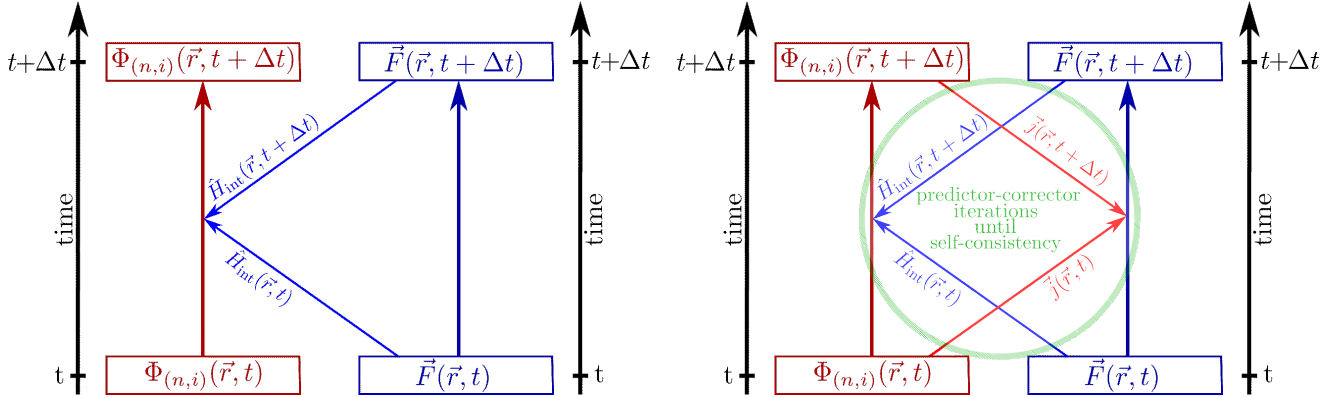


Figure 5.3: The figure on the left-hand side illustrates the most common coupling situation for light-matter coupling in quantum mechanical many-body simulations. The electromagnetic fields (in blue) propagate freely and only influence the propagation of the matter (in red). The back reaction of the matter currents on the electromagnetic fields is neglected. As a consequence, the Maxwell propagation is not calculated numerically, since in most cases, the time-evolution is taken from analytical solutions of Maxwell’s equations or the paraxial wave equation. In case of taking the back reaction into account, the Maxwell propagation is in general not solvable analytically and requires a numerical propagation as for the matter evolution. In the figure on the right-hand side, we show a fully self-consistent predictor-corrector scheme for a coupled Maxwell-Pauli-Kohn-Sham time step. As before, the electromagnetic field influence the propagation of the matter (forward coupling), and additionally the arising currents influence the electromagnetic fields and their time-evolution (backward coupling). Both propagations have to be self-consistent, and therefore, a given coupled time-step is repeated with successively corrected variables until self-consistency is found. Only then the simulation continues to perform the next time step.

5.6.6 Forward and backward coupling

The back-reaction of matter on the Maxwell field appears in the MPKS formulation due to the current density in Eq. (5.1.10) which is caused by the motion of matter. The three current types, paramagnetic, diamagnetic and magnetization current, influence the Maxwell propagation Eq. (5.2.17). The influence of the paramagnetic current, the magnetization current and optional external currents result directly summed up in the inhomogeneity $\mathcal{J}_{\text{loc}}(\vec{r}, t)$ term in Eq. (5.1.13). The diamagnetic current implicitly effects the time-evolution due to the modified Maxwell time-evolution operator $\mathcal{U}_{\mathcal{J}_{\text{dmc}}}(t, t_0) \star \mathcal{F}(\vec{r}, t)$ for this case given in (5.2.11). The full forward and backward coupling scheme is shown on the right-hand side in Figure 5.3.

In a fully self-consistent scheme, both systems and accordingly their time-evolution propagation equations, i.e., Eq. (5.2.17) and Eq. (5.4.4), couple to each

other. First we apply the extrapolation of the future matter Hamiltonian to get a prediction for the Kohn-Sham orbitals. These orbitals and the initial ones give us the necessary current density, which couple to the Maxwell fields. Using the first predicted updated current density at time $(m+1)\Delta t_{\text{KS}}$ leads to an updated Riemann-Silberstein vector. At this point, the predictor-corrector loop restarts by updating the Kohn-Sham orbitals, but now with a corrected matter Hamiltonian, which includes the updated Riemann-Silberstein vector. As a consequence, the previously predicted variables get a correction closer to the values which make the coupled system self-consistent. We additionally check the consistency of the Maxwell fields by comparing the Maxwell energy inside the simulation box for two successive updated Riemann-Silberstein vectors. Therefore, we use the same threshold value $1e^{-6}$ like for the matter convergence. Additionally, we chose the system propagation time Δt that the predictor-corrector step iterates at least two times until the self-consistency thresholds are fulfilled for weak perturbations. Again, the number of iterations for strong perturbation periods should not be larger than five steps.

5.7 Ehrenfest-Maxwell-Pauli-Kohn-Sham approach

In Sec. (4.5) we introduced the Maxwell-Pauli-Kohn-Sham equations that determines a species quantum state as an one particle wave function only interacting with an external Kohn-Sham potential. In most cases, the different matter particle species consist of different nuclei and electrons. As discussed in Sec. (4.6) the electron and nuclei masses differ significantly. To simulate both, electron and nuclei systems, it is a common way to separate both description, i.e., treating electrons quantum mechanically and nuclei classically.

Therefore, combining the results of Sec. (4.5) with Sec. (4.6) leads to our final Ehrenfest-Maxwell-Pauli-Kohn-Sham approach (EMPKS) to describe classical motion of nuclei plus quantum mechanical multi-species systems. A general discussion of classical nuclei and quantum mechanical electrons propagation with so called Ehrenfest dynamics is given in Ref. [116, 125], which we modify by implementing the coupled Maxwell-Kohn-Sham propagation including the self-consistent predictor-corrector scheme from Sec. (5.6.4)

According to the ETRS in Sec. 5.3, we first propagate the electromagnetic field from time t_0 to $t_0 + \Delta t/2$, optionally with intermediate time-steps to keep the Maxwell field simulation stable. The next step moves the nuclei from the initial time $t = t_0$ to time $t = t_0 + \Delta t/2$ using classical equation of motion in Eq. (4.6.12), which is the common known Lorentz force. Next, the electron system is time-evolved with the new introduced Maxwell-Pauli-Kohn-Sham Eq. (4.5.12) from the initial time $t = t_0$ for a half time-step to time $t = t_0 + \Delta t/2$.

Then the three steps were repeated. The electromagnetic field evolves from time $t_0 + \Delta t/2$ to time $t_0 + \Delta t$ with the previously updated nuclei and electron states, that effects the current density of the Maxwell propagator. Again, the nuclei move

also from time $t_0 + \Delta t/2$ to $t_0 + \Delta t$ taking the updated Maxwell fields and electron states into account. Finally, the last step propagates again the electrons from $t = t_0 + \Delta t/2$ to time $t = t_0 + \Delta t$ using the last calculated electromagnetic fields and nuclei positions. These six partial substeps describe a whole propagation step of the Ehrenfest-Maxwell-Pauli-Kohn-Sham system for a chosen time-step Δt from time t_0 to $t_0 + \Delta t$.

Taking our predictor-corrector method, the previous summarized EMPKS steps are first employed with a predictor step. Since the coupled system equations depends on some variables of the other considered system and future time-step (matter or Maxwell), we assume that all necessary future variables are constant for the first run of the EMPKS steps. The second run uses the previous updated variables for the future variables inside the propagation equation. Such correction runs of the EMPKS steps will be repeated, until the all future variables of both systems are self-consistent.

Finally, we note here that the classical approximation of the nuclei determines their corresponding charge current that contributes to the total current of the system and also to the Kohn-Sham vector potential $A_{\text{KS}}^\mu(\vec{r}, t)$. We denote this limit of classical nuclei for our MPKS scheme the Ehrenfest-Maxwell-Pauli-Kohn-Sham (EMPKS) approach, analogous to matter-only quantum dynamics.

5.8 Simulation of open quantum systems with the Maxwell-Kohn-Sham propagation

In Sec. 3.4 we introduced absorbing boundaries for the electromagnetic field to simulate outgoing fields. While this is a standard procedure in FDTD simulations, we emphasize here that such absorbing boundaries effectively allow to turn our coupled light-matter system into an open quantum system from first principles. Therefore, the forward-backward coupled light-matter simulation damps the quantum-mechanical system, due to the fact that the matter transfers energy to the electromagnetic field, which in turn transfers the energy via radiation to the absorbing boundaries. Consequently, no artificial bath degrees of freedom have to be introduced in our simulation scheme as commonly done in the description of open quantum systems.

5.9 Electromagnetic detectors

Due to the self-consistent forward-backward coupling, we have established a methodology to investigate the local field distribution of the electromagnetic fields inside the simulation box. Hence, we can measure the optical properties of the matter directly from the electromagnetic observables. Since we can evaluate the field values at each grid point, we can examine in this way near field effects of the field. Furthermore, if

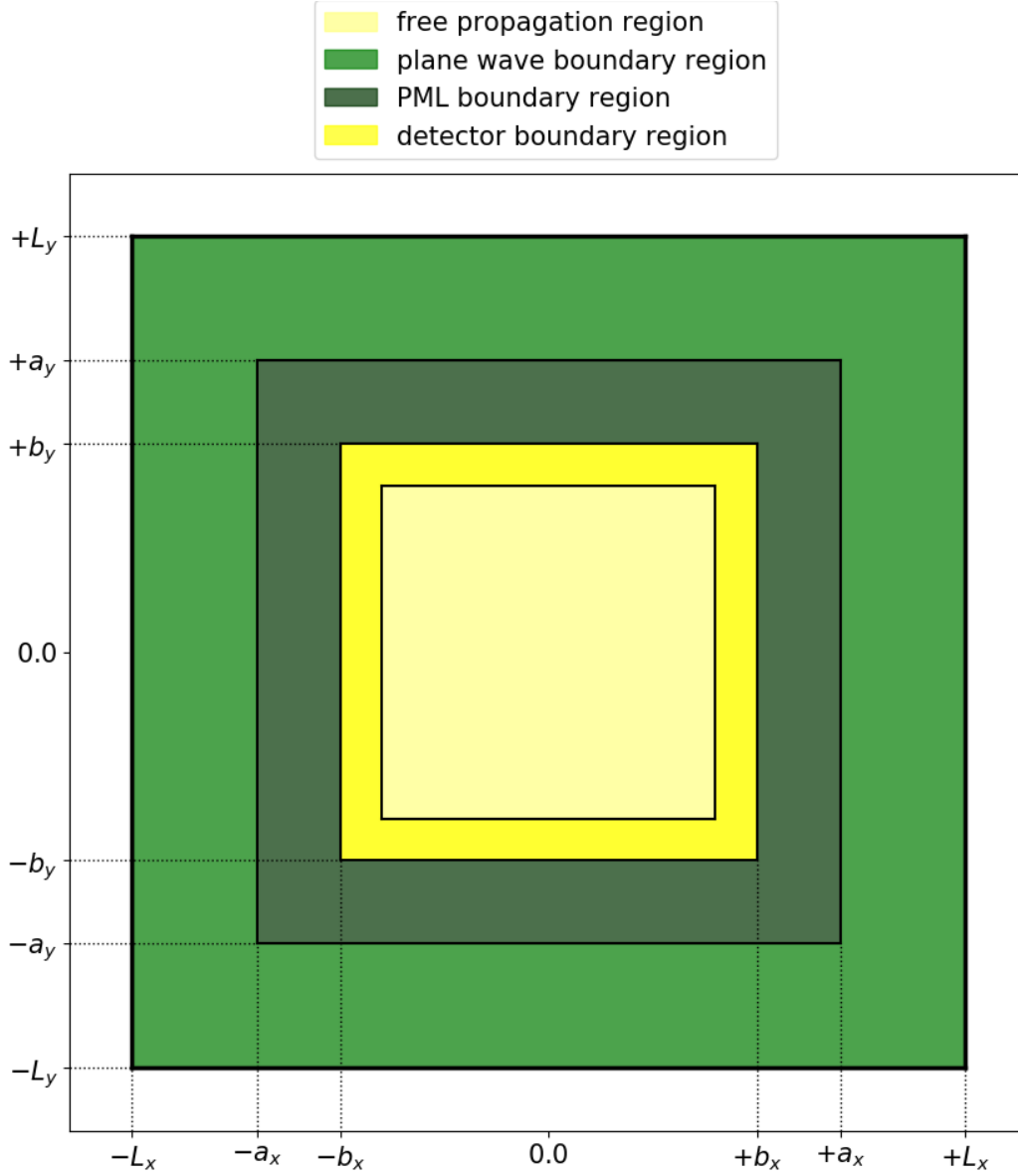


Figure 5.4: A small blue closed area at boundaries of the inner free Maxwell propagation area illustrates the detector region, where the included grid point values are used to analyze the Maxwell far-field.

the matter system is surrounded by vacuum, the outgoing waves propagate analytically. In other words, whatever arrives in the boundary region would propagate to the far field and contributes to what can be measured in the far field by a detector. For this purpose, we define right before the boundary region a small closed area as a far field detector. This detector region can consist of only a closed surface to get field values, e.g., the energy flow through the surface, or the region builds a three-

dimensional frame box. We illustrate such a detector frame region in Figure 5.4, where we use the incident plane wave plus PML boundaries simulation box from Sec. 3.4.6. Hence, the electromagnetic field inside the detector box can be used to extrapolate the far field beyond the simulation box. Detecting the electromagnetic field directly and not indirectly by matter variables, as it is done in common methods of spectroscopy, is a paradigm shift to measure optical spectra, to avoid possible errors and to reveal new effects.

5.10 Broken time reversal symmetry

In Secs. 5.3 and 5.4 we discuss the time-reversal symmetry of the total Pauli-Fierz Hamiltonian of our system given in Eq. (4.5.2). This property only holds if we consider the total Maxwell-matter system as a closed system. For instance, the incident plane wave boundaries simulate an open system since energy enters the system through the analytical calculated boundaries. The time-reversal symmetry does not hold for open systems, especially in presence of magnetic fields [67], and consequently the ETRS propagator in Eq. (5.3.4) does not hold. However, we assume in the present work that the full coupled Hamiltonian stays time-reversal since the main breaking of the symmetry arises if we consider the magnetic field propagation without any back-reaction of the matter.

Chapter 6

Applications

In this section, we demonstrate the significance of simulating the fully self-consistent coupling of the time-dependent Kohn-Sham equations for the electrons, Ehrenfest dynamics for the nuclei, and Maxwell's equations for the electromagnetic fields. We use our Ehrenfest-Maxwell-Pauli-Kohn-Sham (EMPKS) implementation in the Octopus code, which we introduced in the previous chapter 3 and chapter 5 to simulate different scenarios and coupling levels. They range from conventional forward light-matter coupling in dipole approximation with fixed nuclei to a theory level with forward-backward self-consistent light-matter coupling including electric quadrupole and magnetic dipole terms. In addition, we can include the motion of the ions and classical Lorentz forces on the ions. An overview of the various EMPKS theory levels, that we use in the present work, is shown in Table 6.1. The advantage of switching on and off different degrees of freedom and coupling levels lies in the direct study of the impact and significance of physical mechanisms.

Acronym	Description
<u>F@ED</u>	Forward coupling with E lectric D ipole term
<u>FB@ED</u>	Forward and B ackward coupling with E lectric D ipole term
<u>F@(ED+MD+EQ)</u>	Forward coupling with E lectric D ipole, M agnetic D ipole and E lectric Q uadrupole term
<u>FB@(ED+MD+EQ)</u>	Forward and B ackward coupling with E lectric D ipole, M agnetic D ipole and E lectric Q uadrupole term

Table 6.1: Table of acronyms that are used in the present work to indicate the level of EMPKS theory.

6.1 Laser pulse simulation scheme for a plasmonic nanoparticle system and simulation parameters

In a typical experimental setup, a molecule gets excited by an incoming laser pulse. The molecule gets excited, absorbs and emits light. The absorbed and emitted light is detected by the outgoing electromagnetic fields. Analyzing the incident and outgoing light draws conclusions about the optical properties of the studied molecule. In the following, we apply our novel ab-initio EMPKS propagation to simulate such laser pulse experiments.

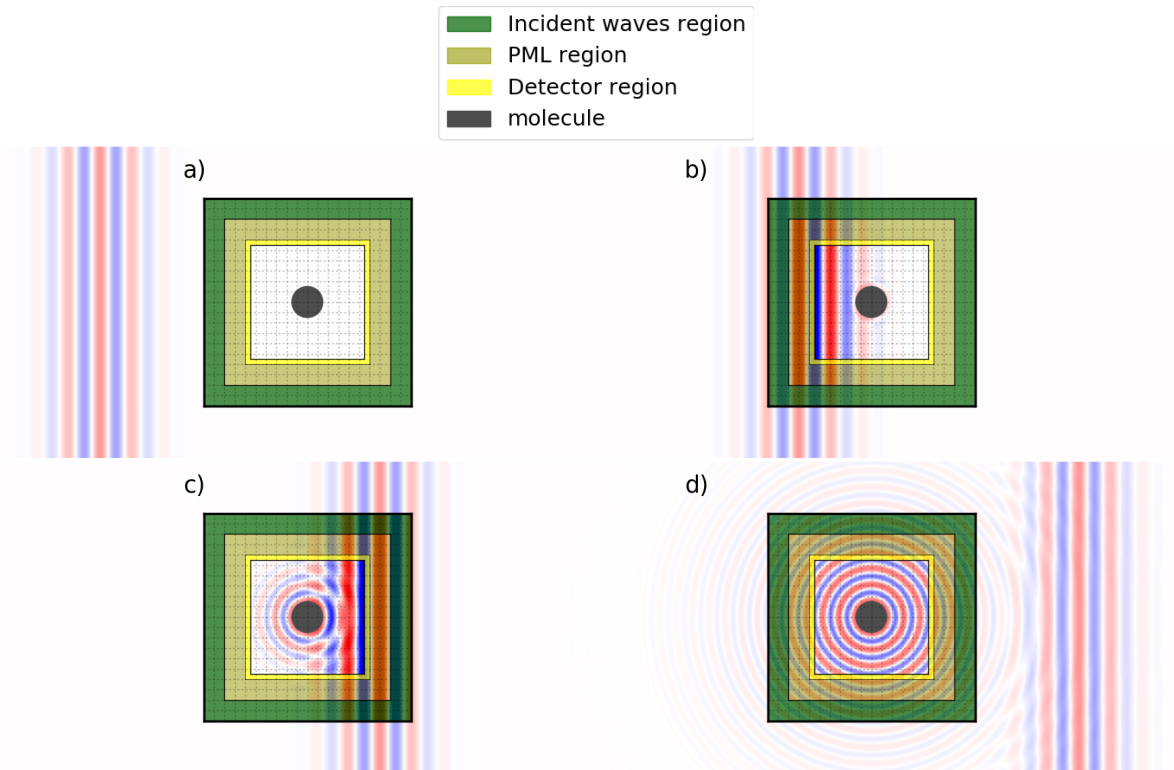


Figure 6.1: Simulation scheme of a laser pulse excitation of a quantum-mechanical system. a) Inside the simulation Box, the quantum mechanical system is grounded in its initial state. Outside the box we place a laser pulse that propagates into the direction of the matter system. b) The incident waves boundaries simulate the incoming wave and the matter system gets excited. c) Due to this excitation, the induced charge motion and current cause an electromagnetic reaction. d) The induced motion of charges leads still to a radiation although the laser pulse left the box.

In principle, the simulation setup is very similar to the one in Sec. 3.6, where we hit a linear medium box with a laser pulse. Instead of the medium box, we can place any matter system inside the simulation. Hence, according to the medium box simulation,

we use a simulation box with combined incident plane waves and perfectly matched layer boundaries, which we introduced in Sec. 3.4.6. In addition to the boundaries, we define a small detector region as it is described in Sec. 5.9.

A schematic overview of the entire simulation is presented in Figure 6.1.

The first illustration a) shows the initial setup. The matter system in its ground state is placed in the center of the simulation box. In the beginning, the external laser pulse is outside the box, here represented by its electric field polarized perpendicular to the drawing plane. The wave vector is perpendicular to the laser wave front and heads into the direction of the matter.

After several time steps shown in b), the laser pulse enters the simulation box and excites the matter system. Due to the electric field oscillation, the electrons and hence the corresponding charge density starts to oscillate, which induce an electric current density. This arising current density influences the total Maxwell field.

The external laser field and the induced inner Maxwell field, both interfere which is illustrated in c). Since our implementation solves the forward-backward Maxwell-matter coupling, we can directly analyze the localized electromagnetic field inside the simulation box to examine near-field effects. If we drive the molecule by its resonance frequency, the charge oscillation of the electrons will continue even when the laser passed the simulation box.

As shown in d) the corresponding electromagnetic radiation can be measured at the detector region to get information about far-field effects. Although the driven laser left the simulation box, the matter system still radiate a electromagnetic field. Due to this radiation, energy from the excited matter system transfers via the electromagnetic field to the boundaries of the box. The Maxwell PML simulates the outgoing waves and as a consequence, the matter loses energy, in principle until it returns into the ground state.

6.1.1 Na₂₉₇-dimer geometry and optical spectra

Recent experiments and theoretical considerations have revealed that large nanoparticles, excited by a laser pulse, create large induced currents. Hence, to test and demonstrate our EMPKS implementation, we select a nanoplasmonic particle, which was already examined in previous work by Alejandro Varas et. al. [126].

The system consists of two almost spherical nanoparticles with 297 sodium atoms each, which are arranged in a dimer configuration. A corresponding illustration of the dimer geometry with two different distances between the dimer is shown in Figure 6.2. Both nanoclusters have together 594 sodium atoms and also 594 valence electrons [127, 128]. All inner electrons of the sodium inner electron shell and the valence electron are approximated by Troullier-Martins pseudo-potentials in Octopus [93, 123, 129].

The icosahedral polyhydron is the most stable geometry for one sodium dimer. After performing standard geometry optimization with octopus, we obtain some characteristic parameters of the dimer geometry. The quite large polyhydron is

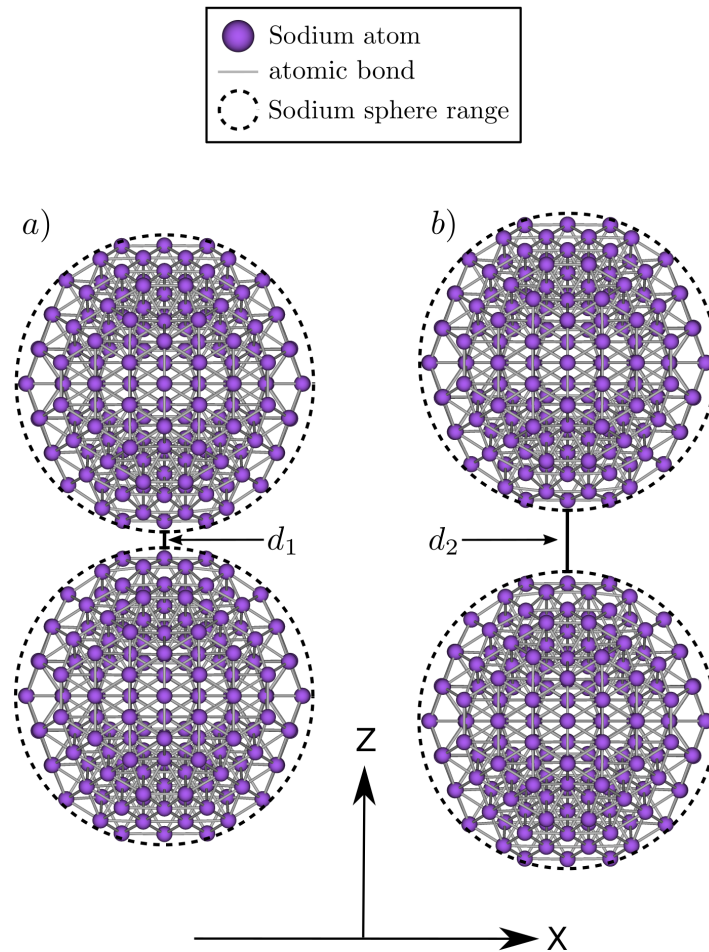


Figure 6.2: Geometry of the Na_{297} dimer in E2E configuration with different distances $d_1 = 0.1$ nm and $d_2 = 0.5$ nm between the two effective spheres of the clusters which are illustrated by the black dashed circle.

approximately a sphere with an effective diameter of $2R$, with an effective radius $R \approx 2.61$ nm, given by the optimization calculation. Further geometry parameters describe the distance between the two nanoparticles. First, the parameter b gives the distance between the two centered sodium atoms of each icosahedron so that d is defined as $d = b - 2R$, and does not depend on the relative orientation of the two clusters to each other. The two icosahedrons can be orientated in several constellations. We use a relative orientation such that the 3-atoms edge of the hexagons are lying face to face. This so called E2E configuration is illustrated in Figure 6.2. The dimer axis is oriented parallel to the z-axis, therefore the dimer is symmetric in x- and y-axis.

To investigate the effect of internal dipole and quadrupole of the system on the coupled time-evolution, we consider two different distances $d_1 = 0.1$ nm and $d_2 = 0.5$ nm. By computing the optical absorption cross section of the dimer which is illustrated in Figure 6.3, it was shown in Ref. [126] that the maximum absorbing frequency shows a quadrupole (Q mode) localized surface plasmon resonance (LSPR) for the d_1 dimer, and a dipole (D mode) resonance for the d_2 dimer.

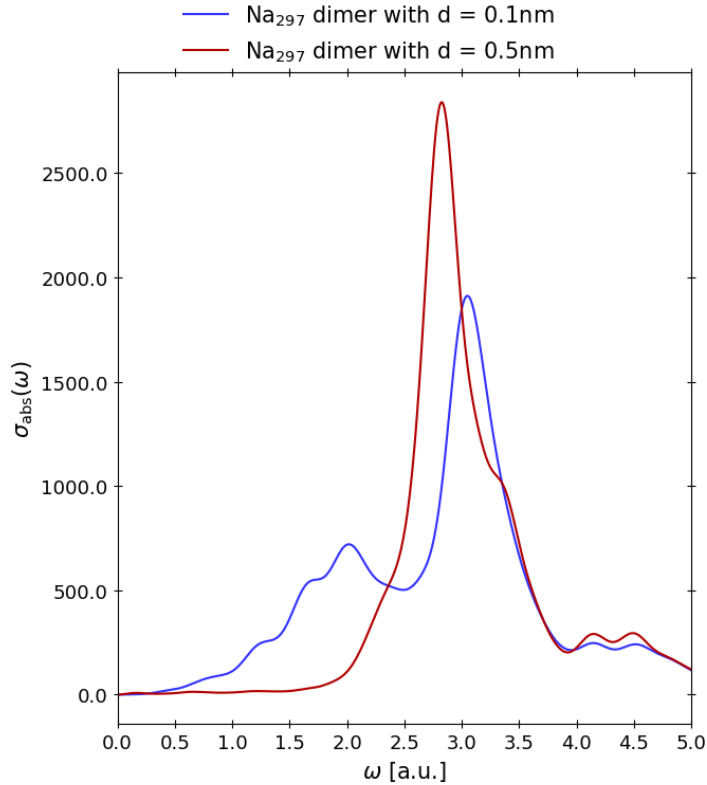


Figure 6.3: Absorption spectrum of the Na_{297} dimer for light that is polarized along the dimer axis. In case of the d_1 dimer (blue) curve, two peaks arise. The first one corresponds to a plasmon dipole mode and the second one to a quadrupole mode. The d_2 dimer (red) curve shows a slightly broader peak for the dipole resonance. The data for these spectra corresponds identically to Ref. [126].

6.1.2 Simulation boxes and grid alignment

According to Sec. 6.1, we place the Na_{297} -dimer in the middle of the Maxwell-Kohn-Sham simulation box which corresponds to grid type f) in Figure 5.1. The matter Kohn-Sham grid is smaller than the Maxwell grid, but both grids have the same grid spacing in each direction and all Kohn-Sham grid points lie on top of a Maxwell grid point. The Kohn-Sham grid geometry is based on the so called minimum box

construction [93]. The minimum box of a molecule consists of the union of all Cartesian grid points which lie inside a fixed radius around each ion of the system. For all simulations, we select a radius of $R_{\min} = 0.794$ nm (15 a.u.). Taking the corresponding geometries for d_1 and d_2 into account, we obtain maximal extensions $L_{KS,x}$, $L_{KS,y}$, $L_{KS,z}$ in each direction given in Table 6.2. The matter grid is surrounded by a significant larger parallelepiped shaped box for the Maxwell grid points with the extensions $L_{Mx,x}$, $L_{Mx,y}$, $L_{Mx,z}$ in negative and positive direction which is illustrated in Figure 5.4. As grid spacing for both grids we select 0.053 nm (1.0 a.u.).

For the Kohn-Sham grid we use a zero Dirichlet boundary condition, whereas for the Maxwell grid we employ the combined incident plane waves plus absorbing boundaries via PML as introduced in Sec. 3.4.6. Hence, the Maxwell simulation grid is separated into two areas, one outer for the incident plane wave boundaries and one inner for the PML. The incident plane wave boundary width depends on the derivative order for the operation stencil times the grid spacing. In the present case, we use a finite difference order of four, which corresponds to the width of the plane wave boundary region of 0.212 nm (4.0 a.u.). Additionally, we use 0.265 nm (5.0 a.u.) as PML region. The total inner simulation box for the free Maxwell propagation is therefore limited by $b_{Mx,x}$, $b_{Mx,y}$, and $b_{Mx,z}$ also given in Table 6.2.

variable	distance d_1		distance d_2	
	conv. units	[a.u.]	conv. units	[a.u.]
ω	3.05 eV	0.112	2.83 eV	0.104
k_x	$1.55 \cdot 10^{-11} \text{ m}^{-1}$	$8.17 \cdot 10^{-4}$	$1.43 \cdot 10^{-11} \text{ m}^{-1}$	$7.59 \cdot 10^{-4}$
λ	406.5 nm	7681.84	438.1 nm	8279.02
$E_{0,z}$	$5.142 \cdot 10^7 \text{ V/m}$	$1.0 \cdot 10^{-4}$	$5.142 \cdot 10^7 \text{ V/m}$	$1.0 \cdot 10^{-4}$
Intensity	$3.51 \cdot 10^{12} \text{ W/m}^2$	$5.45 \cdot 10^{-4}$	$3.51 \cdot 10^{12} \text{ W/m}^2$	$5.45 \cdot 10^{-4}$
ξ	2034.08 nm	38438.5	2034.08 nm	41395.1
x_0	4068.16 nm	76877.0	4381.07 nm	82790.2
$L_{KS,x}$	1.993 nm	37.658	1.993 nm	37.658
$L_{KS,y}$	1.993 nm	37.658	1.993 nm	37.658
$L_{KS,z}$	3.347 nm	63.258	3.547 nm	67.037
$L_{Mx,x}$	2.646 nm	50.000	2.646 nm	50.000
$L_{Mx,y}$	2.646 nm	50.000	2.646 nm	50.000
$L_{Mx,z}$	4.498 nm	85.000	4.498 nm	85.000
$a_{Mx,x}$	2.170 nm	41.000	2.170 nm	41.000
$a_{Mx,y}$	2.170 nm	41.000	2.170 nm	41.000
$a_{Mx,z}$	4.022 nm	76.000	4.022 nm	76.000
Δx_{KS}	0.053 nm	1.000	0.053 nm	1.000
Δx_{Mx}	0.053 nm	1.000	0.053 nm	1.000
Δt_{KS}	$5.096 \cdot 10^{-3} \text{ fs}$	0.211	$5.096 \cdot 10^{-3} \text{ fs}$	0.211
Δt_{Mx}	$1.019 \cdot 10^{-4} \text{ fs}$	$4.21 \cdot 10^{-3}$	$1.019 \cdot 10^{-4} \text{ fs}$	$4.21 \cdot 10^{-3}$

Table 6.2: Simulation parameters for the sodium dimer for distances $d_1 = 0.1$ nm and $d_2 = 0.5$ nm.

6.1.3 Measurement and detector regions

As mentioned before in Sec. 6.1 for the simulation scheme description, we can measure the electromagnetic field at all points inside the free Maxwell simulation region. However, in principle to show the main properties of the near-field and far-field effects it is sufficient to evaluate the variables only at distinguished points, which give characteristic information about the effects. Instead of taking just one point, we can integrate over several points, surfaces or volumes of interest to get a mean value for evaluating the field.

For this application, we define three distinguished points, the mid point \vec{r}_{cp} at the origin of the box

$$\vec{r}_{\text{cp}} = (0, 0, 0), \quad (6.1.1)$$

which is the junction between the two dimer spheres to analyze the near-field. To measure the far-field, we select two off-center points, one along the x-axis with

$$\vec{r}_{\text{ocpx}} = (1.957 \text{ nm}, 0, 0) = (37.0 \text{ a.u.}, 0, 0), \quad (6.1.2)$$

and one along the y-axis with

$$\vec{r}_{\text{ocpy}} = (0, 1.957 \text{ nm}, 0) = (0, 37.0 \text{ a.u.}, 0). \quad (6.1.3)$$

Furthermore, we define a detector surface given by the parametrization

$$\vec{r}_{\text{sfx}}(\alpha, \beta) = \vec{r}_{\text{ocpx}} + \alpha \vec{e}_y + \beta \vec{e}_z, \quad \begin{cases} -37.0 \leq \alpha \leq 37.0 \\ 81.0 \leq \beta \leq 71.0 \end{cases}. \quad (6.1.4)$$

The detector surface for calculating a mean value of a measurable variable includes the off-center point \vec{r}_{ocpx} and the extension is determined by the box limits. We choose the limits such that all points have sufficient distance to the absorbing PML region.

The detector surfaces include the off-center points \vec{r}_{ocpx} or \vec{r}_{ocpy} and the extension is determined by the box limits. We chose the limits such that all points have sufficient distance to the absorbing PML region. For ease of comparison, we compute the average of the electric field over the detector surface. The location of the detector points and surfaces is schematically depicted in Fig. 6.4.

6.1.4 Laser pulse shape

The external laser pulse propagates with a wavevector $\vec{k} = (k_x, 0, 0)$ along the x-axis. The electric field polarization is oriented along the z-axis and consequently the magnetic field oscillates parallel to the y-axis. The spatial and time-dependent analytical expression for the external laser electric field $\vec{E}_{\text{pw}}(\vec{r}, t)$ has a cosinoidal envelope and is given by

$$\vec{E}_{\text{pw}}(\vec{r}, t) = \vec{e}_z E_{0,z} \cos(k_x(x - x_0) - \frac{2\pi}{\lambda}t) \cos\left(\frac{\pi(x - 2\xi - x_0 - c_0t)}{2\xi} + \pi\right) \cdot \theta\left(\xi - \frac{|k_x(x - x_0) - \frac{2\pi}{\lambda}t|}{|k_x|}\right). \quad (6.1.5)$$

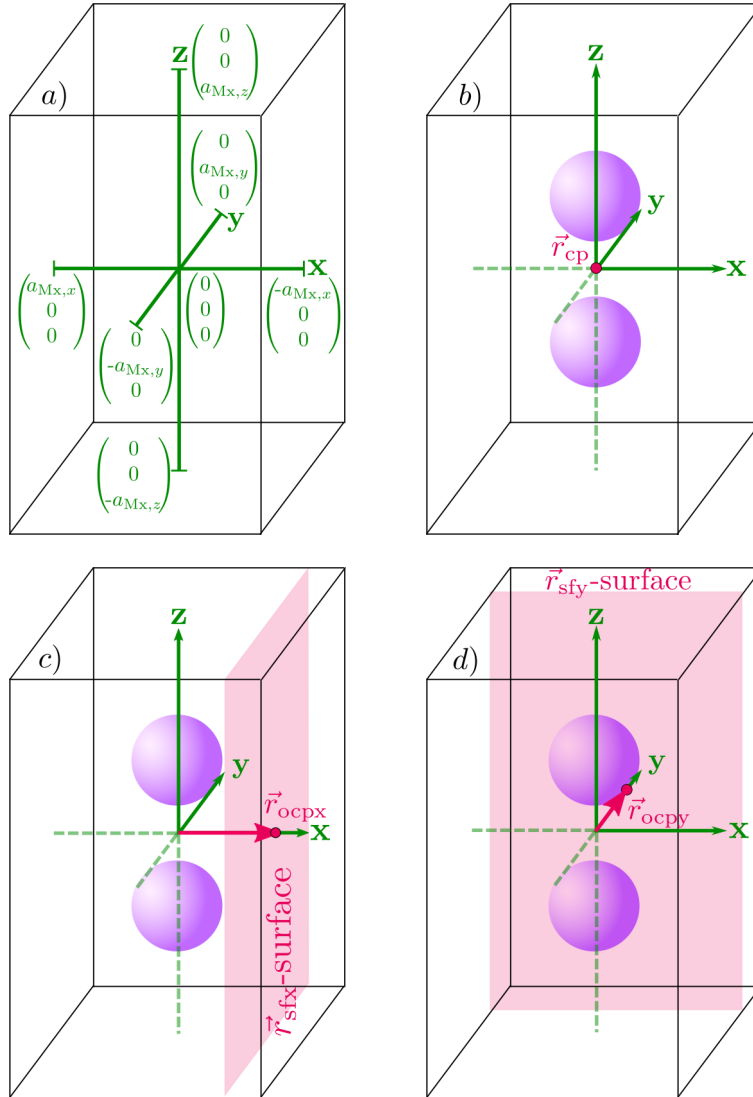


Figure 6.4: Visualization of the inner simulation box limits and detector points and surfaces. Panel a) shows the axis end points of the inner simulation box without the PML region where the physical Maxwell-Kohn-Sham equations are solved numerically. The two blue spheres inside the box in panels b), c) and d) illustrate schematically the location of the sodium dimer. For the electronic ground state, the electron density and the longitudinal electric field is non-zero inside these spheres. We evaluate the electromagnetic field at three different detector points. The first point is the box center point \vec{r}_{cp} in b), the second one is an off-center point \vec{r}_{ocpx} along the x-axis in c), and the last one is an off-center point \vec{r}_{ocpy} along the y-axis in d). In addition, we evaluate the average electric field on the two surfaces perpendicular to \vec{r}_{ocpx} and \vec{r}_{ocpy} which are also illustrated in c) and d).

We used the Heaviside-theta function $\theta(x)$. Since the wavevector $\vec{k} = (k_x, 0, 0)$ contributes only along the x-axis and the direction of the electric field \vec{E}_{pw} polarization is along the z-direction, the corresponding magnetic field \vec{B}_{pw} reads

$$\vec{B}_{\text{pw}}(\vec{r}, t) = -\vec{e}_y \frac{1}{c_0} \vec{E}_{\text{pw}}(\vec{r}, t). \quad (6.1.6)$$

Using $\vec{E}_{\text{pw}}(\vec{r}, t)$ and $\vec{B}_{\text{pw}}(\vec{r}, t)$, we can build the Riemann-Silberstein six-vector $\mathcal{F}_{\text{pw}}(\vec{r}, t)$

$$\mathcal{F}_{\text{pw}}(\vec{r}, t) = \begin{pmatrix} \sqrt{\frac{\epsilon_0}{2}} \vec{E}_{\text{pw}}(\vec{r}, t) + i\sqrt{\frac{1}{2\mu_0}} \vec{B}_{\text{pw}}(\vec{r}, t) \\ \sqrt{\frac{\epsilon_0}{2}} \vec{E}_{\text{pw}}(\vec{r}, t) - i\sqrt{\frac{1}{2\mu_0}} \vec{B}_{\text{pw}}(\vec{r}, t) \end{pmatrix}, \quad (6.1.7)$$

which is used to update the incident plane wave boundaries for each propagation time step. The laser pulse parameter differ for the two runs, since we drive both systems with their corresponding resonance frequency of maximum absorption. In case of the $d_1 = 0.1$ nm dimer, the Q-mode plasmon frequency reads $\omega_1 = 3.05$ eV, and $\omega_2 = 2.83$ eV for D-mode frequency of the $d_2 = 0.5$ nm dimer [126]. The cosinoidal envelope width ξ of the laser pulse is coupled to the frequency respectively the corresponding wavelength. Both pulses are placed by x_0 outside the simulation box. All laser pulse parameters can be taken from Table 6.2.

6.1.5 Propagators

In Sec. (5.7), we introduced the Ehrenfest-Pauli-Kohn-Sham approach and Sec. (6.1.2) contains all necessary simulation parameters.

First, we consider the matter propagation. Inside the minimum region with the maximum limits of $-l_{\text{KS},x} \leq x \leq l_{\text{KS},x}$, $-l_{\text{KS},y} \leq y \leq l_{\text{KS},y}$, $-l_{\text{KS},z} \leq z \leq l_{\text{KS},z}$, we propagate the Kohn-Sham system with the matter ETRS propagator Eq. (5.4.10) that is already implemented in Octopus [123]. We use the Power-Zienau-Woolley transformed MPKS Hamiltonian from Eq. (5.5.10) with the multipole expansion in Sec. (5.5.2). We implemented the first three coupling terms of Eq. (5.5.10), which we can be separately switched on or off for each run. In the same manner, we can run a simulation with or without ion motion. The updated ion positions and velocities are calculated by the Ehrenfest dynamics. The corresponding implemented ion motion propagator in Octopus is described in Ref. [116]. Since we have the electromagnetic fields available in the simulation box, we also include the classical Lorentz force that acts on the ions according to Eq. (4.6.12).

The Maxwell system inside the Maxwell simulation $-l_{\text{Mx},x} \leq x \leq l_{\text{Mx},x}$, $-l_{\text{Mx},y} \leq y \leq l_{\text{Mx},y}$, $-l_{\text{Mx},z} \leq z \leq l_{\text{Mx},z}$ without the PML region is evolved in time by the Maxwell ETRS propagator Eq. (5.3.4) respectively Eq. (5.6.3). For the present thesis, we only consider paramagnetic current density, that means that the first time-evolution operation $\mathcal{U}_{\mathcal{J}_{\text{dmc}}}(t, t_0) \star \mathcal{F}(\vec{r}, t_0)$ on the right-hand side of Eq. (5.3.4) and

Eq. (5.6.3) becomes equivalent to the one in Eq. (5.2.14), i.e., $\mathcal{U}_{\mathcal{J}_{\text{dmc}}}(t, t_0) \star \mathcal{F}(\vec{r}, t_0) \rightarrow \mathcal{U}(t, t_0) \mathcal{F}(\vec{r}, t_0)$, with time-evolution operator Eq. (5.2.15). Furthermore, the current density term $\mathcal{J}_{\text{loc}}(\vec{r}, t)$ given in Eq. (5.1.13) only contains the paramagnetic current contribution $\mathcal{J}_{\text{pmc}}(\vec{r}, t)$ for our applications in the thesis. We propagate the Riemann-Silberstein vector corresponding to the total vector potential

$$A^k(\vec{r}, t) = A_{\text{mat}}^k(\vec{r}, t) + A_{\text{ext}}^k(\vec{r}, t) \quad (6.1.8)$$

of external and internal fields. For the transversal Kohn-Sham field we use the mean-field approximation Eq. (4.5.21)

$$A_{\text{KS}}^k(\vec{r}, t) \approx A_{\text{mat}}^k(\vec{r}, t) + A_{\text{ext}}^k(\vec{r}, t) = A^k(\vec{r}, t) \quad (6.1.9)$$

as well as the physical mass of the particles to take into account the bare vacuum fluctuations of the photon field. For the longitudinal Kohn-Sham field we use

$$A_{\text{KS}}^0(\vec{r}, t) \approx A_{\text{mat}}^0(\vec{r}, t) + A_{\text{ext}}^0(\vec{r}, t) + A_{\text{xc,LDA}}(\vec{r}, t), \quad (6.1.10)$$

respectively

$$A_{\text{KS}}^0(\vec{r}, t) \approx A_{\text{mat}}^0(\vec{r}, t) + A_{\text{ext}}^0(\vec{r}, t) + A_{\text{xc,PBE}}(\vec{r}, t), \quad (6.1.11)$$

where $A_{\text{xc,LDA}}(\vec{r}, t)$ is the adiabatic local density approximation (LDA) exchange-correlation approximation [114, 123], and $A_{\text{xc,PBE}}(\vec{r}, t)$ the generalized gradient approximation PBE (Perdew, Burke, Ernzerhof) [123, 130].

In addition to the fully coupled EMPKS simulation, we propagate in addition the unperturbed Maxwell system inside the inner simulation box to get the required values for the incident plane waves plus PML boundaries according to Sec. 3.4.6. Hence, the Maxwell Hamiltonian has to be updated inside the PML boundaries by the additional PML matrix $\tilde{\mathcal{G}}(\vec{r}, m\Delta t)$ according to Eq. (3.4.55) and Eq. (3.4.51).

For all exponential operations of both, the Maxwell and matter propagators, a series expansion of the exponential of order of four is used, and we chose a finite difference stencil order of four for the derivative operations.

6.2 Results from Ehrenfest-Maxwell-Pauli-Kohn-Sham simulations

After introducing the simulation scheme with external laser and the nanoplasmonic sodium dimer in the previous section, we provide in the following the most relevant results of the actual EMPKS simulations of the dimer for different theory levels according to Table 6.1. We compare the results of self consistently coupled light-matter propagation with conventional forward-coupling once with dipole approximation and beyond.

First, we produced a movie of four representative variables to visualize vividly the arising dynamics of the dimer interacting with the laser pulse. The full movies

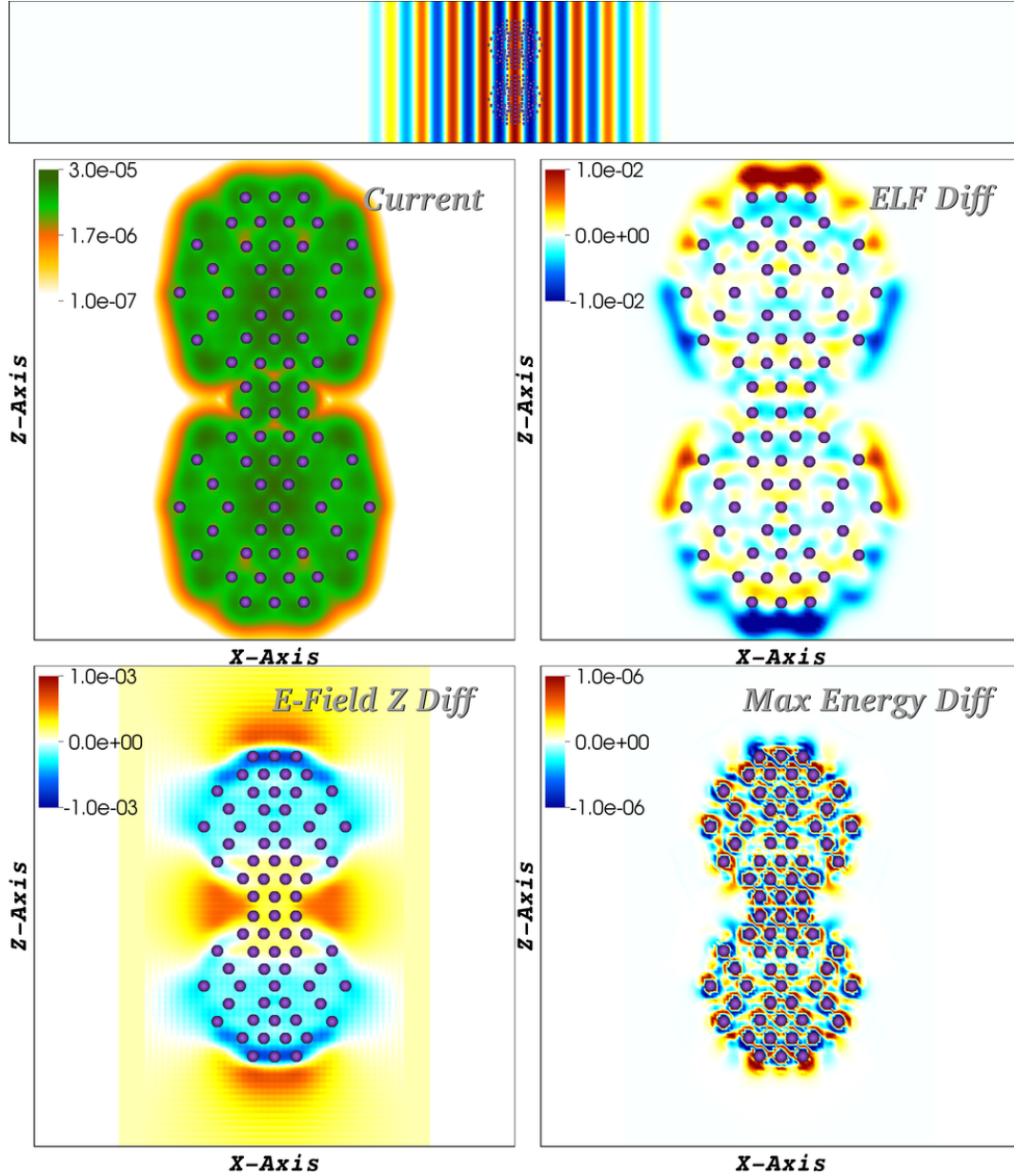


Figure 6.5: In the supplemental material we provide a movie that shows the real-time dynamics of the nanoplasmonic dimer with distance $d_1 = 0.1$ nm. In the figure, we show a frame of the movie at time 6.89 fs. The upper two panels show contour plots of matter variables, the absolute value of the current density and the electron localized function (ELF). The most relevant Maxwell field variables, the electric field along the laser polarization direction z and the total Maxwell energy are presented in the lower panels. In the top of the figure, we show the incident laser pulse and at the center the geometry of the nanoplasmonic dimer.

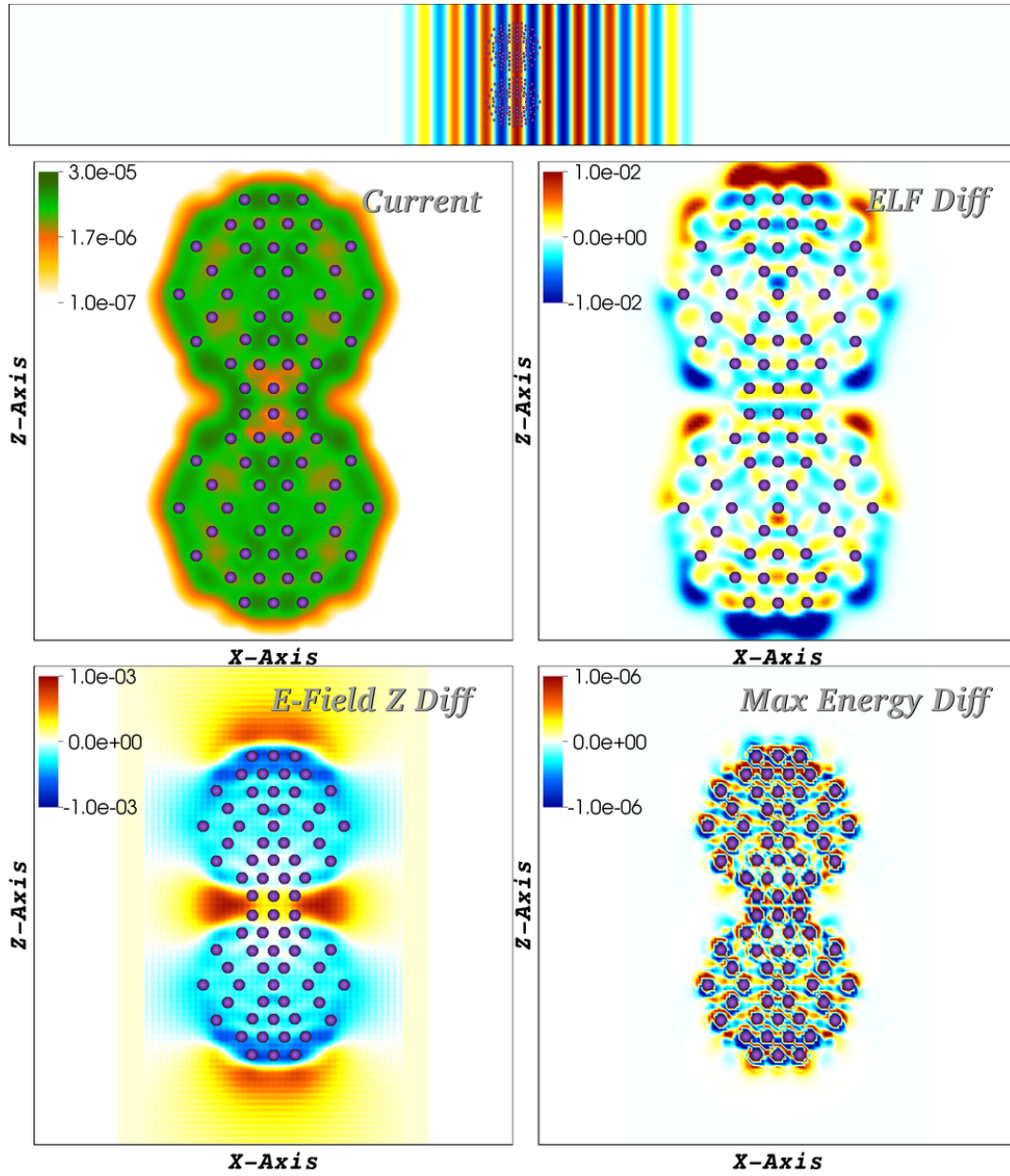


Figure 6.6: Similar movie frame as Figure 6.5, but with the frame at time 8.33 fs.

for the two different cluster distances d are provided in Ref. [131] for $d_1 = 0.1$ nm and Ref. [132] for $d_2 = 0.5$ nm. Two representative snapshots of the first movie are presented in Figures 6.5 - 6.6. The first one was taken at time $6.89fs$ when the external laser maximum reached the center of the dimer, and the second one at time $8.33fs$, when the internal induced electric field enhancement becomes maximal. Both snapshots are divided into five figure panels. On the top we find schematically the location of the laser pulse and a two-dimensional enlarged picture of the ion geometry. The four remaining plots are 2D contour plots along the x-y plane of the 3D simulation box. The upper left one shows the induced paramagnetic current density. The other three plotted variables illustrate the differences of the current time step values and the ground state values since the differences are distinctly smaller than their ground state values. Therefore, we present the differences of the electron localization function (ELF) on the upper right, of the electric field on the lower left, and of the Maxwell density. The different opposed amplified ELF contour regions which are located outside the clusters shows clearly the induced surface plasmons. Since we see four extrema, two minima and two maxima, regions, the ELF contour plots emphasizes that the laser excites the dimer with Q-mode plasmons.

6.2.1 Electric field enhancement

The work of Varas et. al. reveals a large field enhancement right at the mid point \vec{r}_{cp} between the two nanoplasmonic clusters. This field enhancement is purely caused by the only longitudinal electric field of the matter plus the transverse external laser. In such conventional time-dependent Kohn-Sham calculations, the longitudinal component of the electric field can be obtained from the scalar Kohn-Sham potential. Solving Eq. (4.5.20) for the external potential plus the matter potential (Hartree potential), i.e., $\vec{A}(\vec{r}, t) = \vec{A}_{mat}(\vec{r}, t) + \vec{A}_{ext}(\vec{r}, t) = \vec{A}_{KS}(\vec{r}, t) - \vec{A}_{xc}(\vec{r}, t)$, gives

$$\vec{E}_{||}(\vec{r}, t) = -\vec{\nabla} \left(\vec{A}_{mat}(\vec{r}, t) + \vec{A}_{ext}(\vec{r}, t) \right). \quad (6.2.1)$$

The total electric field \vec{E}_{fw} for conventional forward-coupling simulations is the superposition of the longitudinal field from the matter plus the external transverse field, i.e., the laser

$$\vec{E}_{fw}(\vec{r}, t) = \vec{E}_{||}(\vec{r}, t) + \vec{E}_{pw}(\vec{r}, t). \quad (6.2.2)$$

In case of a forward-backward simulation, we assume that also the transverse component of the total field influences the field enhancement. To investigate this, we use our EMPKS approach to study the fully coupled electromagnetic field. An overview of the significant electric field behavior for the dimer $d_1 = 0.1$ nm is presented in Figure 6.7. The system is driven by its resonance frequency that induces quadrupole surface plasmons on the dimer. The initial external laser amplitude is plotted in panel a), and the induced current in panel b). The following three panels c) - e) show the electric field enhancement, first for the mid point \vec{r}_{cp} , the far field at

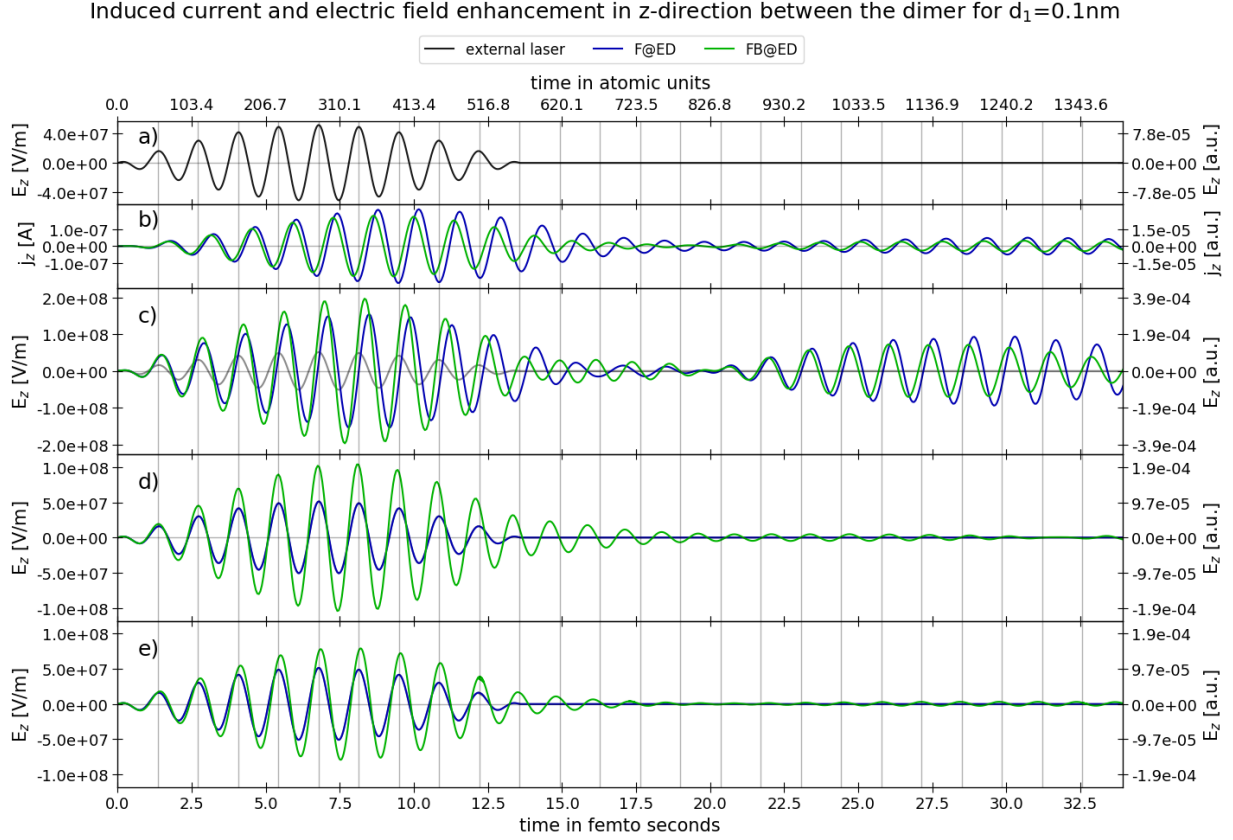


Figure 6.7: Electric field values and current density in z-direction in the center between the two Sodium clusters for $d_1 = 0.1 \text{ nm}$. The first panel *a*) illustrates the incident cosinusoidal laser pulse with frequency $\omega_1 = 3.05 \text{ eV}$ (0.112 a.u.) $\lambda_1 = 406.5 \text{ nm}$ (7681.84 a.u.) and amplitude of $E_z^0 = 5.142 \times 10^7 \text{ V/m}$ (10^{-4} a.u.) which drives the system. The second panel *b*) displays the electric field enhancement in dipole approximation and only in forward coupling, while the red curve includes electric dipole, magnetic dipole and electric quadrupole terms and takes light-matter forward and backward coupling into account. The curve in bright gray illustrates the initial unperturbed laser. The last plots in panel *c*) show the corresponding current densities at the center point between the dimer and in panel *d*) the current density differences. The period $T_1 = 1.36 \text{ fs}$ corresponding to the laser frequency is ω_1 is indicated with grey vertical lines.

point \vec{r}_{ocpx} and last the average electric field over the detector surface (\vec{r}_{sfx}), respectively. All blue curves in that figure refer to the forward coupling theory level with dipole approximation (F@ED) and are identical with the previous results of Varas et. al, but calculated with our EMPKS implementation by switching off the matter to Maxwell back-reaction. The overlap with the data of Varas et. al. provides a

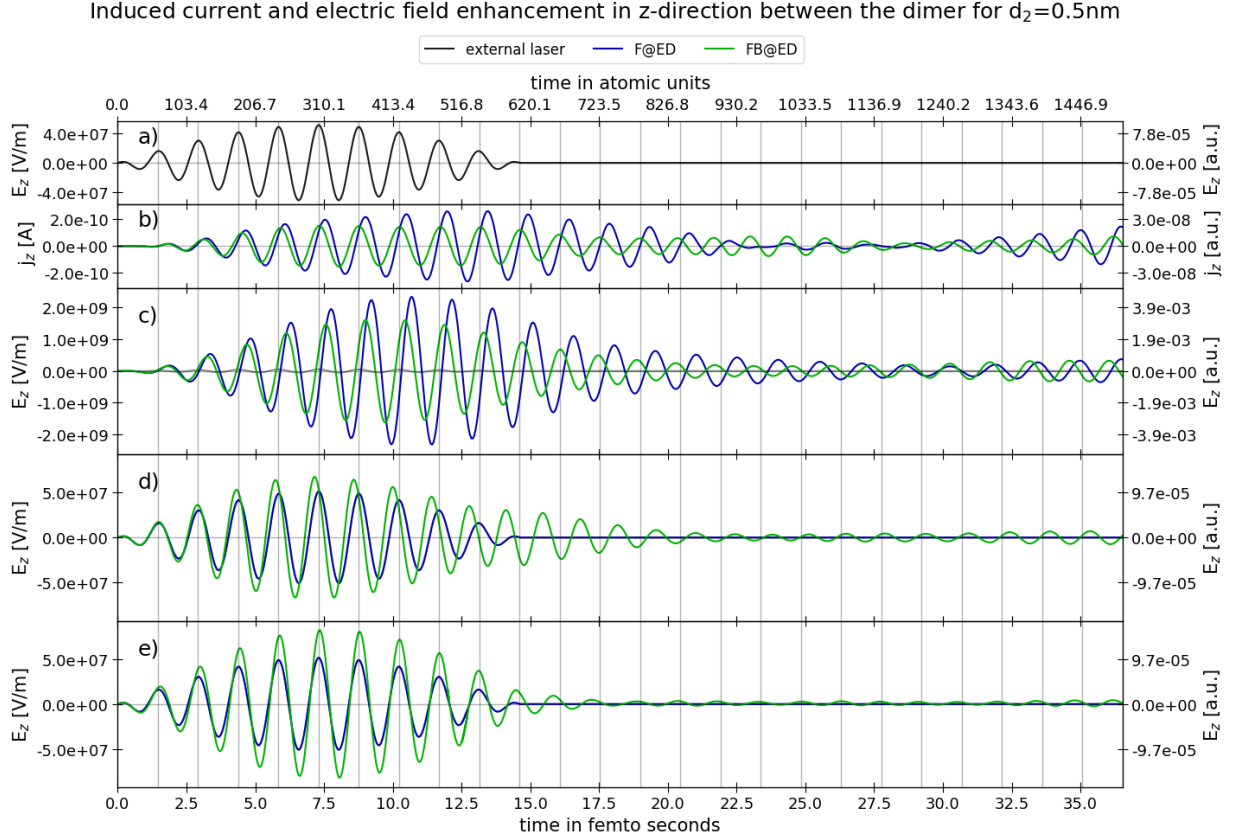


Figure 6.8: Similar to Figure 6.7, we show here the electric field enhancements and current densities for the Sodium dimer with $d_2 = 0.5 \text{ nm}$.

consistency-check of our implementation.

The black curve in panel a) and the light gray curve in panel b) display the same initial cosinoidal shaped free laser that passes through the box without any matter interaction. We include the pulse from panel a) again in panel c) to facilitate the comparison of the incident field amplitude (gray) with the actual field values when light-matter coupling is taking place (blue and green). The blue curve in panel c), our forward coupling simulation F@ED, confirms a field enhancement of Varas et. al. at the mid point of about a factor of three compared to the incident laser amplitude. Additionally, we see the same delay of the total induced electric field maximum compared to the maximum field amplitude of the driving laser. This shift of maxima can also be seen in panel c) by comparing the maxima of the gray and blue curves. For longer times, the mid point field in c) shows a significant beating signal, whereas the far field panels d) and e) present only a weak reaction.

The green curves in Figure 6.7 represent the run including the back-reaction of the matter on the electromagnetic fields in dipole approximation (FB@ED). The full forward-backward coupled system reveals in panel c) a similar enhancement for very

short time, a slightly increased enhancement for intermediate times and a smaller beating for longer times. While the laser drives the dimer, the back-reaction is increasing the field at the mid point. The increasing effect still holds with a small delay when the external laser already decrease. Taking a look at the far field panels d) and e), the differences between the two runs are more significantly. The forward-backward coupled simulation in e) returns a field at the off-center point \vec{r}_{ocpx} twice as large as the one of the forward coupling run. This effect is a bit weaker when we take the average field over the surface in f). Comparing the phases and frequencies of all evaluated fields, we notice that the far-fields are almost in phase with the incident laser whereas the near-field shows a small phase and frequency shift, for both the forward and forward-backward simulations.

The result of electric field for the second dimer configuration with delimiter $d_2 = 0.5$ nm is illustrated in Figure 6.8. The laser pulse a resonance frequency that induces D-mode surface plasmons. We present the same characteristic variables and use the same ordering as before in Figure 6.7. Due to the larger distance between the two Sodium clusters, the absolute value of the current density is significantly smaller than the one in $d_1 = 0.1$ nm run. The induced current densities in Figure 6.8 panel b) of the forward coupling F@ED case are larger than for the forward and backward coupled FB@ED case. The electric near-field enhancement in panel c) shows a opposite behavior than in Figure 6.7, where the forward-backward coupled field enhancement induces larger fields for short times.

In case of the $d_2 = 0.5$ nm run with D-mode plasmons, we find a significantly smaller field enhancement for the forward-backward coupled run compared to the only forward coupling simulation. In turn, the far field behaviors shown in panel d) and e) show a similar picture as for the first dimer configuration. The full coupled system returns a stronger fields at our far field boundary. As before in the case of the $d_1 = 0.1$ nm separation, we find here that the average of the electric field over the detector surface in the far field as shown in panel e) is mostly locked to the phase of the incident laser. In contrast, the near field at the mid point between the two nanoparticles shows phase and frequency shifts. They are larger for the F@ED coupling at short times and the phase turns even to the opposite sign compared to FB@ED coupling for intermediate times.

Due to the electric field construction in Eq. (6.2.2) for the forward coupling runs we know, that all related field enhancements are only longitudinal. To analyze further the nature of the field enhancement for the forward-backward coupling simulations, we performed a Helmholtz-decomposition of the electric field in the fully-coupled FB@ED case. The corresponding decomposed fields can be seen in Figure 6.9 and Figure 6.9, for the $d_1 = 0.1$ nm dimer and $d_2 = 0.5$ nm dimer, respectively. In both figures, panels a) and c) illustrate the total field as a reference and their corresponding longitudinal fields. Since the transverse component is in all cases a magnitude smaller than the total or longitudinal fields, we plot them separately in b) and d). The plots in panel a) and c) respectively b) and d) differ in their evaluation point. The first two upper plots show the field decomposition at the mid point \vec{r}_{mp} , whereas the lower ones evaluate the fields at the far-point \vec{r}_{ocpx} .

In general, we find that the main contribution of the forward-backward coupled field enhancement arises also from the longitudinal field as in the forward coupled case. Besides the fact that the longitudinal enhancement is about one order of magnitude larger for the d_1 distance and even two orders of magnitude larger for the d_2 distance, we see some phase and frequency shifts between the different fields. The phase shift between the longitudinal and the total field in Figure 6.9 a) and Figure 6.9 b) is very small for both distances. Although the phase shift to the transverse field is rather large, its small amplitude leads to a minor contribution for the total field. This behavior differs at the detector surface point \vec{r}_{cpX} illustrated in

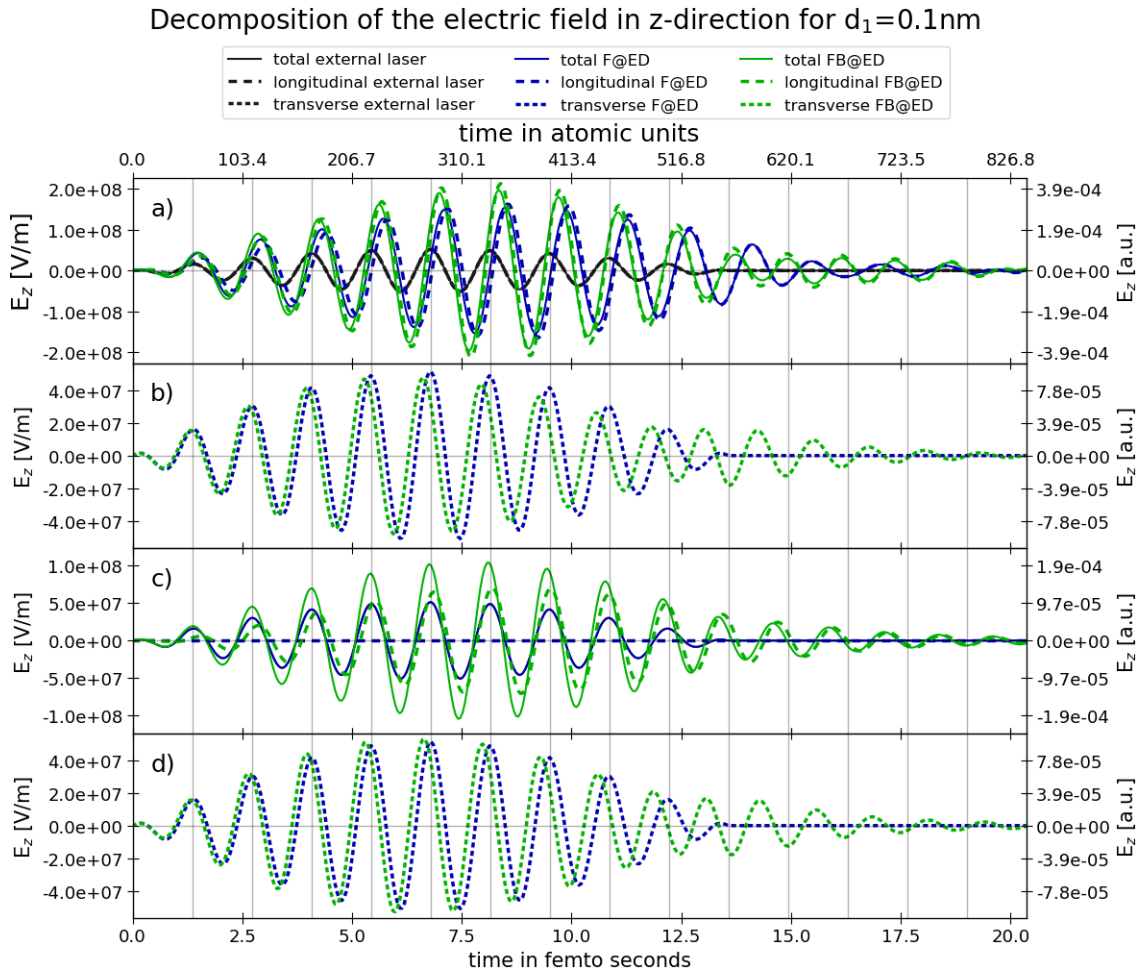


Figure 6.9: Decomposition of the total electric field into transverse and longitudinal components. Panel a) shows the total (solid lines) and the longitudinal (dashed lines) electric field in z-direction at \vec{r}_{cp} . The corresponding transverse field (dotted lines) is plotted in b). The same field decomposition at the surface point \vec{r}_{cpX} is plotted in c) and d).

Figure 6.9 c) and Figure 6.10 c). Here, both the longitudinal and the transverse field have almost the same magnitude and show a clear phase shift. The behaviour in the far field in Figure 6.9 d) and Figure 6.10 d) exhibits besides a phase shift also a slight frequency shift. Consequently, the incident laser pulse interferes with the induced transverse field which results in a frequency modification of the outgoing laser. Since the transverse field, which reaches the far-field detector region, propagates freely, our detector point measures this frequency shift. Figure 6.15 panel d) we shows the Fourier transform of the transverse field at point \vec{r}_{ocpx} which is plotted in the decomposition Figure 6.10. It directly visualizes the frequency shift of the emitted respectively passed electromagnetic field due to the dimer caused electromagnetic fields. The effect is similar to a classical medium.

Up to now, we have looked at the electric field enhancement as function of time.

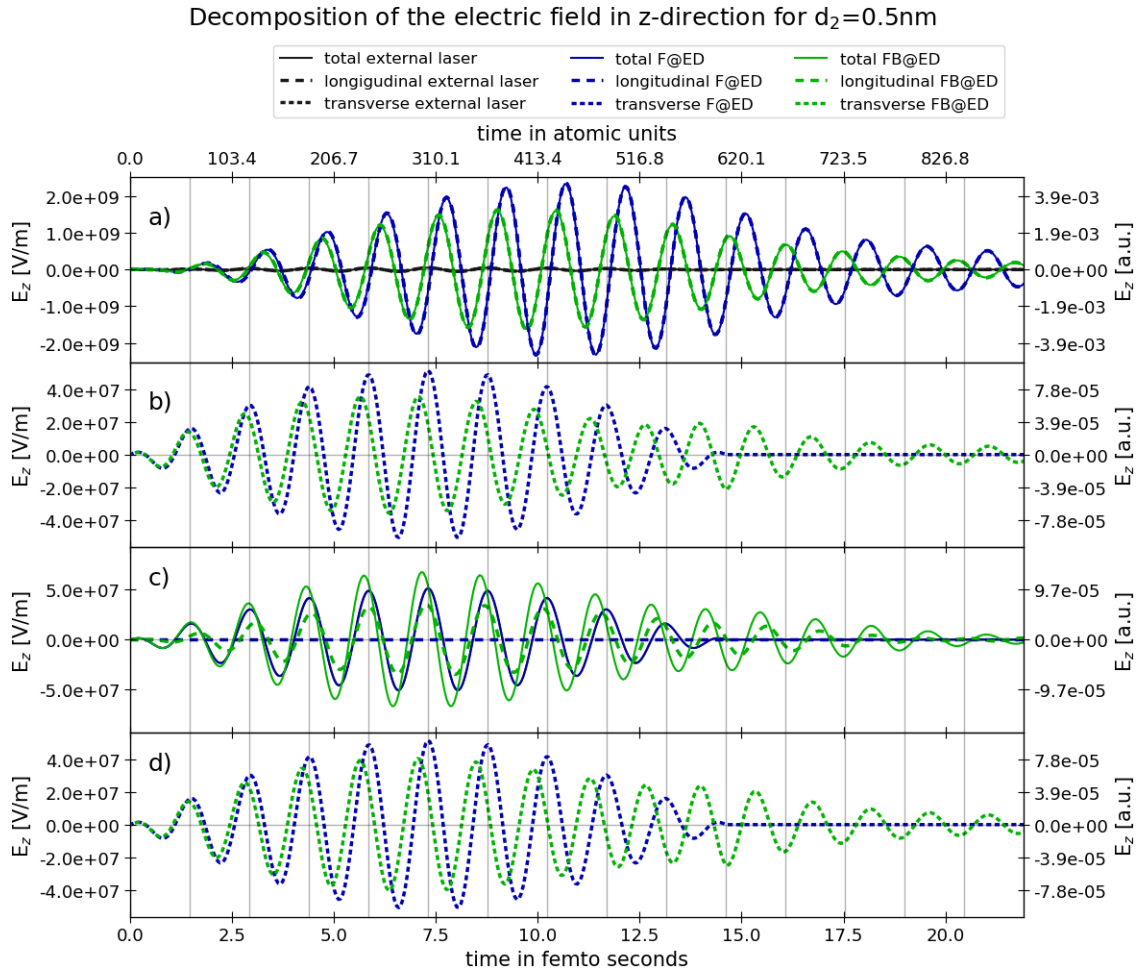


Figure 6.10: Decomposition of the electric field as in Figure 6.9 for the sodium dimer with $d_2 = 0.5 \text{ nm}$.

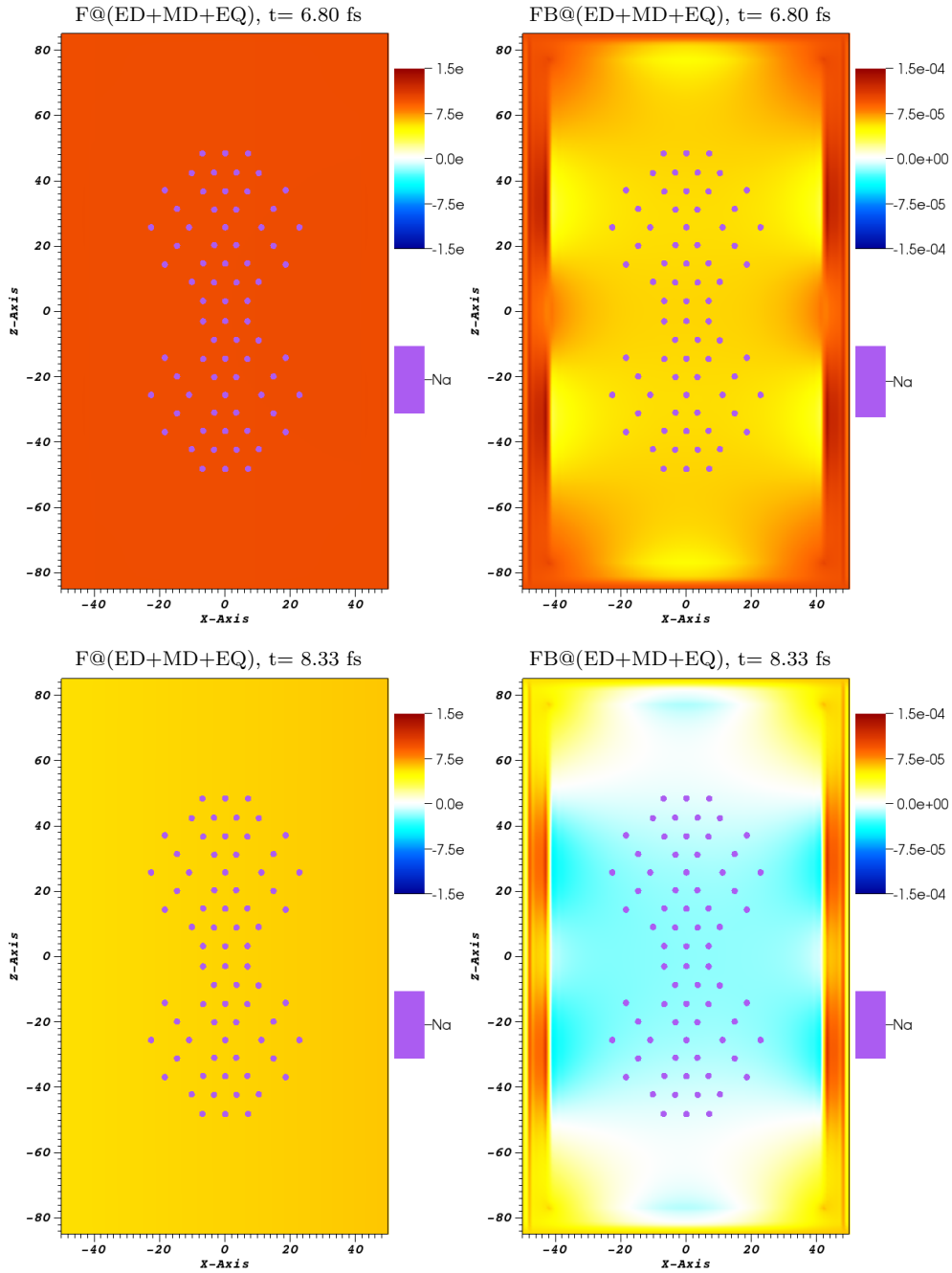


Figure 6.11: Contour plots for the electric field enhancement in the x - z plane of the nanoplasmonic dimer with $d_1 = 0.1$ nm. The upper two panels show the field enhancement when the external laser reaches its maximum and in the lower two panels show the electric field when the field enhancement itself reaches its maximum. The two panels on the left (top and bottom) correspond to the $F@(ED+MD+EQ)$ theory level, whereas the two panels on the right (top and bottom) correspond to $FB@(ED+MD+EQ)$ coupling.

In Figure 6.11, we show contour plots of the transversal electric field enhancement as function of space in the x-z plane of the nanoplasmonic dimer. The two plots in the top row correspond to the point in time where the incoming laser pulse reaches its maximum, whereas the two plots in the bottom row correspond to the point in time where the electric field enhancement reaches its maximum. The two plots in the left column have been computed with light-matter forward coupling only and in the two plots in the right column we have used self-consistent forward-backward coupling. As can be seen, the forward coupled cases show a rather uniform electric field in the plane which is due to the dipole approximation and the fact that the incident wavelength is rather large on the scale of the dimer. On the other hand for the fully coupled case on the right hand side local field effects are clearly visible. In particular in the plot on the bottom right it can be seen that at the maximum of the field enhancement the transversal field contribution in fact counter acts the longitudinal contribution since it has turned to a negative sign in most regions of space.

6.2.2 Next order in multipole coupling and energies

In the previous section, we only focused on the electric dipole Maxwell to matter coupling, since higher order coupling terms do not change the results in Sec. 6.2.2 significantly. This turns when we consider for instance the corresponding matter and Maxwell energies. In that case, higher ordered coupling terms of the Kohn-Sham Hamiltonian, i.e., magnetic dipole (MD) and electric quadrupole (EQ), lead to different energy spectra, which we present in Figure 6.12 and Figure 6.13. As before, we compare only forward coupling with F@ED and the self-consistent forward-backward coupling with FB@ED, but add here also the theory levels F@(ED+MD+EQ) and FB@(ED+MD+EQ) of higher multipole Hamiltonian terms.

First, we consider the corresponding simulations of the d_1 configuration in Figure 6.12. For referencing the amplitude of the actual external laser field on the system, we plot as before the laser pulse curve in panel a). The next panel b) shows the energy of the Kohn-Sham system, which splits significantly in time and stay constant when the laser has passed the simulation box. Similar to the enhanced fields, which exhibit a clear delay of reaction to the initial laser, the energy gain for the matter is very immediate to the external laser intensity. The blue curve shows the conventional F@ED in dipole approximation without back reaction of the matter to the field. If we add the second order multipole coupling terms, the corresponding F@(ED+MD+EQ) run gains more energy than in dipole approximation. This effect can readily be understood, since we drive the system with a Q mode resonance frequency, such that the quadrupole nature of the plasmons results in a larger transfer of energy to the electrons.

Switching on backward coupling reduces the energy absorption of the matter. Both energies of the forward-backward runs remain below the reference F@ED run. Again, the additional multipole terms in the FB@(ED+MD+EQ) run increase the energy curve compared to the FB@ED run, which confirms the higher influence of

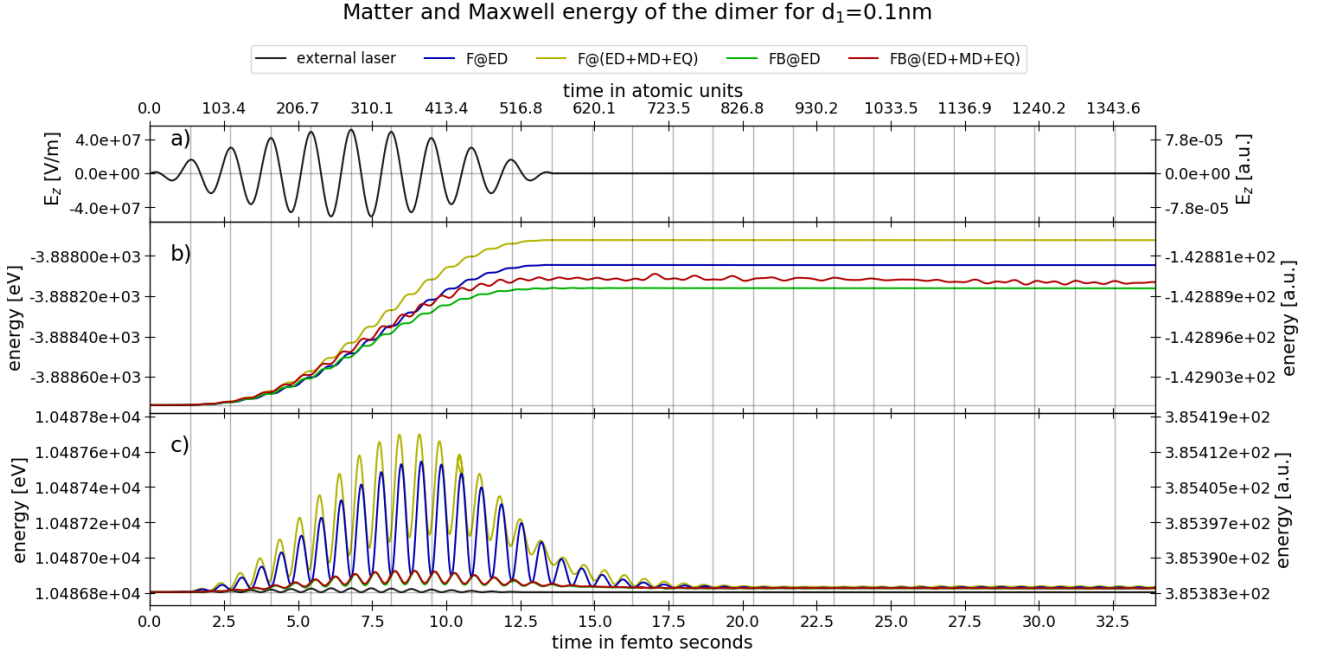


Figure 6.12: Matter and electromagnetic energies for the sodium dimer with $d_1 = 0.1$ nm separation. Panel a) illustrates the external laser amplitude, panel b) displays the electronic energy and in c) we show the corresponding Maxwell energy inside the simulation box.

the magnetic dipole and the electric quadrupole term on the system. If we focus the behavior all increasing curves in detail they are in most cases shaped like cascades with small plateaus between one laser period. This feature indicates that we excite the system with a proper resonance frequency, otherwise the cascades would show some dips due to emitting energy, before the system absorbs energy of the next laser oscillation. Such small dips between the laser periods can only be seen in the red curve of the $\text{FB}@\text{(ED+MD+EQ)}$ which leads to the assumption that the forward and backward coupling system with second order multipole expansion is not exactly resonant to the driven frequency $\omega_1 = 3.05eV$.

In panel c) we show the total electromagnetic energy inside the simulation box, which corresponds to an integration of the Maxwell energy inside the free Maxwell region (b_x, b_y, b_z) of the simulation box $(b_x, b_y, b_z, \text{cf. Figure 5.4})$. First, we note that all Maxwell energies oscillate with twice the frequency of the initial laser due to the squared electric and magnetic field expression of the energy density. The peak positions depend on the phase shift between electric and magnetic fields. Our coupled self consistent forward-backward coupling propagation shows, that the main magnetic field contribution bases on the external plane wave magnetic field. Only very small field amplifications in z and y direction are measured, but negligible. Hence, the magnetic field propagates almost like a plane wave through the simulation

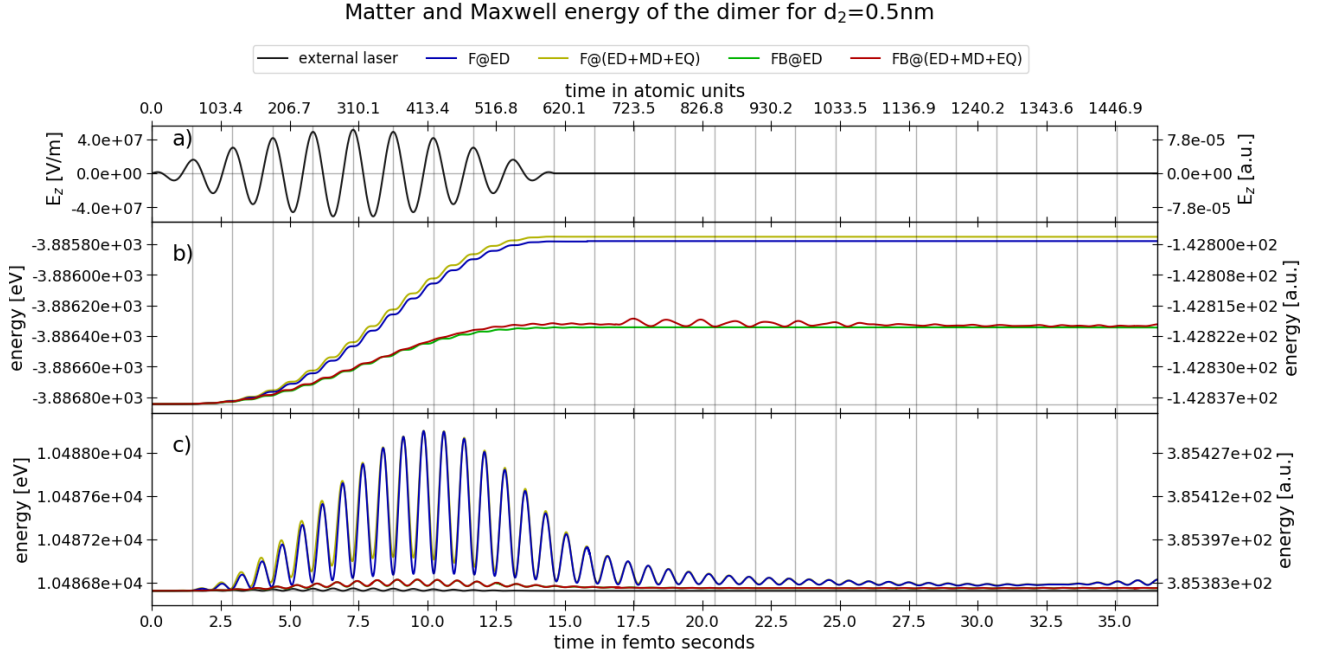


Figure 6.13: Similar to Figure 6.12, we present the matter and electromagnetic energies for the sodium dimer with $d_2 = 0.5$ nm separation.

box. Further detailed observations have shown that the magnetic field increases the total energy peaks only a little. As we already noticed for the electric field enhancement, the dominant part of the total electric field is given by the longitudinal component. This means, that the largest contribution of the Maxwell energies also originates from the longitudinal electric field. This can be seen by comparing the scale of the black curve, which corresponds to the energy of the purely transversal incoming laser pulse, with the blue curve which shows the Maxwell energy for the forward coupled case in dipole approximation. Adding the higher order multipole terms to the Hamiltonian exceeds the Maxwell energy, which corresponds again to the Q mode excitation.

In turn, we focus at the second dimer configuration with $d_2 = 0.5$ nm, which is driven in D mode, which has dipole character. This fact can directly be seen in the corresponding Figure 6.13. While overall a similar situation emerges as for the smaller d_1 distance, the differences between higher order Maxwell to matter coupling and dipole coupling is less significant as before. The small added energies of the MD and EQ terms has only small effects on the electron energies and the electromagnetic fields. The F@ED and F@(ED+MD+EQ) energies as well as the FB@ED and FB@(ED+MD+EQ) energies are almost on top of each other. Therefore, if we couple to a dipole mode of the system, the MD and EQ terms have almost no effect. This corresponds to a perturbative analysis of the system and considering the selection rules of the MD and EQ coupling Hamiltonians. This two exemplary runs

show, that the underlying symmetry of the excited modes if higher order multipole terms become important.

The common fact, that for both distances $d_1 = 0.1$ nm and $d_2 = 0.5$ nm the forward- and backward coupling matter energies remain always below the forward coupling runs demonstrates that the matter absorbs less energy if the back-reaction is taken into account. In addition to the larger absorption of energy, the forward coupling causes larger Maxwell energy amplitudes inside the simulation box. This is remarkable since we observed in Figure 6.7 and Figure 6.8 that the self-consistent forward-backward coupling yields a larger enhancement of the field. As consequence, in some regions of the dimer large field enhancements occur, but the mean amplification is clearly weaker than for the only forward coupled cases. Furthermore, the forward coupling runs break energy conservation, since the laser pumps the matter system without any loss. In the forward-backward coupled simulations this is not as severe anymore, and explains that the energy absorption and the mean Maxwell field enhancement is always smaller compared to the forward coupling runs. The situation would be entirely different if we could enclose the laser pulse completely in the Maxwell box. Then the pulse would not be external anymore and in the forward-backward case full energy conservation holds. For optical wavelengths this requires enormous Maxwell simulation boxes if atomic scale grid spacings are used. But it becomes feasible for hard x-rays, where much smaller Maxwell grids are needed due to the shorter wavelength.

6.2.3 Electromagnetic detectors and harmonic generation

It is a common practice in most quantum simulations to use matter expectation values to approximate optical spectra. For instance, the Fourier transform of the dipole expectation value is often used to compute absorption spectra in the linear case of high-harmonic spectra in the non-linear case. Since we propagate besides the matter system the coupled electromagnetic system, it becomes feasible to directly analyze the emitted radiation. In that sense it is not necessary take the matter observables and the assumption that their properties give approximately the emitted Maxwell field.

According to Sec. 5.9, we define electromagnetic detector regions in the far-field close to the box boundaries, which provides a paradigm shift to perform numerical simulations that very closely resemble the experimental situation. To demonstrate this, we analyzed once the dipole expectation values of the dimer $d_2 = 0.5$ nm separation in Figure 6.14 b) - e) and the x-component of the electric field far field. Panel a) visualizes the external laser field and we notice that the same frequency appears in the corresponding dipole expectation values as well as in the electric field component. According to common optical theoretical methodology, this means the matter oscillates resonantly with its excitation signal, and in turn since we hit the resonance frequency, it is assumed that it emits electromagnetic light with the same frequency perpendicular to the oscillation axis.

For further concrete frequency analysis, we performed a Fourier transform of

panels e) and f), which are shown in Figure 6.15 in panel a) respectively b). Comparing the forward coupling cases, F@ED and FB@(ED+MD+EQ), with the fully coupled ones, FB@ED and FB@(ED+MD+EQ), show the same frequencies, but slightly phase shifted and with different strength. The oscillation amplitudes correspond with our previous considerations about the electric field enhancements and the energies. Adding the additional multipole Hamiltonians reveals new optical features of the system, which can directly be seen in panel e) in Figure 6.14. The two dipole expectation values along the x-axis shows in both cases, the forward and fully coupled runs, oscillate with twice the frequency of the incoming laser. Therefore, second harmonic generation is only found in beyond dipole Maxwell to matter couplings. We emphasize here, that both frequencies, the can directly measured in the electric field x-component at the off-center point \vec{r}_{ocpy} , which we present in panel f). Both runs, F@(ED+MD+EQ) and FB@(ED+MD+EQ), reproduce clearly the incoming frequency of the external laser. However, if we look at the FB@(ED+MD+EQ) curve,

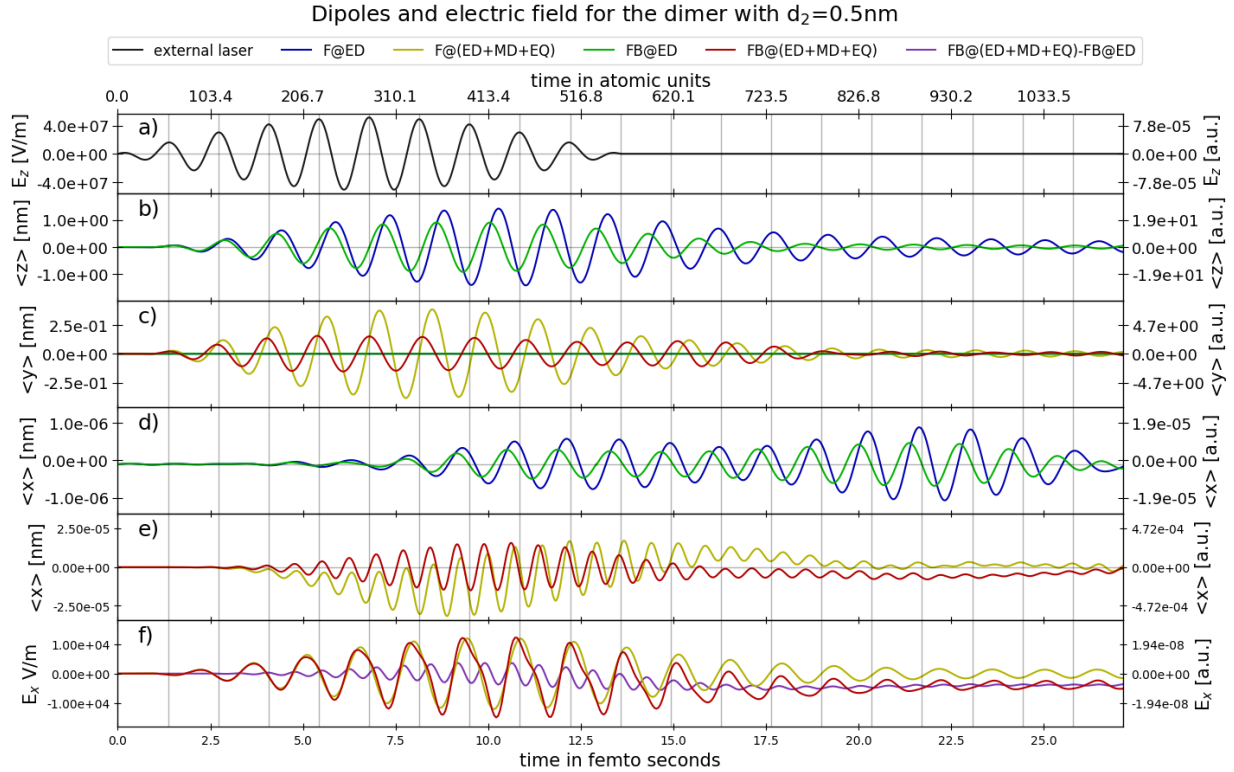


Figure 6.14: Position expectation values $\langle x \rangle$, $\langle y \rangle$, and $\langle z \rangle$ of the nanoplasmonic dimer with $d_1 = 0.1$ nm. In panel a) we show the initial laser pulse as reference signal and in b) - e) the dipoles of the dimer along different axis. Only beyond dipole approximation coupling reveals higher-order harmonics, which is directly detected by the E_x field component at the off-center point \vec{r}_{ocpy} along the y-axis.

Fourier transform of the electric far field and electric dipole

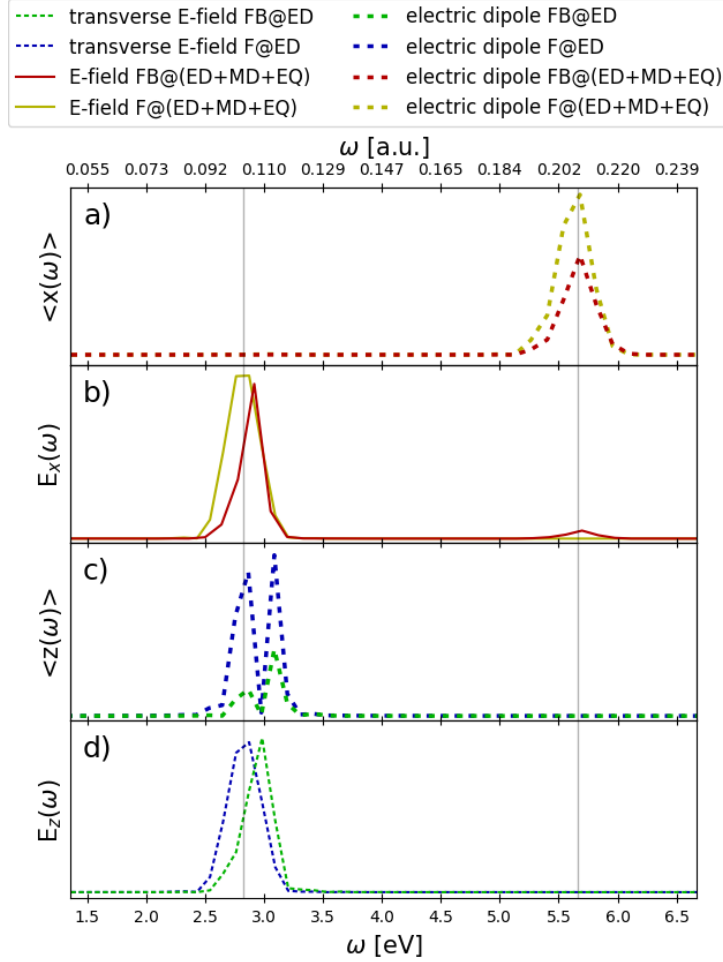


Figure 6.15: Fourier transform of the dipole expectation values and the electric field at the far-field detectors. Panel a) and b) show the Fourier transform of the dipole and the electric field at the off-center point \vec{r}_{ocpy} from panels e) and f) in Figure 6.14 respectively. While in the matter observable in a) only the second harmonic peak is visible, the Fourier spectrum of the electric field in b) contains the fundamental laser frequency and the second harmonic. In panel d) we show the Fourier transform of the electric field at the off-center point \vec{r}_{ocpx} along the laser propagation axis in dipole approximation. The field is shifted in frequency when self-consistent forward-backward coupling is used. The matter dipoles for this case are shown in panel e). The Fourier transform of panel d) correspond to the transverse fields shown in Figure 6.10. In the forward coupled case a spurious peak appears at the energy of the incoming laser (2.83 eV). This peak is suppressed in the forward-backward coupled case and the dipole spectrum also matches better the actual emitted radiation field in panel d).

the field oscillation shows a small distortion compared to the $F@(ED+MD+EQ)$ run, which looks more correctly cosinoidal. Subtracting both fields visualizes directly the reason for the deformed $FB@(ED+MD+EQ)$ signal. It is superposed by the second harmonic frequency, which we do not see in the $F@(ED+MD+EQ)$ curve, since we neglect the full coupled back-reaction of the matter to the electromagnetic field.

We note here, that $F@(ED+MD+EQ)$ includes indeed some back-reaction of the matter, namely the longitudinal field of the matter charge distribution. Otherwise, we would not see any oscillation in the yellow curve, since the x-component of the external laser field is zero. Consequently, we can deduce, that the second harmonic signal is a transverse radiation oscillating along the x-axis but propagating in y-direction, whereas the first harmonic oscillation in that direction(!) seems to be only longitudinal and hence localized to the matter.

6.2.4 Ion motion

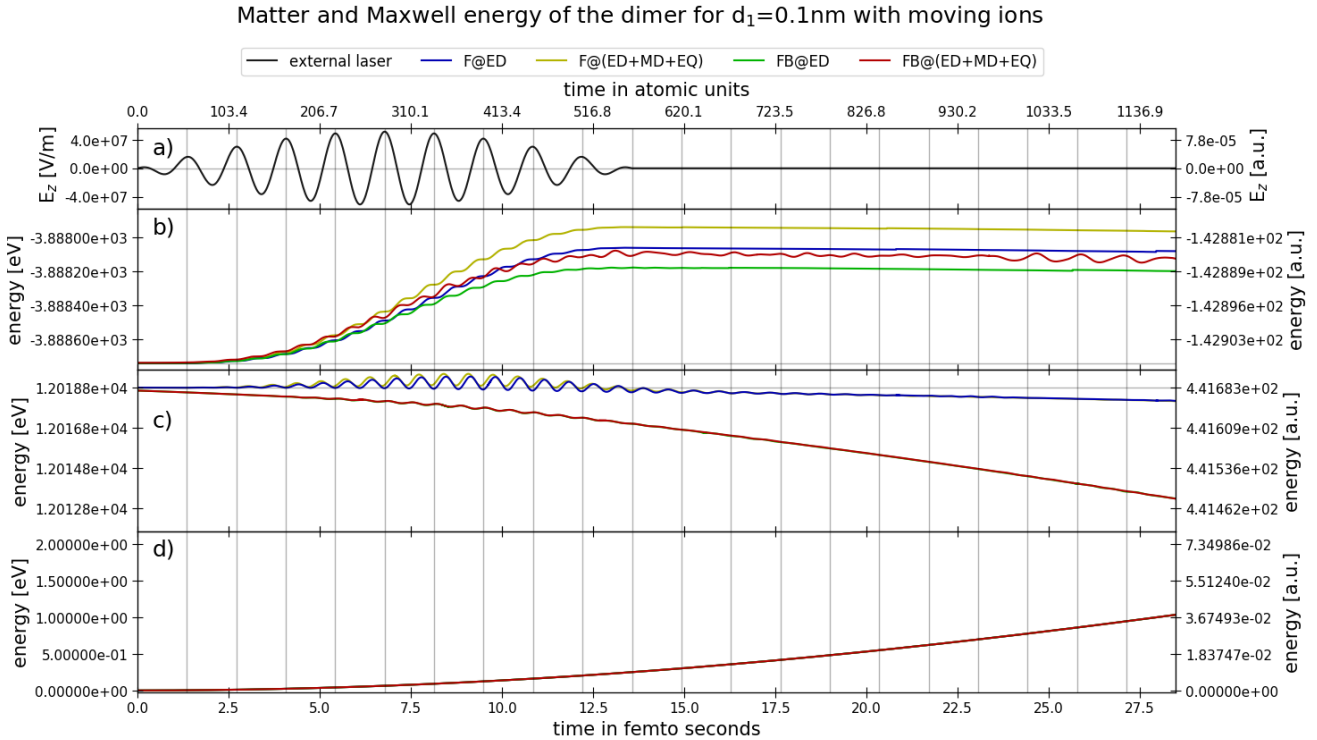


Figure 6.16: Same as Figure 6.12 but now including the motion of the ions in classical Ehrenfest approximation.

In all the simulations that we have considered so far, we have used the Born-Oppenheimer approximation and clamped the classical nuclei at the optimized ground state. In this section, we release this constraint. According to Sec. 4.6, we can propagate the classical motion of the nuclei using Ehrenfest equations of mo-

tion [116] and the Lorentz force, which we introduced in Eq. (4.6.12). In our case, we get the Lorentz forces in terms of the Riemann-Silberstein electric and magnetic field that we propagate in time. This allows to capture nuclear forces due to local field effects. For all the following cases, we take as initial condition for the Ehrenfest equations the atomic positions of the optimized ground state and set the initial velocities to zero. This effectively corresponds to a rather "cold" nuclear subsystem. More sophisticated velocity distributions could be used, e.g., thermalized velocity distributions from molecular dynamics runs coupled to a thermostat, but we leave such temperature studies for the future.

The ionic motion does not significantly change the behavior of the electromagnetic field within the first 50 fs, which is not quite remarkable, since typically ionic effects take place on a pico-second time scale. Nevertheless, taking a look at the corresponding energies reveals a strong difference that we present in Figure 6.16 for the nanoparticle distance d_1 and which corresponds to the clamped ions run in Figure 6.12. As before, panel a) shows the incoming laser, panel b) the matter energies and panel c) the Maxwell energies. In addition we add panel d) which illustrates the sum of kinetic energy of all nuclei as function of time. The additional ionic motion causes some additional fluctuations to the matter energy evolution, but the main behavior is very similar to the fixed ions simulation. Looking at the Maxwell energies in c) reveals a strong decrease of the Maxwell energy in the forward coupling and a rather strong decrease in the self-consistent forward-backward case. Since the electronic energy remains almost identical to the case of clamped ions, the losses in the Maxwell energy are directly transferred to the nuclei. As a consequence, the kinetic energy of the nuclei grows. This rather strong increasing of the ionic kinetic energy is remarkable, since it implies an untypical fast motion of the nuclei.

6.2.5 Comparison of different density functionals

So far, all previous presented results have been computed with TDLDA functionals [123, 114] as choice for the approximate exchange-correlation functional that build the scalar potential for the longitudinal part of the light-matter interaction. In this section we assess the relative importance of exchange-correlation effects versus self-consistent light-matter interaction. For this purpose, we repeat the previous simulations, but using this time the PBE functional [123, 130]. To demonstrate the difference between the two different exchange-correlation runs, we plot in Figure 6.17 some characteristic variables like the electric field at the origin in panel a), the Maxwell energy inside the free-Maxwell region in panel b), and one dipole expectation value in panel c). In all panels, we compare the TDPBE results (dashed lines) with the TDLDA results (solid lines). In all cases the difference between the two different functionals (dashed vs. solid lines) is significantly smaller than the difference between the forward coupled and fully coupled simulation (blue vs. green lines). In case of Maxwell energy and dipole expectation value, the difference between the TDLDA and TDPBE run is rather small, whereas the electric field behaviors are only very similar in the beginning, but differ more and more when the electric field

envelope decreases. However, our presented nanoplasmonic example reveals that it is more important in case of large induced currents and electromagnetic fields to use the self-consistent forward-backward light-matter interactions than to include further exchange-correlation contributions to the effective Kohn-Sham potentials. This supports the need for a self-consistent coupling to Maxwell's equations to achieve a comprehensive description of light-matter interactions.

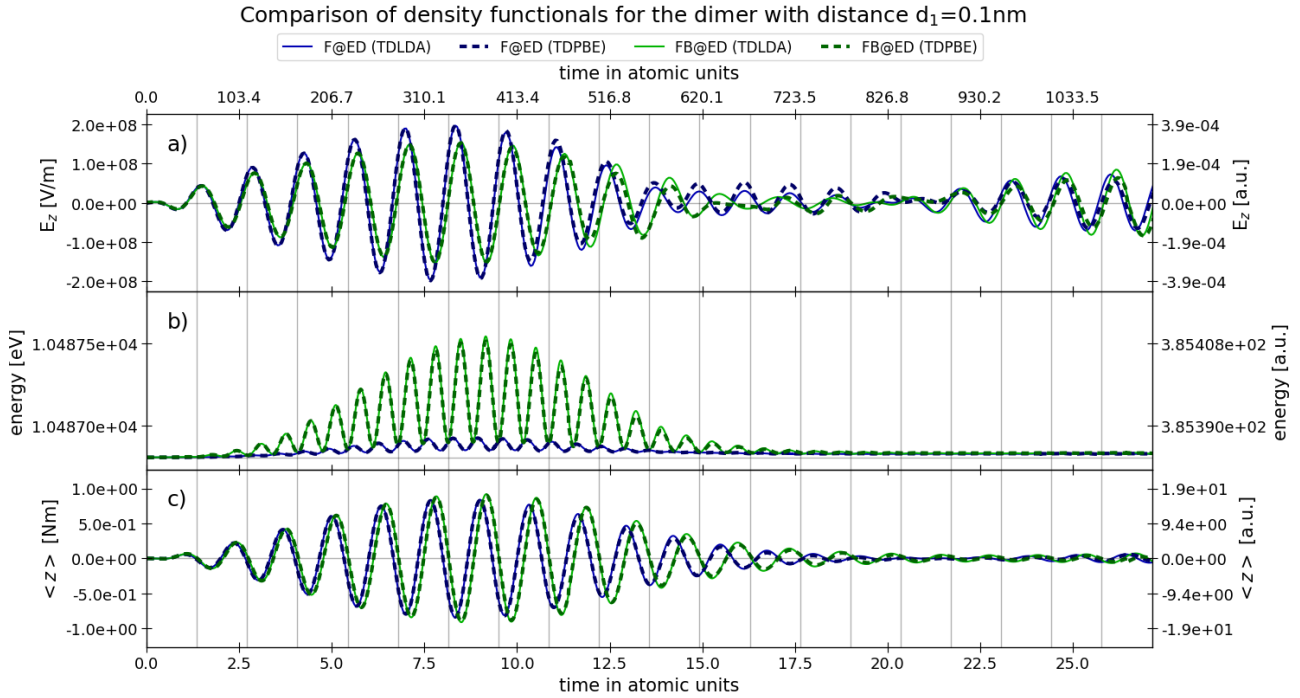


Figure 6.17: In the figure we show in panel a) the electric field at the origin, in panel b) the integrated Maxwell energy in the simulation box, and in panel c) the dipole expectation value in z -direction. We compare TDPBE results (dashed lines) with the TDLDA results (solid lines). The difference between TDPBE and TDLDA (dashed vs. solid lines) is much smaller than the difference between only forward coupling and self-consistent forward-backward coupling (blue vs. green lines). In particular, for forward-backward coupling a clear frequency shift is visible already after a short time.

Summary, conclusion and outlook

In this thesis, we have faced the challenge of finding a feasible methodology and a first implementation of three-dimensional fully forward and backward coupled light-matter interactions. As a first key step, we have transformed the common Maxwell's equation into a Riemann-Silberstein representation, which provides the underlying equation of motion for the electromagnetic field in an inhomogeneous Schrödinger-like equation. This crucial step, gives us the opportunity to use quantum-mechanical time-evolution operators to propagate the electromagnetic field similar to matter wave functions. We use this advantage to implement a fundamental real-time real-space classical electromagnetic equation propagation into the existing quantum-mechanical simulation code Octopus. First, we implemented a stand-alone electromagnetic field simulation, which handles external current densities and linear media. We validate our novel propagation scheme and implementation with the established electromagnetic simulation program MEEP, which uses a standard finite-difference time-domain method for the Maxwell field propagation. The considered test simulations agree very well with the results of MEEP, also with regard to stability and efficiency of the runs.

To extend the possibilities for applications, we have considered adequate electromagnetic boundary conditions. As a first important boundary condition, we considered absorbing boundaries to simulate open Maxwell systems. We employ two different methods, first a mask absorption function which is easy to implement, and secondly a perfectly matched layer propagation. Our comparison of both different techniques has shown, that the PML provides a significantly better absorbing boundary and qualitatively better wave propagations in the simulation box. To simulate incoming signals which enter the simulation box, we have introduced incident plane wave boundaries, which we also combined with the perfectly matched layer boundaries to simulate incoming waves and scattered outgoing fields. This feature is useful to simulate pump-probe experiments or a particle excitation from several laser pulses and different incident angles. One possible way to get scattered fields from plane waves, for instance, is based on the interaction of the plane wave in vacuum and a linear medium, as we have shown in a first propagation example coupled to a linear medium. Our implemented propagator considers besides space- and

time-dependent electric permittivity and magnetic permeability electric and magnetic conductivities. With this feature at hand, one can design a large set of purpose tailored simulation boxes, e.g., perfect and semi-transparent mirrors, wave guides, lossy layers, just to list a view options. Overall, the purely Maxwell propagation based on quantum-mechanical time-evolution operations is an equivalently alternative scheme to common electromagnetic time propagation via finite difference time domain, and it builds the first pillar for simulating fully coupled three-dimensional light-matter systems.

The second pillar is based on the many-body considerations for large matter systems. Starting on the theory level of quantum electrodynamics, we have deduced a multi-species auxiliary system, the Kohn-Sham system on a Pauli level to describe a non-relativistic low energy regime and based on density-functional theory (DFT). Using DFT instead of the full many-body particle problem leads to a feasible but still very computational expensive problem. Hence, the underlying Maxwell-Pauli-Kohn-Sham equations determine the corresponding matter current density, which is used as the classical current inhomogeneity term of our Maxwell propagation equation. In that way, we coupled the matter reaction to the surrounded electromagnetic field.

Furthermore, we have considered the influence of the electromagnetic field on the Kohn-Sham Hamiltonian. Starting with the non-relativistic Pauli equation, we end up at the full minimal coupled Hamiltonian for the quantum mechanical system. We have solved the issue that the full minimal coupling term depends on the gauge dependent vector potential by transforming the Kohn-Sham Hamiltonian with a Power-Zienau-Woolley transformation to get multipole coupling terms, which depend now only on the electromagnetic fields. Since in this picture, only the transverse components of the fields couple to the matter, we use a Poisson solver and solve the Poisson equation which is part of a Helmholtz-decomposition to obtain the correct transverse fields. In a last step, we have handled the problem of a self-consistent time-step of the fully coupled light-matter system by introducing a predictor-corrector scheme. Taking into account, that the dynamics of our considered triad, nuclei, electron, and photon, differ fundamentally, we exploit these properties to get an efficient and accurate approach of the full coupled multi-scale problem. We employ our corresponding implementation to demonstrate fully coupled light-matter effects compared to only conventional forward coupling simulations.

Since nanoplasmonic systems reveal often a remarkable optical activity, we select a sodium dimer cluster as a first test system for our novel approach. Our first simulation uses only a simple subset of the presented full Ehrenfest-Pauli-Kohn-Sham scheme. Using only the paramagnetic current density, no spin matter states, static pseudopotentials and only mean-field vector potentials as a first approximation for the Kohn-Sham vector potential, the corresponding results show clearly the importance of simulating the light-matter system in a fully self-consistent description. All measurable variables, where we only selected the most relevant ones, i.e., energy, dipole, and electric field, reveal a significant different behavior compared to the conventional forward coupling runs. In addition, the direct performed measurements of the electromagnetic fields at our defined electromagnetic detectors to analyze the far

field attributes has shown, that the usual approximation to deduce optical properties only indirectly by using matter variables in general does not hold. Furthermore, we observed that the difference of computed observables between local density approximation and gradient-corrected functional was minor compared to the difference of calculating only forward coupling and the self-consistent forward-backward coupling. Hence, our results contradict the often argued position in common literature, that the discrepancies between theory and experiment are based on missing exchange-correlation effects.

To sum up, based on our results, we come to the conclusion that self-consistent forward-backward couplings should always be included. Their effects can easily reach the magnitude of longitudinal exchange-correlation contributions or even exceed them.

The Ehrenfest-Maxwell-Pauli-Kohn-Sham scheme that we have introduced in this thesis as a mean-field limit of the exact density-functional formulation of the Pauli-Fierz field theory is only a first step. Future investigations have to focus on better approximations closer to the full field theory to go beyond the mean-field limit and to simulate and reveal more quantum effects. However, even in the EMPKS limit ensuing steps are the implementation of remaining mean-field features that we already discussed in this work. For instance, providing a propagation with total system current which includes the diamagnetic current and magnetization current. Taking the magnetization current into account, the electromagnetic field back-reaction becomes spin-dependent, and we can investigate magnetic effects from a fully resolved magnetization of the system. To complete the total current density and get the full back-coupling, we have to add the ionic current of the nuclei.

We already found a relatively strong dispersion with shifted phase and frequency of the transverse electromagnetic field while it passes the dimer. The diamagnetic current should increase this effect since the corresponding current term couples directly the two Riemann-Silberstein helicity states similar to the coupling terms in the Riemann-Silberstein description of a linear medium. In general, since our implemented Maxwell propagation couples to quantum mechanical matter as well as linear media, the interesting question arises, to find a relation between these two different description of matter. In other words, a quantum mechanical simulation leads to classical space- and time-dependent electric permittivity and magnetic permeability, which approximately reproduce the electromagnetic field propagation replacing the quantum system by an artificially designed linear medium. In this case, we can exploit that our propagation can combine both, microscopic and macroscopic systems, in one simulation.

According to our observations for the sodium dimer, the fully coupled system induces effects on every system variable. Therefore, conventional used variables have to be modified to reach accurate approximated simulations. One important task is the construction of adapted exchange-correlation scalar and vector potentials to go beyond the classical mean-field approximation for photons to consider their quantum nature, for instance, vacuum fluctuations. In turn, the quantum nature

of the matter can be shown by correcting the physical-mass approximation. Besides the scalar and vector exchange-correlation potentials, the pseudo-potentials require a dependency on the electromagnetic fields, starting from an all-electron consideration, since they have to take the full coupled electromagnetic field into account. Further, our nanoplasmonic simulations including ion motion and their remarkable raise in kinetic energy show that the electromagnetic fields very close to the ions is not correct. It seems that the calculated Lorentz-forces acting on the ions are too strong, which could be a consequence of the incorrect pseudo-potential behavior at that level.

Additionally, referring to the vector potential, which we already calculate in a first mean-field approximation using the Poisson solver, we can employ in principle the full minimal coupling interaction instead of the multipole expansion terms. However, having both interaction levels gives us the opportunity to find the order of the multipole expansion that shows the main responsibility of an observed effect. In our presented nanoplasmonic example we already show, that only the beyond dipole coupling terms cause the detected radiation of the second harmonic generation.

In this work, we found the nanoparticle groundstate by a conventional diagonalization of the Hamiltonian, since we focused on the electromagnetic time-propagation. However, fully coupled light-matter interactions should also already be considered to find the correct groundstate. This requires to solve stationary Maxwell equations self-consistently coupled to the stationary Kohn-Sham equations. The groundstate can also be modified by starting from a thermal initial state for the ions to catch temperature effects.

Expanding our so far used simulation box for finite quantum systems to infinite periodic systems in one, two or three dimensions also opens a whole new class of possibilities. For instance, the investigation of the influence of the self-consistent forward-backward reaction for large crystal structures, e.g., to improve the efficiency of solar cells.

As a final conclusion, we note that our fully coupled Ehrenfest-Maxwell-Pauli-Kohn-Sham implementation provides a rather practicable, flexible, and comprehensive simulation approach to push research forward in optical material science (nanooptics, nano-plasmonics, (photo) electrocatalysis), in condensed matter or even in understanding chemical reactions, since they are mainly determined by the electromagnetic interactions between ions and electrons.

Appendices

Appendix A

Non-relativistic Pauli Hamiltonian in Coulomb gauge

In this appendix, we introduce step-by-step the full QED Hamiltonian. First, we briefly summarize the basic relativistic wave equations and their properties, which lead to the free matter Hamiltonians for different matter species and the free photon Hamiltonian. The full Hamiltonian includes an additional interaction Hamiltonian that is due to the minimal-coupling prescription. In the appendix we also use the relativistic notation introduced in Sec. 4.1.

A.1 Vector potential and Coulomb gauge

Instead of the common Maxwell's Eqs. (1.1.8) - (1.1.11) or the Riemann-Silberstein complex vector expressions in Eq. (1.1.42) and Eq. (1.1.47), the Maxwell's equations can also be described by the more common four-vector potential $A^\mu(\vec{r}, t)$. In the present work, we define $A^\mu(\vec{r}, t)$ as

$$A^\mu(\vec{r}, t) = \begin{pmatrix} A^0(\vec{r}, t) \\ A^k(\vec{r}, t) \end{pmatrix}, \quad (\text{A.1.1})$$

with a scalar potential $A^0(\vec{r}, t)$ and a spatial vector potential $\vec{A}(\vec{r}, t)$. Common textbooks usually define the four-vector potential $\tilde{A}^\mu(\vec{r}, t)$ including a factor $1/c_0$ compared to $A^\mu(\vec{r}, t)$, which reads [75, 102]

$$\tilde{A}^\mu(\vec{r}, t) = \begin{pmatrix} \tilde{A}^0(\vec{r}, t) \\ \tilde{A}^k(\vec{r}, t) \end{pmatrix}, \quad \tilde{A}^\mu(\vec{r}, t) = \frac{1}{c_0} A^\mu(\vec{r}, t). \quad (\text{A.1.2})$$

For both four-vector potentials, the the corresponding four-vector current density $j^\mu(\vec{r}, t)$ is [75, 102]

$$j^\mu(\vec{r}, t) = \begin{pmatrix} j^0(\vec{r}, t) \\ j^k(\vec{r}, t) \end{pmatrix} = \begin{pmatrix} c_0 \rho(\vec{r}, t) \\ \vec{j}(\vec{r}, t) \end{pmatrix}. \quad (\text{A.1.3})$$

The two general inhomogeneous Maxwell's equations with non-zero charge density $\rho(\vec{r}, t) = c_0^{-1} j^0(\vec{r}, t)$ and current density $j^k(\vec{r}, t)$ can be expressed by [75, 102]

$$\partial_\nu F^{\nu\mu}(\vec{r}, t) = \mu_0 j^\mu(\vec{r}, t) \quad (\text{A.1.4})$$

with the electromagnetic tensor $F_{\mu\nu}(\vec{r}, t)$ defined in terms of in this thesis used four-vector potential $A^\mu(\vec{r}, t)$

$$F^{\nu\mu}(\vec{r}, t) = \frac{1}{c_0} \partial^\nu A^\mu(\vec{r}, t) - \frac{1}{c_0} \partial^\mu A^\nu(\vec{r}, t) . \quad (\text{A.1.5})$$

This leads to the inhomogeneous Maxwell's equations expression

$$\partial_\nu \partial^\nu A^\mu(\vec{r}, t) - \partial^\mu \partial_\nu A^\nu(\vec{r}, t) = c_0 \mu_0 j^\mu(\vec{r}, t) . \quad (\text{A.1.6})$$

The homogeneous Maxwell's equations in terms of $F_{\mu\nu}(\vec{r}, t)$ are given by [75, 102]

$$\partial_\lambda F^{\mu\nu}(\vec{r}, t) + \partial_\mu F^{\nu\lambda}(\vec{r}, t) + \partial_\nu F^{\lambda\mu}(\vec{r}, t) = 0 \quad (\text{A.1.7})$$

and takes with Eq. (A.1.5) the form

$$\partial_\lambda (\partial^\mu A^\nu(\vec{r}, t) - \partial^\nu A^\mu(\vec{r}, t)) + \partial_\mu (\partial^\nu A^\lambda(\vec{r}, t) - \partial^\lambda A^\nu(\vec{r}, t)) + \partial_\nu (\partial^\lambda A^\mu(\vec{r}, t) - \partial^\mu A^\lambda(\vec{r}, t)) = 0 . \quad (\text{A.1.8})$$

If two indices are equal, the left-hand side of Eq. (A.1.8) is equal to zero, and in all other cases, we obtain the homogeneous Maxwell's equations in vector potential expression.

In contrast to the physical measurable electromagnetic fields, the vector potential $A^\mu(\vec{r}, t)$ has a gauge freedom since the field variables and the vector potential are connected by the relations [75, 102]

$$E^k(\vec{r}, t) = -\partial_k A^0(\vec{r}, t) - \partial_0 A^k(\vec{r}, t) , \quad (\text{A.1.9})$$

$$B^k(\vec{r}, t) = -\frac{1}{c_0} \varepsilon^{klm} \partial_l A_m(\vec{r}, t) . \quad (\text{A.1.10})$$

Therefore, $E^k(\vec{r}, t)$ and $B^k(\vec{r}, t)$ are invariant under the vector potential transformation [75]

$$A^0(\vec{r}, t) \rightarrow A'^0(\vec{r}, t) = A^0(\vec{r}, t) - \frac{\partial \chi(\vec{r}, t)}{\partial t} , \quad (\text{A.1.11})$$

$$A^k(\vec{r}, t) \rightarrow A'^k(\vec{r}, t) = A^k(\vec{r}, t) + \partial_k \chi(\vec{r}, t) , \quad (\text{A.1.12})$$

where $\chi(\vec{r}, t)$ is a scalar differentiable function. If $\rho(\vec{r}, t)$ and $j^k(\vec{r}, t)$ are equal to zero, Eq. (A.1.6) becomes homogeneous, i.e.,

$$\partial^\nu \partial_\nu A^\mu(\vec{r}, t) = 0 . \quad (\text{A.1.13})$$

According to standard textbooks [75, 102] and Sec. 1.1, Eq. (A.1.6) is equivalent to the Riemann-Silberstein Maxwell's equations, i.e., Eq. (4.2.21) and Eq. (4.2.27).

The Maxwell-matter coupling that we discuss in the following sections is determined in most cases by the gauge-dependent vector potential. Taking into account, that our Riemann-Silberstein description for the homogeneous case allows only two independent polarizations, we remain using the vector potential in Coulomb gauge, when we couple to matter. In Coulomb gauge $A^\mu(\vec{r}, t)$ obeys [101]

$$\partial_l A^l(\vec{r}, t) = 0, \quad (\text{A.1.14})$$

and with Eq. (A.1.9) for the electric field $E^k(\vec{r}, t)$ means, that the electric field decomposition in a longitudinal one $E_{\parallel}^k(\vec{r}, t)$ and a transverse one $E_{\perp}^k(\vec{r}, t)$ leads to

$$E_{\parallel}^k(\vec{r}, t) = -\partial_k A^0(\vec{r}, t) \quad (\text{A.1.15})$$

$$E_{\perp}^k(\vec{r}, t) = -\partial_0 A^k(\vec{r}, t). \quad (\text{A.1.16})$$

Taking the Coulomb gauge, Eq. (A.1.6) is equivalent to

$$\partial_\nu \partial^\nu A^\mu(\vec{r}, t) - \partial^\mu \partial_0 A^0(\vec{r}, t) = c_0 \mu_0 j^\mu(\vec{r}, t). \quad (\text{A.1.17})$$

The zero-component ($\mu = 0$) equation leads with Eq. (A.1.3), Eq. (4.1.10) and $c_0 = 1/\sqrt{\epsilon_0 \mu_0}$ to

$$\begin{aligned} \partial_l \partial^l A^0(\vec{r}, t) &= c_0 \mu_0 j^0(\vec{r}, t), \\ \Leftrightarrow A^0(\vec{r}, t) &= -\frac{1}{c_0 \epsilon_0} \vec{\nabla}^{-2} j^0(\vec{r}, t). \end{aligned} \quad (\text{A.1.18})$$

In Coulomb gauge, the zero-component of the vector potential $A^0(\vec{r}, t)$ depends only on the zero component of the total arising current density, which can be seen by using the Green's function of the Laplacian in real-space representation

$$G(\vec{r}, \vec{r}') = \left\langle \vec{r} \left| \left(\vec{\nabla}^{-2} \right) \right| \vec{r}' \right\rangle, \quad (\text{A.1.19})$$

and

$$w(\vec{r}, \vec{r}') = -\frac{1}{\epsilon_0} G(\vec{r}, \vec{r}') = \frac{1}{4\pi \epsilon_0 |\vec{r} - \vec{r}'|}. \quad (\text{A.1.20})$$

Therefore, the scalar potential $A^0(\vec{r}, t)$ is given by [101]

$$A^0(\vec{r}, t) = \frac{1}{c_0} \int_{\Omega} d^3 r' \left(-\frac{1}{\epsilon_0} G(\vec{r}, \vec{r}') \right) j^0(\vec{r}', t) \underset{\substack{\Omega = \mathbb{R}^3 \\ \mathbb{R}^3}}{=} \frac{1}{c_0} \int_{\mathbb{R}^3} d^3 r' w(\vec{r}, \vec{r}') j^0(\vec{r}', t). \quad (\text{A.1.21})$$

Due to the continuity equation

$$\begin{aligned} \partial_\mu j^\mu(\vec{r}, t) &= 0 \\ \Leftrightarrow \partial_0 j^0(\vec{r}, t) &= -\partial_l j^l(\vec{r}, t), \end{aligned} \quad (\text{A.1.22})$$

Using the scalar potential Eq. (A.1.21) and the continuity Eq. (A.1.22) yields for the components $\mu = k$ of Eq. (A.1.17)

$$\partial_\nu \partial^\nu A^k(\vec{r}, t) + \frac{1}{c_0} \partial^k \int_{\mathbb{R}^3} d^3 r' \frac{\partial'_l j^l(\vec{r}', t)}{4\pi\epsilon_0 |\vec{r} - \vec{r}'|} = c_0 \mu_0 j^k(\vec{r}, t). \quad (\text{A.1.23})$$

Each spatial current density vector can be split into a longitudinal one $j_{\parallel}^k(\vec{r}, t)$ and transverse part $j_{\perp}^k(\vec{r}, t)$ with

$$j^k(\vec{r}, t) = j_{\parallel}^k(\vec{r}, t) + j_{\perp}^k(\vec{r}, t), \quad (\text{A.1.24})$$

and using the Helmholtz decomposition [75, 102], the longitudinal current density can be expressed as

$$\begin{aligned} j_{\parallel}^k(\vec{r}, t) &= -\vec{\nabla} \int d^3 r' \frac{\vec{\nabla}' \cdot \vec{j}(\vec{r}', t)}{4\pi |\vec{r} - \vec{r}'|} \\ \Leftrightarrow j_{\parallel}^k(\vec{r}, t) &= \partial^k \int d^3 r' \frac{\partial'_l j^l(\vec{r}', t)}{4\pi |\vec{r} - \vec{r}'|}. \end{aligned} \quad (\text{A.1.25})$$

In this manner, Eq. (A.1.6) can be simplified with $c_0 = 1/\sqrt{\epsilon_0 \mu_0}$ to [75]

$$\begin{aligned} \partial_\nu \partial^\nu A^k(\vec{r}, t) + \frac{1}{c_0 \epsilon_0} j_{\parallel}^k(\vec{r}, t) &= c_0 \mu_0 \left(j_{\parallel}^k(\vec{r}, t) + j_{\perp}^k(\vec{r}, t) \right) \\ \Leftrightarrow \left(\partial_0^2 + \partial_l \partial^l \right) A^k(\vec{r}, t) &= c_0 \mu_0 j_{\perp}^k(\vec{r}, t), \end{aligned} \quad (\text{A.1.26})$$

where $j_{\perp}^k(\vec{r}, t)$ represents the transverse field of the total current density $j^k(\vec{r}, t)$.

A.2 Pauli-equation as non-relativistic limit of coupled light-matter systems

In Sec. 4.2, we introduced the relativistic equations of motion for different spin particles with and without mass. We mentioned that the same considerations can be repeated for other spins, but they are restricted due to not finding simple and physical side conditions similar to the one for spin-1 particles. Another feature of the Dirac-like description leads to an unfeasible method for numerical calculations. The energy spectrum of the full relativistic description of the system is in general unbound from below [133]. Therefore, we continue in the following by using the non-relativistic Pauli-equation for all different spins and particles with mass. For the Pauli-equation, we can find stable ground states and have a well-defined non-perturbative theory [62]. The Pauli-equation describes a particle with mass including an external classical Maxwell field, which is determined by its vector potential $A_{\text{ext}}^\mu(\vec{r}, t)$. Replacing the

Dirac operator by the corresponding one coupled to $A_{\text{ext}}^\mu(\vec{r}, t)$ with the minimal coupling prescription

$$\partial_\mu \rightarrow \partial_\mu + i \frac{q}{\hbar c_0} A_{\text{ext},\mu}(\vec{r}, t) \quad (\text{A.2.1})$$

leads in first order of $\frac{1}{Mc_0^2}$ to the Pauli equation [134]

$$\hat{h}(\vec{r}, t) = -\frac{1}{2M} \hat{P}_{\text{ext},k}(\vec{r}, t) \hat{P}_{\text{ext}}^k(\vec{r}, t) + q A_{\text{ext}}^0(\vec{r}, t) + \frac{q\hbar}{2M} \mathbf{S}_k B_{\text{ext}}^k(\vec{r}, t) \quad (\text{A.2.2})$$

with the external magnetic field

$$B_{\text{ext}}^k(\vec{r}, t) = -\frac{1}{c_0} \varepsilon^{klm} \partial_l A_{\text{ext},m}(\vec{r}, t) \quad (\text{A.2.3})$$

the canonical momentum

$$\hat{P}_{\text{ext}}^k(\vec{r}, t) = -i\hbar \partial^k + \frac{q}{c_0} A_{\text{ext}}^k(\vec{r}, t). \quad (\text{A.2.4})$$

In the Pauli Eq. (A.2.2), q denotes the charge of the particle species with corresponding mass M and the general spin-matrices \mathbf{S}^k , which also depend on the species. We use this generalized Pauli equation for particles with mass, i.e., electrons and nuclei, together with the homogeneous Maxwell's equations for photons to build our basic theory, a generalized form of the Pauli-Fierz Hamiltonian [62]. Although, there are some further developments beyond the Pauli-Fierz limit to deal with semi-relativistic problems [135, 136, 137], our considerations in the present work stay in the non-relativistic limit for matter.

We continue by considering first the non-interacting Hamiltonians with external Maxwell fields for particles with mass and the free Maxwell Hamiltonian before we discuss the interacting Hamiltonians between the different species including the interacting Maxwell fields.

A.3 Free matter Hamiltonians

In general, many-body Hamiltonians without forcing a fixed particle number for the total system are described in Fock-space, where particles can be created and annihilated by corresponding operators for the matter and photon fields [101]. To find a fundamental form for our many-body system coupled to Maxwell fields, we consider first non-interacting particles in Fock-space, but note here, that the description in Fock space is mathematically problematic [138]. However, since it eases formal derivations, we work in Fock space here. Later, we use particle conserved Hamiltonians of particle number $\mathcal{N}_{\square|\square}$, so that we can switch back to the $\mathcal{N}_{\square|\square}$ -particle Hilbert space, where every object is well-defined.

The Fock space field operators for particle creation, $\hat{\Phi}^\dagger(\vec{r}, s)$, and annihilation, $\hat{\Phi}(\vec{r}, s)$, obey the the common QED commutation and anti-commutation rules [101]

$$\left[\hat{\Phi}(\vec{r}, s, t), \hat{\Phi}^\dagger(\vec{r}', s', t) \right]_{\pm} = \delta_{(ss')} \delta^3(\vec{r} - \vec{r}'), \quad (\text{A.3.1})$$

where s denotes the possible spin states, $+$ represents the anti-commutation relation for fermions and $-$ the commutation relation for bosons. Using these field operators, we can construct the non-interacting many-particle Hamiltonian. We build the total Hamiltonian of N different particle species coupled to the classical external $A_{\text{ext}}^\mu(\vec{r}, t)$ which we label with ' \vec{A}_{ext} '. Since we consider all particles here as non-interacting, we can use Eq. (A.2.2) for each species of particles. Therefore, for N different particle species, i.e., electrons and different effective nuclei species, the total non-interacting Hamiltonian $\hat{H}_{\vec{A}_{\text{ext}}}(t)$ coupled to an external vector potential is defined as a sum of Fock spaces and given by

$$\begin{aligned} \hat{H}_{\vec{A}_{\text{ext}}}(t) &= \sum_n^N \int d^3r \sum_s \hat{\Phi}_{(n)}^\dagger(\vec{r}, s, t) \hat{h}(\vec{r}, t) \hat{\Phi}_{(n)}(\vec{r}, s, t) \\ &= - \sum_n^N \int d^3r \frac{1}{2M_{(n)}} \sum_s \hat{\Phi}_{(n)}^\dagger(\vec{r}, s, t) \hat{P}_{\text{ext},(n),k}(\vec{r}, t) \hat{P}_{\text{ext},(n)}^k(\vec{r}, t) \hat{\Phi}_{(n)}(\vec{r}, s, t) \\ &\quad + \sum_n^N \int d^3r q_{(n)} A_{\text{ext}}^0(\vec{r}, t) \sum_s \hat{\Phi}_{(n)}^\dagger(\vec{r}, s, t) \hat{\Phi}_{(n)}(\vec{r}, s, t) \\ &\quad - \sum_n^N \int d^3r \frac{\hbar q_{(n)}}{2M_{(n)}} \sum_{s,s'} \hat{\Phi}_{(n)}^\dagger(\vec{r}, s, t) [\mathbf{S}_{(n),k}]_{ss'} \hat{\Phi}_{(n)}(\vec{r}, s', t) \left(\frac{1}{c_0} \epsilon^{klm} \partial_l A_{\text{ext},m}(\vec{r}, t) \right). \end{aligned} \quad (\text{A.3.2})$$

Here, $[\mathbf{S}_{(n),k}]_{ss'}$ denotes the matrix element of the spin matrix vector $\mathbf{S}_{(n),k}$ of index s, s' and the index n enumerates different particle species (electrons and effective nuclei here) with its corresponding canonical momentum

$$\hat{P}_{\text{ext},(n)}^k(\vec{r}, t) = -i\hbar\partial^k + \frac{q_{(n)}}{c_0} A_{\text{ext}}^k(\vec{r}, t). \quad (\text{A.3.3})$$

The first term in Eq. (A.3.2) represents the n-particle non-interacting kinetic Hamiltonian

$\hat{H}_{\text{kin},\vec{A}_{\text{ext}}}(t)$ coupled to an external classical Maxwell field, which takes the form

$$\hat{H}_{\text{kin},\vec{A}_{\text{ext}}}(t) = - \sum_n^N \int d^3r \frac{1}{2M_{(n)}} \sum_s \hat{\Phi}_{(n)}^\dagger(\vec{r}, s, t) \hat{P}_{\text{ext},(n),k}(\vec{r}, t) \hat{P}_{\text{ext},(n)}^k(\vec{r}, t) \hat{\Phi}_{(n)}(\vec{r}, s, t). \quad (\text{A.3.4})$$

The second term in Eq. (A.3.2), which we denote by $\hat{H}_{\text{int},\vec{A}_{\text{ext}}}(t)$, gives the interaction Hamiltonian of the n-particle with an external electromagnetic field, and the last

term represents the corresponding Stern-Gerlach Hamiltonian $\hat{H}_{\text{Stern}, \vec{A}_{\text{ext}}}(t)$. Both are given by

$$\hat{H}_{\text{int}, \vec{A}_{\text{ext}}}(t) = \sum_n^N \int d^3r q A_{\text{ext}}^0(\vec{r}, t) \sum_s \hat{\Phi}_{(n)}^\dagger(\vec{r}, s, t) \hat{\Phi}_{(n)}(\vec{r}, s, t), \quad (\text{A.3.5})$$

and

$$\begin{aligned} \hat{H}_{\text{Stern}, \vec{A}_{\text{ext}}}(t) = & \\ & - \sum_n^N \int d^3r \frac{\hbar q_{(n)}}{2M} \int d^3r' \sum_{s, s'} \hat{\Phi}_{(n)}^\dagger(\vec{r}, s, t) [\mathbf{S}_{(n), k}]_{ss'} \hat{\Phi}_{(n)}(\vec{r}', s', t) \left(\frac{1}{c_0} \epsilon^{klm} \partial_l A_{\text{ext}, m}(\vec{r}, t) \right). \end{aligned} \quad (\text{A.3.6})$$

The set of the corresponding field operators, i.e., masses, charges and spin matrices is given by

$$\left\{ \hat{\Phi}_{(n)}(\vec{r}, s, t); \hat{\Phi}_{(n)}^\dagger(\vec{r}, s, t); M_{(n)}; q_{(n)}; \mathbf{S}_{(n)} \right\}. \quad (\text{A.3.7})$$

We note, that the different particles do not interact, but they are all influenced by the same classical field $A_{\text{ext}}^\mu(\vec{r}, t)$ in Coulomb gauge. Later in this chapter, we change the classical field to a quantum field and consider the particles interacting via the gauge bosons, i.e., the photons.

A.4 Photon Hamiltonian

In chapters 1 - 3 we have treated the electromagnetic field only classically. To build the coupled Photon-matter Hamiltonian, we start here from the fundamental QED Hamiltonian for photons [101]. Additionally, we show the connection to the Riemann-Silberstein formulation of QED which is discussed in more details in Ref. [78].

Quantizing the Maxwell field vector potential $A^\nu(\vec{r}, t)$ means that the vector potential gets operator valued $A^\nu(\vec{r}, t) \rightarrow \hat{A}^\nu(\vec{r}, t)$. It shows, that in Coulomb gauge only the transverse fields, i.e., $\hat{E}_\perp^k(\vec{r}, t)$ are affected [101], since $\partial_0 \hat{A}^k(\vec{r}, t) = -\hat{E}_\perp^k(\vec{r}, t)$. The resulting canonical commutation relations read

$$\left[\hat{A}_k(\vec{r}, t), \epsilon_0 \hat{E}_{\perp, l}(\vec{r}', t) \right] = -i\hbar c_0 \delta_{\perp, kl}(\vec{r} - \vec{r}'), \quad (\text{A.4.1})$$

where we employed the transversal delta distribution

$$\delta_{\perp, kl}(\vec{r} - \vec{r}') = \left(\delta_{kl} \partial_k \frac{1}{\nabla^2} \partial_l \right) \delta^3(\vec{r} - \vec{r}'). \quad (\text{A.4.2})$$

Here, $\frac{1}{\nabla^2}$ is defined as the inverse Laplacian operator $\Delta = \vec{\nabla}^2$ with $\frac{1}{\nabla^2} \vec{\nabla}^2 = \mathbb{1}$. The longitudinal part of the electromagnetic field stays classical and does not influence the quantized degrees of freedom. The vector-potential operator $\hat{A}^k(\vec{r}, t)$ in terms

of creation and annihilation field operators $\hat{a}^\dagger(\vec{k}, s, t)$, $\hat{a}(\vec{k}, s, t)$ in momentum space with wavevector \vec{k} , spin state s and time t reads [101]

$$\hat{A}^k(\vec{r}, t) = \sqrt{\frac{\hbar c_0^2}{\epsilon_0 (2\pi)^3}} \int \frac{d^3k}{\sqrt{2\omega_k}} \sum_{s=1}^2 \epsilon^k(\vec{k}, s) \left[\hat{a}(\vec{k}, s, t) e^{i\vec{k}\cdot\vec{r}} + \hat{a}^\dagger(\vec{k}, s, t) e^{-i\vec{k}\cdot\vec{r}} \right]. \quad (\text{A.4.3})$$

In Eq. (A.4.3) we use $\omega_k = c_0 |\vec{k}|$, $\mathbf{k} = |\vec{k}|$ and $\epsilon^k(\vec{k}, s)$ is the transversal polarization vector with $\vec{k} \cdot \vec{\epsilon}(\vec{k}, s) = \vec{\epsilon}(\vec{k}, 1) \cdot \vec{\epsilon}(\vec{k}, 2) = 0$ [101]. The momentum-space annihilation and creation field operators obey the usual commutation relations. The transversal electric field is in accordance to the classical case given by $\partial_0 \hat{A}^k(\vec{r}, t) = -\hat{E}_\perp^k(\vec{r}, t)$, i.e., as [101]

$$\hat{E}_\perp^k(\vec{r}, t) = \sqrt{\frac{\hbar c_0^2}{\epsilon_0 (2\pi)^3}} \int \frac{d^3k i\omega_k}{\sqrt{2\omega_k}} \sum_{s=1}^2 \epsilon^k(\vec{k}, s) \left[\hat{a}(\vec{k}, s, t) e^{i\vec{k}\cdot\vec{r}} - \hat{a}^\dagger(\vec{k}, s, t) e^{-i\vec{k}\cdot\vec{r}} \right], \quad (\text{A.4.4})$$

and the magnetic field is $\hat{B}^k = -\frac{1}{c_0} \epsilon^{klm} \partial_l \hat{A}_m$, i.e., [101]

$$\hat{B}^k(\vec{r}, t) = -\sqrt{\frac{\hbar c_0^2}{\epsilon_0 (2\pi)^3}} \int \frac{d^3k}{\sqrt{2\omega_k}} \sum_{s=1}^2 i \epsilon^{klm} k_l \epsilon_m(\vec{k}, s) \left[\hat{a}(\vec{k}, s, t) e^{i\vec{k}\cdot\vec{r}} - \hat{a}^\dagger(\vec{k}, s, t) e^{-i\vec{k}\cdot\vec{r}} \right]. \quad (\text{A.4.5})$$

Following the classical definition of the energy of the electromagnetic field including an external classical current density $j_{\text{ext}}^\mu(\vec{r}, t)$ that couples to the free photon field, we find in Ref. [101] for the corresponding photon Hamiltonian $\hat{H}_{\text{Ph}}(t)$ in terms of $\hat{A}^k(\vec{r}, t)$, $\hat{E}^k(\vec{r}, t)$, and $\hat{B}^k(\vec{r}, t)$

$$\begin{aligned} \hat{H}_{\text{Ph}}(t) = & \frac{\epsilon_0}{2} \int d^3r : \left(\hat{E}_k(\vec{r}, t) \hat{E}^k(\vec{r}, t) + c_0^2 \hat{B}_k(\vec{r}, t) \hat{B}^k(\vec{r}, t) \right) : \\ & + \frac{1}{c_0} \int d^3r j_{\text{ext}}^k(\vec{r}, t) \hat{A}_k(\vec{r}, t) + \frac{1}{c_0} \int d^3r j_{\text{ext}}^0(\vec{r}, t) \hat{A}_0(\vec{r}, t). \end{aligned} \quad (\text{A.4.6})$$

Here, we use normal ordering, denoted by two colons around the corresponding term, i.e., $: * :$, to discard the constant energy shift [101]. Furthermore in Coulomb gauge, the zero component of the scalar potential operator $\hat{A}^0(\vec{r}, t)$ reads with Eq. (A.1.21)

$$\hat{A}^0(\vec{r}, t) = \frac{1}{c_0} \int_{\mathbb{R}^3} d^3r' w(\vec{r}, \vec{r}') j_{\text{ext}}^0(\vec{r}', t), \quad (\text{A.4.7})$$

and deduce the electric field with $\hat{E}_\parallel^k(\vec{r}, t) = -\partial_k \hat{A}^0(\vec{r}, t)$ according to Eq. (A.1.15).

Hence, the scalar product of $\vec{\hat{E}}_{\parallel}(\vec{r}, t) \cdot \vec{\hat{E}}_{\perp}(\vec{r}, t)$ can be expressed by

$$\begin{aligned}
 \vec{\hat{E}}_{\parallel}(\vec{r}, t) \cdot \vec{\hat{E}}_{\perp}(\vec{r}, t) &= -\hat{E}_{\parallel, k}(\vec{r}, t) \hat{E}_{\perp}^k(\vec{r}, t) \\
 &= -\left(\partial_k \hat{A}^0(\vec{r}, t)\right) \cdot \hat{E}_{\perp}^k(\vec{r}, t) \\
 &= -\partial_k \left(\hat{A}^0(\vec{r}, t) \hat{E}_{\perp}^k(\vec{r}, t)\right) + \hat{A}^0(\vec{r}, t) \underbrace{\partial_k \hat{E}_{\perp}^k(\vec{r}, t)}_{=0} \\
 &= -\partial_k \left(\hat{A}^0(\vec{r}, t) \hat{E}_{\perp}^k(\vec{r}, t)\right) .
 \end{aligned} \tag{A.4.8}$$

Since the scalar product can be written as a divergence, the corresponding integral over space in Eq. (A.4.6) can be expressed as a surface integral due to the Gauss's divergence theorem [75]. Assuming that the integral surface effects are negligible, we can discard the $\hat{E}_{\parallel}(\vec{r}, t) \cdot \hat{E}_{\perp}(\vec{r}, t)$ term and Eq. (A.4.6) takes the form

$$\begin{aligned}
 \hat{H}_{\text{Ph}}(t) &= \frac{\epsilon_0}{2} \int d^3r : \left(\hat{E}_{\perp, k}(\vec{r}, t) \hat{E}_{\perp}^k(\vec{r}, t) + c_0^2 \hat{B}_k(\vec{r}, t) \hat{B}^k(\vec{r}, t)\right) : \\
 &\quad - \frac{\epsilon_0}{2} \int d^3r \hat{E}_{\parallel, k}(\vec{r}, t) \hat{E}_{\parallel}^k(\vec{r}, t) \\
 &\quad + \frac{1}{c_0} \int d^3r j_{\text{ext}}^k(\vec{r}, t) \hat{A}_k(\vec{r}, t) + \frac{1}{c_0} \int d^3r j_{\text{ext}}^0(\vec{r}, t) \hat{A}_0(\vec{r}, t) .
 \end{aligned} \tag{A.4.9}$$

After substituting the field operators $\hat{E}_{\perp}^k(\vec{r}, t) = \partial_0 \hat{A}^k(\vec{r}, t)$ and $\hat{B}^k = -\frac{1}{c_0} \epsilon^{klm} \partial_l \hat{A}_m$ and using Eq. (A.4.3) plus the electromagnetic commutation Eq. (A.4.1), the first term on the right-hand side of Eq. (A.4.12), the free photons Hamiltonian $\hat{H}_{\text{Ph, free}}(t)$ creates or annihilates only transverse photons, which propagate through the vacuum, and reads

$$\begin{aligned}
 \hat{H}_{\text{Ph, free}}(t) &= \frac{\epsilon_0}{2} \int d^3r : \left(\hat{E}_{\perp}^2(\vec{r}, t) + c_0^2 \hat{B}^2(\vec{r}, t)\right) : \\
 &= \sum_s \int d^3k \hbar \omega_k \hat{a}^\dagger(\vec{k}, s, t) \hat{a}(\vec{k}, s, t) .
 \end{aligned} \tag{A.4.10}$$

According to that, Eq. (A.4.12) becomes

$$\begin{aligned}
 \hat{H}_{\text{Ph}}(t) &= \sum_{s=1}^2 \int d^3k \hbar \omega_k \hat{a}^\dagger(\vec{k}, s, t) \hat{a}(\vec{k}, s, t) \\
 &\quad - \frac{\epsilon_0}{2} \int d^3r \hat{E}_{\parallel, k}(\vec{r}, t) \hat{E}_{\parallel}^k(\vec{r}, t) \\
 &\quad + \frac{1}{c_0} \int d^3r j_{\text{ext}}^k(\vec{r}, t) \hat{A}_k(\vec{r}, t) + \frac{1}{c_0} \int d^3r j_{\text{ext}}^0(\vec{r}, t) \hat{A}_0(\vec{r}, t) .
 \end{aligned} \tag{A.4.11}$$

Using Eq. (A.1.21) plus the electric field property, that the longitudinal electric field in Eq. (A.1.9) is caused in Coulomb gauge only by the scalar vector potential, i.e., $\hat{E}_{\parallel}^k(\vec{r}, t) = -\partial_k \hat{A}^0(\vec{r}, t)$, and after partial integration, the free electromagnetic Hamiltonian $\hat{H}_{\text{Ph}}(t)$ can be written as [101]

$$\begin{aligned} \hat{H}_{\text{Ph}}(t) = & \sum_s \int d^3k \hbar \omega_k \hat{a}^\dagger(\vec{k}, s, t) \hat{a}(\vec{k}, s, t) + \frac{1}{c_0} \int d^3r j_{\text{ext}}^k(\vec{r}, t) \hat{A}_k(\vec{r}, t) \\ & + \frac{1}{2c_0^2} \int \int d^3r d^3r' w(\vec{r}, \vec{r}') j_{\text{ext},0}(\vec{r}, t) j_{\text{ext}}^0(\vec{r}', t). \end{aligned} \quad (\text{A.4.12})$$

Therefore the last term on the right-hand side of Eq. (A.4.12) is equivalent to

$$\begin{aligned} \frac{1}{2c_0^2} \int \int d^3r d^3r' w(\vec{r}, \vec{r}') j_{\text{ext},0}(\vec{r}, t) j_{\text{ext}}^0(\vec{r}', t) = \\ \frac{1}{c_0} \int d^3r j_{\text{ext}}^0(\vec{r}, t) \hat{A}_0(\vec{r}, t) - \frac{\epsilon_0}{2} \int d^3r \hat{E}_{\parallel,k}(\vec{r}, t) \hat{E}_{\parallel}^k(\vec{r}, t). \end{aligned} \quad (\text{A.4.13})$$

The second term in Eq. (A.4.12) couples the photon field with transverse degrees of freedom of the external current density $j_{\text{ext}}^\mu(\vec{r}, t)$, which we therefore denote by an index $\vec{j}_{\text{ext}}(\vec{r}, t)$, i.e., $\hat{H}_{\text{Ph},\vec{j}_{\text{ext}},\perp}(t)$

$$\hat{H}_{\text{Ph},\vec{j}_{\text{ext}},\perp}(t) = \frac{1}{c_0} \int d^3r j_{\text{ext}}^k(\vec{r}, t) \hat{A}_k(\vec{r}, t). \quad (\text{A.4.14})$$

The last term in Eq. (A.4.12) corresponds to the longitudinal degrees of freedom of the field and gives rise to the longitudinal interaction to an external vector potential. Using Eq. (A.1.21) for that term, the longitudinal Hamiltonian $\hat{H}_{\text{Ph},\vec{j}_{\text{ext}},\parallel}(t)$ reads

$$\hat{H}_{\text{Ph},\vec{j}_{\text{ext}},\parallel}(t) = \frac{1}{2c_0^2} \int \int d^3r d^3r' w(\vec{r}, \vec{r}') j_{\text{ext}}^0(\vec{r}, t) j_{\text{ext},0}(\vec{r}', t). \quad (\text{A.4.15})$$

Since $j_{\text{ext}}^0(\vec{r}, t)$ is a classical field, the operator $\hat{H}_{\text{Ph},\vec{j}_{\text{ext}},\parallel}(t)$ commutes with all observables.

Using the Hamiltonian of Eq. A.4.12, which describes a photon field coupled to a classical external current, the operator form of the inhomogeneous Maxwell equation in Coulomb gauge can be derived by applying the Heisenberg equation of motion twice, i.e., [101]

$$(\partial_0^2 + \partial_i \partial^i) \hat{A}^k(\vec{r}, t) = \mu_0 c_0 j_{\text{ext}}^k(\vec{r}, t) - \partial^k \partial^0 \frac{1}{c_0} \int d^3r' w(\vec{r}, \vec{r}') j_{\text{ext},0}(\vec{r}', t). \quad (\text{A.4.16})$$

We assume that the external current density $j_{\text{ext}}^\mu(\vec{r}, t)$ obeys the continuity equation $\partial_\mu j_{\text{ext}}^\mu(\vec{r}, t) = 0$ and the external current density splits by $j_{\text{ext}}^k(\vec{r}, t) = j_{\text{ext},\parallel}^k(\vec{r}, t) + j_{\text{ext},\perp}^k(\vec{r}, t)$ into a longitudinal current density $j_{\text{ext},\parallel}^k(\vec{r}, t)$ and transverse one $j_{\text{ext},\perp}^k(\vec{r}, t)$.

According to the inhomogeneous Maxwell's Eq. (A.1.6), the last term of Eq. (A.4.16) becomes [75]

$$\partial^k \partial^0 \frac{1}{c_0} \int d^3 r' w(\vec{r}, \vec{r}') j_{\text{ext},0}(\vec{r}', t) = \mu_0 c_0 j_{\text{ext},\parallel}^k(\vec{r}, t), \quad (\text{A.4.17})$$

and the k-component of the inhomogeneous Maxwell equation in terms of the vector potential in Coulomb gauge yields with Eq. (A.1.26)

$$(\partial_0^2 + \partial_l \partial^l) \hat{A}^k(\vec{r}, t) = \mu_0 c_0 j_{\text{ext},\perp}^k(\vec{r}, t). \quad (\text{A.4.18})$$

As a consequence of Eq. (A.4.16), only the transverse current density $j_{\text{ext},\perp}^k(\vec{r}, t)$ couples to the transverse photon field. Additionally, the operator valued Eq. (A.4.16) is equivalent to the classical one in Eq. (A.1.26).

To build a bridge from the QED photon Hamiltonian to the Riemann-Silberstein formulation, we can define the Riemann-Silberstein transverse field operator by [78]

$$\hat{F}_{\pm,\perp}^k(\vec{r}, t) = \sqrt{\frac{\epsilon_0}{2}} \left(\hat{E}_{\pm,\perp}^k(\vec{r}, t) \pm i c_0 \hat{B}^k(\vec{r}, t) \right). \quad (\text{A.4.19})$$

Using this definition, we can express Eq. (A.4.10) by

$$\begin{aligned} \hat{H}_{\text{Ph,free}}(t) &= \frac{\epsilon_0}{2} \int d^3 r : \left(\hat{E}_{\perp,k}(\vec{r}, t) \hat{E}_{\perp}^k(\vec{r}, t) + c_0^2 \hat{B}_k(\vec{r}, t) \hat{B}^k(\vec{r}, t) \right) : \\ &= \int d^3 r : \hat{F}_{+,\perp,k}(\vec{r}, t) \hat{F}_{-,\perp}^k(\vec{r}, t) : . \end{aligned} \quad (\text{A.4.20})$$

Similar to Eq. (A.4.16), which represents the inhomogeneous Maxwell's equation in terms of the scalar and vector potential $\hat{A}^\mu(\vec{r}, t)$, we can apply the Heisenberg equation of motion to the Riemann-Silberstein vector $\hat{F}_{\pm,\perp}^k(\vec{r}, t)$ and obtain the Maxwell's equation with first-order derivatives

$$i \hbar c_0 \partial_0 \hat{F}_{\pm,\perp}^k(\vec{r}, t) = \mp i \hbar c_0 \left(S^l \partial_l \right)^{km} \hat{F}_{\pm,\perp,m}(\vec{r}, t) - i \frac{\hbar}{\sqrt{2\epsilon_0}} j_{\text{ext},\perp}^k(\vec{r}, t) \quad (\text{A.4.21})$$

for the transverse electromagnetic field. It obeys the divergence side condition

$$\partial_k \hat{F}_{\pm,\perp}^k(\vec{r}, t) = 0. \quad (\text{A.4.22})$$

Therefore, only the transverse component of the classical current density $j^\mu(\vec{r}, t)$ couples to the transverse quantized electromagnetic field. Since the longitudinal electromagnetic field stays classical in Coulomb gauge, it is determined classically by the longitudinal part of the classical current density with

$$i \hbar c_0 \partial_0 F_{\pm,\parallel}^k(\vec{r}, t) = \mp i \hbar c_0 \left(S^l \partial_l \right)^{km} F_{\pm,\parallel,m}(\vec{r}, t) - i \frac{\hbar}{\sqrt{2\epsilon_0}} j_{\text{ext},\parallel}^k(\vec{r}, t) \quad (\text{A.4.23})$$

The divergence side condition leads now to the inhomogeneous Gauß law

$$\partial_k F_{\pm,\parallel}^k(\vec{r}, t) = \frac{1}{\sqrt{2\epsilon_0}} j_{\text{ext},\parallel}^0(\vec{r}, t), \quad (\text{A.4.24})$$

which gives the zero-component of the external current density. Consequently, similar to Sec. (3.3.2), we split up the electromagnetic field into a longitudinal with corresponding classical Eqs. (A.4.23) - (A.4.24) and transverse Eqs. (A.4.21) - (A.4.22), so that the total electromagnetic field is the sum of both.

The Riemann-Silberstein operator $\hat{F}_{\pm,\perp}^k(\vec{r}, t)$ expressed by creation and annihilation field operators is given with Eq. (A.4.4) and Eq. (A.4.5) by

$$\begin{aligned} \hat{F}_{\pm,\perp}^k(\vec{r}, t) = & \\ & -\sqrt{\frac{\hbar c_0^2}{2(2\pi)^3}} \int \frac{d^3\mathbf{k}}{\sqrt{2\omega_k}} \sum_{s=1}^2 \left[\mp c_0 \epsilon^{klm} k_l \epsilon_m(\vec{k}, s) + i\omega_k \epsilon^k(\vec{k}, s) \right] \left[\hat{a}(\vec{k}, s, t) e^{i\vec{k}\cdot\vec{r}} - \hat{a}^\dagger(\vec{k}, s, t) e^{-i\vec{k}\cdot\vec{r}} \right]. \end{aligned} \quad (\text{A.4.25})$$

In Sec. 1.1.6, we discussed that the classical Riemann-Silberstein vectors can be decomposed in positive and negative frequency parts. This can also be applied to Eq. (A.4.25) (cf. [78]). First, the transversal polarization vector times the creation and annihilation operator expressed in spin states, can be equivalently expressed in helicity states. Using the helicity unit vectors $\vec{\epsilon}_+(\vec{k}, t)$ and $\vec{\epsilon}_-(\vec{k}, t)$, we get the identity for the spin sum in Eq. (A.4.25) [78]

$$\hat{a}(\vec{k}, 1, t) \vec{\epsilon}(\vec{k}, 1) + \hat{a}(\vec{k}, 2, t) \vec{\epsilon}(\vec{k}, 2) = \hat{a}_+(\vec{k}, t) \vec{\epsilon}_+(\vec{k}, t) + \hat{a}_-(\vec{k}, t) \vec{\epsilon}_-(\vec{k}, t), \quad (\text{A.4.26})$$

$$\hat{a}^\dagger(\vec{k}, 1, t) \vec{\epsilon}(\vec{k}, 1) + \hat{a}^\dagger(\vec{k}, 2, t) \vec{\epsilon}(\vec{k}, 2) = \hat{a}_+^\dagger(\vec{k}, t) \vec{\epsilon}_+(\vec{k}, t) + \hat{a}_-^\dagger(\vec{k}, t) \vec{\epsilon}_-(\vec{k}, t). \quad (\text{A.4.27})$$

The creation and annihilation operators $\hat{a}^\dagger(\vec{k}, s, t)$, $\hat{a}(\vec{k}, s, t)$ transform to $\hat{a}_\pm^\dagger(\vec{k}, t)$, $\hat{a}_\pm(\vec{k}, t)$ with [78]

$$\hat{a}_+(\vec{k}, t) = \frac{1}{\sqrt{2}} \left(\hat{a}(\vec{k}, 1, t) - i\hat{a}(\vec{k}, 2, t) \right), \quad (\text{A.4.28})$$

$$\hat{a}_-(\vec{k}, t) = \frac{1}{\sqrt{2}} e^{-i\delta} \left(-i\hat{a}(\vec{k}, 1, t) + \hat{a}(\vec{k}, 2, t) \right),$$

$$\hat{a}_+^\dagger(\vec{k}, t) = \frac{1}{\sqrt{2}} \left(\hat{a}^\dagger(\vec{k}, 1, t) + i\hat{a}^\dagger(\vec{k}, 2, t) \right), \quad (\text{A.4.29})$$

$$\hat{a}_-^\dagger(\vec{k}, t) = \frac{1}{\sqrt{2}} e^{i\delta} \left(i\hat{a}^\dagger(\vec{k}, 1, t) + \hat{a}^\dagger(\vec{k}, 2, t) \right),$$

where δ denotes a free parameter. Hence, using the identities of Eq. (A.4.26) and Eq. (A.4.27) and the relation $\vec{k}/|\vec{k}| \times \vec{\epsilon}_\pm = \mp i\vec{\epsilon}_\pm$ for Eq.(A.4.25) leads to the positive and negative frequency decomposition of the Riemann-Silberstein operator [78]

$$\hat{F}_{\pm,\perp}^k(\vec{r}, t) = \hat{F}_{\pm,\perp}^{(+),k}(\vec{r}, t) + \hat{F}_{\pm,\perp}^{(-),k}(\vec{r}, t) \quad (\text{A.4.30})$$

with

$$\hat{F}_{\pm,\pm}^{(+),k}(\vec{r}, t) = i\sqrt{\frac{\hbar c_0^2}{4(2\pi)^3}} \int d^3k \sqrt{\omega_k} \tilde{\epsilon}_{\pm}^k(\vec{k}) \hat{a}_{\pm}(\vec{k}, t) e^{i\vec{k}\cdot\vec{r}}, \quad (\text{A.4.31})$$

$$\hat{F}_{\pm,\pm}^{(-),k}(\vec{r}, t) = i\sqrt{\frac{\hbar c_0^2}{4(2\pi)^3}} \int d^3k \sqrt{\omega_k} \tilde{\epsilon}_{\pm}^k(\vec{k}) \hat{a}_{\pm}^{\dagger}(\vec{k}, t) e^{-i\vec{k}\cdot\vec{r}}. \quad (\text{A.4.32})$$

The positive frequency Riemann-Silberstein operator $\hat{F}_{\pm,\pm}^{(+),k}(\vec{r}, t)$ annihilates a photon in case of $\hat{F}_{+,\pm}^{(+),k}(\vec{r}, t)$ with positive helicity or in turn $\hat{F}_{-,\pm}^{(+),k}(\vec{r}, t)$ with negative helicity. In contrast, $\hat{F}_{\pm,\pm}^{(-),k}(\vec{r}, t)$ creates a photon with corresponding helicity [78].

A.5 Interaction Hamiltonians

After introducing the non-interacting Hamiltonians for different species in Eq. (A.3.2) and uncoupled Photons in Eq. (A.4.12), we consider in this section the corresponding interaction Hamiltonians. According to QED with minimal coupling interaction [101], the conserved matter current density operator $\hat{j}_{\text{mat}}^{\mu}(\vec{r}, t)$ of all species couples to the total vector potential operator $\hat{A}^{\mu}(\vec{r}, t)$ [108]. Being in Coulomb gauge allows us to separate the total interaction into a longitudinal and transverse one.

A.5.1 Longitudinal (Coulomb) interactions

The last term on the right-hand side of Eq. (A.4.12), i.e., Eq. (A.4.15), represents the longitudinal interaction Hamiltonian between an external current and the photon field in Coulomb gauge and takes the form

$$\hat{H}_{\text{Ph},\vec{j}_{\text{ext}},\parallel}(t) = \frac{1}{2c_0^2} \int \int d^3r d^3r' w(\vec{r}, \vec{r}') j_{\text{ext}}^0(\vec{r}', t) j_{\text{ext},0}(\vec{r}, t). \quad (\text{A.5.1})$$

To consider the interaction of the matter current density to the photon field, we take that equation and replace the classical zero component of the external current density $j_{\text{ext}}^0(\vec{r}, t)$ with the corresponding matter representation $\hat{j}_{\text{mat}}^0(\vec{r}, t)$. This leads to an operator-valued matter-photon interaction Hamiltonian $\hat{H}_{\text{mat,int},\parallel}(t)$

$$\hat{H}_{\text{mat,int},\parallel}(t) = \frac{1}{2c_0^2} \int \int d^3r d^3r' w(\vec{r}, \vec{r}') \hat{j}_{\text{mat},0}(\vec{r}, t) \hat{j}_{\text{mat}}^0(\vec{r}', t). \quad (\text{A.5.2})$$

The zero component of the internal matter four-current density operator $\hat{j}_{\text{mat}}^0(\vec{r}, t)$, caused by n different species, is given by [101, 78]

$$\hat{j}_{\text{mat}}^0(\vec{r}, t) = \sum_{n=1}^N c_0 q_{(n)} \sum_s \hat{\Phi}_{(n)}^{\dagger}(\vec{r}, s, t) \hat{\Phi}_{(n)}(\vec{r}, s, t) = \sum_{n=1}^N \hat{j}_{\text{mat},(n)}^0(\vec{r}, t). \quad (\text{A.5.3})$$

It is based on the internal matter charge density

$$\hat{\rho}_{\text{mat}}(\vec{r}, t) = \sum_{n=1}^N q_{(n)} \sum_s \hat{\Phi}_{(n)}^\dagger(\vec{r}, s, t) \hat{\Phi}_{(n)}(\vec{r}, s, t) \quad (\text{A.5.4})$$

multiplied by the speed of light c_0 due to unit consistency

$$\hat{j}_{\text{mat}}^0(\vec{r}, t) = c_0 \hat{\rho}_{\text{mat}}(\vec{r}, t). \quad (\text{A.5.5})$$

The matter caused longitudinal interaction Hamiltonian can be rewritten as

$$\begin{aligned} \hat{H}_{\text{mat,int},\parallel}(t) &= \frac{1}{2c_0^2} \int d^3r d^3r' w(\vec{r}, \vec{r}') : \hat{j}_{\text{mat}}^0(\vec{r}, t) \hat{j}_{\text{mat},0}(\vec{r}', t) : \\ &= \frac{1}{2c_0^2} \int d^3r d^3r' w(\vec{r}, \vec{r}') \sum_{n,n'} : \hat{j}_{\text{mat},(n)}^0(\vec{r}, t) \hat{j}_{\text{mat},(n'),0}(\vec{r}', t) : , \end{aligned} \quad (\text{A.5.6})$$

with normal ordering for the usual Coulomb form. This expression can also be written as

$$\begin{aligned} \hat{H}_{\text{mat,int},\parallel}(t) &= \frac{1}{c_0^2} \int d^3r d^3r' w(\vec{r}, \vec{r}') \sum_{n>n'} \hat{j}_{\text{mat},(n)}^0(\vec{r}, t) \hat{j}_{\text{mat},(n'),0}(\vec{r}', t) \\ &\quad + \frac{1}{2c_0^2} \int d^3r d^3r' w(\vec{r}, \vec{r}') \sum_n : \hat{j}_{\text{mat},(n)}^0(\vec{r}, t) \hat{j}_{\text{mat},(n),0}(\vec{r}', t) : \end{aligned} \quad (\text{A.5.7})$$

and consists of two terms. The first one describes the interaction of different effective nuclei and electrons with longitudinal photons, which we call the inter-species Coulomb interaction. Since their operators commute, the normal ordering does not affect this term. In contrast, the operators in the second term of the last line do not commute and require a time ordering. This intra-species Coulomb interaction describes the longitudinal interaction of particles within each species with each other. Since $w(\vec{r}, \vec{r}')$ denotes the Green's function of the Poisson equation, given in Eq. (A.1.20), we can define an internal scalar potential operator $\hat{A}_{\text{mat},(n)}^0(\vec{r}, t)$ with

$$\hat{A}_{\text{mat},(n)}^0(\vec{r}, t) = \sum_{\substack{n' \\ n' \neq n}} \frac{1}{c_0} \int d^3r' w(\vec{r}, \vec{r}') \hat{j}_{\text{mat},(n')}^0(\vec{r}', t). \quad (\text{A.5.8})$$

It describes the scalar potential that acts on species n , caused by all remaining species, and it commutes with all the electromagnetic field variables, and Eq. (A.5.6) can be expressed as

$$\begin{aligned} \hat{H}_{\text{mat,int},\parallel}(t) &= \frac{1}{2c_0} \int d^3r \sum_{n>n'} : \hat{j}_{\text{mat},(n)}^0(\vec{r}, t) \hat{A}_{\text{mat},(n),0}(\vec{r}, t) : \\ &\quad + \frac{1}{2c_0^2} \int d^3r d^3r' w(\vec{r}, \vec{r}') \sum_n : \hat{j}_{\text{mat},(n)}^0(\vec{r}, t) \hat{j}_{\text{mat},(n),0}(\vec{r}', t) : . \end{aligned} \quad (\text{A.5.9})$$

The scalar potential $\hat{A}_{\text{mat}}^0(\vec{r}, t)$ of all interacting particles that arises due to the scalar current density $\hat{j}_{\text{mat}}^0(\vec{r}, t)$ of the matter reads with Eq. (A.1.21)

$$\hat{A}_{\text{mat}}^0(\vec{r}, t) = \frac{1}{c_0} \int d^3r' w(\vec{r}, \vec{r}') \hat{j}_{\text{mat},0}(\vec{r}', t) . \quad (\text{A.5.10})$$

Finally, we discuss the total longitudinal interaction Hamiltonian of a n -species system plus an external scalar vector potential $A_{\text{ext}}^0(\vec{r}, t)$. We start with the total current density operator $\hat{j}^\mu(\vec{r}, t)$

$$\hat{j}^\mu(\vec{r}, t) = \hat{j}_{\text{mat}}^\mu(\vec{r}, t) + j_{\text{ext}}^\mu(\vec{r}, t) . \quad (\text{A.5.11})$$

Taking Eq. (A.4.7) gives the scalar potential induced by an external current density $j_{\text{ext}}^\mu(\vec{r}, t)$ and reads

$$\hat{A}_{\text{ext}}^0(\vec{r}, t) = \frac{1}{c_0} \int_{\mathbb{R}^3} d^3r' w(\vec{r}, \vec{r}') j_{\text{ext}}^0(\vec{r}', t) . \quad (\text{A.5.12})$$

Replacing $j_{\text{ext}}^\mu(\vec{r}, t)$ with the corresponding current density $\hat{j}_{\text{mat}}^\mu(\vec{r}, t)$ that arises due to the matter

$$\hat{A}_{\text{mat}}^0(\vec{r}, t) = \frac{1}{c_0} \int_{\mathbb{R}^3} d^3r' w(\vec{r}, \vec{r}') j_{\text{mat}}^0(\vec{r}', t) . \quad (\text{A.5.13})$$

The total scalar vector potential $\hat{A}^0(\vec{r}, t)$ in presence of a matter current density $\hat{j}_{\text{mat}}^\mu(\vec{r}, t)$ plus an external current density $j_{\text{ext}}^\mu(\vec{r}, t)$ takes the form

$$\begin{aligned} \hat{A}^0(\vec{r}, t) &= \hat{A}_{\text{mat}}^0(\vec{r}, t) + A_{\text{ext}}^0(\vec{r}, t) \\ &= \frac{1}{c_0} \int d^3r' w(\vec{r}, \vec{r}') j_{\text{mat}}^0(\vec{r}', t) + A_{\text{ext}}^0(\vec{r}, t) . \end{aligned} \quad (\text{A.5.14})$$

According to Eq. (A.5.2), the interaction Hamiltonian of the corresponding zero component to the photon field is given by

$$\begin{aligned} \hat{H}_{\text{mat,int},j_{\text{ext}},\parallel}^0(t) &= \frac{1}{2c_0^2} \int \int d^3r d^3r' w(\vec{r}, \vec{r}') \hat{j}_0(\vec{r}, t) \hat{j}^0(\vec{r}', t) \\ &= \frac{1}{2c_0^2} \int \int d^3r d^3r' w(\vec{r}, \vec{r}') \hat{j}_{\text{mat},0}(\vec{r}, t) \hat{j}_{\text{mat}}^0(\vec{r}', t) \\ &\quad + \frac{1}{c_0^2} \int \int d^3r d^3r' w(\vec{r}, \vec{r}') j_{\text{ext},0}(\vec{r}, t) \hat{j}_{\text{mat}}^0(\vec{r}', t) \\ &\quad + \frac{1}{2c_0^2} \int \int d^3r d^3r' w(\vec{r}, \vec{r}') j_{\text{ext},0}(\vec{r}, t) j_{\text{ext}}^0(\vec{r}', t) . \end{aligned} \quad (\text{A.5.15})$$

According to Eq. (A.1.21) and Eq. (A.5.10), the zero component of the current density is directly related to the scalar vector potential. Consequently Eq. (A.5.15) becomes

$$\begin{aligned}\hat{H}_{\text{mat,int},j_{\text{ext},\parallel}^0}(t) &= \frac{1}{2c_0^2} \int \int d^3r d^3r' w(\vec{r}, \vec{r}') \hat{j}_{\text{mat},0}(\vec{r}, t) \hat{j}_{\text{mat}}^0(\vec{r}, t) \\ &+ \frac{1}{c_0} \int d^3r A_{\text{ext},0}(\vec{r}, t) \hat{j}_{\text{mat}}^0(\vec{r}, t) \\ &+ \frac{1}{2c_0} \int d^3r A_{\text{ext},0}(\vec{r}, t) j_{\text{ext}}^0(\vec{r}', t) .\end{aligned}\quad (\text{A.5.16})$$

On the other hand, the zero component of the external current density changes effectively only the zero component of the external scalar potential. In this manner, considering both variables for our interaction Hamiltonian means, that we would "double count" both later when we establish a corresponding Runge-Gross type mapping. Hence, we discard the last term in Eq. (A.5.16) for the longitudinal interaction Hamiltonian that we use in the Sec. 4.3. The final longitudinal Hamiltonian $\hat{H}_{\text{int},\parallel}(t)$ takes after substituting $j_{\text{mat}}^\mu(\vec{r}, t)$ with Eq. (A.5.3) the form

$$\begin{aligned}\hat{H}_{\text{int},\parallel}(t) &= \frac{1}{2c_0^2} \int \int d^3r d^3r' w(\vec{r}, \vec{r}') \hat{j}_{\text{mat},0}(\vec{r}, t) \hat{j}_{\text{mat}}^0(\vec{r}', t) \\ &+ \sum_{n=1}^N \sum_s \int d^3r q_{(n)} A_{\text{ext},0}(\vec{r}, t) \hat{\Phi}_{(n)}^\dagger(\vec{r}, s, t) \hat{\Phi}_{(n)}(\vec{r}, s, t) .\end{aligned}\quad (\text{A.5.17})$$

A.5.2 Transverse interactions

For considering the transverse contribution of light-matter interaction, we use the corresponding Hamiltonian term given in Eq. (A.4.14). The arising total vector potential $A^k(\vec{r}, t)$ of the coupled system is the sum of the internal vector potential operator $\hat{A}_{\text{mat}}^k(\vec{r}, t)$ from the matter and an external one $A_{\text{ext}}^k(\vec{r}, t)$

$$\hat{A}^k(\vec{r}, t) = \hat{A}_{\text{mat}}^k(\vec{r}, t) + A_{\text{ext}}^k(\vec{r}, t) .\quad (\text{A.5.18})$$

After using the continuity equation $\partial_\mu j_{\text{mat}}^\mu(\vec{r}, t) = 0$ and the Pauli Hamiltonian in Eq. (A.3.2), the total matter current density consists of three different terms [139, 140]

$$\hat{j}_{\text{mat}}^k(\vec{r}, t) = \hat{j}_{\text{pnc}}^k(\vec{r}, t) + \hat{j}_{\text{dnc}}^k(\vec{r}, t) + \hat{j}_{\text{mc}}^k(\vec{r}, t) .\quad (\text{A.5.19})$$

The first term is the paramagnetic current density operator $\hat{j}_{\text{pnc}}^k(\vec{r}, t)$, which depends only on matter variables and reads

$$\hat{j}_{\text{pnc}}^k(\vec{r}, t) = \sum_{n=1}^N \sum_s \frac{\hbar q_{(n)}}{2M_{(n)}i} \left[\left(\partial^k \hat{\Phi}_{(n)}^\dagger(\vec{r}, s, t) \right) \hat{\Phi}_{(n)}(\vec{r}, s, t) - \hat{\Phi}_{(n)}^\dagger(\vec{r}, s, t) \left(\partial^k \hat{\Phi}_{(n)}(\vec{r}, s, t) \right) \right] .\quad (\text{A.5.20})$$

In contrast, the second term, the diamagnetic current density operator $\hat{j}_{\text{dmc}}^k(\vec{r}, t)$, depends additionally on the vector potential operator $\hat{A}^k(\vec{r}, t)$ of the total electromagnetic field and is given by

$$\hat{j}_{\text{dmc}}^k(\vec{r}, t) = \sum_{n=1}^N -\frac{q(n)}{M(n)c_0^2} \hat{j}_{(n)}^0(\vec{r}, t) \hat{A}^k(\vec{r}, t). \quad (\text{A.5.21})$$

The fact that the Maxwell field is part of the diamagnetic current density is based on the quadratic expression of the Pauli-Hamiltonian, which arises due to the antiparticle (positronic) contribution in the non-relativistic Pauli approximation [108]. The last current density term $\hat{j}_{\text{mc}}^k(\vec{r}, t)$ is the magnetization current

$$\hat{j}_{\text{mc}}^k(\vec{r}, t) = \sum_{n=1}^N \sum_{s,s'} -\varepsilon^{klm} \partial_l \hat{\Phi}_{(n)}^\dagger(\vec{r}, s, t) \left(\frac{\hbar q(n)}{2M(n)} [\mathbf{S}_{(n),m}]_{ss'} \right) \hat{\Phi}_{(n)}(\vec{r}, s', t), \quad (\text{A.5.22})$$

which comes from the Stern-Gerlach term of the Pauli-equation.

The total current density $\hat{j}^k(\vec{r}, t)$ of the system includes the internal matter current density $\hat{j}_{\text{mat}}^k(\vec{r}, t)$ plus a classical external current density $j_{\text{ext}}^k(\vec{r}, t)$

$$\hat{j}^k(\vec{r}, t) = \hat{j}_{\text{mat}}^k(\vec{r}, t) + j_{\text{ext}}^k(\vec{r}, t). \quad (\text{A.5.23})$$

According to Eq. (A.4.14), the transverse interaction Hamiltonian $\hat{H}_{\text{Ph}, \vec{j}_{\text{ext}}, \perp}(t)$ of an external current density $\vec{j}_{\text{ext}}(\vec{r}, t)$ with the photon field is given by

$$\hat{H}_{\text{Ph}, \vec{j}_{\text{ext}}, \perp}(t) = \frac{1}{c_0} \int d^3r j_{\text{ext}}^k(\vec{r}, t) \hat{A}_k(\vec{r}, t). \quad (\text{A.5.24})$$

Consequently, in the same manner, replacing the external current density Eq. (A.5.24) by the matter current density $\hat{j}_{\text{mat}}^k(\vec{r}, t)$ leads to the transverse interaction Hamiltonian $\hat{H}_{\text{int}, \perp}(t)$

$$\hat{H}_{\text{int}, \perp}(t) = \frac{1}{c_0} \int d^3r \hat{j}_{\text{mat}}^k(\vec{r}, t) \hat{A}_k(\vec{r}, t). \quad (\text{A.5.25})$$

Substituting $\hat{j}_{\text{mat}}^k(\vec{r}, t)$ with all current terms from Eq. (A.5.19) and integrating by parts yields

$$\begin{aligned} \hat{H}_{\text{int}, \perp}(t) = & - \sum_{n=1}^N \int d^3r \frac{i\hbar q(n)}{2M(n)c_0} \sum_{s,s'} \hat{\Phi}_{(n)}^\dagger(\vec{r}, s, t) \partial_k \hat{A}^k(\vec{r}, t) \hat{\Phi}_{(n)}(\vec{r}, s, t) \\ & - \sum_{n=1}^N \int d^3r \frac{i\hbar q(n)}{2M(n)c_0} \sum_{s,s'} \hat{\Phi}_{(n)}^\dagger(\vec{r}, s, t) \hat{A}_k(\vec{r}, t) \partial^k \hat{\Phi}_{(n)}(\vec{r}, s, t) \\ & + \sum_{n=1}^N \int d^3r \frac{q(n)^2}{2M(n)c_0^2} \sum_{s,s'} \hat{\Phi}_{(n)}^\dagger(\vec{r}, s, t) \hat{A}_k(\vec{r}, t) \hat{A}^k(\vec{r}, t) \hat{\Phi}_{(n)}(\vec{r}, s, t) \\ & + \sum_{n=1}^N \int d^3r \frac{\hbar q(n)}{2M(n)} \sum_{s,s'} \hat{\Phi}_{(n)}^\dagger(\vec{r}, s, t) [\mathbf{S}_{(n),k}]_{s,s'} \hat{\Phi}_{(n)}(\vec{r}, s', t) \left(\frac{1}{c_0} \varepsilon^{klm} \partial_l \hat{A}_m(\vec{r}, t) \right). \end{aligned} \quad (\text{A.5.26})$$

The last term on the right-hand side is the Stern-Gerlach Hamiltonian term $\hat{H}_{\text{Stern}}(t)$ and reads

$$\hat{H}_{\text{Stern}}(t) = \sum_{n=1}^N \int d^3r \frac{\hbar q(n)}{2M(n)} \sum_{s,s'} \hat{\Phi}_{(n)}^\dagger(\vec{r}, s, t) [\mathbf{S}_{(n),k}]_{s,s'} \hat{\Phi}_{(n)}(\vec{r}, s', t) \left(\frac{1}{c_0} \varepsilon^{klm} \partial_l \hat{A}_m(\vec{r}, t) \right). \quad (\text{A.5.27})$$

Comparing Eq. (A.5.26) with Eq. (A.3.2) after replacing $A_{\text{ext}}^\mu(\vec{r}, t)$ with $A^\mu(\vec{r}, t)$ reveals that adding the zero Maxwell field kinetic Hamiltonian term $\hat{H}_{\text{kin},(0)}(t)$

$$\hat{H}_{\text{kin},(0)}(t) = \sum_{n=1}^N \int d^3r \frac{\hbar^2}{2M(n)} \sum_{s,s'} \hat{\Phi}_{(n)}^\dagger(\vec{r}, s, t) \partial_k \partial^k \hat{\Phi}_{(n)}(\vec{r}, s, t) \quad (\text{A.5.28})$$

to the first three terms on the right-hand side of Eq. (A.5.26) gives the kinetic Hamiltonian $\hat{H}_{\text{kin}}(t)$ coupled to a Maxwell field

$$\begin{aligned} \hat{H}_{\text{kin}}(t) = & \sum_{n=1}^N \int d^3r \frac{\hbar^2}{2M(n)} \sum_{s,s'} \hat{\Phi}_{(n)}^\dagger(\vec{r}, s, t) \partial_k \partial^k \hat{\Phi}_{(n)}(\vec{r}, s, t) \\ & - \sum_{n=1}^N \int d^3r \frac{i\hbar q(n)}{2M(n)c_0} \sum_{s,s'} \hat{\Phi}_{(n)}^\dagger(\vec{r}, s, t) \partial_k \hat{A}^k(\vec{r}, t) \hat{\Phi}_{(n)}(\vec{r}, s, t) \\ & - \sum_{n=1}^N \int d^3r \frac{i\hbar q(n)}{2M(n)c_0} \sum_{s,s'} \hat{\Phi}_{(n)}^\dagger(\vec{r}, s, t) \hat{A}_k(\vec{r}, t) \partial^k \hat{\Phi}_{(n)}(\vec{r}, s, t) \\ & + \sum_{n=1}^N \int d^3r \frac{q(n)^2}{2M(n)c_0^2} \sum_{s,s'} \hat{\Phi}_{(n)}^\dagger(\vec{r}, s, t) \hat{A}_k(\vec{r}, t) \hat{A}^k(\vec{r}, t) \hat{\Phi}_{(n)}(\vec{r}, s, t). \end{aligned} \quad (\text{A.5.29})$$

Using the canonical momentum for particle species n coupled to the total vector potential operator $\hat{A}(\vec{r}, t)$

$$\hat{P}_{(n)}^k(\vec{r}, t) = -i\hbar \partial^k + \frac{q(n)}{c_0} \hat{A}^k(\vec{r}, t). \quad (\text{A.5.30})$$

simplifies the expression for $\hat{H}_{\text{kin}}(t)$

$$\hat{H}_{\text{kin}}(t) = - \sum_{n=1}^N \int d^3r \frac{1}{2M(n)} \sum_s \hat{\Phi}_{(n)}^\dagger(\vec{r}, s, t) \hat{P}_{(n),k}(\vec{r}, t) \hat{P}_{(n)}^k(\vec{r}, t) \hat{\Phi}_{(n)}(\vec{r}, s, t). \quad (\text{A.5.31})$$

Therefore, since we can write

$$\begin{aligned} \hat{H}_{\text{kin,Stern}}(t) &= \hat{H}_{\text{kin},(0)}(t) + \hat{H}_{\text{int}}^\perp(t), \\ &= \hat{H}_{\text{kin}}(t) + \hat{H}_{\text{Stern}}(t), \end{aligned} \quad (\text{A.5.32})$$

it means that the transverse interaction of the considered matter with the photon field is implied in terms of the canonical kinetic energy Hamiltonian, only complemented by the Stern-Gerlach term.

As a final note, in quantum electrodynamics to get physically correct results, $M_{(n)}$ has to be renormalized by the electromagnetic mass $\delta_{M_{(n)}}$, so that $M_{(n)} = M_{\text{bare},(n)} + \delta_{M_{(n)}}$. The electromagnetic mass depends on the photon energy, which means that the matter couples implicitly to the transverse photon field and vice versa via the electromagnetic mass $\delta_{M_{(n)}}$. In many cases, if the electromagnetic mass contribution is rather small compared to the bare mass of the species, we can approximate $M_{(n)} \approx M_{\text{bare},(n)}$. We use this approximation in our applications later in this work.

List of Figures

3.1	Two-dimensional slice of a three-dimensional simulation box with different simulation regions	49
3.2	Two-dimensional stencil	54
3.3	Parallelization scheme for dividing the Maxwell grid into four partitions	56
3.4	Spatial external current density distribution	60
3.5	Electromagnetic variables for external current signals, calculated by Octopus and MEEP	63
3.6	Contour snapshots along the xy-plane of the electric field in z-direction for the electromagnetic field propagation with four different external currents	65
3.7	Spatial distribution of a transverse current density along the xy-plane.	68
3.8	Snapshots of the electric field in z-direction for the longitudinal current density	69
3.9	Snapshots of the electric field in z-direction for the transverse current density	69
3.10	Electric and magnetic field reaction in z-direction for the longitudinal and transverse current density	70
3.11	Mask function along a Cartesian axis	72
3.12	A three-dimensional contour plot of the mask function in the x-y plane	72
3.13	Relative variation of the energy and the electric field at two points for different parameters q	85
3.14	Comparison of absorbing mask and perfectly matched layer boundary conditions	86
3.15	Two-dimensional scheme of incident waves boundaries	87
3.16	Incident plane waves simulation of two interfering plane waves	90
3.17	Numerical dispersion of the free Riemann-Silberstein Maxwell propagation	94
3.18	Two-dimensional scheme of incident waves boundaries combined with PML	95
3.19	Simulation box illustration for a laser pulse hitting a linear medium box	98
3.20	Sequence of the electric field simulated by a Riemann-Silberstein Maxwell propagation including a linear medium box	100

5.1	Multiscale grid types for the Kohn-Sham and Maxwell grid	147
5.2	Domain parallelization of matter and Maxwell grid	150
5.3	Predictor-corrector scheme of a Maxwell-Kohn-Sham propagation step	152
5.4	Electromagnetic detectors at the simulation boundaries	155
6.1	Simulation scheme of a laser pulse excitation of a quantum-mechanical system.	158
6.2	Geometry of the Na ₂₉₇ dimer in E2E configuration with different distances $d_1 = 0.1$ nm and $d_2 = 0.5$ nm	160
6.3	Absorption spectrum of the Na ₂₉₇ dimer for light that is polarized along the dimer axis	161
6.4	Visualization of the inner simulation box limits and detector points and surfaces	164
6.5	Contour plots in the x-y plane for the current density, the electron localization function, electric field difference, and Maxwell energy difference	167
6.6	Similar movie frame as Figure 6.5, but with the frame at time 8.33 fs.	168
6.7	Electric field values and current density in z-direction in the center between the two Sodium clusters for $d_1 = 0.1$ nm	170
6.8	Electric field values and current density in z-direction in the center between the two Sodium clusters for $d_2 = 0.5$ nm	171
6.9	Decomposition of the total electric field into transverse and longitudinal components for the dimer with $d_1 = 0.1$ nm	173
6.10	Decomposition of the electric field as in Figure 6.9 for the sodium dimer with $d_2 = 0.5$ nm.	174
6.11	Contour plots for the electric field enhancement in the x-z plane of the nanoplasmonic dimer with $d_1 = 0.1$ nm	175
6.12	Matter and electromagnetic energies for the sodium dimer with $d_1 = 0.1$ nm separation	177
6.13	Matter and electromagnetic energies for the sodium dimer with $d_2 = 0.5$ nm separation	178
6.14	Position expectation value of the nanoplasmonic dimer with $d_1 = 0.1$ nm separation	180
6.15	Fourier transform of the dipole expectation values and the electric field at the far-field detectors	181
6.16	Same as Figure 6.12 but now including the motion of the ions in classical Ehrenfest approximation.	182
6.17	Electric field, Maxwell energy and dipole expectation value for the comparison between TDLDA, TDPBE, and fully coupled Maxwell to matter simulations	184

List of Tables

3.1	Simulation parameters for the Octopus and MEEP comparison run.	61
3.2	Physical and simulation parameters of external current simulation for screening the parameters of the PML absorbing boundaries.	83
3.3	Simulation parameters for the incident plane waves run with two interfering incident waves.	89
3.4	Simulation box and time parameters for the numerical dispersion run with an incident wave pulse	93
3.5	Simulation box and time parameters for the numerical dispersion run with an incident wave pulse	93
3.6	Simulation parameters for the laser pulse run that hits a cubic linear medium box	99
6.1	Table of acronyms that are used in the present work to indicate the level of EMPKS theory.	157
6.2	Simulation parameters for the sodium dimer for distances $d_1 = 0.1$ nm and $d_2 = 0.5$ nm.	162

Bibliography

- [1] A. Szabo and N. Ostlund, Modern Quantum Chemistry: Introduction to Advanced Electronic Structure Theory. Dover Books on Chemistry, Dover Publications, 2012.
- [2] R. Martin, L. Reining, and D. Ceperley, Interacting Electrons: Theory and Computational Approaches. Cambridge University Press, 2016.
- [3] U. Schollwöck, “The density-matrix renormalization group in the age of matrix product states,” Annals of Physics, vol. 326, no. 1, pp. 96 – 192, 2011.
- [4] E. Engel and R. M. Dreizler, Density functional theory: an advanced course. Springer Science & Business Media, 2011.
- [5] R. Loudon, The quantum theory of light. Oxford Science Publications, 1988.
- [6] G. Grynberg, A. Aspect, and C. Fabre, Introduction to quantum optics: from the semi-classical approach to quantized light. Cambridge University Press, 2010.
- [7] M. Born and E. Wolf, Principles of optics: electromagnetic theory of propagation, interference and diffraction of light. Elsevier, 2013.
- [8] R. Chikkaraddy, B. de Nijs, F. Benz, S. J. Barrow, O. A. Scherman, E. Rosta, A. Demetriadou, P. Fox, O. Hess, and J. J. Baumberg, “Single-molecule strong coupling at room temperature in plasmonic nanocavities,” Nature, vol. 535, no. 7610, pp. 127–130, 2016.
- [9] D. Wang, H. Kelkar, D. Martin-Cano, T. Utikal, S. Götzinger, and V. Sandoghdar, “Coherent coupling of a single molecule to a scanning fabry-perot microcavity,” Physical Review X, vol. 7, no. 2, p. 021014, 2017.
- [10] M. Sukharev and A. Nitzan, “Optics of exciton-plasmon nanomaterials,” Journal of Physics: Condensed Matter, vol. 29, no. 44, p. 443003, 2017.
- [11] T. W. Ebbesen, “Hybrid light–matter states in a molecular and material science perspective,” Accounts of Chemical Research, vol. 49, no. 11, pp. 2403–2412, 2016.

- [12] J. A. Hutchison, T. Schwartz, C. Genet, E. Devaux, and T. W. Ebbesen, “Modifying chemical landscapes by coupling to vacuum fields,” Angewandte Chemie International Edition, vol. 51, no. 7, pp. 1592–1596, 2012.
- [13] Y. S. Yamamoto, Y. Ozaki, and T. Itoh, “Recent progress and frontiers in the electromagnetic mechanism of surface-enhanced raman scattering,” Journal of Photochemistry and Photobiology C: Photochemistry Reviews, vol. 21, pp. 81–104, 2014.
- [14] X. Zhong, T. Chervy, L. Zhang, A. Thomas, J. George, C. Genet, J. A. Hutchison, and T. W. Ebbesen, “Energy transfer between spatially separated entangled molecules,” Angewandte Chemie International Edition, vol. 56, no. 31, pp. 9034–9038.
- [15] A. Shalabney, J. George, H. Hiura, J. A. Hutchison, C. Genet, P. Hellwig, and T. W. Ebbesen, “Enhanced raman scattering from vibro-polariton hybrid states,” Angewandte Chemie International Edition, vol. 54, no. 27, pp. 7971–7975, 2015.
- [16] T. Byrnes, N. Y. Kim, and Y. Yamamoto, “Exciton-polariton condensates,” Nature Physics, vol. 10, no. 11, pp. 803–813, 2014.
- [17] A. Sommer, E. Bothschafter, S. Sato, C. Jakubeit, T. Latka, O. Razskazovskaya, H. Fattahi, M. Jobst, W. Schweinberger, V. Shirvanyan, et al., “Attosecond nonlinear polarization and light–matter energy transfer in solids,” Nature, vol. 534, no. 7605, p. 86, 2016.
- [18] J. J. Maki, M. S. Malcuit, J. Sipe, and R. W. Boyd, “Linear and nonlinear optical measurements of the Lorentz local field,” Physical Review Letters, vol. 67, no. 8, p. 972, 1991.
- [19] T. H. Taminiau, S. Karaveli, N. F. Van Hulst, and R. Zia, “Quantifying the magnetic nature of light emission,” Nature communications, vol. 3, p. 979, 2012.
- [20] C. T. Schmiegelow, J. Schulz, H. Kaufmann, T. Ruster, U. G. Poschinger, and F. Schmidt-Kaler, “Transfer of optical orbital angular momentum to a bound electron,” Nature communications, vol. 7, p. 12998, 2016.
- [21] I. Bialynicki-Birula and Z. Bialynicka-Birula, “Quantum numbers and spectra of structured light,” Physica Scripta, vol. 93, no. 10, p. 104005, 2018.
- [22] Z. Yue, H. Ren, S. Wei, J. Lin, and M. Gu, “Angular-momentum nanometrology in an ultrathin plasmonic topological insulator film,” Nature Communications, vol. 9, no. 1, p. 4413, 2018.
- [23] H. R. Zengji Yue and M. Gu, “Angular-momentum nanometrology in an ultrathin plasmonic topological insulator film,” Nature Communications, vol. 9, 2018.

- [24] D. M. Coles, Y. Yang, Y. Wang, R. T. Grant, R. A. Taylor, S. K. Saikin, A. Aspuru-Guzik, D. G. Lidzey, J. K.-H. Tang, and J. M. Smith, “Strong coupling between chlorosomes of photosynthetic bacteria and a confined optical cavity mode,” Nature communications, vol. 5, 2014.
- [25] M. Ruggenthaler, N. Tancogne-Dejean, J. Flick, H. Appel, and A. Rubio, “From a quantum-electrodynamical light–matter description to novel spectroscopies,” Nature Reviews Chemistry, vol. 2, no. 3, p. 0118, 2018.
- [26] G. H. Booth, A. J. W. Thom, and A. Alavi, “Fermion monte carlo without fixed nodes: A game of life, death, and annihilation in slater determinant space,” The Journal of Chemical Physics, vol. 131, no. 5, p. 054106, 2009.
- [27] R. Orus, “A practical introduction to tensor networks: Matrix product states and projected entangled pair states,” Annals of Physics, vol. 349, pp. 117 – 158, 2014.
- [28] U. Schollwöck, “The density-matrix renormalization group,” Rev. Mod. Phys., vol. 77, pp. 259–315, Apr 2005.
- [29] G. Kotliar, S. Y. Savrasov, K. Haule, V. S. Oudovenko, O. Parcollet, and C. A. Marianetti, “Electronic structure calculations with dynamical mean-field theory,” Rev. Mod. Phys., vol. 78, pp. 865–951, Aug 2006.
- [30] E. Gull, A. J. Millis, A. I. Lichtenstein, A. N. Rubtsov, M. Troyer, and P. Werner, “Continuous-time Monte Carlo methods for quantum impurity models,” Rev. Mod. Phys., vol. 83, pp. 349–404, May 2011.
- [31] W. Metzner, M. Salmhofer, C. Honerkamp, V. Meden, and K. Schönhammer, “Functional renormalization group approach to correlated fermion systems,” Rev. Mod. Phys., vol. 84, pp. 299–352, Mar 2012.
- [32] H. Aoki, N. Tsuji, M. Eckstein, M. Kollar, T. Oka, and P. Werner, “Nonequilibrium dynamical mean-field theory and its applications,” Rev. Mod. Phys., vol. 86, pp. 779–837, Jun 2014.
- [33] A. Abedi, N. T. Maitra, and E. K. Gross, “Exact factorization of the time-dependent electron-nuclear wave function,” Physical Review Letters, vol. 105, no. 12, p. 123002, 2010.
- [34] A. Abedi, N. T. Maitra, and E. Gross, “Correlated electron-nuclear dynamics: Exact factorization of the molecular wavefunction,” The Journal of Chemical Physics, vol. 137, no. 22, p. 22A530, 2012.
- [35] R. Kapral, “Quantum dynamics in open quantum-classical systems,” Journal of Physics: Condensed Matter, vol. 27, no. 7, p. 073201, 2015.
- [36] J. C. Tully, “Perspective: Nonadiabatic dynamics theory,” The Journal of Chemical Physics, vol. 137, no. 22, p. 22A301, 2012.

- [37] W. H. Miller, “Perspective: Quantum or classical coherence?,” The Journal of Chemical Physics, vol. 136, no. 21, p. 210901, 2012.
- [38] E. Lorin, S. Chelkowski, and A. Bandrauk, “A numerical Maxwell–Schrödinger model for intense laser–matter interaction and propagation,” Computer Physics Communications, vol. 177, no. 12, pp. 908–932, 2007.
- [39] K. Lopata and D. Neuhauser, “Multiscale Maxwell–Schrödinger modeling: A split field finite-difference time-domain approach to molecular nanopolaritonics,” The Journal of chemical physics, vol. 130, no. 10, p. 104707, 2009.
- [40] K. Yabana, T. Sugiyama, Y. Shinohara, T. Otobe, and G. F. Bertsch, “Time-dependent density functional theory for strong electromagnetic fields in crystalline solids,” Phys. Rev. B, vol. 85, p. 045134, Jan 2012.
- [41] M. Lucchini, S. A. Sato, A. Ludwig, J. Herrmann, M. Volkov, L. Kasmi, Y. Shinohara, K. Yabana, L. Gallmann, and U. Keller, “Attosecond dynamical Franz-Keldysh effect in polycrystalline diamond,” Science, vol. 353, no. 6302, pp. 916–919, 2016.
- [42] Y. Li, S. He, A. Russakoff, and K. Varga, “Accurate time propagation method for the coupled maxwell and kohn-sham equations,” Phys. Rev. E, vol. 94, p. 023314, Aug 2016.
- [43] A. Yamada and K. Yabana, “Energy transfer from intense laser pulse to dielectrics in time-dependent density functional theory,” ArXiv e-prints, July 2018.
- [44] A. Yamada and K. Yabana, “Time-dependent density functional theory for a unified description of ultrafast dynamics: pulsed light, electrons, and atoms in crystalline solids,” ArXiv e-prints, Oct. 2018.
- [45] M. Uemoto, Y. Kuwabara, S. A. Sato, and K. Yabana, “Nonlinear polarization evolution using time-dependent density functional theory,” ArXiv e-prints, Oct. 2018.
- [46] S. Yamada, M. Noda, K. Nobusada, and K. Yabana, “Time-dependent density functional theory for interaction of ultrashort light pulse with thin materials,” ArXiv e-prints, Oct. 2018.
- [47] M. Ruggenthaler, F. Mackenroth, and D. Bauer, “Time-dependent Kohn-Sham approach to quantum electrodynamics,” Physical Review A, vol. 84, no. 4, p. 042107, 2011.
- [48] I. Tokatly, “Time-dependent density functional theory for many-electron systems interacting with cavity photons,” Physical Review Letters, vol. 110, no. 23, p. 233001, 2013.

- [49] M. Ruggenthaler, J. Flick, C. Pellegrini, H. Appel, I. V. Tokatly, and A. Rubio, “Quantum-electrodynamical density-functional theory: Bridging quantum optics and electronic-structure theory,” Physical Review A, vol. 90, no. 1, p. 012508, 2014.
- [50] M. Ruggenthaler, “Ground-state quantum-electrodynamical density-functional theory,” arXiv preprint arXiv:1509.01417, 2015.
- [51] J. Galego, F. J. Garcia-Vidal, and J. Feist, “Cavity-induced modifications of molecular structure in the strong-coupling regime,” Physical Review X, vol. 5, no. 4, p. 041022, 2015.
- [52] J. Flick, N. Rivera, and P. Narang, “Strong light-matter coupling in quantum chemistry and quantum photonics,” Nanophotonics, vol. 7, no. 9, pp. 1479–1501, 2018.
- [53] J. Feist, J. Galego, and F. J. Garcia-Vidal, “Polaritonic chemistry with organic molecules,” ACS Photonics, 2017.
- [54] R. F. Ribeiro, L. A. Martínez-Martínez, M. Du, J. Campos-Gonzalez-Angulo, and J. Y. Zhou, “Polariton chemistry: controlling molecular dynamics with optical cavities,” Chemical Science, 2018.
- [55] P. M. M. C. de Melo and A. Marini, “Unified theory of quantized electrons, phonons, and photons out of equilibrium: A simplified ab initio approach based on the generalized Baym-Kadanoff ansatz,” Phys. Rev. B, vol. 93, p. 155102, Apr 2016.
- [56] J. Flick, H. Appel, M. Ruggenthaler, and A. Rubio, “Cavity Born–Oppenheimer approximation for correlated electron–nuclear–photon systems,” Journal of chemical theory and computation, vol. 13, no. 4, pp. 1616–1625, 2017.
- [57] J. Flick and P. Narang, “Cavity correlated electron-nuclear dynamics from first principles,” ArXiv e-prints, 2018.
- [58] C. Schäfer, M. Ruggenthaler, and A. Rubio, “Ab initio nonrelativistic quantum electrodynamics: Bridging quantum chemistry and quantum optics from weak to strong coupling,” Physical Review A, vol. 98, no. 4, p. 043801, 2018.
- [59] J. Flick, D. M. Welakuh, M. Ruggenthaler, H. Appel, and A. Rubio, “Light-matter response functions in quantum-electrodynamical density-functional theory: Modifications of spectra and of the maxwell equations,” arXiv preprint arXiv:1803.02519, 2018.
- [60] J. Flick, M. Ruggenthaler, H. Appel, and A. Rubio, “Atoms and molecules in cavities, from weak to strong coupling in quantum-electrodynamics (QED) chemistry,” Proceedings of the National Academy of Sciences, p. 201615509, 2017.

- [61] J. Flick, C. Schäfer, M. Ruggenthaler, H. Appel, and A. Rubio, “Ab Initio Optimized Effective Potentials for Real Molecules in Optical Cavities: Photon Contributions to the Molecular Ground State,” ACS photonics, vol. 5, no. 3, pp. 992–1005, 2018.
- [62] H. Spohn, Dynamics of charged particles and their radiation field. Cambridge university press, 2004.
- [63] R. Jestädt, M. Ruggenthaler, M. J. Oliveira, A. Rubio, and H. Appel, “Light-matter interactions within the ehrenfest-maxwell-pauli-kohn-sham framework: fundamentals, implementation, and nano-optical applications,” Advances in physics, vol. 68, pp. 225–333, Dec 2019.
- [64] K. Yee, “Numerical solution of initial boundary value problems involving Maxwell’s equations in isotropic media,” Antennas and Propagation, IEEE Transactions on, vol. 14, pp. 302–307, May 1966.
- [65] A. Taflove and S. Hagness, Computational Electrodynamics: The Finite-difference Time-domain Method. Artech House antennas and propagation library, Artech House, 2005.
- [66] R. Dreizler and E. Gross, Density Functional Theory. Berlin: Springer Verlag, 1990.
- [67] M. A. Marques, Time-Dependent Density Functional Theory, vol. 706 of Lecture Notes in Physics. Springer, berlin, heidelberg ed., 2006.
- [68] L. Silberstein, “Elektromagnetische Grundgleichungen in bivectorieller Behandlung,” Annalen der Physik, vol. 327, pp. 579–586, 1907.
- [69] M. H. L. Pryce, “The mass-centre in the restricted theory of relativity and its connexion with the quantum theory of elementary particles,” Proceedings of the Royal Society of London A: Mathematical, Physical and Engineering Sciences, vol. 195, no. 1040, pp. 62–81, 1948.
- [70] A. Gersten, “Maxwells Equations as the One-Photon Quantum Equation,” Foundations of Physics Letters, vol. 12, no. 3, pp. 291–298, 1999.
- [71] P. J. Mohr, “Solutions of the maxwell equations and photon wave functions,” Annals of Physics, vol. 325, no. 3, pp. 607 – 663, 2010.
- [72] I. Bialynicki-Birula, “On the wave function of the photon,” Acta Physica Polonica A, vol. 86, pp. 97–116, 1994.
- [73] I. Bialynicki-Birula, “V photon wave function,” vol. 36 of Progress in Optics, pp. 245–294, Elsevier, 1996.

- [74] S. A. Khan, “An Exact Matrix Representation of Maxwell’s Equations,” Physica Scripta, vol. 71, no. 5, p. 440, 2005.
- [75] J. Jackson, Classical Electrodynamics. Wiley, 1998.
- [76] E. Wigner and J. Griffin, Group Theory and Its Application to the Quantum Mechanics of Atomic Spectra. Pure and applied Physics, Academic Press, 1959.
- [77] O. Keller, “Space-time description of photon emission from an atom,” Phys. Rev. A, vol. 62, p. 022111, Jul 2000.
- [78] O. Keller, Quantum Theory of Near-Field Electrodynamics. Springer, 2011.
- [79] M. Fox, Quantum optics: an introduction. Oxford Master Series in Atomic, Optical and Laser Physics, Oxford: Oxford Univ. Press, 2006.
- [80] D. J. Griffiths, Introduction to electrodynamics; 4th ed. Boston, MA: Pearson, 2013. Re-published by Cambridge University Press in 2017.
- [81] E. Schrödinger, “An undulatory theory of the mechanics of atoms and molecules,” Phys. Rev., vol. 28, pp. 1049–1070, Dec 1926.
- [82] D. Griffiths, Introduction to Quantum Mechanics. Always learning, Pearson, 2014.
- [83] V. Moretti, Spectral Theory and Quantum Mechanics. Springer-Verlag Mairland, 2013.
- [84] I. Serban, J. Werschnik, and E. K. U. Gross, “Optimal control of time-dependent targets,” Phys. Rev. A, vol. 71, p. 053810, May 2005.
- [85] M. Ndong, H. Tal-Ezer, R. Kosloff, and C. P. Koch, “A Chebychev propagator for inhomogeneous Schrödinger equations,” The Journal of Chemical Physics, vol. 130, no. 12, 2009.
- [86] R. Parr and Y. Weitao, Density-Functional Theory of Atoms and Molecules. International Series of Monographs on Chemistry, Oxford University Press, 1994.
- [87] J. Bérenger, Perfectly Matched Layer (PML) for Computational Electromagnetics. Synthesis lectures on computational electromagnetics, Morgan & Claypool Publishers, 2007.
- [88] A. F. Oskooi, D. Roundy, M. Ibanescu, P. Bermel, J. Joannopoulos, and S. G. Johnson, “Meep: A flexible free-software package for electromagnetic simulations by the FDTD method,” Computer Physics Communications, vol. 181, no. 3, pp. 687 – 702, 2010.
- [89] A. Itkin, Pricing Derivates Under Lévy Models. Pseudo-Differential Operators, Birkhäuser Basel, 2017.

- [90] J. Strikwerda, Finite Difference Schemes and Partial Differential Equations. Other Titles in Applied Mathematics, Society for Industrial and Applied Mathematics (SIAM, 3600 Market Street, Floor 6, Philadelphia, PA 19104), 2004.
- [91] H. Levy and F. Lessman, Finite Difference Equations. Macmillan, 1961.
- [92] G. Smith, Numerical Solution of Partial Differential Equations: Finite Difference Methods. Oxford Applied Mathematics and, Clarendon Press, 1985.
- [93] A. Castro, H. Appel, M. Oliveira, C. A. Rozzi, X. Andrade, F. Lorenzen, M. A. L. Marques, E. K. U. Gross, and A. Rubio, “octopus: a tool for the application of time-dependent density functional theory,” physica status solidi (b), vol. 243, no. 11, pp. 2465–2488.
- [94] R. Courant, K. Friedrichs, and H. Lewy, “Über die partiellen Differenzgleichungen der mathematischen Physik,” Mathematische Annalen, vol. 100, pp. 32–74, 1928.
- [95] R. Courant, K. Friedrichs, and H. Lewy, “On the Partial Difference Equations of Mathematical Physics,” IBM Journal of Research and Development, vol. 11, pp. 215–234, Mar. 1967.
- [96] J.-M. Jin, M. Zunoubi, K. C. Donepudi, and W. C. Chew, “Frequency-domain and time-domain finite-element solution of maxwell’s equations using spectral lanczos decomposition method,” Computer Methods in Applied Mechanics and Engineering, vol. 169, no. 3, pp. 279 – 296, 1999.
- [97] V. Dolean, H. Fol, S. Lanteri, and R. Perrussel, “Solution of the time-harmonic maxwell equations using discontinuous galerkin methods,” Journal of Computational and Applied Mathematics, vol. 218, no. 2, pp. 435 – 445, 2008. The Proceedings of the Twelfth International Congress on Computational and Applied Mathematics.
- [98] J.-P. Berenger, “Three-dimensional perfectly matched layer for the absorption of electromagnetic waves,” Journal of Computational Physics, vol. 127, no. 2, pp. 363 – 379, 1996.
- [99] R. J. Luebbers and F. Hunsberger, “FDTD for nth-order dispersive media,” IEEE Transactions on Antennas and Propagation, vol. 40, pp. 1297–1301, Nov 1992.
- [100] S. Weinberg, The Quantum Theory of Fields. No. Bd. 2 in The Quantum Theory of Fields 3 Volume Hardback Set, Cambridge University Press, 1995.
- [101] W. Greiner and J. Reinhardt, Field quantization. Springer, 2013.
- [102] W. Greiner, Classical electrodynamics. Classical theoretical physics, New York: Springer, first edition ed., 1998. Includes index.

- [103] E. Zeidler, Quantum Field Theory II: Quantum Electrodynamics. Springer, 2009.
- [104] A. L. Fetter and J. D. Walecka, Quantum Theory of Many-Particle Systems. Boston: McGraw-Hill, 1971.
- [105] P. Hohenberg and W. Kohn, “Inhomogeneous electron gas,” Phys. Rev., vol. 136, pp. B864–71, 1964.
- [106] E. Runge and E. K. U. Gross, “Density-functional theory for time-dependent systems,” Phys. Rev. Lett., vol. 52, pp. 997–1000, Mar 1984.
- [107] R. Jestädt, M. Ruggenthaler, M. J. Oliveira, A. Rubio, and H. Appel, “Real-time solutions of coupled ehrenfest-maxwell-pauli-kohn-sham equations: fundamentals, implementation, and nano-optical applications,” The Archive (ArXiv.org), pp. 1–54, Dec 2018.
- [108] M. Ruggenthaler, J. Flick, C. Pellegrini, H. Appel, I. V. Tokatly, and A. Rubio, “Quantum-electrodynamical density-functional theory: Bridging quantum optics and electronic-structure theory,” Phys. Rev. A, vol. 90, Jul 2014.
- [109] W. Kohn and L. J. Sham, “Self-consistent equations including exchange and correlation effects,” Phys. Rev., vol. 140, p. A1133, 1965.
- [110] I. Tokatly, “Quantum many-body dynamics in a Lagrangian frame: II. Geometric formulation of time-dependent density functional theory,” Physical Review B, vol. 71, no. 16, p. 165105, 2005.
- [111] M. Ruggenthaler, M. Penz, and R. Van Leeuwen, “Existence, uniqueness, and construction of the density-potential mapping in time-dependent density-functional theory,” Journal of Physics: Condensed Matter, vol. 27, no. 20, p. 203202, 2015.
- [112] H. O. John W. Negele, Quantum many-particle systems. Advanced books classics, Westview Press, 1998.
- [113] J. W. Furness, J. Verbeke, E. I. Tellgren, S. Stopkowicz, U. Ekström, T. Helgaker, and A. M. Teale, “Current density functional theory using meta-generalized gradient exchange-correlation functionals,” Journal of Chemical Theory and Computation, vol. 11, no. 9, pp. 4169–4181, 2015. PMID: 26575912.
- [114] W. Kohn and L. Sham, “Self-consistent equations including exchange and correlation effects,” Phys. Rev., vol. 140 (4A), pp. 1133–1138, 1965.
- [115] S. K. Min, F. Agostini, I. Tavernelli, and E. K. Gross, “Ab initio nonadiabatic dynamics with coupled trajectories: A rigorous approach to quantum (de) coherence,” The journal of physical chemistry letters, vol. 8, no. 13, pp. 3048–3055, 2017.

- [116] X. A. et al., “Modified ehrenfest formalism for efficient large-scale ab initio molecular dynamic,” Journal of Chemical Theory and Computation, vol. 5, pp. 728–741, Apr 2009.
- [117] G. Arfken and H. Weber, Mathematical Methods For Physicists International Student Edition. Elsevier Science, 2005.
- [118] J. J. Sakurai, Modern Quantum Mechanics (Revised Edition). Addison Wesley, 1 ed., Sept. 1993.
- [119] A. Castro, M. A. L. Marques, and A. Rubio, “Propagators for the time-dependent KohnSham equations,” The Journal of Chemical Physics, vol. 121, no. 8, pp. 3425–3433, 2004.
- [120] A. Gmez Pueyo, M. A. L. Marques, A. Rubio, and A. Castro, “Propagators for the time-dependent kohnsham equations: Multistep, rungekutta, exponential rungekutta, and commutator free magnus methods,” Journal of Chemical Theory and Computation, vol. 14, no. 6, pp. 3040–3052, 2018. PMID: 29672048.
- [121] R. Loudon, The Quantum Theory of Light. Oxford: Clarendon Press, second ed., 1983.
- [122] V. Rokaj, D. M. Welakuh, M. Ruggenthaler, and A. Rubio, “Light–matter interaction in the long-wavelength limit: no ground-state without dipole self-energy,” Journal of Physics B: Atomic, Molecular and Optical Physics, vol. 51, no. 3, p. 034005, 2018.
- [123] X. Andrade, D. Strubbe, U. De Giovannini, A. H. Larsen, M. J. T. Oliveira, J. Alberdi-Rodriguez, A. Varas, I. Theophilou, N. Helbig, M. J. Verstraete, L. Stella, F. Nogueira, A. Aspuru-Guzik, A. Castro, M. A. L. Marques, and A. Rubio, “Real-space grids and the octopus code as tools for the development of new simulation approaches for electronic systems,” Phys. Chem. Chem. Phys., vol. 17, pp. 31371–31396, 2015.
- [124] M. A. Marques, A. Castro, G. F. Bertsch, and A. Rubio, “octopus: a first-principles tool for excited electronion dynamicse-mail: octopus@tddft.org,” Computer Physics Communications, vol. 151, no. 1, pp. 60 – 78, 2003.
- [125] e. a. A. Ojanpera, “Nonadiabatic ehrenfest molecular dynamics within the projector augmented-wave method,” J. Chem. Phys., vol. 136, 2012.
- [126] A. Varas, P. Garca-Gonzlez, F. J. Garca-Vidal, and A. Rubio, “Anisotropy effects on the plasmonic response of nanoparticle dimers,” The Journal of Physical Chemistry Letters, vol. 6, no. 10, pp. 1891–1898, 2015. PMID: 26263265.
- [127] E. G. Noya, J. P. Doye, D. J. Wales, and Aguado, “Geometric magic numbers of sodium clusters: Interpretation of the melting behaviour,” The European Physical Journal D, vol. 43, pp. 57–60, Jul 2007.

- [128] D. J. W. et. al. <http://www-wales.ch.cam.ac.uk/CCD.html>, 2018. The relaxed atomic structure of the dimer is taken from the Cambridge Cluster Database.
- [129] X. G. et. al., “Abinit: First-principles approach to material and nanosystem properties,” Computer Physics Communications, vol. 180, no. 12, pp. 2582–2615, 2009.
- [130] J. P. Perdew, K. Burke, and M. Ernzerhof, “Generalized gradient approximation made simple,” Phys. Rev. Lett., vol. 77, pp. 3865–3868, Oct 1996.
- [131] R. Jestädt, M. Ruggenthaler, M. J. Oliveira, A. Rubio, and H. Appel, “Real-time dynamics of nanoplasmonic dimer, distance $d = 0.1$ nm,” nov 2018.
- [132] R. Jestädt, M. Ruggenthaler, M. J. Oliveira, A. Rubio, and H. Appel, “Real-time dynamics of nanoplasmonic dimer, distance $d = 0.5$ nm,” nov 2018.
- [133] B. Thaller, The dirac equation. Springer Science & Business Media, 2013.
- [134] A. Komech, Quantum Mechanics Genesis and Achievements. Dordrecht: Springer, 2013.
- [135] T. Miyao and H. Spohn, “Spectral analysis of the semi-relativistic Pauli–Fierz hamiltonian,” Journal of Functional Analysis, vol. 256, pp. 2123–2156, 2009.
- [136] M. Könenberg, O. Matte, and E. Stockmeyer, “Existence of ground states of hydrogen-like atoms in relativistic QED I: the semi-relativistic Pauli–Fierz operator,” Reviews in Mathematical Physics, vol. 23, no. 04, pp. 375–407, 2011.
- [137] F. Hiroshima, “Functional integral approach to semi-relativistic Pauli–Fierz models,” Advances in Mathematics, vol. 259, pp. 784 – 840, 2014.
- [138] W. Thirring, Quantum mathematical physics: atoms, molecules and large systems. Springer Science & Business Media, 2013.
- [139] P. W. Atkins and R. S. Friedman, Molecular quantum mechanics. 4th ed ed., 2005.
- [140] M. Nowakowski, “The quantum mechanical current of the pauli equation,” American Journal of Physics, vol. 67, no. 10, pp. 916–919, 1999.

Publications

Title: Light-matter interactions within the Ehrenfest-Maxwell-Pauli-Kohn-Sham framework: fundamentals, implementation, and nano-optical applications

Authors: René Jestädt¹, Michael Ruggenthaler¹, Micael J. T. Oliveira¹, Angel Rubio^{1,2}, and Heiko Appel¹

Affiliations: ¹ Max Planck Institute for the Structure and Dynamics of Matter, Center for Free Electron Laser Science, 22761 Hamburg, Germany
² Center for Computational Quantum Physics (CCQ), Flatiron Institute, 162 Fifth Avenue, New York NY 10010, USA

Journal: Advances in physics

Volume: 68

Issue: 4

Pages: 225-333

URL: <https://doi.org/10.1080/00018732.2019.1695875>

No. of pages: 106

Year: 2019

Title: Real-time solutions of coupled Ehrenfest-Maxwell-Pauli-Kohn-Sham equations: fundamentals, implementation, and nano-optical applications

Authors: René Jestädt¹, Michael Ruggenthaler¹, Micael J. T. Oliveira¹, Angel Rubio^{1,2}, and Heiko Appel¹

Affiliations: ¹ Max Planck Institute for the Structure and Dynamics of Matter, Center for Free Electron Laser Science, 22761 Hamburg, Germany
² Center for Computational Quantum Physics (CCQ), Flatiron Institute, 162 Fifth Avenue, New York NY 10010, USA

Journal: The Archive (ArXiv.org)

Article No.: 1812.05049

URL: <https://arxiv.org/abs/1812.05049>

No. of pages: 54

Year: 2018

- Title:** Octopus, a computational framework for exploring light-driven phenomena and quantum dynamics in extended and finite systems
- Authors:** Nicolas Tancogne-Dejean, Micael J. T. Oliveira, Xavier Andrade, Heiko Appel, Carlos H. Borca, Guillaume Le Breton, Florian Buchholz, Alberto Castro, Stefano Corni, Alfredo A. Correa, Umberto De Giovannini, Alain Delgado, Florian G. Eich, Johannes Flick, Gabriel Gil, Adrián Gomez, Nicole Helbig, Hannes Hubener, René Jestädt, Joaquim Jornet-Somoza, Ask H. Larsen, Irina V. Lebedeva, Martin Lüders, Miguel A. L. Marques, Sebastian T. Ohlmann, Silvio Pipolo, Markus-Rampp, Carlo A. Rozzi, David A. Strubbe, Shunsuke A. Sato, Christian Schäfer, Iris Theophilou, Alicia Welden, and Angel Rubio
- Journal:** Journal of Chemical Physics
- Article status:** submitted
- No. of pages:** 81
- Year:** 2020

Acronyms

Acronym	Description
DFT	Density-functional theory
ED	Electric dipole
EQ	Electric quadrupole
F	Forward coupling
F@ED	Forward coupling in ED approximation
F@(ED+MD+EQ)	Forward coupling in ED, MD and EQ approximation
FB	Forward-backward coupling
FB@ED	Forward-backward coupling in ED approximation
FB@(ED+MD+EQ)	Forward-backward coupling in ED, MD and EQ approximation
FDTD	Finite difference time domain
KS	Kohn-Sham
lm	Linear medium
MD	Magnetic dipole
MEEP	MIT Electromagnetic Equation Propagation
MIT	Massachusetts Institute of Technology
MPKS	Maxwell-Pauli-Kohn-Sham equations
Mx	Maxwell
PML	Perfectly matched layer
QED	Quantum electrodynamics
QEDFT	Quantum-electrodynamical density-functional theory
RS	Riemann-Silberstein

Acknowledgements

Successful work nowadays is never done alone and this thesis would never be possible without the help and support of many people

First of all, I want to thank my supervisor Heiko Appel for his amazing support, advices, group leading. I appreciate all the discussions and help for my thesis, also for the advises in using efficiently the computer.

I want to thank Angel Rubio for admitting me into his theory group at the MPSD, the advises, discussions, and providing a nice atmosphere for the scientific work.

I also want to thank Matthias Scheffler for his support at the beginning of my thesis, where I started to work for the FHI. It was very kind that I still could use my office some month longer although the group moved to Hamburg.

I am very thankful to all of my proofreaders, Michael Ruggenthaler, Christian Schäfer, Norah Hoffmann and again especially Heiko for correcting and improving my text, and to Michael Ruggenthaler for supporting me in the deeper theory background with our skype sessions.

I appreciate the whole affable working group first at the FHI and now at the MPSD, namely Christian, Florian, Guillem, Heiko, Henning, Johannes, Micael, Michael, Norah, Uliana, Tanja, Theresa.

I want to thank all my friends for supporting me, "spending power" and thinking of me during the harder time of the work, especially Agnes, Andres, Aquiles, Deniz, Didi, Freddy, Juan, Joe, Julia, Katja, Matthias, Raffi, Peter, and Rufina.

Finally, I want to thank my family, my mother, my dad, and my brother, for all the support in the last few years to go my way.

Colophon

The presented work was written with L^AT_EX with "Computer Modern" font. Graphical plots that show curves have been created using Python-Matplotlib. Technical and schematic drawings have been illustrated by using Python-Matplotlib and Inkscape. The contour plots and the movies of the three-dimensional simulation have been created by Visit 2.12.